Alma Mater Studiorum – Università di Bologna

DOTTORATO DI RICERCA IN

SCIENZE E TECNOLOGIE DELLA SALUTE

Ciclo 35

Settore Concorsuale: 09/G2 - BIOINGEGNERIA

Settore Scientifico Disciplinare: ING-IND/34 - BIOINGEGNERIA INDUSTRIALE

NUMERICAL SIMULATIONS OF THE SPINE FOR PATIENT-SPECIFIC MODELS OF SEVERE SCOLIOSIS

Presentata da: Samuele Luca Gould

Coordinatore Dottorato

Marco Viceconti

Supervisore

Luca Cristofolini

Co-Supervisore

Marco Viceconti

Tiziana Greggi

Esame finale anno 2022

Abstract

Many pathologies and disabilities are associated with the spine, including scoliosis. Scoliosis is a curving and twisting of the spine, which in severe cases may require highly invasive and complex surgical treatment. *In silico* methods, such as musculoskeletal modelling, may aid the selection of the optimal surgical treatment. However, computational models must be credible for use in clinical decision-making. Establishing credibility requires extensive model testing and validation. Many musculoskeletal models use a generic, simplified representation of the intervertebral joints. The intervertebral joint models the lumped behaviour of the ligaments and the intervertebral disc, which connect adjacent vertebrae and are fundamental to the flexibility of the spine. Therefore, to model and simulate the spine, a suitable representation of the intervertebral joint is crucial. This thesis developed and applied pipelines to investigate the characterisation of the intervertebral joint and created personalised scoliotic spine models. The aim of this PhD was to characterise specimen-specific models of the intervertebral joint for multi-body models from experimental datasets, in order to integrate the representation of the joint into a scoliotic musculoskeletal model. First, the project investigated the characterisation of a specimen-specific lumped parameter model of the intervertebral joint from an experimental dataset of a four-vertebra lumbar spine segment. A methodology using multibody modelling and optimisation techniques was established to determine the specimen-specific stiffness parameters. The stiffnesses in multiple degrees of freedom were simultaneously optimised for the specimen under an eccentric compressive load. A sensitivity study of the parameters to the joint pose was conducted to investigate the robustness of the method. The accuracy of the predicted motion was highly depended on both the joint pose and the stiffness. The variation in the joint stiffness between subjects and between spinal levels is well established. Following the first study, the method was reapplied to another dataset that included six complete lumbar spine segments under three different loading conditions. For each specimen, a homogeneous stiffness across the joints was calculated with an optimisation algorithm by minimising the kinematic error. Further, to investigate the assumption of a homogeneous stiffness across levels, a fixed ratio of the stiffnesses between levels was introduced. Comparisons of the kinematic error and the stiffnesses pre- and post-optimisation showed the optimised stiffness to be representative only in the loading condition for which it was optimised. Further, when considering a specimen-specific stiffness, generic ratios were unable to suitably account for level dependency, thus optimisation methods should consider each joint level individually. Secondly, a framework to create subject-specific musculoskeletal models of individuals with severe scoliosis was developed. An existing healthy spine model was modified, and a virtual landmark palpation protocol was established on CT data of an individual with severe scoliosis. A code was developed to create a patient-specific scoliotic spine musculoskeletal model from the landmarks and the modified model. The intra- and inter-operator variability of the virtually palpated landmark positions was analysed, and the accuracy of the model was assessed. This resulted in a codified pipeline for creating subject-specific, severely scoliotic spine models from CT data. In conclusion, this thesis showed that specimen-specific intervertebral joint stiffnesses were highly sensitive to joint pose definition and the importance of level-dependent optimisation. Further, an open-source codified pipeline to create patient-specific scoliotic spine models from CT data was released. These studies and this pipeline can facilitate the specimen-specific characterisation of the scoliotic intervertebral joint and its incorporation into scoliotic musculoskeletal spine models.

List of the main Abbreviations

3D	-	Three-dimensional
AIS	-	Adolescent idiopathic scoliosis
CA	-	Cobb angle
CoM	-	Centre of mass
CoR	-	Centre of rotation
CT	-	Computed Tomography
DIC	-	Digital image correlation
DoF	-	Degree of freedom
EMG	-	Electromyogram
FE	-	Finite element
FEM	-	Finite Element Modelling
FJF	-	Facet joint forces
FSU	-	Functional spinal unit
IDP	-	Intradiscal pressure
ICC	-	Intraclass correlation coefficient
IQR	-	Interquartile range
ISB	-	International Society of Biomechanics
IVD	-	Intervertebral disc
IVJ	-	Intervertebral joint
LL	-	Lumbar lordosis
MBM	-	Multi-body model
MRI	-	Magnetic resonance imaging
MSK	-	Musculoskeletal

RMSE	-	Root mean square error

Table of Contents

Thesis overview

Here the structure of this thesis will be explained, and a broad overview of the different chapters will be provided.

This thesis is structured in four sections. Each section addresses a broad aspect of the thesis (introduction, characterisation of the intervertebral joint, scoliotic spine modelling, and conclusions of the thesis). Chapters are contained within sections and discuss a specific topic or research question. The three chapters (chapters 3, 4, and 5) which address a research question are structured as journal articles with an introduction, methodology, results, and discussion.

Section 1 – Introduction, contains two chapters:

- Chapter 1: The Spine and Scoliosis – Presents the background, rationale and aim of this thesis.
- Chapter 2: Computational modelling of the scoliotic spine: A literature review – a discussion of the state-of-the-art knowledge on finite element (FE) and musculoskeletal (MSK) modelling of the spine. It addresses the modelling of the healthy and scoliotic spine and the application and limitations of the current models.

Section 2 – Characterization of the intervertebral joint for multibody models of the spine, focuses on the characterisation of the IVJ for MSK models from experimental data of non-pathological specimens. This section is divided into two chapters:

- Chapter 3: Experimental identification of a lumped-parameter model of the intervertebral disc (IVD) – A methodology using an optimisation technique to determine a specimen-specific lumped parameter model of the IVJ from an experimental dataset is established. Recommendations are given regarding the data required to determine specimen-specific models of the IVJ. Additionally, the sensitivity of this optimisation technique to the joint pose is explored.
- Chapter 4: Variability of intervertebral joint stiffness between spine levels and between specimens – The methodology previously determined is reapplied to a dataset of specimens with more vertebral levels and is used to investigate the inter-specimen variability and the level dependency.

Section 3 – Scoliotic spine modelling, is a single chapter:

- Chapter 5: Generation of severely scoliotic subject-specific musculoskeletal models – discusses the code which generates a severely scoliotic MSK model from a generic MSK spine model and a set of virtually palpated landmarks. The generic model was developed from an existing model, the modifications are presented and explained. The accuracy of the model is assessed by examining the curvature and vertebrae positions, and the inter- and intra-operator variability of the virtual palpations is investigated.

Section 4 – Closing remarks, a section to maintain structure consistency for the concluding chapter:

- Chapter 6: Conclusions and future work, which presents the conclusion of this thesis and the next steps that should be taken in the Author's opinion to develop MSK models to be used as a pre-operative planning tool to aid the surgeon in the correction of severe scoliosis.

Section 1 – Introduction

The Spine and Scoliosis

The current chapter provides a brief overview of the human spinal anatomy and physiology. The underlying motivation for this thesis was to aid the treatment of the spinal disorder scoliosis. Therefore, in addition to the description of spinal anatomy and physiology, a definition of scoliosis is given, as well as a description of its impacts on those who live with it, its treatment, and why there is a need for further research in this area. Although the spine is substantially more complex than what is presented, the intention is to provide a basic overview of the spine and sufficient detail to understand the later chapters. Next, the current knowledge is briefly discussed, which includes an overview of the tools used in this research project. Finally, the aims and the structure of the thesis are presented.

1.1. Overview of the anatomy and physiology

1.1.1. The spine

The spine plays three vital roles in the daily functioning of the human body. It provides a supporting structure, protects the spinal cord, and enables motion of the trunk [1,2]. To perform these functions, it is organised as a series of functional spinal units (FSU) (Figure 1.1), an FSU is defined as two adjacent vertebrae and the connecting ligaments and IVD [2] – grouped together with the facet joints these soft tissues are often referred to as the intervertebral joint (IVJ). This forms the smallest motion unit of the spine [2].

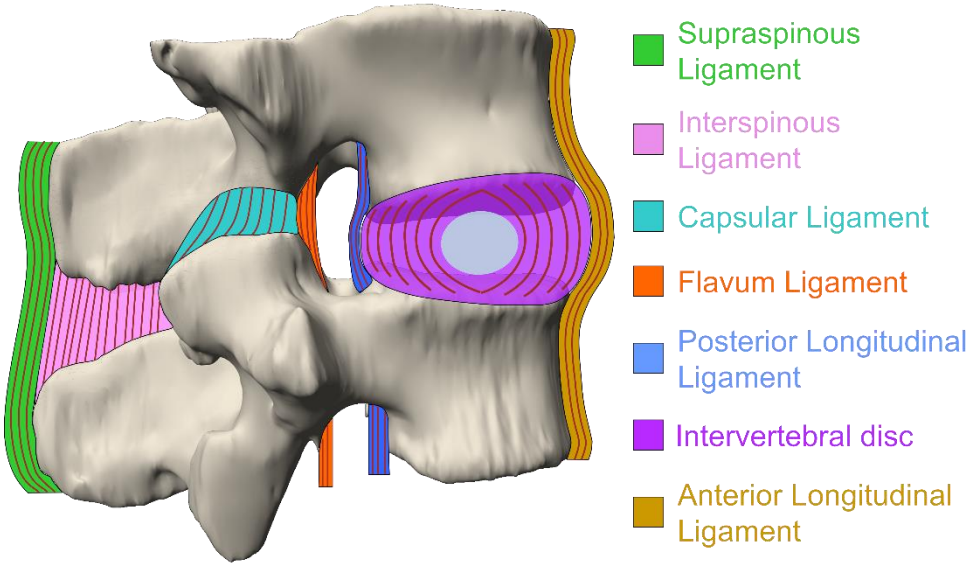

Figure 1.1: Anatomy of the FSU, showing two adjacent vertebrae and the connecting ligaments, synovial facet joints and the intervertebral disc (inspired by Ruspi et al. 2019 [3]).

These units are organised into distinct sections, the lumbar spine (five vertebrae), the thoracic spine (twelve vertebrae), the cervical spine (seven vertebrae), the sacrum (five vertebrae), and the coccyx (three-four vertebrae) (Figure 1.2) [2]. In adulthood the coccyx and sacrum fuse to form a single bony structure. Typically, a healthy spine is symmetric and straight in the frontal plane. In the sagittal plane, there are three main curves, the anteriorly convex cervical and lumbar curves (lordosis), and the posteriorly convex thoracic curve (kyphosis).

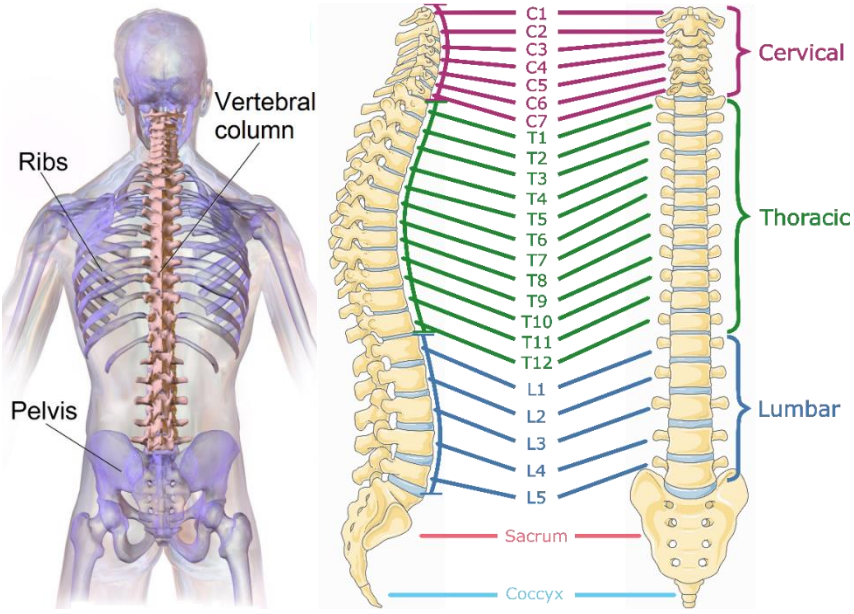

Figure 1.2: Left – Spine in the centre of the body providing a supporting structure, connected to the ribs and the pelvis (Image: BruceBlaus DOI:10.15347/wjm/2014.010, CC by 3.0, via Wikimedia Commons) Right – Lateral and frontal view of the spine, with the cervical (purple), thoracic (green), lumbar (blue), sacrum (pink), and coccyx (pink) labelled (Adapted (labels added) from original image: Laboratoires Servier, CC by 3.0, via Wikimedia Commons).

1.1.2. The vertebra

The vertebrae (Figure 1.3) are irregular bones and their morphology changes with the spinal level [2]. However, the basic structure from C3 to L5 is the same. The vertebral body is mostly cancellous bone with a thin surface of cortical bone surrounding it. Moving inferiorly from C3, the bodies become larger to support the increasing compressive loads [2]. The neural arch is the posterior part of the vertebra. This surrounds the spinal cord and includes the processes to which many of the spinal ligaments attach (Figure 1.1) [2]. The neural arches play a load-bearing role in flexion and extension [4], and as people age, an increasing share of the compressive forces are also transferred through it [4,5]. The main biomechanical function of the facet joints (the joint between the superior articular process of one vertebra and the inferior articular process of another) is to limit axial rotation of the spine, in addition to this, they resist anterior shear loading [2,6].

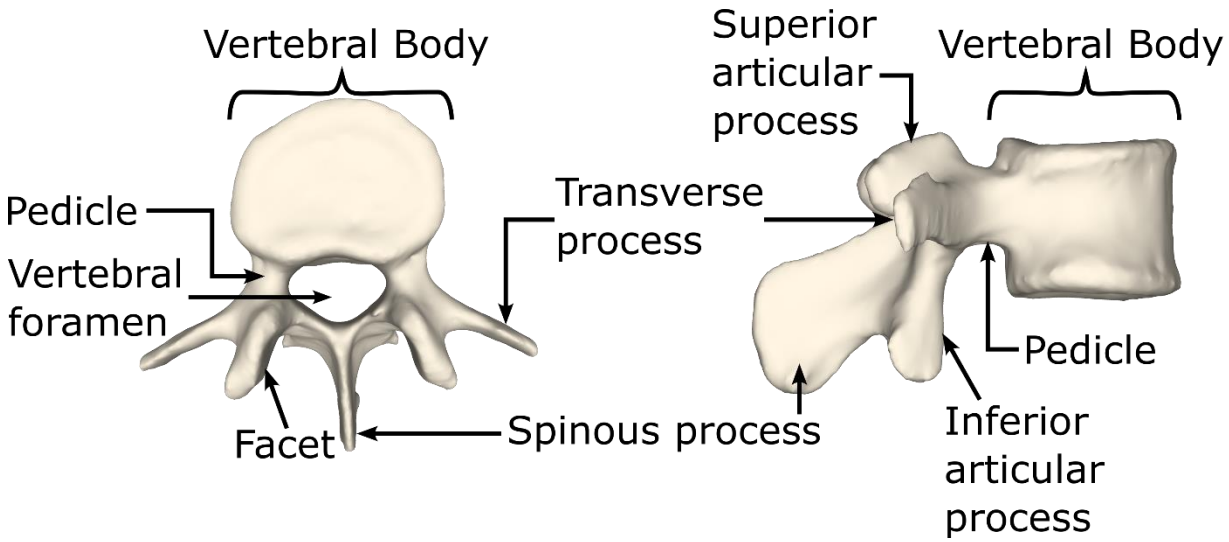

Figure 1.3: Structure of an L3 vertebra, left–superior view, right–lateral view.

1.1.3. The intervertebral disc and ligaments

The IVD is formed of three main components: the nucleus pulposus, the annulus fibrosus and the cartilaginous end plates [2,7]. The nucleus pulposus has a high water content [2,7] and also contains collagen type II and proteoglycan [7]. Surrounding the nucleus pulposus is the annulus fibrosus, which mostly consists of concentric layers of collagen type 1 fibre bundles, with alternating orientations between layers and water [2,7]. They attach to the cartilaginous end plates [2], which, like the nucleus pulposus is comprised of largely water, collagen type II and proteoglycan [7]. The cartilaginous endplates help with load distribution within the IVD and its thickness changes over time [2,7].

In general, the ligaments are uniaxial structures consisting of mostly collagen fibres running parallel to the ligaments' orientation [2,4]. They provide a resistive force along the fibre orientation in tension, which limits the extent of motion to protect the spinal cord and contributes to the stabilisation of the spine [2,4]. The anterior longitudinal ligament, posterior longitudinal ligament, and supraspinous ligament connect to multiple vertebrae, while the intertransverse ligaments (between transverse processes), interspinous ligaments, flavum ligament, and capsular ligaments connect adjacent vertebrae. Although they all share similar functions, the morphology and composition (in terms of elastin, proteoglycan, and water content in addition to the collagen fibres) of the ligaments are unique to reflect their biomechanical functions [2,4].

The ligaments and the IVD exhibit nonlinear viscoelastic behaviour as well as creep and relaxation [2,4,8]. Additionally, these properties differ between IVJ levels and vary with age and between individuals. Therefore, the FSU behaves in a highly nonlinear fashion, and its motion is coupled.

1.2. Scoliosis

Scoliosis is a three-dimensional (3D) deformity of the spine, presenting a lateral curvature of the spine (Figure 1.4) in the frontal plane, rotation of the vertebrae as well as potential alteration of the lordotic and kyphotic curvature [9–11]. Scoliosis is diagnosed when there is a Cobb angle, defined as the angle between the endplates of the vertebrae at the ends of the curve [12], greater than 10° and axial rotation of the vertebrae can be identified [10,11]. There are two broad categories of scoliosis: structural and non-structural (or functional) [10,13]. Non-structural scoliosis is a secondary result of a separate known medical issue, such as a difference in leg length

[10,13]. In this section, the focus will be on the more common, structural scoliosis [10,14]. Structural scoliosis can be further classified as: degenerative, idiopathic, congenital, or neuromuscular [13]. The cause of the most common type, idiopathic, remains unknown [10,13,15]. The reported prevalence of idiopathic scoliosis within the adolescent population is often around 3%, although higher and lower prevalence has been reported [10,11].

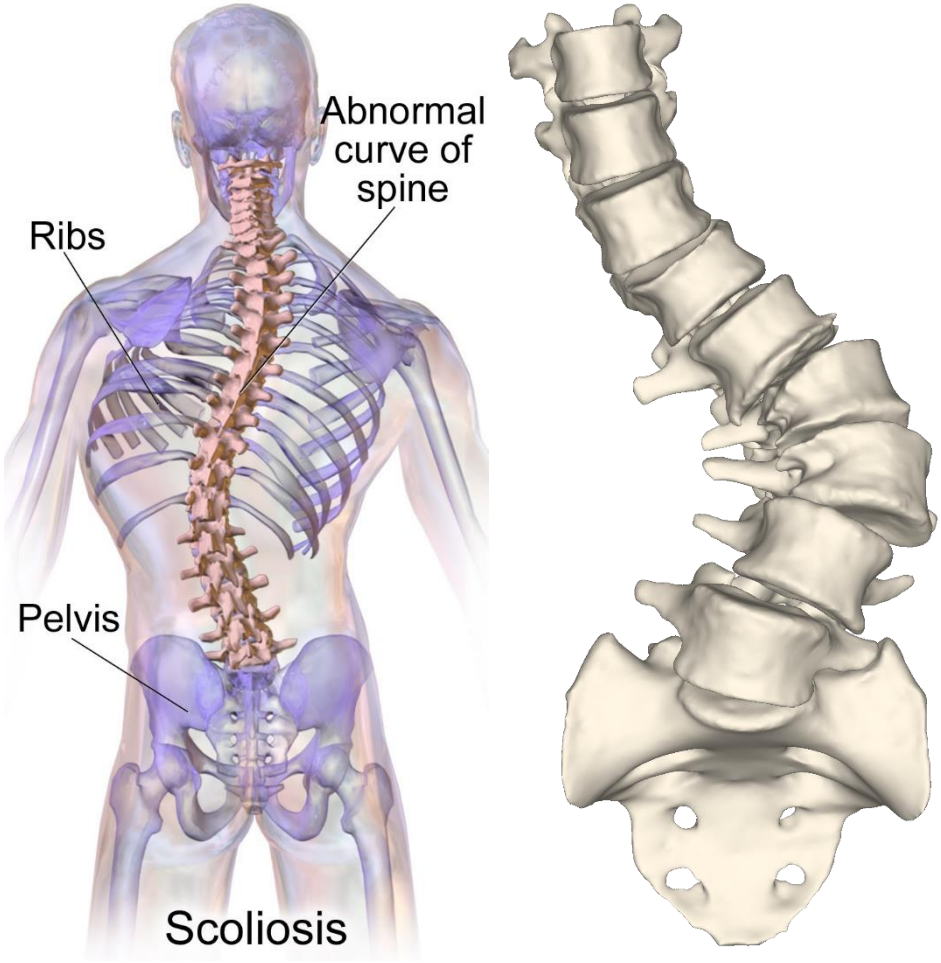

Figure 1.4: Left – Posterior view of a scoliotic spine within the human body, showing a rib hump (Image: BruceBlaus DOI:10.15347/wjm/2014.010*, CC by 3.0, via Wikimedia Commons), right – Anterior view of a segmentation of a scoliotic spine T9 to sacrum isolated from the rest of the body, showing the axial rotation of the vertebrae and how the vertebrae may deform.*

The severity of scoliosis varies. When the Cobb angle is less than 25° the scoliosis is considered mild, while Cobb angles greater than 40-45° are considered severe [10,11]. Scoliosis may initially be mild, or not even greater than 10°, yet there is the risk of curvature progression (especially during growth) and that can develop into severe scoliosis [10]. In severe cases, scoliosis can cause back pain, pulmonary function problems, further disability, mental health problems (such as self-esteem), and a general reduction in the quality of life for an individual, therefore treatment is required [10,11,16].

To aid treatment planning different classification systems, such as the Lenke classification and the King classification systems, have been introduced [17], as well as different methods (Ferguson and Cobb angles) to measure the extent of the curvature [12]. Different treatment options are considered for different curves, physical therapy may be the first recommendation in mild and

low-risk cases, while bracing (of which there are many types) may be used to prevent curvature progression [10,11]. In severe cases, surgical treatment may be considered [10,11]. The approaches as to which therapy to apply and when vary internationally [11], especially when surgical intervention is recommended. However, there is little consensus regarding the aims of the treatment and how they should be prioritised [10,16,18]. Not only is opinion divided over treatment aims, but surgeons hold different views as to the best way to achieve these aims [18].

1.3. Surgical Treatments

Surgeons are presented with many possible techniques to correct scoliosis which may be used in isolation or combination with others [19]. Many of these techniques, such as direct vertebral rotation (Figure 1.5), posteromedial translation, segmental vertebral derotation, *en block* derotation, distraction, and compression are highly invasive [19–24]. Alternatively, less invasive techniques such as vertebral body stapling and vertebral body tethering can also be options [22]. Furthermore, multiple devices can be used to apply the same technique [24]. These surgeries are further complicated by the fact that for the same surgical principles and techniques, the implementation may vary by way of the number of implants and instrumented vertebrae [23], the ligaments released (cut), and patient positioning [20]. This is not an exhaustive list of the possible options a surgeon must consider when planning a surgery but is sufficient to highlight the complexity of these corrective surgeries.

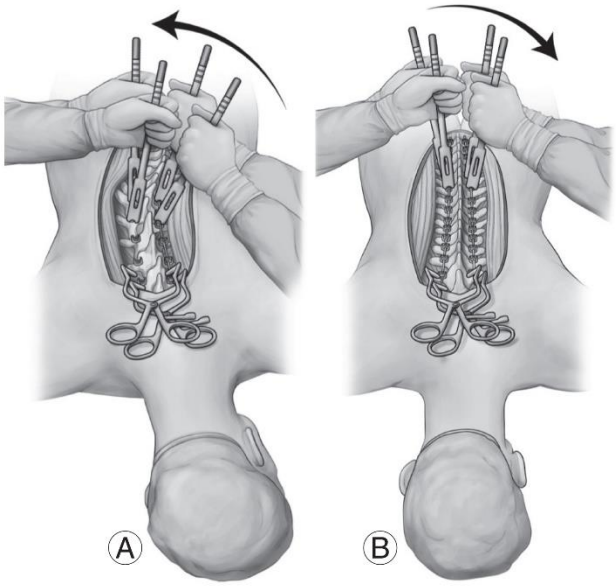

Figure 1.5: Sketch of surgical correction of scoliosis, showing direct vertebral rotation, A) direct vertebral rotation of the apical vertebra, B) rotation of the distal vertebrae (Image from: Chang et al. 2023, CC by 4.0, via Asian Spine Journal [23]).

These surgeries are effective at treating scoliosis. They reduce the risk of curve progression and are effective at correcting or reducing the Cobb angle [11,25]. Moreover, they have been reported to improve patients' quality of life, self-image, and pulmonary function while reducing pain and disability [11,25]. However, in most cases, these surgeries result in a loss of range of motion (RoM) [16] and, although pain reduction has been reported for some patients, 35% still experience significant pain 5 years after the operation [11]. Furthermore, in addition to the usual perioperative complications associated with highly invasive surgeries, other postoperative complications arise, such as pseudarthrosis, surgical site infection, junctional kyphosis, and instrumentation failure

mean of which require revision surgeries to correct [11,26,27]. Reported revision rates vary depending on the patient group and instrumentation used among other factors, for example, one study reported a rate of 24% and another of 75% [22,28].

In addition to the personal cost to the patient, these surgeries and complications have substantial financial costs. Indeed, one study reported a total cost for the initial corrective surgery and revision surgeries to exceed $100,000 [28,29].

The variation in outcome criteria and methods available to surgeons likely influence the success of the surgical outcome [30]. These multiple factors help explain the little consensus on the optimal treatment for a given patient/curve type [31,32]. Computation models may be able to simulate surgical interventions [33], and incorporated into a surgical planning tool they may help identify the optimal procedure or help investigate the trade-offs of the various techniques for a given patient [34,35].

1.4. Research methods

1.4.1. A brief overview - Finite Element Modelling & Musculoskeletal Modelling

There are two broad categories of *in silico* methods which have been used to study the spine, namely FE models and multibody models (MBM) [36]. When multi-body dynamics is used and the models include soft tissues such as the muscles, tendons, and ligaments they are often referred to as MSK models.

Model construction

Finite element models of the spine are created using medical imaging data, such as computed tomography (CT) or magnetic resonance imaging (MRI). Detailed anatomical structures, including vertebrae, ligaments, IVDs, and facet joints are explicitly modelled. Accurately modelling these geometries, in particular the disc height, thickness of the cartilage at the facet joint, and pedicle length is necessary as predicted RoM, intradiscal pressure (IDP), and facet joint forces (FJF) are highly sensitive to these parameters [37–39]. Furthermore, the nature of FE models allows for the level of detail to be tailored to suit the research question.

By comparison, most studies MSK modelling studies use or create by adapting pre-existing models [40–47]. They tend to focus on a spine segment (lumbar [40,42,43,48,49], thoracic spine and rib cage [50], cervical [51–53], and the whole spine [41,44–47]) rather than just a single FSU. Medical images are still used in some studies, most often for informing muscle modelling [41,48,51], but some studies have also used them to define subject-specific bone geometries [48,52]. MSK models of the spine explicitly model the vertebrae and the muscles [40,41,44,47,48,50,53]. The IVJ is in some cased reduced to a joint without mechanical properties [44,49]. Noting a couple of exceptions [40,48], the individual soft tissues are rarely explicitly modelled but rather represented with a lumped parameter model [43,45,47,48,50,52].

Soft tissue representation

Modelling ligaments in FE models of the spine involves using simple, uniaxial, tensile-only spring elements [38,39,54–61]. The modelling of facet joints and IVDs is more complex. Facet joints are typically modelled with friction and soft contact formulation [37], while IVDs include the nucleus pulposus and annulus ground substance with hyperelastic materials, and the annular collagen fibres are modelled as multiple layers of nonlinear springs [55,56,58–60,62–65]. More complex models have incorporated the effects of IVD pore pressure [66]. Some studies have also considered the cartilaginous endplate as an elastic material [37]. The muscles have been explicitly modelled as

force generators and pressurized volumes [67], although this in an uncommon approach. Rather, they are often modelled as forces applied at attachment and insertion points [61,68].

The representation of the IVJ soft tissues is simpler in MSK models compared to FE models, all of the soft tissues are represented with a lumped parameter model using a spring-damper system [43,45,47,48,50,52], and is comparatively simpler to implement [52]. In the few cases where ligaments [40,48] and facet joints [48] have been individually modelled, they are represented with springs. Both linear and nonlinear models have been used to define the characteristics of these tissues [43,48,52,69]. The muscles are most commonly represented as actuators, with a number of parameters that define them, including the pennation angle, a force-length curve, passive stiffness, and a slack length [45]. A further consideration is the attachment points of the muscles [48], and the path along which they act [51].

Personalisation

Accurately assigning material properties to spinal components is crucial for representative models, but literature values may not reflect inter-subject variability. Variation of generic material parameters to reflect intersubject variability (±25%) can lead to RoM changes of over 10% [65], thus necessitating subject-specific properties, especially for clinical applications [70]. However, determining subject-specific values is challenging due to multiple possible solutions when characterizing multiple tissues simultaneously from single tests [71]. Some studies have used FE modelling to characterize tissues, by simulation of stepwise reduction experiments [57]. But, this method is not suitable for characterizing *in vivo* subject-specific values.

Although the representation of the soft tissues in MSK models may be simpler than in FE models, using appropriate material properties is just as important. Additionally, as models are not always created from imaging data the appropriateness of geometrical features also needs to be considered. The simplest approach used is to scale both geometries and muscle properties based on anthropometric data such as height and body weight [43,44,46–48,53]. However, this approach may not result in models that can make accurate predictions for specific individuals [51]. For a subject-specific model, the muscle paths must accurately reflect the muscle paths of the individual [53]. Further, the muscle properties need to be specimen specific [51] due to the high sensitivity of spine loads to changes in properties such as the force-length curve, passive stiffness, and slack length [45]. Likewise, the accuracy of the model is sensitive to the properties of the lumped parameter model [52,72]. The use of a lumped parameter model offers the advantage that it can be easier to determine subject-specific properties of the IVJ than it is for the individual soft tissue properties needed for a FE model. Recent studies have investigated methods to determine subject-specific properties for the lumped parameter model, both *in vivo* and *ex vivo* [52,69]. However, as is also the case for FE models, the lack of experimental data makes it challenging to subject-specific determine muscle properties [45].

Applications

The detail that FE models include means they are well-suited for investigating load sharing across different soft tissues within an FSU [57,60,61]. Researchers use these models to investigate load distributions within anatomical structures, particularly the IVD, to identify the parts of the annulus that experience higher or lower stresses and strains, which can contribute to lower back pain [60,61]. Additionally, FE models of scoliosis enable the investigation of forces at facet joints and their role in pathological cases [55,56,59] that would otherwise be difficult to investigate experimentally. However, detailed FE models can be computationally expensive, and modelling

cartilage at the facet joint in detail may make simulations too expensive with current technology [37]. Internal stresses and strains can be analysed using FE techniques, this has been used to improve surgical instrumentation design for correcting scoliosis which could reduce the failure of instrumentation through screw pull-out and rod breakage [56,62,73]. Additionally, they have explored surgical techniques, analysing the impact of mispositioning screws and the required number of screws [74]. FE models have investigated muscle contributions to spinal stability [68,75], and spinal response to daily activities like driving vibrations [76] or standing for extended periods [63]. Furthermore, they have explored tissue engineering [77]. The impact of modelling choices and assumptions has also been addressed. Boundary conditions in FE modelling involve constraints with applied loads, often taken from musculoskeletal simulations to simulate muscle activity. An alternative, kinematically-driven simulations, has shown variables to be highly sensitive to these input kinematics, potentially leading to over or underestimation of IDP, axial compressive, and shear forces [61,66,78]. Moreover, many FE models are derived from CT data, and the model's pose matches that of the CT data, not accounting for changes in posture when the spine is upright. Follower loads may be applied to account for this, but the resulting motion and IDP differ from those of a true supine pose; this is an initial condition assumption that still warrants further research [58].

MSK models have been utilized in a range of applications as the techniques allow for the modelling of *in vivo* behaviours without the high complexity of FE [52]. It is also easier to inform them with *in vivo* data [52]. They are also highly effective for the analysis of muscle behaviour which is an important factor in vertebra loading and therefore fracture risk [44,47]. Further, they are able to predict muscle activity and the load distribution of the spine for a wide range of activities, including static activity [44], lifting [42–44,50], and highly dynamic scenarios such as car crashes and sporting injury events [51,52]. They have also been used to investigate the influence of anatomical features such as the rib cage and the curvature of the spine on the load distribution across the spine [44,48,50]. They have also been used for various clinical applications including investigating the influence of sarcopenia on spinal loads and determining optimal surgical techniques for correcting scoliosis [35,47]. MSK models are often driven by motion data, this technique has been investigated to determine the most appropriate constraints [46].

Validation

Validation is crucial for FE models to be used in clinical settings [79]. It involves comparing predicted motions, strains, and loads to experimental data. While FE models commonly validate the predicted RoM, IDP, and FJF, validation against strain is necessary to predict bone failure [80], though not yet commonplace in spine models. Validation is limited by the scarcity of experimental data, particularly for IDP and FJF [37,65]. To compensate, models validate parameters by comparing them to limited experimental data and predictions of other computer models, however, this remains only an indirect validation.

The validation of MSK models is most often indirect and involves comparing model predations to experimental RoM, velocities, accelerations, IDP, and an *in vivo* dataset of the forces acting on a telemeterized vertebral body replacement [40,42,42,45,49–52]. One of the few direct validations that can be made is against muscle activity [42], however, this is limited if the muscles of interest are deep muscles due to the difficulty of detecting electromyogram (EMG) signals [51]. The lack of experimental data remains a challenge to validation for MSK models as well [42,43].

In conclusion, FE modelling of the spine has proven valuable in investigating spinal stability, surgical instrumentation design, and tissue engineering, among other research areas. In particular,

the use of medical imaging data to create detailed anatomical models has allowed for the investigation of load sharing across different soft tissues within an FSU, as well as the design of surgical instrumentation. MSK models do not include the same level of anatomical detail and are therefore less computationally expensive. The lack of detail means they cannot be used to analyse the load distribution within the IVD for instance, however, it makes them better suited to examining the load distributions across larger segments of the spine. Furthermore, they are effective for investigating whole-body motion in both static and highly dynamic conditions. They are also an ideal approach for investigating muscle behaviour. The simplification of the details at the joint means determination of subject-specific properties is potentially more feasible *in vivo*. However, further work is needed to establish methods of determining subject-specific soft tissue material properties for both MSK and FE modelling approaches.

Of the two methods, due to its applicability to modelling the whole spine and the simplified FSU representation, this thesis uses MSK modelling techniques. A general description of the fundamental concepts is provided below. An in-depth literature review of FE and MSK modelling of the spine and scoliosis is given in the next chapter.

1.4.2. Musculoskeletal modelling – Bodies

When modelling the human body, rigid multi-body dynamics represent reality as a series of infinitely rigid bodies connected by joints. Under an applied force the bodies will move relative to each other about the joints. In the case of MSK modelling the bones are considered to be rigid, which assumes they do not undergo any deformation when loaded. Depending on the application this assumption can be suitable, or it can be considered an oversimplification, leading to inaccurate or incorrect results.

The bodies of an MSK model are defined as reference frames with inertial parameters (mass – defined as a point mass at the centre of mass (CoM) and an inertia matrix). A body may represent a specific bone, or multiple bones, and the inertial properties of a body represent the bone and the associated body segment including soft tissues such as fat, skin, and the mass of muscles. The data to construct the bodies may come from anthropometric cadaveric datasets to create generic models. Subject-specific models, to varying degrees of accuracy, can be created by scaling a generic model to a subject's specific anthropometrics. Alternatively, an imaged-based subject-specific model can be created from segmenting imaging data such as CT or MRI data.

1.4.3. Musculoskeletal Modelling – Joints

The bodies are connected by joints. The locations of a body relative to another can be defined based on offsets in translation and orientation to the connecting joint. Thus, the joint pose is described by a reference frame, the origin of which is the centre of rotation (CoR) of the joint. This origin can be fixed or defined to move in time [81]. MSK models typically define the joint locations and orientations (and thus the body offsets in translation and orientation) based on anatomical definitions following established guidelines, such as those provided by the International Society of Biomechanics (ISB) [82]. These definitions are based on palpations, performed (virtually or physically) to identify anatomical landmarks on a bone. Of particular interest to this thesis is the definition of the IVJ according to the ISB recommendations. The origin of the joint is defined as the point where the lines passing through the centres of the endplates of the adjacent vertebrae are coincident, if the lines are parallel then the mid-point between the adjacent endplates is taken (Figure 1.6). To define the orientation, the Y axis points cephalad, the Z axis passes through the

origin and is parallel to a line defined by similar points on the bases of right and left pedicles, and the X axis points anteriorly and is perpendicular to the Y and Z axis.

The joint themselves are frictionless, and the number of degrees of freedom (DoF) can be constrained. When modelling the IVJ there are six DoF to consider. The translation along and rotation around each axis are the following: the Y axis is inferior-superior translation, and about the Y axis is axial rotation, along the Z axis is left-right translation, and about the Z axis is flexion-extension, along the X axis is posterior-anterior translation, and about the X axis is right left-bending [82].

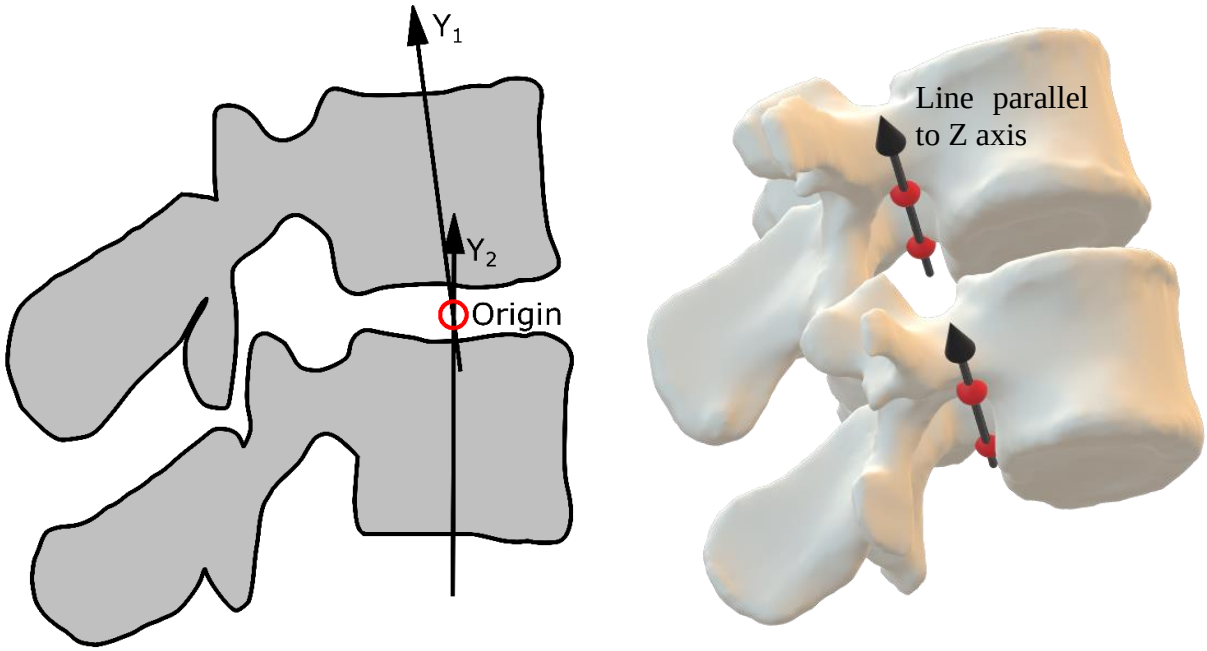

Figure 1.6: Illustration of the intervertebral joint definition following the ISB recommendations, left - the origin of the joint is the intersection of the lines passing through the centres of the endplates, assuming the vertebrae are coplanar, right - definition of the Z axis is parallel to a line connecting two points placed on similar points of the base of the right and left pedicles.

1.4.4. Musculoskeletal Modelling – Muscles

A rigid MBM will move following Newton's laws of motion under the application of a force. These forces may be internal to the model in the form of actuators or passive elements such as springs or they may be externally applied loads. The representation of muscles is especially important in MSK models. Muscles have been represented with various models including Huxley-type models [83], continuum models [84], non-linear analytical models [85], and most commonly Hill-type models [86]. Huxley-type models explicitly model the actin and myosin interaction, thus allowing for accurate real-time forces estimation (for example grasping forces) by detailed modelling of the muscle motion [87]. Continuum models can account for the effect of contact between bone and muscle, internal load distributions, and spatial properties (such as fibre field architecture and local activation) [84,88]. A non-linear analytical model has enabled more accurate modelling of high-frequency muscle twitch than other types of models [85]. However, all of these models are more complex and computationally expensive than the Hill-type model [84–87]. Hill-type models have acceptable predictive capabilities for many applications, have been validated for many cases, and have been used in conjunction with various experimental inputs [86]. Further,

they have become easily accessible as they are included within widely used MSK modelling softwares such as OpenSim and AnyBody [89–91].

The Hill-type muscle model

Given the extensive use of the Hill-type model and OpenSim is used in this thesis, a succinct description of the Hill-type model is presented, while recognising that the modelling of muscles is not central to this thesis. For an in-depth and comprehensive discussion see the review by *Caillet et al.* [86].

To simplify the reality of biological systems, the Hill-type muscle model represents the muscle (which has a volume, and active (muscle) and passive (tendon) components) with a passive spring element (to represent the tendon), in series with an active contractile element and a passive spring element in parallel (to represent the muscle) (Figure 1.7) [92]. The muscle is attached to the tendon at an angle, known as the pennation angle (α), therefore the muscle force is the sum of the active force ($af^L(\tilde{l}^M)f^v(\tilde{v}^n)$) and passive force ($f^{PE}(\tilde{l}^m)$), scaled by the pennation angle:

$$f^M = \left(af^L\left(\tilde{l}^M\right)f^v(\tilde{v}^n) + f^{PE}\left(\tilde{l}^m\right)\right)cos(\alpha)$$

Eqn. 1.1

And this, assuming an elastic tendon and negligible muscle mass must equal the tendon force (f^T). A damping factor ($\beta\tilde{v}^M$) can also be introduced, therefore:

$$f^M = \left(af^L\left(\tilde{l}^M\right)f^v(\tilde{v}^n) + f^{PE}\left(\tilde{l}^m\right) + \beta\tilde{v}^M\right)cos(\alpha)$$

Eqn. 1.2

The force-length curves (both passive and active) are created by fitting the curves to experimental data and it is recommended to adjust these curves to represent the subject of study [92,93]. Likewise, the other parameters, such as the pennation angle, the force-velocity curves, and the tendon slack length are obtained from experimental data, although calibration to the subject is recommended [93]. Further modifications can be made to these equations by assuming rigid tendons when appropriate.

The parameters which describe the muscle model are crucial to the predictive capabilities of MSK models [94]. Depending on the complexity of the model up to 23 properties can be included in the model which can be described by up to 60 parameters [86]. Of these, muscle forces are most sensitive to the tendon slack length, optimal contractile element length, and muscle isometric force [86]. Thus, the determination of the correct parameter values is a necessary although challenging step for accurate simulations, and personalisation of these parameters is essential in personalised models [86,94]. To this end, imaging data, such as MRI data, can be help [94].

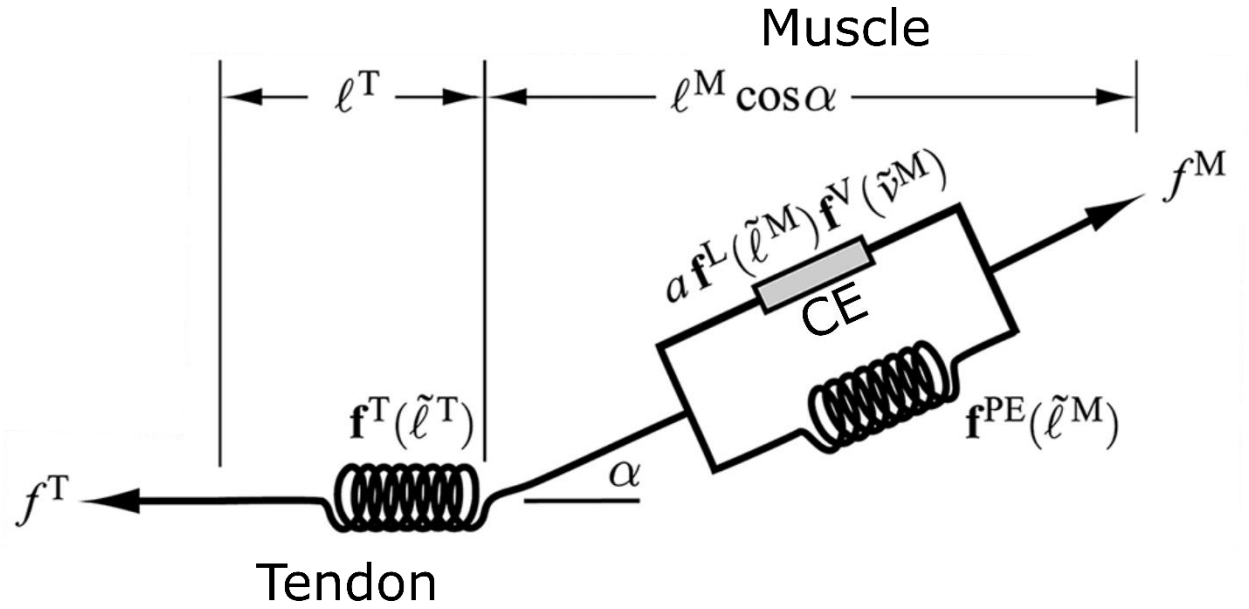

Figure 1.7: Hill-type musculotendon model, where: f^T is the tendon force, f^M is the muscle force, l^T is the tendon length, $l^M \cos \alpha$ is the length of the muscle in the direction of the tendon, α is the pennation angle, $f^T(\tilde{l}^T)$ is the tendon-force-length curve, $f^{PE}(\tilde{l}^M)$ is the passive force length curve, and the contractile element (CE) – $af^L(\tilde{l}^M)f^v(\tilde{v}^M)$ is the active force length curve, where the a term is the muscle activation, the $f^L(\tilde{l}^M)$ term is the active force length curve, the $f^v(\tilde{v}^M)$ term is the force velocity curve. Figure adapted from Millard et al. 2013 [92].

Attachment points between the muscles and the bodies specify the path of the muscle and where it applies a force. The accuracy of the location of the attachment points can be improved by basing them on imaging data. The muscle paths determine the line of action of the force produced by the muscle. The simplest path is a direct path between the attachment points. However, this may be unrealistic, and within an MSK model points and surfaces can be specified to better guide the muscle path [93].

The Hill-type muscle model has been applied in a range of use-cases, including muscle-tendon interaction [95], neuromechanics (such as the electro-mechanical delay) [96], neuromuscular and age-related disabilities [47], motor control [97], response to perturbations [97], as well as for various sports [98,99] and clinical-related applications [100,101]. Estimated muscle forces are also a critical factor in joint reaction forces [102,103].

1.4.5. Musculoskeletal Modelling – Motion

Motion, such as bending over to pick an object up, is the result of a neuromuscular process, where a signal is set to the muscles, which apply a force to cause the desired motion. MSK modelling uses different methods to investigate motion, neuromuscular control and the associated forces depending on the research question and the data available.

Inverse Kinematics

A motion capture system records the three-dimensional (3D) position of reflective markers through time. With this data, an MSK model with corresponding virtual markers uses inverse kinematics to calculate the joint angles and positions at a specific time step. The kinematics is calculated by minimising the error between the generalised coordinates of the experimental markers and the corresponding virtual markers.

Inverse Dynamics

Inverse dynamics calculates the joint forces and moments in an MSK model necessary to produce a particular motion. As $F = ma$, given the joint coordinates and angles and the inertial properties of the bodies in the MBM, the joint forces and moments can be calculated by differentiation.

Forward Dynamics

Alternatively, the motion of an MBM can be calculated for a given force by integrating multi-body dynamics equations forward through time:

$$\ddot{q} = [M(q)]^{-1}\{\tau + C(q, \dot{q}) + G(q) + F\}$$

Eqn. 1.3

Where $\ddot{q}$ is the accelerations, $[M(q)]^{-1}$ is the inverse mass matrix, τ is the joint torques, $C(q, \dot{q})$ are the Coriolis and centrifugal forces, with q the coordinates, and $\dot{q}$ the velocities, $G(q)$ is gravity and F is the other forces applied to the model. This requires the forces, internal (for example muscle) and external (for example ground reaction forces) to be known, which can be collected using instruments such as force plates and electromyography.

1.4.6. Application of musculoskeletal modelling to spinal research

Passive Structure Modelling

The spinal ligaments and the IVD (Figure 1.1) are passive structures, limiting the joint RoM [2,4], which aids spine stabilisation and are important for flexibility and load distribution [2,7]. The representation of the mechanical properties (nonlinear, viscoelastic, creep, relaxation [2,4,8]) of these passive structures within the IVJ of MSK models is necessary for an improved understanding of the motion and loading of the spine; although they have not been consistently included in MSK models [104]. MSK models of the spine have, with some exceptions [40,105], represented these structures using a lumped parameter model using a spring-damper system [43,51,69,106,107]. Experimentally a 6-by-6 stiffness matrix (Eqn. 1.4) can be used to describe the load-response curve of the joint [108].

$$\begin{bmatrix} M_x \\ M_y \\ M_z \\ F_x \\ F_y \\ F_z \end{bmatrix} = \begin{bmatrix} k_{11} & k_{12} & k_{13} & k_{14} & k_{15} & k_{16} \\ k_{21} & k_{22} & k_{23} & k_{24} & k_{25} & k_{26} \\ k_{31} & k_{32} & k_{33} & k_{34} & k_{35} & k_{36} \\ k_{41} & k_{42} & k_{43} & k_{44} & k_{45} & k_{46} \\ k_{51} & k_{52} & k_{53} & k_{54} & k_{55} & k_{56} \\ k_{61} & k_{62} & k_{63} & k_{64} & k_{65} & k_{66} \end{bmatrix} \begin{bmatrix} \theta_x \\ \theta_y \\ \theta_z \\ T_x \\ T_y \\ T_z \end{bmatrix}$$

Eqn. 1.4

Where M_x, M_y, and M_z are the generalised moments and F_x, F_y, and F_z are the generalised forces that act at the joint; calculated as the product of the elements (k) of the 6-by-6 stiffness matrix and the generalised rotations (θ_x, θ_y, and θ_z) and translations (T_x, T_y, and T_z) of the joint

To include the damping properties of the spring-damper system a damping term is introduced (Eqn. 1.5).

$$\begin{bmatrix} M_x \\ M_y \\ M_z \\ F_x \\ F_y \\ F_z \end{bmatrix} = \begin{bmatrix} k_{11} & k_{12} & k_{13} & k_{14} & k_{15} & k_{16} \\ k_{21} & k_{22} & k_{23} & k_{24} & k_{25} & k_{26} \\ k_{31} & k_{32} & k_{33} & k_{34} & k_{35} & k_{36} \\ k_{41} & k_{42} & k_{43} & k_{44} & k_{45} & k_{46} \\ k_{51} & k_{52} & k_{53} & k_{54} & k_{55} & k_{56} \\ k_{61} & k_{62} & k_{63} & k_{64} & k_{65} & k_{66} \end{bmatrix} \begin{bmatrix} \theta_x \\ \theta_y \\ \theta_z \\ T_x \\ T_y \\ T_z \end{bmatrix} + \begin{bmatrix} c_{11} & c_{12} & c_{13} & c_{14} & c_{15} & c_{16} \\ c_{21} & c_{22} & c_{23} & c_{24} & c_{25} & c_{26} \\ c_{31} & c_{32} & c_{33} & c_{34} & c_{35} & c_{36} \\ c_{41} & c_{42} & c_{43} & c_{44} & c_{45} & c_{46} \\ c_{51} & c_{52} & c_{53} & c_{54} & c_{55} & c_{56} \\ c_{61} & c_{62} & c_{63} & c_{64} & c_{65} & c_{66} \end{bmatrix} \begin{bmatrix} \dot{\theta}_x \\ \dot{\theta}_y \\ \dot{\theta}_z \\ \dot{T}_x \\ \dot{T}_y \\ \dot{T}_z \end{bmatrix}$$

Eqn. 1.5

Where the generalised moments (M_x, M_y, and M_z) and forces (F_x, F_y, and F_z) are the sum of the product of the stiffness matric (k) and the generalised rotations and translations of the joint (θ_x, θ_y, θ_z, T_x, T_y, and T_z) and the product of the damping matric (c) and the generalised velocities of the rotations and translations ($\dot{\theta}_x$, $\dot{\theta}_y$, $\dot{\theta}_z$, $\dot{T}_x$, $\dot{T}_y$, and $\dot{T}_z$). This description includes coupled motion of the IVJ. A study of the coupling behaviour showed that coupled and uncoupled parameters should not be used interchangeably; further research is required to determine if coupled parameters are necessary or if uncoupled parameters are sufficient [107]. The most common approach is to assume uncoupled properties, in which case the lumped parameter model simplifies to a diagonal matrix (Eqn. 1.6). Another motiving factor for the uncoupled assumption is the lack of available data on coupled motion which means characterisation of the coupled behaviour across all spine levels is not possible [109].

$$\begin{bmatrix} M_x \\ M_y \\ M_z \\ F_x \\ F_y \\ F_z \end{bmatrix} = \begin{bmatrix} k_{11} & 0 & 0 & 0 & 0 & 0 \\ & k_{22} & 0 & 0 & 0 & 0 \\ & & k_{33} & 0 & 0 & 0 \\ & & & k_{44} & 0 & 0 \\ & & & & k_{55} & 0 \\ & & & & & k_{66} \end{bmatrix} \begin{bmatrix} \theta_x \\ \theta_y \\ \theta_z \\ T_x \\ T_y \\ T_z \end{bmatrix} + \begin{bmatrix} c_{11} & 0 & 0 & 0 & 0 & 0 \\ & c_{22} & 0 & 0 & 0 & 0 \\ & & c_{33} & 0 & 0 & 0 \\ & & & c_{44} & 0 & 0 \\ & & & & c_{55} & 0 \\ & & & & & c_{66} \end{bmatrix} \begin{bmatrix} \dot{\theta}_x \\ \dot{\theta}_y \\ \dot{\theta}_z \\ \dot{T}_x \\ \dot{T}_y \\ \dot{T}_z \end{bmatrix}$$

Eqn. 1.6

With this formulation, the lumped parameter model includes six DoF, in many cases the model is further simplified by reducing the number of DoF [104]. The IVJ load response curves are non-linear, MSK models have defined the parameters have been as linear and non-linear [35,104,106,110,111]. The suitability of the linear simplification is dependent on the use case [72].

MSK models usually assign these stiffness parameters based on literature values from *in vitro* or *in vivo* experiments, which exhibit substantial variability [109]. The stiffness properties are expected to differ between IVJ levels, however, even at the same IVJ levels substantial variation is observed. This is expected due to differences in age, sex, and state of the discs, however, more work is necessary to assess the effect of these parameters on the stiffness of the joints [109]. Additionally, inter-specimen is expected. Thus, selecting the appropriate stiffness parameters is challenging. This challenge is further complicated by the diverse range of testing devices and methods, compressive loads and moments, loading directions, maximum RoM, and the use of multi-segment or single FSU in experimental studies, all of which are known to affect joint stiffness [109]. Damping parameters have not been extensively studied, and the limited available data also shows large variability [112,113].

The selection of the appropriate stiffness parameters is important as they affect predicted IDPs and muscle forces [72,106,107]. Another important consideration is the pose of the spring-damper elements, they should be coincident and aligned with the joint to ensure the moments and forces are applied in the correct directions [106]. The joint location and pose therefore determine the location and direction of the spring damper elements. Studies have also demonstrated the sensitivity of the joint force and predicted muscle forces to the joint location and pose [72,114]. Thus, there is likely an interaction between the joint pose and the stiffness properties which influence model predictions [72].

A less common approach is to represent each passive structure (IVD, supraspinous, interspinous, anterior and posterior longitudinal, intertransverse, flavum, and capsular ligaments) with a different element [40,105,115]. Ligaments were modelled as non-linear springs acting in a straight line [40,105]. Parameters were based on literature data and attachment points based on CT data [40,105]. Different approaches were used to calculate the parameters, Rupp *et al.* used experimental data to define three regions (an initial region for ligament lengths less than the slack length where no force is generated, a non-linear transition region, and a linear region past the transition region) [105] while Han *et al.* fitted an exponential curve to experimental data [40]. Third-order non-linear polynomials [40,105] and second-order non-linear curves [115] have been used to model the stiffness of the IVD. Damping parameters have also been included within the models of the ligaments and discs [105,115]. The studies suggest that the inclusion of the structures is necessary to accurately model the spine [40,105,115], however, there is limited data available to determine the properties of the ligaments [105]. This introduces the potential of unexpected model predictions due to the influence of the dataset used and modelling choices (such as attachment points) [115], which may be challenging to identify or understand due to the number of parameters present. Additionally, this approach requires experimental data for the individual ligaments and discs in isolation, or step-wise reduction experiments to determine passive structure properties [115]. The experimental datasets available for this thesis were from spine segments that included all of the ligaments and the IVD (without any step-wise reduction studies) therefore a lumped parameter modelling approach was considered more suitable.

Model personalisation

If such models are to be clinically useful a degree of personalisation is required [116], which has been achieved to varying extents. Most studies introduce a degree of personalisation by scaling the models and the relevant muscle properties [43,46,47,53,117]. More detailed personalisation has been achieved with imaging data, for example, CT-based methods have been used to personalise musculature and spine curvature in healthy individuals [117]. The subject-specific geometries of the individual vertebrae have been created through segmentation of CT data [48,52,118], this is necessary if subject landmarks are to be accurately identified [48]. The landmarks determine the pose of the joints [82,118], the muscle attachment points [53], and when ligaments are modelled the attachment points of the ligaments [40,48]. The location of these components influences the force they exert on the bodies [53,72]. Studies have investigated the sensitivity of spinal loads to muscle parameters, concluding that the line of action, the passive stiffness, the force-length curve, the maximal isometric force, and the slack length are all highly influential [45,47,51,53]. To some extent, these subject-specific parameters can be determined from medical images [51,117]. Given the high intersubject variability [45], this suggests a need for subject-specific muscle models.

Another study has investigated the personalisation of mass distribution across the spine levels [119]. However, such studies were often based on healthy adults which are not representative of the elderly or adolescent populations. Indeed, MSK models of adolescents are rare, with one study having developed a set of models to represent individuals 6-18 years of age [120]. Although these are generic models, they are a promising starting point for the development of personalised adolescent models. The development of scoliotic MSK models is uncommon as well, with one method having been established by Bassani *et al.* [121], reused in a number of studies [122–124], and another approach was established by Overbergh *et al*. [118]. However, these methods rely on EOS imaging data. Some of these scoliotic MSK models have been used to investigate vertebral compressive forces and muscle activity [122,123] and, within commercial software, surgical correction of scoliosis [34].

Personalisation of the passive structures is crucial when creating personalised MSK spine models and simulating surgical corrections [125]. Methods to find personalised IVJ parameters have recently been introduced [52,126], while another method relying on functional bending tests has been used to personalise the stiffness in scoliotic patients [127]. Further research is required to investigate the sensitivity of parameter personalisation to the joint pose definition, as well as investigations into the spinal level dependency and inter-subject variability for these optimisation techniques.

Clinical application and modelling of spinal deformities

Generic MSK models have been for clinically related research questions. Sensitivity studies have varied the spinal curvature, muscle morphology [44], and muscle strength (to represent ageing and sarcopenia) [47] to investigate vertebral fracture risk.

In order for MSK models to be applicable within clinical scenarios and to accurately represent spinal deformities patient-specific models are necessary. A number of studies have established methods of generating patient-specific models from radiographs [34,118,121], most often using the EOS imaging system. This enables the personalisation of the individual vertebral geometries with a manual segmentation step [118,121]. The resulting models accurately represent the vertebral orientation within 4° and position within 4mm [118,121]. Despite the accuracy of these models, the musculature is either excluded from the model or without wrapping surfaces to guide the muscle paths [118,121].

Personalized models have been used to investigate the biomechanical behaviour in the case of spinal deformities. Muscle activity and compressive vertebral loads have been studied [122,123], which has found a correlation between the curvature asymmetry and asymmetric muscle forces as well as a correlation between the curvature and the compressive forces [122,123]. However, the muscle parameters were personalised by scaling the physiological cross-sectional area, this simple approach may not be sufficient for personalising the muscle properties in the case of spinal deformities. Furthermore, only mild to moderate scoliosis cases were considered [122,123].

A more direct clinical application of MSK models has been to investigate and predict surgical corrections [34,35,128,129]. Aubin *et al.* developed a software platform to aid surgical planning, implementing the simulation of several different correction techniques [34]. Others have focused on the influence of the role of different parameters when a surgical intervention is considered by simulating the correction achieve for many different combinations of the parameters. A study focusing on screw density found that density did not seem to greatly influence the degree of correction in the coronal and sagittal planes, but it did in the transverse plane and that lower screw

density was associated with lower forces at the bone-screw interface [129]. However, another study, which simulated the correction from 1080 different possible combinations of 5 parameters found that higher density was correlated with greater correction [35]. Although, of the 5 parameters considered, the parameter with the strongest correlation to the degree of correction was the number of fused levels, not screw density [35]. The possibility of complications post-operation has also been considered, by running inverse simulations, muscle forces and joint forces were calculated pre and post-operation [122]. Correlations were found between the joint loads and the change in alignment due to the surgery, implying the change in alignment could contribute to post-operation complication risks [122].

In summary, MSK models have been applied to model spinal deformity in a range of different clinical contexts. However, efforts to accurately generate patient-specific models of spinal deformities are still ongoing. Additionally, they can be useful to investigate 'what if' questions in surgical scenarios, but the results from such studies need to be carefully interpreted as results can be contradictory which may be due to simplifications and assumptions applied to the model and there is a lack of experimental data available for validation.

1.5. Aims of the thesis

This thesis aims to investigate the characterization of the IVJ for MSK models, with the scope of contributing to the development of patient-specific models of severe scoliosis. The work attempts to meet this aim by dividing it into several objectives:

- Implement an optimization method to determine subject-specific stiffness parameters of the IVJ.
- To better understand the sensitivity of these optimized parameters to the joint pose.
- To investigate the importance of the level and subject dependency.
- To prepare a framework which would enable the incorporation of subject-specific IVJ parameters into a scoliotic model by developing a patient-specific scoliotic MSK model from a generic healthy spine model.

Computational modelling of the scoliotic spine: A literature review

Samuele L Gould[1,2], Luca Cristofolini[1], Giorgio Davico[1,2], and Marco Viceconti[1,2]

[1] Department of Industrial Engineering, Alma Mater Studiorum - University of Bologna (IT)

[2] Medical Technology Lab, IRCCS Istituto Ortopedico Rizzoli, Bologna (IT)

Adapted from a publication in:

International Journal for Numerical Methods in Biomedical Engineering

(2021)

10.1002/cnm.3503

The authors wish to thank International Journal For Numerical Methods In Biomedical Engineering for providing the permissions to re-use the manuscript titled “Computational modelling of the scoliotic spine: A literature review” in the present PhD thesis.

2.1. Abstract

Scoliosis is a deformity of the spine that in severe cases requires surgical treatment. There is still disagreement among clinicians as to what the aim of such treatment is as well as the optimal surgical technique. Numerical models can aid clinical decision-making by estimating the outcome of a given surgical intervention. This paper provided some background information on the modelling of the healthy spine and a review of the literature on scoliotic spine models, their validation, and their application. An overview of the methods and techniques used to construct scoliotic finite element and multibody models was given as well as the boundary conditions used in the simulations. The current limitations of the models were discussed as well as how such limitations are addressed in non-scoliotic spine models. Finally, future directions for the numerical modelling of scoliosis were addressed.

2.2. Keywords

Scoliosis, scoliotic spine, review, multibody modelling, musculoskeletal modelling, finite element modelling

2.3. Introduction

Scoliosis is a pathological bending and twisting of the spine [10] in three dimensions [9,130]. It is defined as a spinal curvature in the coronal plane (i.e. the Cobb angle, the angle between the endplate of the two vertebrae on either side of the coronal plane curve [12], see Stokes *et al.* for further details [12]) exceeding 10° [10], with recognizable rotation of the vertebrae [10,131]. In adolescents, scoliosis is a common, yet poorly understood, spinal deformity. Reported occurrences normally range between 2 and 5% [10,131,132], and roughly 80% of cases are idiopathic [10]. Notably, above a Cobb angle of 30°, risks to health seem to increase with the angle [10,131]. These risks include back pain, mental health issues related to appearance, cardiac, respiratory and other physiological problems which in severe cases may lead to death [10,131,132]. Therefore, based on studies of the North American population treatment is suggested for Cobb angles above 20° [131] (i.e. approximately 0.3% of cases) [131]. Surgery is only recommended in severe cases of Cobb angles above 50° [10,133]. Surgery is associated with a complication risk of 5% to 25% which includes neurological injury, blood loss, injuries due to positioning, infections, flatback deformity, and proximal junctional kyphosis [134] and results in a permanent reduction in mobility when fusion is used [133]. The surgical planning for scoliosis treatment is complex and multi-facetted, thus there is a high variability in the treatment that is considered optimal [30–32]. While there is clear scope for patient-specific models to predict the outcome of corrective surgery [135], we are far from widespread use in clinical practice. While there is extensive literature on the computer modelling of spine biomechanics, there is a clear need for a systematic review of such literature, specifically targeting the modelling of the scoliotic spine, and its use in the planning of corrective surgery, as it would provide an essential starting point for any computer-aided surgery development in this area.

The biomechanics of the spine can be idealised by modelling the dynamics assuming vertebral bodies as infinitely rigid, muscles as linear actuators, and all the other connective tissues as lumped-parameter idealised joints that link the rigid bodies in a multi-body model (MBM). Under these assumptions, the biomechanical behaviour can be described in terms of Ordinary Differential Equations (ODE). However, MBMs are not suitable for investigating internal stresses and strains. To do this, we need to assume that all tissues are deformable continua, whose biomechanical

behaviour can be described in terms of partial differential equations (PDE). Being these boundary-value problems the most convenient numerical integration scheme for such mathematical models is the Finite Element Modelling (FEM) scheme. FEM assumes appropriate constitutive equations for each tissue type to predict the deformability of all different tissues. These two modelling methods can also be combined to produce hybrid models [136]. Hybrid models integrate FE and MSK models, utilizing the FE model for a detailed representation of passive structures (IVDs, ligaments, facet joints, vertebrae, surgical instrumentation) and the MSK model for the muscles and any bodies which the researcher considers rigid [136–140]. This approach seeks to overcome the limitations of the two modelling techniques. There are two categories of hybrid models: coupled and uncoupled. Uncouple models combine the independent models by using them in separate distinct steps. MSK models are used to calculate the muscle forces and loads and large deformations [136,139], these are used as inputs to the FE model which calculated the stresses and strains within passive elements [136,138,139]. This approach maintains the computational efficiency of the MSK model simulation of the muscles while providing more realistic boundary conditions to the FE model to simulate internal stresses and strains. Coupled hybrid models follow the same principles, using MSK models for the muscles, and FE models for passive structures (IVD, ligaments, etc.), however, the models are either directly integrated or integrated within an iterative feedback loop [137,140]. The MSK calculates the muscle forces and applies them to the FE model to calculate the reaction forces from the passive elements. These forces can then be used to inform the next MSK simulation, and the loop repeats until convergence. Coupled hybrid models are considered the gold standard with better accuracy than other modelling methods, however, these benefits require much higher computational costs [137,139,140]. These models vary in complexity and detail, with differing degrees of personalisation. The importance of model personalisation has been highlighted in many studies; height, weight, muscle and bone morphology, and subject-specific material properties have all been shown to play an important role in simulations [117],[70].

In the last two decades, the interest in computer models of the spine rapidly increased. Several papers and a few reviews were produced on the topic. Driescharf *et al.* reviewed the literature focusing on the quantification of the loads acting on the lumbar spine [141]. They reviewed both *in vivo* and modelling studies, focusing the latter on MBM models, and categorising them on the basis of the approach used to estimate muscle forces. They concluded that the main limitation of current models is the modelling of the intervertebral joint (IVJ) without a translational degree of freedom, and the balancing of net external moments at a single joint [141]. Alizadeh *et al.* reviewed the literature focusing on studies modelling the cervical spine, which are most commonly employed to study impact conditions [51]. MBMs were the most commonly used, followed by hybrid models and then FEMs. They suggested that in this case, the main limitation was the lack of detail in the musculature modelling [51]. Both reviews identified greater personalisation of models, and the use of patient-specific electromyogram (EMG) and kinematic data, as promising areas of future work [51,141]. Wang *et al.* reviewed publications studying the biomechanics of scoliosis, but they only considered studies using FEM [142]. To the best of the Authors' knowledge, the only review on the computational modelling of scoliosis which also addresses some studies using MBM was the paper by Jalalian *et al.* [143]. They reported quite a few FEM-based studies, but a very limited number of MBM-based ones. In the context of scoliotic spine models, MBMs rarely include the facet joints explicitly but often included the muscles. Conversely, as the review by Jalalian *et al.* [143] noted FEMs often included the facet joints but

rarely the muscles. Other reviews on the computational modelling of scoliosis and related surgery are not in English [144,145].

These papers [142,143] provide systematic reviews of the literature which models the scoliotic spine until 2014, however, none of these papers review the literature published after 2014. Some focus only on specific segments of the spine and do not specifically target the modelling of scoliosis which typically spans over long spine regions. Some consider only specific modelling methods. The Jalalian *et al.* review was published in 2013, and since then a considerable number of modelling studies were published, and the methods for patient-specific modelling have significantly improved.

The aim of the present study is to systematically review the literature focusing on the numerical modelling of the scoliotic spine, its use for surgical planning, and understanding the biomechanical properties of the scoliotic spine. Papers will be reviewed in terms of: whether the model is scoliotic, the segment of the spine being modelled, the patient specificity, if the model targets paediatric subjects, and how the model is used in a surgical context. First FEM and then MBM will be discussed; the capabilities of state-of-the-art models and their limitations for both methods will be discussed and avenues for future work will be identified. Since scoliotic spine models (both FEMs and MBMs) are often developed from models of healthy human spines, it seems appropriate to begin with an introduction to healthy spine modelling.

2.4. Method

A first list of potentially relevant publications was generated by running systematic searches on the PubMed and Scopus indexing services between the period of March 2020 to October 2020. The two searches were conducted using the keywords ‘scoliosis' AND (‘finite element’ OR ‘multibody’) and (‘normal’ OR ‘healthy’) AND ‘spine’ AND (‘finite element’ OR ‘multibody’). In addition, an unstructured search was conducted on Google Scholar looking for papers missed in this first search. A second list was generated by scanning the bibliography of the paper in the first list.

Articles in this master list were first filtered by title if they were animal studies or were not studying the spine. Additionally, they were excluded if they failed to address one of the following categories:

- Scoliosis
- Surgical procedures related to scoliosis
- Biomechanical nature of the spine
- Paediatric/adolescent spine

Following an initial filtering by title, the studies were filtered by abstract. Studies were excluded if:

- FEM or MBM was not used
- the focus of the study was on bracing treatments
- solely the instrumentation was modelled, or prosthetic device design was the focus
- less than one functional spinal unit was modelled
- the study examined the aetiopathogenesis or progression of scoliosis
- the focus of the study was gait analysis

Searches focused on articles post-2013 as previous review papers have looked at both FEM and MBM of the scoliotic spine until that date, however, articles pre-2013 were not excluded.

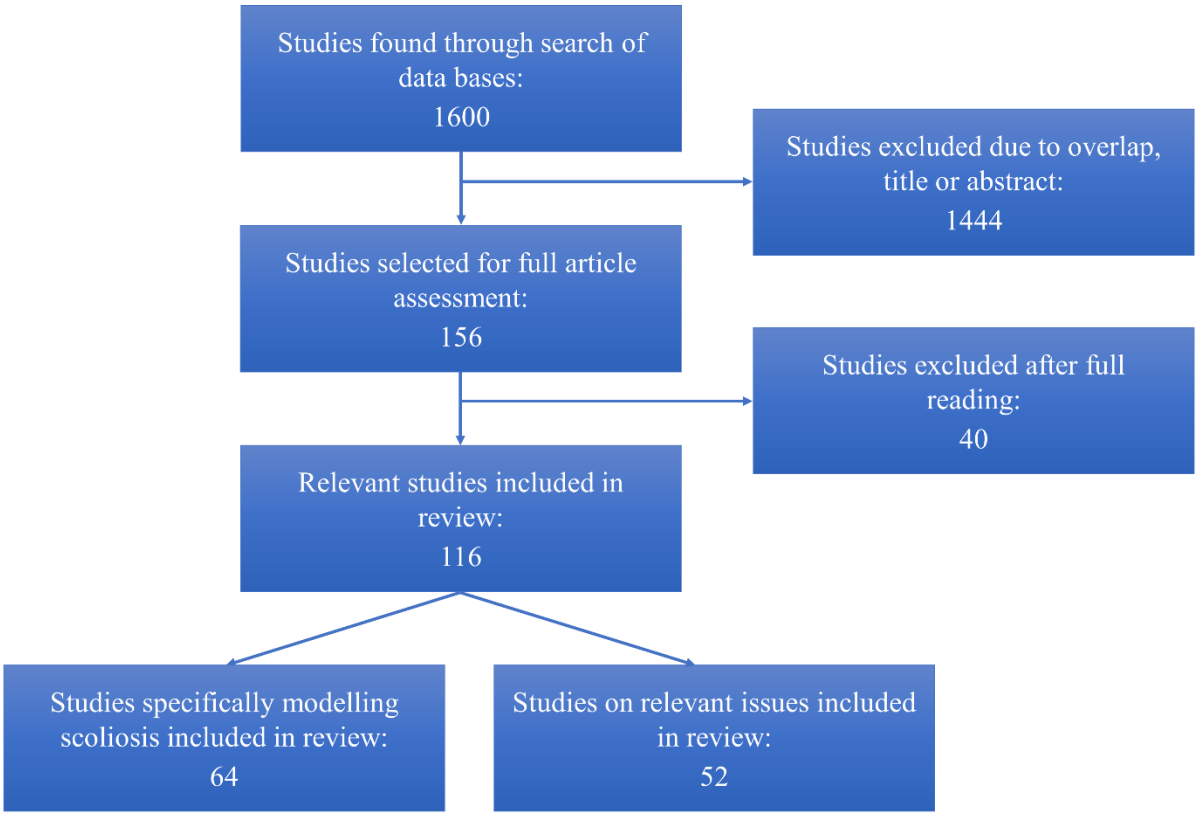

Figure 2.1: Flowchart of article selection

2.5. Finite Element Models of the healthy spine

2.5.1. 2D FEM Models

2D models have been used in preliminary studies and to study large numbers of spine shapes. Galbusera *et al.* investigated the influence of sagittal balance on lumbar loading. Galbusera *et al.* simulated many (1000) different spine profiles and included muscle forces [146]. This approach enabled them to investigate trends rather than specific cases and to show that the C7 plumb line, the sacral slope, and the lumbar lordosis are all critical factors affecting the lumbar loading. The C7 plumb line is the horizontal distance between a vertical line passing through the centre of C7 and S1 [147]; the sacral slope is the angle between the upper sacral plate and the horizontal [148]. The author would direct the Reader to Jackson and McManus [147] and Duval-Beaupère *et al.* [148] for the respective definitions.

Zanjani-Pour *et al.* [66] developed a 2D model with a poroelastic intervertebral disc (IVD). Their results showed that pore pressure was highly sensitive to the applied vertical translation and marginally sensitive to the Young's modulus of the annulus and the porosity of the nucleus.

2.5.2. 3D FEM Models

Geometry

Most models are created from computed tomography (CT) scans, either directly or by the scaling of a previous model, however, the musculature is rarely included. A few studies have focused on the creation and validation of models [65,149]. The model developed from CT images by Mills and Sarigul-Klijn is one of the first young (20-year-old) female models [149]. This provided an initial model for future studies on the young female spine.

The natural curvature of the spine affects its response to loading. Naserkhaki *et al.* showed the degree of lumbar lordosis substantially affected the load sharing in the facet joints and the ligaments when a follower load (a compressive force which acts along a line which follows the curvature of the spine) and moment were applied [150]. Based on the investigation of 480 different curvatures, increasing lordosis correlated strongly with higher anterior-posterior shear loads in the IVDs, in particular the L5-S1 and L1-L2 IVDs [151].

Others [38,152] investigated the influence of the IVD geometry on the FJF, the intradiscal pressure (IDP), range of motion (RoM) and kinematics. These studies highlighted that the FJF, IDP, and RoM are most sensitive to the disc height, width and sagittal dimension, the influence of each geometrical parameter depended on the movement.

Constitutive Equations

The material properties are an especially important consideration when creating a subject-specific model due to the natural variation between subjects, which will be exacerbated by pathologies; however, these are most commonly taken from literature. Jebaseelan *et al.* investigated the sensitivity of displacement and deformation of the spinal components to different material parameters under different loading conditions of an L1-S1 model of an eight-year-old. The material parameter the response was most sensitive to depended on the loading condition, for example, the model was most sensitive to IVD properties in compression but to ligament properties in flexion [153]. A sensitivity study of the RoM and the IDP to the IVD material model showed less than a 3% difference between linear and non-linear (hyperelastic Mooney-Rivlin for the nucleus pulposus and the annular ground substance and non-linear stress-strain curves from literature for the fibres) models [65]. They found no significant difference between the results for the linear and non-linear models when a compression of 300N and flexion 7.5Nm were simultaneously applied [65]. Typically, 300N is less than 0.5 body weight and thus is a smaller load than the IVD will normally experience, especially in dynamic conditions and activities [42]. Non-linear models of the IVD show rapidly increasing stiffness compared to a linear model as the load increases. Therefore, a linear model that predicts comparable motion to a nonlinear model under 300N, will predict larger motions at higher loads, hence, linear models have limited applicability.

The use of generic material parameters from literature is a common simplification in many lumbar spine models [154]. Schmidt *et al.* established a method for calibrating the material parameters of a specimen-specific annulus (the ground substance and the fibres) to accurately predict the RoM. A unique combination of parameters could accurately predict the RoM for each bending moment (flexion, bending, axial torsion), ie. three unique combinations. However, to find a single combination of parameters that accurately predicted the RoM for all bending moments, the annulus needed to be modelled in greater detail by dividing it into five regions with local weighting factors. They concluded that only one specific set of material parameters and weightings would correctly

predict the RoM for all loading conditions [154]. This model only included the IVD. When Naserkhaki *et al.* used eight different databases as the source for the material parameters of ligaments and were unable to predict the RoM, IDP, ligament force/deformation and FJF within one standard deviation of the mean from *in vivo* and *in vitro* data. They suggested validation using solely RoM is insufficient because of the large variation of ligament material properties between subjects [57]. For a stronger validation, comparisons should be made with ligament, IVD, and facet joint strains and forces, CoRs, and IDP, however, the paucity of such data limits the extent to which these comparisons can be made.

As Fan *et al.* noted, poroelasticity is an important consideration under vibrational loads in order to observe the time-dependent vibrational characteristics; however, in most studies, the porous material properties were not modelled [155].

Boundary Conditions

The term "boundary conditions" refers to the forces and kinematics defined by the researcher for a part or all of the simulation. This should not be confounded with initial conditions which are the forces and kinematics of the model in the first instant of a simulation. Both force and displacement have been used as boundary conditions, force boundary conditions are often applied via follower loads which require careful tuning; while displacement boundary conditions require kinematic data, which can be challenging to gather.

Boundary conditions in terms of displacements have been derived from quantitative fluoroscopy [156], plane radiographs [61], stereophotogrammetry [157], and motion capture [158]. Quantitative fluoroscopy allows continuous imaging and is accurate for motions over 3.9˚ however is limited to 2D imaging [159]; alternatively, biplanar fluoroscopy enables 3D imaging however exposure to high radiation dosage is a concern [160]; stereophotogrammetry has been accurate to 0.5˚ but the subject must be stationary during the imaging process [161]; single plane radiographs have achieved similar accuracy and are less invasive but are limited to static images in 2D [162]; motion capture provides a continuous position however suffers from associated soft tissue artefacts [163]. Zanjani-Pour *et al.* predicted intervertebral disc stresses consistent with literature using displacement boundary conditions. However further work is needed to reduce errors in mapping the motion [156]. Dehghan-Hamani *et al.* [61] used displacement boundary conditions to validate a model against the loading in the ligaments and IVDs. Validation against FJF proved challenging due to the lack of data and the difficulty in modelling the facets [61]. Shojaei *et al.* suggested that displacement boundary conditions could be used in conjunction with optimisation techniques to estimate muscle forces in FEMs [164].

Boundary conditions can also be applied in terms of loads, which can represent body weight, muscle forces, and external loads. For a simpler representation of the local muscle forces, Rohlmann *et al.* lumped them together into a single follower load – loads that represent body weight and occasionally muscle forces [68] and intra-abdominal forces [165]. They were then able to include individual loads for a few global muscles and simulated realistic results. However, representing the local muscles with a follower load caused the IDP to be slightly larger than it should have been [68]. Investigations have demonstrated alterations to the follower load path substantially influenced the deformation the spinal segment undergoes, thus the path should be optimised in order to achieve more realistic motions and load-carrying capabilities [166–168]. Studies have modified the location of the path to optimise it such that bending moments and shear loads were minimised [168] or the predicted RoM, IDP and disc bulging matched those reported in the literature [167], both studies concluded the path should be posterior to the centre of the disc.

The inclusion of a follower load influenced and limited the possible position of the centre of rotation (CoR) [57], through which the follower load should ideally pass [168]. Foresto *et al.* found spinal stability was only maintained if the path passed through a specific region for a given posture [169]. In addition to the posture, the optimal path was influenced by the magnitude of the follower load [168]. Dreischarf *et al.* simulated realistic motions by optimising the magnitude to minimize the intervertebral rotations [170], in another study the magnitude was optimised to minimize the IVJ load [169]. In a number of studies, the follower load has been assumed to be task-independent [60,141,150]. According to Azari *et al.* [171] this is not the case. They used a hybrid L4-L5 model to determine the follower load for specific tasks. Hybrid models have used MBM to calculate the muscle forces which are then applied as force vectors at the relevant attachment points in the FEM [172,173].

Occasionally, the muscles and the intra-abdominal pressure are explicitly modelled, with various degrees of complexity [67,151,174]. One approach is to combine a FEM and an optimization method to calculate muscle forces [151,158,164,169]. In other cases, muscles are modelled simply using tension elements [174] while a more sophisticated model has also accounted for the muscle geometry and architecture [67]. The inclusion of the muscles and the intra-abdominal pressure decreased the predicted stress in the IVDs [67,174].

Non-linearities

It is generally accepted that the biomechanical properties of soft tissues show marked non-linearities, although there has been little investigation into the error caused by neglecting such non-linearities. Linear [156] and non-linear elements [158] have been used to model the intervertebral joint (IVJ), a lumped parameter which represents some or all of the passive components (IVD, ligaments, cartilages) between two adjacent vertebrae.

Other studies have modelled the individual components of the IVJ. Linear [153] and non-linear (most often hyperelastic) models [57,61,65,149,150,155,167,169] have been used for the IVD, often modelling the nucleus pulposus and the annulus fibrosus separately. Non-linear hyperelastic equations described the RoM much better than linear equations, due to the intrinsic nature of the IVD [175]. However, this model does not account for the viscoelastic behaviour of the IVD which has been experimentally observed [176].

The ligaments have been modelled as both linear [153,169] and non-linear [61,65,149,150,155,167]. Naserkhaki *et al.* found a piecewise linear model from an *in vivo* dataset best predicted the mean *in vitro* rotations, and higher non-linearity caused greater movement of the instantaneous centre of rotation [57].

Personalisation

Models can be personalised by the geometry, the material properties and the loading conditions; the extent of personalisation of each can vary, both geometric and material personalisation have been shown to be crucial for accurate simulations. As Naserkhaki *et al.* noted, to fully personalise a model in all of these aspects is nearly impossible. Personalisation of the curvature of the spine was an important factor in the load sharing between the various spinal components and in the spine stiffness as it determined the disc wedging [150]. However, personalisation of the curvature was insufficient to accurately predict the load sharing [150]. Scaling a model to personalise existing models was not suitable for estimating FJF due to high sensitivity to the facet surface shape and orientation [61].

The FE models of hybrid models have been personalised using scaling methods. Considering FE models in this context, when passive joint properties were personalised based on subject sex, age, body weight, and height, for subjects of similar body weight (5 kg range), at large angles substantial differences in shear and compression loads were predicted [165]. This supports the findings of a similar study that found body weight had the greatest effect on predicted loads [177]. This is to be expected as body weight was also a factor defining the boundary conditions. Further analysis of factors used to inform the scaling of the properties revealed load predictions were most sensitive to the factors that defined model boundary conditions, ie. trunk flexion angle, load and moment magnitude, and loading asymmetry [178]. Other factors that informed the scaling factors (sex and body height) but had little influence on the boundary conditions had little impact [178]. Thus, for subject-specific models, defining subject/task-specific boundary conditions are more important than the material parameters.

A limitation of personalised models is that they cannot be used to infer the mechanical behaviour of the spine in the wider population as there is much inter-subject variability in such models [54].

A brief overview of the FEM modelling of the healthy spine has been presented. The present paper aims to address the modelling of the scoliotic spine thus a more in-depth review of healthy FEM spine modelling is outside the present scope. Recently, both Ghezelbash *et al.* [179] and Dreischarf *et al.* [141] have conducted literature reviews that focus on the *in vitro, in vivo* (respectively) and *in silico* studies (both); the Author recommends referring to these reviews for greater depth.

2.6. Finite element models of the scoliotic spine

Geometry

The majority of scoliotic spine FEMs are developed from planar and tomographic radiographic images

Table 2.1) and include the entire spine in the model (Table 2.2) however the rib cage was rarely included. The curvature and rib cage have played important roles in the loading of the spine. This enables a high level of geometrical detail to be captured, including the facets which require manual segmentation as automatic segmentation tools cannot yet detect the gap between articulating cartilages [180]. In the creation of such models, geometric uncertainty due to user identification of landmarks and bony structures needs to be considered. Little and Adam measured intra-observer geometric uncertainty. The most substantial geometrical uncertainty was in the angle of the facet joints in the coronal plane, and consequently, the endplate angle, which was comparable to the accepted clinical variation. The effect of the operator-dependent geometrical uncertainty was minimal on all the measured output parameters except the estimated IDP [39]. The geometrical variation of the intravertebral disc space was important in determining the degree of deformity and the extent of possible correction [181]. As the authors stress, these results are intra-observer rather than inter-observer variations and the sensitivity of the parameters was only tested for a fulcrum bending test [39]. Inter-observer uncertainty could be greater than the intra-observer uncertainty and the effect could be greater under different loading conditions.

Manual segmentation of the spine is a time-consuming process [182]. Hadagali *et al.* proposed a semi-automatic technique to morph an already segmented spine onto a scoliotic spine based on landmark selection using a dual-kriging method [182] (see [183] and [184] for further details). Jobidon-Lavergne *et al.* have also investigated the use of an automatic segmentation method. Additionally, they investigated the possibility of using the pre-operative shape to enable intra-

operative surgery planning, by registration of the pre-operative geometry onto intra-operative images [185].

Geometries are often constructed from pre-operative standing images, which may result in a different geometry to the intra-operative one, as scoliotic curvature reduces when in a prone position [186]. Simulations have modelled the reduction in curvature due to prone positioning, patient weight, and surgical bed configuration [187]. This has resulted in curvature reduction ranging from 7% to 26% depending region of curvature [187]. Therefore, accounting for the difference could improve surgical simulation predictions [186] and as the prone position may inform surgical planning it is an important consideration. Further, FEM studies are required to fully understand the impact of assuming an upright position on surgical predictions.

Scoliotic spines are categorised by different types of curves. The importance of accounting for the curvature type was demonstrated by Jia *et al*. They modelled three different curve types, under axial vibrational loading (exposure to vibrations has been associated with spinal problems), and there was a different response for each type [188]. Validation proved challenging, and the model excluded any poroelastic effects which as discussed earlier can be important under vibrational loading. Other studies have further evidenced the importance of the curve type. Thoracic curve types have been shown to lead to asymmetric pressure distributions in the lumbar IVD [189]. Curve type and severity influenced the centre of pressure in the S1 endplate; lumbar curves affected the sacral loading more so than other curve types [190]. Scoliotic severity also affected the FJF; under compression and a bending moment higher FJFs were predicted on the convex and concave side when the Cobb angle was above and below 20° [59].

Very few studies have included the rib cage (Table 2.2). However, Jia *et al.* showed that the rib cage played an important role in the stabilisation of the spine, especially the scoliotic one, and reduced the maximum Von Mises stresses and displacements [191]. The rib cage, ligaments, vertebrae and IVD were examined and the magnitude of the maximum Von Mises stress and displacements reduction ranged between 19.7-53.4% (in axial compression an increase of 31.5%) and 2.1-16.9%, respectively, depending on the loading direction [191].

Constitutive Equations

The material properties of both bone and soft tissues are often taken from literature measurements without personalisation (Table 2.1). In the case of adolescent idiopathic scoliosis (AIS), this presents a twofold problem, firstly there is very little literature data on the mechanical properties of adolescent tissues. Secondly, there has been very little consideration regarding potential differences between the tissue properties of scoliotic and non-scoliotic subjects. Cheuk *et al.* suggested there could be differences in the stiffness and failure load of bone. Using personalised micro-FE they found the scoliotic subjects had weaker bones, however, this is potentially accounted for by differences in levels of physical activity and calcium intake [192], regardless of the cause the differences need to be accounted for in models. Although the study was performed on the radii rather than vertebrae, other studies have suggested changes in bone properties of the radii are reflected in changes in the vertebrae [192]. A review paper by Li *et al.* supported the view that lower bone quality was prevalent in scoliotic subjects [193], building on this Song *et al.* investigated the effect of low bone quality. With a geometrically personalised scoliotic model, three different Young's moduli were assigned to the cortical and cancellous bone. They found that lower bone quality elevated the asymmetrical loading effect, already present due to the curvature of the scoliotic spine [189].

Berger *et al.* determined personalised IVJ stiffnesses for five AIS subjects from *in vivo* spinal suspension tests using a FEM. Despite simplifying the joint as a lumped parameter, this still demonstrated a statistically significant difference in subject-specific stiffnesses [194]. Zheng *et al.* created a geometrically personalised degenerative scoliotic model, they used two sets of material properties one represented normal young subjects and the other represented elderly degenerative scoliotic subjects [195]. They simulated an *ex vivo* study conducted on young and elderly non-scoliotic spines (data for scoliotic cases was not available) and compared the predicted motion to the measured motion. The model representing elderly degenerative scoliosis predicted a difference in motion of up to 24% compared to *ex vivo* data of the elderly non-scoliotic spines, a similar difference was observed between the model representing normal young subjects and the *ex vivo* data of young non-scoliotic spines. Zheng *et al.* suggested this evidenced the need for pathology-specific material properties [195].

Boundary Conditions

While healthy spine FEM have used displacement and force boundary conditions scoliotic FEM used almost exclusively force boundary conditions with the lowermost body completely constrained, often to simulate scoliotic correction or study vibrational effects. To simulate the scoliotic correction of patient-specific models created from CT scans of 8 different patients Little *et al.* used intraoperative force profiles measured *in vivo* by strain gauge force transducers attached to the tools used to apply a compressive load between the vertebral body screws [196] during the scoliotic correction of 15 different patients. Applying one of three force profiles, the mean or the mean plus/minus one standard deviation of the *in vivo* data, they were able to predict the correct Cobb angle for 7 out of the 8 subjects [181].

Li *et al.* investigated the effect of vibrational loading, an important consideration as vibrational loading increased the risk of further deformation and has contributed to the lower back pain of which scoliotic subjects are at greater risk [188,191,197]. Several differences were noted between their results and similar studies on non-scoliotic spines. The scoliotic spine was less affected by the follower load, but was more sensitive to vibration with lower resonant frequencies and larger amplitudes, especially in rotation [198]. These differences can probably be attributed to geometric differences because the study used literature data for the material properties which is based on healthy spines [198]. Other studies have investigated the scoliotic spine under vibrational loading, expanding the knowledge to include the effect in adult degenerative scoliosis cases [197], the effect of curve type [188], and the rib cage [191]. The findings of these studies have supported those of Li *et al.*, that the scoliotic spine has more resonant frequencies and a larger response than a healthy spine. Thus scoliotic subjects are exposed to a greater risk of increasing deformity, lesions at the resonant frequencies [188,197], and injuries associated with vibrations [191]. Further, sagittal alignment of the scoliotic spine changed the response to be more similar to a healthy spine, which would decrease the risk for scoliotic subjects when exposed to whole-body vibrations [199].

The joints applied between bodies are also an important consideration. Ye *et al* investigated the simultaneous correction of scoliosis and pectus excavatum. The type of joint applied between the sternum and the clavicles influenced the behaviour of the model: with the joint fully constrained they showed a simple correction of scoliosis via spine stretching did not affect the pectus excavatum, however, with the joint free in the sagittal plane spine stretching affected the chest deformity [200]. As such, modelling solely the spine can miss important effects scoliotic corrections may have on surrounding bodies.

Haddas *et al.* used methods they had previously validated [65] to create scoliotic spine models [56]. They investigated the effect of fusion of vertebrae on load transfer. They found fusion increased the FJF and the IDP at the adjacent levels, and decreased them at the fused level [56].

As with healthy spine models, scoliotic FEMs have included intra-abdominal pressure [190,201]. They found the predicted IDP to be comparable to the IDP of non-scoliotic subjects measured *in vitro* and *in vivo*. The predicted vertebral compressive forces were closer to the predictions from other scoliotic models when the intra-abdominal pressure was included, comparison to *in vitro* or *in vivo* data was not possible to a lack of data [190]. Muscles have been represented by a follower load [197], or force vectors (calculated by MBMs) in hybrid models [110].

Non-linearities

Some scoliotic models considered the ligaments, the nucleus pulposus, and the annulus fibrosus as linear, and others as non-linear (Table 2.2). When the facet joints are modelled, they are often modelled as frictionless with a gap and a spring. In all cases, the parameters assigned have been taken from the literature. To the best of the Author's knowledge, there have been no studies investigating the suitability of non-linear compared to linear material properties in the case of the scoliotic spine, whereas such studies have been conducted in health spine FEM.

Personalisation

Personalisation of geometry was common, though less common material personalisation was also performed (Table 2.1), personalisation of both has been crucial to accurately predict scoliotic corrections. Kamal *et al.* compared the spines of a healthy subject and a scoliotic subject. In the subject with a Cobb angle of 24.4° higher muscle forces on the convex side were required for the equilibrium. Increased muscle forces shifted the CoR, which increased the stress in specific parts of the growth plate [110].

The geometric personalisation alone was not enough to accurately represent the scoliotic spine [186]. Personalised geometry and individually representing all the soft tissue structures and including the rib cage, was not sufficient to consistently predict a scoliotic correction within an acceptable margin [70]. This suggested that patient-specific soft tissue properties are also required [70]. Additionally, Duke *et al.* included the effects of anaesthesia on the muscles and spine stiffness by modifying the stiffness of the IVJ, in doing so they improved the simulation predictions of the intra-operative position [186]. Personalizing the spine flexibility and stiffness has substantially improved the predicted axial rotation due to a correction manoeuvre [202].

Using *in vivo* side bending tests to personalise the overall stiffness of the spine, some studies have predicted the post-operative curvature to within five degrees of clinical measurements [136,203] however an accuracy of ten degrees has been reported [187]. As Little and Adam noted, side bending tests rely on the patient's muscle activation. They studied the characterization of the soft tissue properties of scoliotic subjects using a fulcrum bending test (the patient lies on their side over a rigid cylinder) which has the benefit of using the subject's weight and does not rely on muscle activation [204]. They simulated a fulcrum bending test using literature-reported values for the soft tissue stiffnesses and an imaging-based geometry. For six out of ten cases, there was more than a 10% difference between the predicted and clinical flexibility. In these cases, the sensitivity of the predicted flexibility to the costovertebral joint stiffness was investigated. The sensitivity was subject-dependent. In addition to supporting the need for patient-specific soft tissue stiffness they suggest finding the stiffness of a single tissue in this way is not possible. Rather several tissues contribute to the stiffness and it is better to consider an overall stiffness [204].

Another method to personalise the soft tissue properties is to use a suspension test [185,205]. The concept for all the personalisation methods is the same, to measure the spine curvature under a certain loading and then to simulate the action. The component material properties or lumped IVJ stiffnesses are then calibrated such that the predicted curvature is similar to the measured curvature.

Table 2.1: Degree of personalisation for scoliotic FEM

Study	Models source	Personalisation	
		Geometry	Materials
Agarwal *et al. (2015)* [206]	Adapted a previous model	No	Literature
Agarwal *et al. (2018)* [207]	Previous model adapted to CT scan	No	Literature
Aubin *et al. (2018)* [208]	Coronal and lateral radiographs	Yes	Literature
Berger *et al. (2015)* [194]	Coronal and lateral radiographs	Yes	Literature, personalised with suspension test
Cahill *et al. (2012)* [209]	3D model atlas	No	Literature, adjusted to reproduce *in vitro* results
Chen *et al. (2020)* [210]	CT scan	Yes	Literature and bone based on CT scan
Clin *et al. (2019)* [211]	Coronal and lateral radiographs	Yes	Literature
Cobetto *et al. (2018)* [205]	Coronal and lateral radiographs	Yes	Literature, personalise with suspension test
Driscoll *et al. (2012)* [187]	Previous model adapted to coronal and lateral radiographs	Yes	Literature, personalise with side bending
Driscoll *et al. (2013)* [212]	Coronal and lateral radiographs	Yes	Literature
Duke *et al. (2005)* [186]	Standing and prone radiographs	Yes	Literature, personalise with side bending
Galbusera *et al. (2015)* [213]	Biplanar radiographs	Yes	Literature
Hadagali *et al.* (2018) [182]	CT scan	Yes	Literature
Haddas *et al. (2019)* [56]	CT scan	Yes	NA – just recreating geometry
Jia *et al. (2019)* [188]	CT scan	Yes	Literature
Jia *et al. (2020)* [191]	CT scan	Yes	Literature
Jobidon-Lavergne *et al. (2019)* [185]	Coronal and lateral radiographs	Yes	Literature, personalise with suspension test
Lafage *et al. (2004)* [202]	Stereo-radiograph	Yes	Literature
Li *et al. (2011)* [198]	Previous model developed from a CT scan	Yes	Literature

Little & Adam *(2015)* [39]	CT scan	Yes	Literature
Little *et al. (2013)* [181]	CT scan	Yes	Literature, from multiple sources, derived from adults
Little & Adam *(2012)* [204]	CT scan	Yes	Literature, personalised with fulcrum bending
Little & Adam *(2011)* [70]	CT scan	Yes	Literature
Musapoor *et al. (2018)* [74]	CT scan	Yes	Literature
Pasha *et al. (2014)* [190]	Atlas adapted to coronal and lateral radiographs	Yes	Literature
Pasha *et al. (2015)* [201]	Atlas adapted to coronal and lateral radiographs	Yes	Literature
Rohlmann *et al. (2005)* [214]	X-ray	Yes	Literature
Rohlmann *et al. (2008)* [215]	CT scan	Yes	Literature
Song *et al. (2018)* [189]	CT scan	Yes	Literature
Wang *et al. (2016)* [59]	CT scan	Yes	Literature
Xu *et al. (2017)* [197]	CT scan	Yes	Literature
Xu *et al. (2019)* [199]	CT scan	Yes	Literature
Ye *et al. (2017)* [200]	CT scan	Yes	Literature
Zhang *et al. (2013)* [216]	Previous model developed from CT scan	Yes	Literature, personalise with side bending
Zheng *et al. (2015)* [195]	CT scan	Yes	Literature
Zhou *et al. (2020)* [217]	CT scan	Yes	Literature

Table 2.2: Components included in scoliotic FEM

Study	Spinal segment studied	Components modelled				Follower loads
		Rib cage	Facet joints	Intervertebral disc	Ligament	
Agarwal *et al. (2015)* [206]	S1-T1	-	Non-linear Soft contact	Matrix – Hyperelastic Fibres – Non-linear Nucleus – Hydrostatic	Tension only	14% BW* at T1 +2.6% per vertebra
Agarwal *et al. (2018)* [207]	S1-T1	-	-	Matrix – Hyperelastic Fibres – Non-linear Nucleus – Hydrostatic	-	14% BW at T1 +2.6% per vertebra
Aubin *et al. (2018)* [208]	Pelvis - T1	CVJ* -Linear Bone -Linear	Non-linear contact	Lumped linear	Linear Tension only	BW & muscles

Berger *et al. (2015)* [194]	L4 - T3/C5	-	-	Lumped linear	-	-
Cahill *et al. (2012)* [209]	T12-C6	-	-	Matrix – Hyperelastic Fibres – Non-linear Nucleus – Incompressible	Tension only	-
Chen *et al. (2020)* [210]	T4-T12	-	Frictionless Soft contact	Lumper linear	-	-
Clin *et al. (2019)* [211]	Pelvis - T1	-	-	Matrix – Linear Fibres – Linear Nucleus – Linear	Linear	Sectional BW
Cobetto *et al. (2018)* [205]	Pelvis - T1	CVJ - Tension only	-	Lumped linear	Linear Tension only	Segmental BW
Driscoll *et al. (2012)* [187]	S1-L1	CVJ - 3D elastic springs with contact	-	Lumped linear	-	BW
Driscoll *et al. (2013)* [212]	L5-T1	-	Linear	Annulus – Linear Nucleus – Linear	Linear tension only	-
Duke *et al. (2005)* [186]	S1-T1	3D elastic springs	Contact, piecewise linear	3D elastic elements	3D elastic elements	Segmental BW
Galbusera *et al. (2015)* [213]	L5-T1	-	Frictionless Gap 0.4mm	Matrix – Elastic Fibres – Non-linear Nucleus – Incompressible	Non-linear	-
Hadagali *et al.* (2018)	T12-T1	-	-	-	-	-
Haddas *et al. (2019)* [56]	S1-T11	-	Frictionless contact	Matrix – Hyperelastic Fibres – Non-linear Nucleus – Hyperelastic	Non-linear	BW & muscle optimised path
Jia *et al. (2019)* [188]	S1-L1	-	Frictionless Linear Contact	Matrix – Hyperelastic Fibres – Non-linear Nucleus – Incompressible	Non-linear	400N optimised path
Jia *et al. (2020)* [191]	Sacrum-T1	Linear joint	-	Annulus – Linear Nucleus - Linear	Linear Tension only	BW
Jobidon-Lavergne *et al. (2019)* [185]	Pelvis-T1	Tension only spring	-	Solid elements	Tension only spring	Yes
Lafage *et al. (2004)* [202]	S1-T1	-	Contact	Lumped torsional and bending properties	Linear tension only	-
Li *et al. (2011)* [198]	S1-T1	-	Non-linear Friction	Matrix – Linear Fibres – Linear Nucleus – Incompressible	Linear tension only	BW at T1

Little & Adam *(2015)* [39]	L5-T1	CVJ and ribs linear elastic	Frictionless Soft contact	Matrix – Hyperelastic Fibres – Linear Nucleus – Hydrostatic	Linear and non-linear	-
Little *et al. (2013)* [181]	L5-T1	Non-linear joint	-	Matrix – Hyperelastic Fibres – Linear Nucleus – Incompressible	Linear & non-linear	-
Little & Adam *(2012)* [204]	L5-T1	CVJ and ribs linear elastic	Linear	Matrix – Hyperelastic Fibres – Linear tension only Nucleus – Incompressible	Linear	-
Little & Adam *(2011)* [70]	L5-T1	CVJ and ribs linear elastic	Linear	Matrix – Hyperelastic Fibres – Non-linear Nucleus – Incompressible	Non-linear	-
Musapoor *et al. (2018)* [74]	L5-T1	-	Non-linear, pressure overclosure	Matrix – Linear Fibres – Linear Nucleus – Incompressible	Non-linear Tension only	-
Pasha *et al. (2014)* [190]	S1 - T1	CVJ - Linear tension only springs Ribs - Linear	Non-linear Friction Contact	Lumped linear	Tension only	-
Pasha *et al. (2015)* [201]	S1-T1	Non-linear joint	Contact	Lumped linear	-	Segmental BW
Rohlmann *et al. (2005)* [214]	T12-T1	-	-	Annulus – Linear Nucleus – Linear	-	Local muscles at vertebrae
Rohlmann *et al. (2008)* [215]	L2-T3	-	Linear Compression only	Matrix – Hyperelastic Nucleus – Incompressible	Non-linear Tension only	-
Song *et al. (2018)* [189]	S1-T1	-	Non-linear Contact	Matrix – Linear Fibres – Linear Nucleus – Incompressible	Linear Tension only	-
Wang *et al. (2016)* [59]	L5-L1	-	Frictionless Contact Gap 0.5mm	Annulus – Linear Nucleus – Incompressible	Linear Tension only	400N at L1
Xu *et al. (2017)* [197]	Sacrum-L5	-	Frictionless Soft contact	Matrix – Hyperelastic Fibres – Non-linear Nucleus – Hyperelastic	Non-linear	BW & muscle optimised path
Xu *et al. (2019)* [199]	S1-T12	-	Non-linear	Matrix – Hyperelastic Fibres – Non-linear Nucleus – Hyperelastic	Non-linear	BW & muscle optimised path
Ye *et al. (2017)* [200]	T12-T1	Ribs linear elastic	-	Lumped linear	-	-

Zhang *et al. (2013)* [216]	Sacrum-T1	Yes	-	Yes	Yes	-
Zheng *et al. (2015)* [195]	S1-T12	-	Contact Friction Non-linear	Matrix – Linear Fibres – Linear Nucleus – Incompressible & viscoelastic	Non-linear	-
Zhou *et al. (2020)* [217]	L5-T12	-	-	Lumped linear	Linear	-
* BW = body weight * CVJ = costovertebral joint				Muscles were not explicitly modelled in any of the studies		

2.7. Multibody Models of the healthy spine

Geometry

MBM are often developed for a particular purpose and then used as an initial model which is modified and personalised in future studies. The curvature, rib cage and to a lesser extent the muscles have to be accounted for in order to obtain realistic results; the most suitable method of positioning the IVJ location is still being studied.

Bruno *et al.* developed and validated a fully articulated MBM of the entire thoracolumbar spine [41]. Other fully articulated whole spine models exist [50], as well as ones which assume a rigid thorax [218–220]. Models of just the lumbar spine are most common [72,221].

A common assumption in spine models is that the thoracic region can be treated as rigid or the rib cage structure can be excluded [72,114,220,222]. Ignasiak *et al.* compared the loading and motion for a model with and without a rib cage. The comparison showed the rigid thorax assumption was suitable in activities where there was little thoracic deformation [223] and was only suitable for predictions of the lower lumbar spine [50]. Modelling the articulation of the rib cage improved the accuracy of the results [50].

Bruno *et al.* used an MBM of the entire thoracolumbar spine to investigate the effect of lumbar lordosis and thoracic kyphosis on the risk of vertebral fracture. While the curvature affected the loading, their analysis suggested that the muscle forces played a greater role [44], which are influenced by the muscle cross-sectional areas [117].

The position of the CoR of the IVJ affected the joint and muscle forces [114,224]. A sensitivity study by Abouhossein *et al.* showed variations of the CoR location by 1 – 5 mm lead to differences of 66% in shear load and 10% in the axial force in the intervertebral disc [225]. Abouhossein *et al.* and Senteler *et al.* postulated that the CoR may migrate during motion [114,224], potentially minimizing the joint reaction forces [114]. Abouhossein *et al.* suggested that the migration is necessary to predict the kinematics of the spine [224]. While the literature supports the concept of CoR migration there is a lack of direct evidence [114,224].

Identification of component parameters

The IVJ has been modelled without stiffness, with linear stiffness and with non-linear stiffness, studies have established the inclusion of a stiffness is essential for accurate simulations, whether modelling the joint as a lumped parameter is suitable or not is still unclear.

In addition to the location of the joint that defines the IVJ, stiffness plays a critical role in characterising the flexibility of the spine. Simply including the stiffness of the joint reduced the muscle activation and the IDP, improving agreement with *in vivo* results [226]. Incorrect implementation of the IVD stiffness in OpenSim can cause undesired moments to be generated. Christophy *et al.* modified the element (bushing element) used to model the IVD in OpenSim. The modified element, calculated the force to apply as a function of the displacement relative to the initial position of the element rather than the displacement relative to a zero offset position [106]. In other terms, these elements are defined by two reference frames, the modified element allowed for the initial position of the frames to be offset without any force being generated, and displacement relative to this position would generate a force.

Often all the passive stiffness components are modelled as a single lumped parameter. The impact of the lumped parameter (ie. the intervertebral disc and ligaments modelled with a single component) simplification depended on the direction of motion and the extent of motion [226]. Therefore for flexion above 40° explicitly modelling the ligaments may improve IDP prediction [226], but in other directions and for smaller flexion angles the lumped parameter assumption may be suitable. The ligament stiffness also affected the location of the estimated CoR, if it is allowed to migrate [224].

Muscles played an important role in the stabilisation of the spine. The muscles have been shown to have a notable effect on both the magnitude and the distribution of the intervertebral forces [225]. Han *et al.* incorporated muscles, ligaments, and rotational disc stiffness into an existing MBM, without any material personalisation. They simulated an upright posture and compared predicted joint reaction forces and muscle activation to *in vivo* measurements from the literature of vertebral body replacement implant forces, IDP and muscle activation. This showed a considerable improvement in muscle force and joint reaction predictions on the base model, which demonstrated the importance of the passive soft tissue structures in spine models [40].

Boundary Conditions

In most models, the pelvis or the lowermost vertebra is fixed in all degrees of freedom, and loading is applied at the most superior vertebra in the model [226] and/or the arms if they are included [41,50]. Alternatively, some models specified motions at the bodies based on *in vivo* or *in vitro* data [69,72,120].

Bruno *et al.* investigated the compressive loads on the vertebrae for many activities represented by a large range of boundary conditions. Substantial variation in the vertebral loading was seen for different activities [44]. In addition to the vertebral loads, the predicted muscle forces were shown to be sensitive to the loading conditions; the muscle forces increased with the introduction of an external moment [220] and the activation patterns changed with variation of the follower loads [40]. Differences noted between the *in vivo* load data from sensorised telemetric vertebral body replacements and the predicted results were attributed to the differences in the definition of ‘standing’, while well defined in simulations, standing position *in vivo* is ambiguous without motion capture [220].

An important input for MSK models is the muscle forces, as they inform joint loads and moments and therefore in the case of spine models the risk of vertebral fracture [44,47]. There are three general approaches are used to calculate muscle forces, a solely mathematical optimisation of muscle excitation to minimise/maximise a cost function, an EMG-driven method which uses EMG signals to determine the muscle excitation and an EMG-assisted which combines EMG-driven

methods and the optimisation techniques [227,228]. Solely mathematical optimisation (for example minimisation of activation to satisfy joint loads and moments) techniques are often used by MSK models to first predict muscle activity which is then used as an input for forward dynamic simulations [123,229]. However, they fail to capture the inter- and intra-subject variations of muscle recruitment [227,228]. EMG-driven techniques may not accurately predict the joint moments due to the inability to record deep muscle activity and noise contamination, challenges which are only exacerbated when recording EMG signals in spine muscles [20,99,227]. This challenge is highlighted by reported muscle magnitude intraclass correlation coefficients of 0.41–0.69 trunk muscles [230]. The EMG-assisted method seeks to overcome the limitations of the other two approaches by tuning the muscle activity for the available EMG signals and or if no signal is available, predicts the muscle activity while trying to satisfy optimisation criteria [227]. EMG-assisted approaches have been successfully used in a number of applications (lower back loads, submaximal activities, joint moments within the cervical spine) and have shown to outperform both EMG-drive and solely mathematical optimisation approaches [99,231,232]. Although the joint loads are sensitive to the variation within the EMG signal, this is not substantial when comparing different tasks [232]. This approach is also sensitive to the cost function used, with a number of different ones used throughout the literature [99,228,231,232]. Early lumbar models assumed the muscle force equilibrium could be achieved by considering it at each joint individually [221]. However, solving for equilibrium across all joints simultaneously improved muscle force estimations and joint loads [221]. One toolbox for calculating the muscles that has been used widely for the lower limb and has also been applied more recently to the spine is CEINMS [99,227,233,234]. Recent studies have improved predictions from models using EMG-assisted by incorporating calibration for the specific activity and accounting for subject-specific muscle properties from MRI data [99,231]. Future studies should incorporate EMG-assisted approaches when applying muscle loads as they result in more accurate predictions for spinal loads, muscle activity, and muscle co-contraction. However suitable cost function must be selected [228] and the incorporation of subject-specific properties from MRI data needs to be extended to the thoracic and lumbar regions.

Non-linearities

Studies of the spine using MBM have simulated joints with no stiffness [41,120,220] or with linear stiffness [40,223]. The IVJ has often been modelled with a non-linear stiffness [40,69,72,222,224,226]. Byrne *et al.* investigated the effect of the linear stiffness assumption by comparing the predicted compressive and shear joint reaction forces for no stiffness, linear stiffness and non-linear stiffness for a flexion-extension motion under different external loads (4.5kg and 13.6kg), in different neutral positions (supine and upright), and different kinematics (dynamic stereo X-ray and motion at each joint defined as a fraction of the total motion (rhythm-based)) [72]. The trends were similar for both neutral positions. The linear model tended to predict larger joint reaction forces than the non-linear model, the difference between the prediction increased towards the end of the motion. Generally, a larger difference was seen in the predicted forces for the 4.5kg than the 13.6kg external load. The differences in predicted forces between the non-linear and the linear model were smaller for the rhythm-based than the dynamic stereo X-ray based kinematics [72]. Bryne *et al.* also found using a non-linear stiffness instead of linear stiffness had a minimal effect on muscle activation [72].

Wang *et al.* introduced a model with a highly sophisticated IVJ that accounted for the non-linearity, the stabilizing effect of the rib cage, the stiffening effect due to compression from the follower

load, and the multi-segment interaction in the thoracic spine. They used this to simulate *in vivo* experiments and accurately predicted the RoM [69]. This work demonstrated the numerous factors that need consideration when modelling the IVJ.

Personalisation

The spine curvature and the musculature have been personalised in a number of studies and shown to improve predictions. Personalising models by scaling them to a patient's height neglected the patient-specific spinal curvature [72]. This altered predicted compressive joint force reactions by 15% [72]. This finding is supported by the earlier work of Bruno *et al.*[117].

Bruno *et al.* found their model to be more sensitive to the personalisation of spine curvature than the muscle morphology although both had a substantial influence, the influence of the muscle morphology increased with greater muscle activation [117]. The effect of the personalisation was seen more in the thoracic spine than the lumbar spine [117].

During posterior spinal surgery the muscles are often damaged, Jamshidnejad and Arjmand investigated the effect of muscle damage on the loading seen in other muscles. Muscle damage led to higher predicted activation in the undamaged muscles [222].

The work by Schmid *et al.* was, to the best of the Author's knowledge, the only to develop MBMs of the child's spine. They developed them through the non-linear scaling of adult models and attempted to validate the models with a number of parameters against experimental data [120].

This is just a brief overview of healthy spine MBMs, a more in-depth review is outside the scope of this paper. For a more in-depth review of MBM spine models outside of the context of scoliosis, the Authors would direct the Reader to the review of cervical spine MBMs by Alizadeh *et al.* [51]. Some lumbar MBMs are addressed by Dreischarf *et al.* [141]. To the best of the Authors' knowledge, there are no other review papers on spine MBMs.

2.8. Multibody Models of the scoliotic spine

Geometry

This section on the geometry of multibody models of the scoliotic spine will address the anatomical structures included in the models, the overall geometry of the spine ie. the spinal curvature, the geometry of the individual vertebrae, and the geometry of the muscles ie. the muscle paths. The impact that these different considerations have on model predictions will also be briefly expanded upon.

Spinal curvature and occasionally the muscles have been included, however, the individual component of the IVJ (disc, ligaments and facet joints) are rarely included (Table 2.3). Some MBM unlike FEM of the scoliotic spine incorporated the muscles; however, the IVJs were often simplified by lumping the contribution of the facet joints, intervertebral ligaments, and the intervertebral disc together (Figure 2.2).

The reconstruction of the scoliotic spinal curvature from bi-planar radiographs is a common approach, with EOS imaging data being widely used [34,118,121,123,201]. The alignment of the vertebrae from these reconstruction methods is within 4° and 2 mm [118,121]. The accurate reconstruction of the spinal curvature is necessary as compared to a healthy spine model scoliotic curvature results in different predicted muscle force distributions. Unexpectedly, substantial lateral loads were not observed by Bassani *et al.*, however, this was attributed to the modelling of mild scoliosis. Larger forces were seen in the sagittal plane and concave side of the curve for larger

degrees of kyphosis and axial rotation, respectively [121]. The introduction of scoliotic curvature has also resulted in increases in the predicted IVJ compressive load. Although no correlation was observed between curve severity and compressive force, this could be because the curves in the model were mild or moderate [123]. As the curvature becomes more severe its accurate reconstruction becomes more important as it increasingly affects both the load magnitude within the discs and the muscle forces.

Reconstruction of the spinal geometry from EOS data allows for the inclusion of subject-specific vertebral geometries [118]. These geometries in MSK models are mostly for visualisation, however, they can be used to improve the estimation of rigid body parameters of the vertebrae, joint definitions, and the muscle paths as insertion and attachment points can be more accurately selected. The joint pose has been defined through a virtual palpation on the real geometries [118,121]. However, there are at present no guidelines for defining the joint pose in the case of severely deformed spines, thus the ISB recommendations [82] for the joint definition of perfectly aligned vertebrae are used [118] – vertebrae in the severely scoliotic spine are often severely misaligned. Furthermore, there are no reports in the case of scoliotic spines of the intra- and intra-operator variability of the virtual landmark palpation. However, asides from being used to inform the joint pose, subject-specific vertebrae geometries have not been utilised for the other two applications.

Muscles have not been included in all scoliotic models [34,118], although they are necessary if post-operative loads or daily activities are to be simulated. When muscles are included, the paths as with all MSK models are specified by insertion and attachment points. However, scoliotic models have not included wrapping points or surfaces to better guide the muscle paths [121]. This simplification may be acceptable for mild scoliotic curvature based on the validation against EMG data from the literature [121–123]. Further research is needed to investigate if results have substantial differences compared to a model which more accurately reproduces the muscle path. It is unlikely that this simplification remains valid for more severe scoliotic curves as direct paths between attachment and insertion points are likely to intersect with other muscles and vertebrae in a non-physiological way. Another aspect of the muscle geometry to consider is the muscle volume which can inform the force-generating capacity of the muscle. Muscle properties have been scaled based on the muscle cross-sectional area, however, a lack of data requires the initial muscle properties to be taken from non-scoliotic data [122]. Cross-sectional areas of the muscle have been estimated by performing a ‘virtual CT scan’ [123]. This is achieved by dividing the predicted force-generating capacity of the muscles by an assumed uniform maximal muscle stress [123]. This allows for a comparison of the muscle volume of the model to that recorded on a medical image. Using this method Schmid *et al.* observed muscle volume and activity asymmetry in their model [123]. They reported the predicted muscle volume was generally in line with the literature; the majority of the models had larger erector spinae volumes on the convex side of the curve, and one-third had larger volumes on the concave side. However, for the multifidi muscles, Schmid *et al.* reported larger volumes on the concave side for about 90% of the models. Asymmetric muscle activity partially agreed with the literature, however, differences could be attributed to differences between the curvature of the models and the subjects in the literature [123]. Previous studies have also found that the scoliotic spine experienced greater muscle force asymmetry than a healthy spine [225].

Identification of component parameters

The IVJ is most commonly represented as a lumped parameter and personalised based on *in vivo* side bending tests, doing so has resulted in accurate predictions of scoliotic corrections, however unlike the healthy MBMs CoR migration is rarely considered. Petite *et al.* used a model with initial, literature-based, linear stiffnesses at the joints to develop a method to personalise the IVJ stiffness of a scoliotic spine. They optimised the stiffness to minimize the difference between the predicted and measured Ferguson angle of an *in vivo* side bending test. The personalisation based on the *in vivo* side bending test resulted in more than a 40% increase in lumbar and thoracic stiffness compared to cadaver specimens and showed high inter-subject variability [127]. This suggests for scoliotic models to provide accurate predictions the IVJ stiffness needs personalisation.

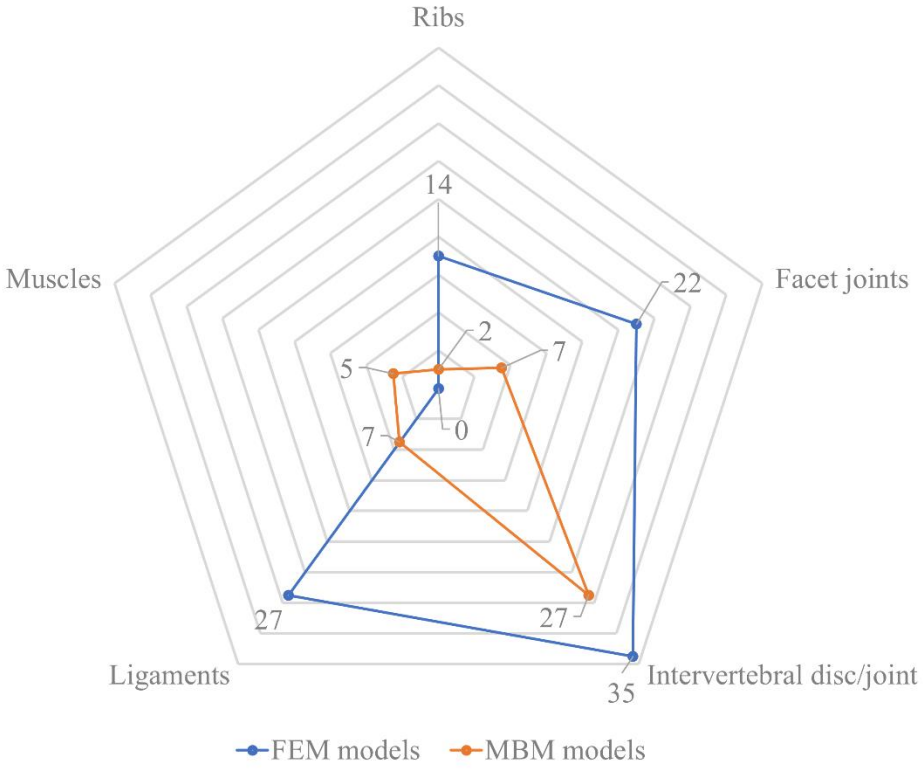

Figure 2.2: Trends of the components included in numerical models of the scoliotic spine with a specific element

In the correction of scoliosis, the disc stiffness can increase due to fusion by inserting bone grafts at the IVD [235]. Desroches *et al.* attempted to account for this. They created a patient-specific model using the personalisation method developed by Petit *et al.* and expanded it to include six degrees of freedom. Desroches *et al.* increased the IVD stiffness to represent the bone graft and performed a sensitivity study which showed that the rod shape and implant positioning had a greater impact on the predictions than the IVD stiffness. It is also worth noting that a higher IVD stiffness led to a better-predicted correction in the sagittal plane but worse in the coronal [235]. This suggests the material properties are highly anisotropic, therefore, to accurately predict the behaviour in all directions this may need to be accounted for. To the best of the Author's knowledge, there have been no studies examining the effect of the non-uniform spatial distribution of the material properties of the IVD in MBM.

Boundary Conditions

Boundary conditions of MSK models reflect a number of modelling choices made, such as the degrees of freedom allowed at the joints and the properties of the muscles in terms of force-length relationships (thus determining the force applied by the muscle). Additionally, external forces can be applied to the models to mimic the forces that might be applied during a surgical manoeuvre, or a kinematic boundary condition can be applied to ensure the model follows the trajectory of markers recorded with motion capture. There have been few studies on the suitability of the boundary conditions applied and few studies in scenarios not involving a correction manoeuvre. Desroches *et al.* analysed the impact of constraining the axial rotation of the uppermost vertebra, showing it had no impact on the predicted post-operative spinal shape. However, the correction of the segments outside of the instrumented region was sensitive to the boundary conditions [235]. Thus, the suitability of the boundary conditions applied is dependent on the spinal region being investigated.

There is an interplay between the load boundary condition and the scoliotic curvature. The compressive load on the vertebrae were sensitive to both load magnitude and direction relative to the scoliotic curvature [123]. Kinematic boundary conditions have also been applied by incorporating gait analysis. The intervertebral forces in the lumbar region during gait have been shown to be substantially higher than in simple standing [225]. Therefore when considering loads within the scoliotic spine, dynamic conditions should also be considered.

Non-linearities

When the IVD stiffness is included, it is often a linear and lumped parameter (Table 2.3), the impact the non-linearity may have has been studied in greater detail with healthy MBMs. This is only suitable for a limited RoM and could result in inaccurate predictions when simulating surgeries where large rotations and loads are present [236]. Jalalian *et al.* developed a method to characterize a non-linear stiffness for the IVD using a 2D model. The non-linear stiffness resulted in better shape predictions for all motions, the improvement was more pronounced for larger motions. It was also able to provide accurate predictions for shapes not used in the characterization of the stiffness. While limited to only being in 2D they suggest the method could easily be expanded to 3D if suitable data is available [236].

Personalisation

Often the geometry was personalised from radiographs, and in comparison, to the healthy MBM, the stiffness of the IVJ has been personalised more frequently. Side bending tests and fulcrum bending tests have been used to personalise, the stiffness of the IVJ (Table 2.4) determining the correct loading directions when simulating these tests was important when personalising the stiffness. Jalalian *et al.* investigated the direction in which the force in the frontal plane should be applied to simulate lateral bending, specifically how it should be personalised to an individual. Personalising the line of action of the force based on the location of the inflexion points measured from radiographs improved the bending prediction. As they note in the context of lateral bending tests, the line of action is crucial as it determines the loads and moments. Incorrect lines of action would potentially lead to inferior characterization of the IVJ stiffness [111].

The study by Jalalian *et al.* used X-rays of left and right bending and erect positions to personalise their model. They were able to establish a relationship between the bent and erect positions and were able to accurately predict positions which were not used in the characterization [237]. This is important if models are to be predictive.

Table 2.3: Components included scoliotic MBM

Study	Spinal segment studied	Components included			Notes
		Facet joints	Intervertebral disc	Ligament	
Abedrabbo Ode *et al. (2017)* [225]	Pelvis-T1	-	DoF* - 6 Elasticity – Linear	-	Muscles – linear spring damper system
Aubin *et al. (2003)* [238]	L3/L2-T4	-	DoF – 3 rotational Elasticity – Linear	-	
Aubin *et al. (2008)* [34]	Pelvis-T1	-	DoF – unclear Elasticity – unclear	-	
Aubin *et al. (2015)* [239]	L5-T1	Non-linear	DoF – unclear Elasticity – Non-linear	Non-linear	Muscles – posterior extensor-flexor at T1 to T3 as spring elements, optimised stiffness. Follower load – Segmental BW*
Bassani *et al. (2017)* [121]	S1-T1	-	DoF – 3 rotational Elasticity – Linear	-	Muscles – 89, tension only, no passive stiffness, or muscle wrapping. Follower load – BW
Cammarata *et al. (2014)* [240]	Pelvis – T1	-	DoF – 6 Elasticity – linear	-	Follower load – Segmental BW
Desroches *et al. (2007)* [235]	Sacrum-T1	-	DoF – 6 Elasticity – Linear	-	
Fradet *et al. (2016)* [136]	L5-T1	-	DoF – 6 Elasticity – linear	-	Regional spine stiffness factors included in IVD
Fradet *et al. (2018)* [241]	Pelvis – T1	-	DoF – 6 Elasticity – linear	-	A hybrid model. Follower load – muscle force
Jalalian *et al. (2016)* [242]	L4-T2	-	DoF – 1 rotational Elasticity – NA	-	
Jalalian *et al. (2017)* [111]	L4-T2	-	DoF – 3 rotational Elasticity – Linear	-	
Jalalian *et al. (2017)* [236]	L4-T2	-	DoF – 3 rotational Elasticity -Non-linear	-	
Jalalian *et al. (2017)* [237]	L4-T2	-	DoF – 1 rotational Elasticity – NA	-	
Kamal *et al. (2019)* [110]	S1-T1	-	DoF – 3 rotational Elasticity – Non-linear	-	A hybrid model. Thorax – rigid structure.

					Muscles – 92, scaled CSA* Follower load – gravity at each vertebra
La Barbera *et al.(2020)* [243]	S1-T1	-	DoF – 6 Elasticity – linear	-	
Le Navéaux *et al. (2016)* [203]	Pelvis-T1	-	DoF – 6 Elasticity – Non-Linear	-	
Majdouline *et al. (2009)* [135]	Pelvis - T1	-	DoF – 6 Elasticity – unclear	-	
Majdouline *et al. (2012)* [30]	Pelvis - T1	-	DoF – unclear Elasticity – unclear	-	
Martino *et al. (2009)* [244]	Pelvis-T1	-	DoF – 6 Elasticity – unclear	-	
Petit *et al. (2004)* [127]	L5-T1	-	DoF – 3 rotational Elasticity – Linear	-	
Robitaille *et al. (2009)* [245]	L5-T1	-	DoF – 6 Elasticity – Linear	-	
Schmid *et al. (2020)* [123]	S1-T1	-	DoF – 3 rotational Elasticity – Non-linear	-	CVJ modelled with point to point actuators Muscles – MF* and ES* muscles at each vertebra, scaled CSA
Wang *et al. (2012)* [246]	Pelvis-T1	Yes	DoF – unclear Elasticity – unclear	Yes	
Wang *et al. (2016)* [247]	L5-T1	DoF – 6 Linear	DoF – 6 Elasticity – Linear	Linear	
Wang *et al. (2017)* [248]	L5-T1	Yes	DoF – unclear Elasticity – unclear	Yes	
Wang *et al. (2017)* [249]	Pelvis-T1	DoF – 6 Linear	DoF – 3 rotational Elasticity – Non-linear	Linear tension only	Rib cage stiffening effect included in IVD stiffness
Wang *et al. (2020)* [250]	L5-T1	DoF – 6 Linear	DoF – 3 rotational Elasticity – Non-linear	Linear tension only	Rib cage stiffening effect included in IVD stiffness

* DoF = degrees of freedom
* CSA = cross-sectional area
* BW = Body weight
* MF = multifidi
* ES = erector spinae
* CVJ = Costovertebral joints

Table 2.4: Degree of personalisation for scoliotic MBM

Study	Model's source	Personalisation	
		Geometry	Materials
Abedrabbo Ode *et al. (2017)* [225]	Coronal and lateral radiographs	Yes	Literature
Aubin *et al. (2003)* [238]	Radiographs	Yes	Unknown
Aubin *et al. (2008)* [34]	Pre-operative standing radiographs	Yes	Literature personalise with side bending tests
Aubin *et al. (2015)* [239]	Coronal and lateral radiographs	Yes	Literature personalise with side bending tests
Bassani *et al. (2017)* [121]	Coronal and lateral radiographs	Yes	Literature
Cammarata *et al. (2014)* [240]	Coronal and lateral radiographs	Yes	Literature personalise with side bending tests
Desroches *et al. (2007)* [235]	Coronal and lateral radiographs	Yes	Literature personalise with side bending tests
Fradet *et al. (2016)* [136]	Coronal and lateral radiographs	Yes	Literature personalise with side bending tests
Fradet *et al. (2018)* [241]	Coronal and lateral radiographs	Yes	Literature personalise with side bending tests
Jalalian *et al. (2016)* [242]	Coronal radiographs	Yes	NA*
Jalalian *et al. (2017)* [111]	Coronal radiographs	Yes	Literature personalise with side bending tests
Jalalian *et al. (2017)* [236]	Coronal radiographs	Yes	Literature personalise with side bending tests
Jalalian *et al. (2017)* [237]	Coronal radiographs	Yes	NA – just applied kinematics
Kamal *et al. (2019)* [110]	CT scan and coronal and lateral radiographs	Yes	Literature data
La Barbera *et al. (2020)* [243]	Coronal and lateral radiographs	Yes	Literature personalise with side bending tests
Le Navéaux *et al. (2016)* [203]	Coronal and lateral radiographs	Yes	Literature personalise with side bending tests
Majdouline *et al. (2009)* [135]	Standing radiographs	Yes	Literature personalise with side bending tests
Majdouline *et al. (2012)* [30]	Coronal and lateral radiographs	Yes	Literature personalise with side bending tests
Martino *et al. (2009)* [244]	Coronal and lateral radiographs	Yes	Literature personalise with side bending tests
Petit *et al. (2004)* [127]	Coronal and lateral radiographs	Yes	Literature personalise with side bending tests

Robitaille *et al. (2009)* [245]	Coronal and lateral radiographs	Yes	Literature personalise with side bending tests
Schmid *et al. (2020)* [123]	Previous model adapted to coronal and lateral radiographs	Yes	Literature
Wang *et al. (2012)* [246]	Coronal and lateral radiographs	Yes	Literature personalise with side bending tests
Wang *et al. (2016)* [247]	Coronal and lateral radiographs	Yes	Literature personalise with side bending tests
Wang *et al. (2017)* [248]	Coronal and lateral radiographs	Yes	Literature personalise with side bending tests
Wang *et al. (2017)* [249]	Coronal and lateral radiographs	Yes	Literature personalise with side bending tests
Wang *et al. (2020)* [250]	Coronal and lateral radiographs	Yes	Literature personalise with fulcrum bending tests

NA = Not applicable

2.9. Validation of scoliotic spine models

Verification and validation are two very important steps in building credibility of numerical models [251,252] Verification, not to be confused with validation, is the process of ensuring the equations of which the computer models comprise are being solved correctly [79,93,252]. Model verification is in fact the quantification of the error due to the numerical approximations introduced by the mathematical model [251,253]. Verification can be achieved through benchmark testing (i.e., solving problems with known solutions), comparisons against results from other software which is known to be valid, and by ensuring physical laws (such as mass conservation) are respected [93,251,252]. In FEMs, this may require convergence analysis and in MBMs ensuring that the uncertainty falls within pre-defined thresholds [93,252,253]. Hence verification should be implicit within published studies.

Validation of numerical models is the process of establishing that the model is representative of reality [79,251,252]. Ideally, a quantitative comparison should be performed between the model prediction and measurements from a dedicated validation experiment [254,255]. Validation is especially important when the models may be used to aid clinical decision-making as the extent of inaccuracy in the model will influence the risk the patient is subject to – less accurate predictions may lead to poorer clinical decisions [79]. Validation has been very challenging in this area due to a lack of data, validation of the surgical correction is often done by comparing the predicted outcome to the clinical one, however, this limits the predictive capability of the models outside of that particular scenario.

MSK and FE models should be validated for the specific task or activity against both load and kinematic data [93,256]. For both modelling techniques validation of spine models has been mostly indirect due to a lack of data [50]. Indirect validation often compared model predictions to experimentally recorded RoM, IDP, *in vivo* compressive vertebral loads, and muscle activity [40,42,45,49,50,52]. Direct validations have been performed by comparing predicted against EMG-recorded muscle activity [42]. FE models often include validation against FJFs [37]. A major limitation in the analysis of fracture risk is the lack of validation against strains on the vertebrae.

Many scoliotic models are validated by simulating the surgical intervention performed and then comparing predicted curvature to the post-operative curvature [34,70,136,181,186,187,202,203,211,212,235,238–241,244] or by simulating a bending test and comparing the predicted curvature to the measured curvature from radiographic images [111,127,204,210,216,236,237,242]. Predicted Cobb angles within five degrees of the clinically measured values are often predicted and are considered acceptable as it corresponds to the clinical accuracy [257].

The downside of this method is that it only offers retrospective validation of the models [235] and in the case of post-operative radiographs only for the procedure performed. In the simulation of scoliotic corrections, if data on the reaction forces at the bone/instrumentation interface was available it could be used for validation [34,235], however, the collection of this data was challenging [211] meaning direct validation for patient-specific models using these parameters was rarely done. Rather, predicted forces can be examined to see if they are in line with literature data [34,235], although this is a much weaker validation.

In vivo, *in vitro*, and/or *in silico* literature data has been used for validation. Model predictions are compared to the reported RoM [188,191,195,209,225], muscle activation [123] or force [121], IDP [110,121,212], screw pull-out forces [212], loads on the vertebrae [201], shear stresses within the IVD [110], and IVD stiffness [194]. These parameters have been compared to the values reported in the literature, sometimes to a single data set from literature and the standard deviation on that data if it is available [121,188,195,209]. Some studies have compared their predictions to multiple data sets reported in the literature and the range represented by these sets [110,123,191]. In certain cases, only a qualitative comparison was performed [201]. Additionally, there is a lack of standardisation in the *in vivo* and *in vitro* testing of spines [258], therefore the variability and lack of data limits the extent of possible validation. Hence, larger sample sizes and more standardised testing methods would enable more robust testing of the accuracy of model predictions. Ideally, the model should be validated under the same conditions in which it is being used: therefore, validation would be performed using data from scoliotic spines [225]. Unfortunately, a lack of *in vivo* and *in vitro* data from scoliotic subjects means scoliotic models have only been validated against normal spine data [110,191].

Alternatively, studies have used models which have been previously validated [135,245,248,250] or developed a new scoliotic spine model using methods validated previously for creating healthy [56,188] or scoliotic spine models [246,249]. While it is not ideal to use a model in a context far from the one for which it was validated, in some cases this is unavoidable due to the lack of *in vivo* or *in vitro* data.

When validating against forces acting on the vertebrae and IDP (for subjects between six and eighteen years old) direct validation was not possible for scoliotic and non-scoliotic alike due to a lack of literature data [40,120]. Further, validation using the FJF was challenging due to the conflicting and limited data available within the literature [65]. Large and conclusive data sets for IDP and FJF would significantly aid the validation of spine models [65,149], and data sets from scoliotic spines would greatly support the verification of scoliotic spine models.

2.10. Applications of FEM and MBM to scoliotic spine surgery

Scoliotic models have been widely applied to simulate surgical corrections and to investigate surgical techniques and instrumentation. Some FEMs with a software platform to aid the development of surgical devices and methods for the correction of scoliosis have been developed

[39,212,213]. Aubin *et al.* developed an MBM spine surgery simulator capable of simulating five different manoeuvres and designed to be used by clinicians [34]. This was based on a geometrically patient-specific model which had been used to compare predicted and clinical outcomes of a Cotrel–Dubousset surgical manoeuvre [238] and incorporated a method to characterize patient-specific flexibility [127].

Using this simulator, Majdouline *et al.* conducted a series of studies [30,135] to find the optimal instrumentation configuration which aimed to meet the optimal outcomes recommended by several different surgeons. La Barbera *et al.* expanded on this work by considering a greater variety of instrumentation options such as different rod contours and screw patterns as well as a more clinically relevant measure of mobility [243]. These studies highlighted the lack of consensus on the optimal outcome of scoliosis surgery as multiple optimal solutions were found [135,243]. The complexity of using such models to find an optimal correction method was demonstrated by Martino *et al.* who varied five surgical parameters and performed a statistical analysis which found that each parameter had a statistically significant influence on either the implant-vertebra force or a geometrical parameter used to measure the degree of correction [244].

The spine surgery simulator developed by Aubin *et al.* has been used to show that pedicle screws allow larger curvature correction than hooks [245]. More recent studies have demonstrated the importance of screw type, with the most suitable screw type being dependent on the individual case [248]. Screw type influences the degree of correction and the loading, with monoaxial screws allowing better correction but experiencing higher post-operative vertebra-implant loads than multiaxial screws [211,244].

Several studies [74,210,211,217,244,249] have simulated the surgical correction of scoliosis to investigate the effect of increasing screw density, concluding that increasing the number of screws did not necessarily improve the correction. The effect of screw density depended on the side of the curve to which it is applied [235]. Le Navéaux *et al.* focused on the effect of screw density in the case of a main thoracic curve. Examining changing densities on each side of the curve, they found increased density on the concave side improved the correction while increasing density on the convex side had little effect [203].

Some studies have shown lower screw density could achieve lower [74,203,235,244] or similar [211] interoperative loads at the screws as higher density constructs, however, the results from the study by Wang *et al* showed lower screw density increased the stress [249]. The literature is more divided over the effect of screw density on bone-instrumentation stress post-operatively, with some studies showing a reduction in stress with increasing density [211,217] and others an increase in stress with increasing density [203,210]. Clin *et al.* offered an explanation for this disagreement: while the increase in screw density might be expected to reduce the stress, increased screw density also increased the number of constraints between the rod and the vertebrae, potentially increasing the stress [211]. In addition to the effect density has, the choice of the level at which to attach the screws [216,217,249] and the anterior-posterior position [203,205] played an important role in the stresses and corrections. Increases in correction force were shown to lead to greater Cobb angle correction [200], until a certain point, when adjacent endplates come into contact [74,181].

Increasing rod diameter and curvature have been seen to increase the intra-operative screw forces [214,247]. It can also improve the degree of correction in certain planes[214,247], while simultaneously increasing kyphosis [247]. In another study, changes in rod shape had a significant effect on the degree of correction for one patient but not for another [235]. The choice of rod

material has influenced scoliotic correction. Rods made from shape memory materials have achieved similar correction to conventional rods but required lower insertion forces and generated lower post-operative stresses at the bone-instrumentation interface [250].

In AIS, growing rods have been used to allow growth to continue while reducing scoliotic curvature. This treatment requires multiple interventions to change the length of the rods, which frequently break. More frequent distractions reduced the risk of rod failure, while higher distraction forces increased the risk but resulted in greater curvature correction and greater growth [206,207]. An optimal frequency and distraction force exist which balances growth and the stresses in the rod [206], which depended on the IVD stiffness as well [207]. Within the context of growing rods, Rohlmann *et al* investigated the effect of screw type on the post-operative motion, assuming a perfect correction ie. a spine in a healthy configuration [215].

Tethers can be used to correct scoliosis. The effectiveness of anterior tethers and costovertebral tethers has been compared, showing the anterior tethers provided better correction of the coronal deformity and axial rotation [208]. Increasing the cable tension reduced the thoracic Cobb angle and increased the stresses in the growth plate [205].

Fusion is used in the correction of severe scoliosis. Haddas *et al.* investigated the effect of fusion on the RoM, the IDP and the FJF at the fused and adjacent levels [56]. Similarly, Pasha *et al.* studied the effect of fusion in adolescents and looked at the stress distribution and the centre of pressure in the endplates [201]. The levels selected for fusion had a substantial effect on the curvature correction and the specifics of which were unique to each case and are highly dependent on the instrumentation strategy and curvature [245].

Differences between the simulated corrections and the clinically observed corrections can be due to assumptions such as determining rod shapes from post-operative scans [216,240,244].

Scoliotic models have also been used to investigate the effect of different surgical techniques on known post-operative complications such as proximal junctional kyphosis [209,239–241] and in cases when pectus excavatum is also present [200].

2.11. Discussion

This review presented the current state-of-the-art modelling techniques for the scoliotic spine and its uses. Subject-specific geometries and material properties are crucial to accurately predict spinal behaviour, especially in clinical scenarios. Personalisation of the geometry is common in FEM, whereas in MBM geometry personalisation rarely extends beyond the overall personalisation of the spinal curvature. A critical component of spine models is the intervertebral joint, FEM explicitly represents each of the soft tissue structures, in contrast, MBMs represent the soft tissue structures with a lumped parameter model. There is no consensus on the modelling of the material properties, both linear and non-linear (typically hyperelastic) representations are used with a wide range of properties from the literature being implemented. Very little work has focused on the personalisation of material properties, especially for scoliotic models. Many different loading conditions have been investigated, including surgical scenarios. The use of force or kinematic boundary conditions is tailored to the research application. The suitability and potential influence of the boundary conditions are less often considered. Validation is most often retrospective and is limited by the availability of experimental data. This leads to the reuse of previously validated models under conditions for which they have not been validated. The lack of experimental data for validation also results in models attempting validation by comparing the prediction to the

predictions of other models. Therefore, in many cases the validation is weak. The application of the models, in the context of scoliosis, has focused on the simulation of surgeries to identify optimal instrumentation design and configurations as well as optimal surgical techniques.

2.11.1. Geometry

FEM are most often constructed from medical images and therefore represent exact geometries of the individual bones and overall structure. However, accurate characterisation of the facet joint geometry remains a challenge. Furthermore, the geometries are often limited to short spine segments excluding the rib cage. MBM have personalised the spinal curvature and a limited number of studies have also included the rib cage which can aid the stabilisation. Pathological or not the personalisation of the curvature is necessary for accurate biomechanical predictions and should be considered necessary for most applications. Muscle geometry, in terms of muscle paths and attachment points, has been included in models although is rarely the focus of studies. MBMs also define a joint between adjacent vertebrae with a number of degrees of freedom (typically three rotational) and a centre of rotation (typically fixed). However, the intervertebral joint has translational degrees of freedom and studies have indicated the centre of rotation may migrate.

2.11.2. Material properties

In FEM the material properties of the bones are derived from CT scans. The material properties of the soft tissues are most often taken from the literature, despite the wide variation of these properties across the population. MBMs represent the bones as infinitely rigid bodies, therefore the material properties of the bones are not considered. The material properties of the soft tissues, specifically the intervertebral joint (represented as a lumped parameter model), the muscles, and in some cases the ligaments are defined. The IVJ has been represented with linear and non-linear models; however, there seems to be no clear consensus on how best to determine the material parameters. Potential differences in the material properties of the muscles in scoliotic cases have not been considered.

2.11.3. Personalisation

As already discussed, the personalisation of model geometry is common. Personalisation of the curvature is considered to be accurate if it is within 5° of the radiographic measurements. Geometric personalisation has focused on adult spines, the paediatric/adolescent population has not been considered.

Personalisation of the material properties is less widely done. A limited amount of research has personalised the properties of the individual soft tissues in the IVJ, and the personalisation of a lumped parameter model of the IVJ has been more challenging. It is generally accepted that the personalisation of these material properties is necessary for accurate model predictions.

The personalisation of the material properties for scoliotic models has been very rarely considered. Most studies have to rely on literature data; this data is representative of non-pathological spines. It should not be assumed that the material properties of non-pathological and pathological spines are the same; however, the lack of experimental data from pathological spines requires modellers to make this assumption.

2.11.4. Applications

MBM and FEM have been utilised in a wide variety of applications. The general biomechanical behaviour of the spine has been investigated. This includes research into load sharing across different spinal structures, load transfer between spinal levels, and the influence of spinal curvature

on muscle activation. Models have also identified risk factors for the spine under various routine activities by simulating vibrational responses which represent the forces applied during driving, other examples include the risk of fracture for different daily activities such as bending and carrying objects. Such studies have also demonstrated the importance of muscles for stabilising the spine.

Scoliotic models have been used extensively to simulate corrections and investigate the effect of different correction manoeuvres, instrumentation configurations, and instrumentation designs. FEM often focus on the details of the instrumentation, such as internal forces and screw pull-out forces. MBM are more often used to investigate the overall correction strategies such as the influence of different manoeuvres and instrumentation density. Scoliotic models have also investigated functional muscle asymmetries. However, muscles are rarely considered during the simulation of surgeries.

The validation of models in all of these applications is limited. Often constrained to retrospective validation, models will compare predicted intradiscal pressures, ranges of motion, facet joint forces, and muscle activity with experimental data and predictions from other computational models.

2.11.5. Future work

The vast majority of research focuses on the adult spine. The biomechanical nature of the paediatric/adolescent spine (both healthy and scoliotic) has been the subject of very few studies, despite the fact it is expected to behave quite differently from the adult spine. Exploring the geometry of the paediatric/adolescent spine would be a logical avenue in this area for future research to pursue.

The careful construction of muscle paths is necessary for accurate predictions from MBM. However, this aspect has not yet been adequately considered in existing thoracolumbar spine models, whether healthy or scoliotic. Therefore, based on the findings of this review, it is strongly recommended that future research focuses on the development of thoracolumbar models that incorporate muscle paths in a more comprehensive and accurate manner.

Healthy models have included and demonstrated the important role of the rib cage in the biomechanical nature of the spine, the same cannot be said for scoliotic models. Thus, future efforts should look to incorporate the rib cage into scoliotic models. This could lead to an improved understanding of the biomechanical behaviour of the spine and potentially improve the treatments.

Although rare, scoliosis can occur in the cervical spine, to the best of the Author’s knowledge this has not been modelled. Doing so would contribute to a more comprehensive knowledge of pathological spine biomechanics.

This review found that the personalisation of the intervertebral joint material properties is often considered necessary for accurate predictive simulations, however, it is rarely done due to a lack of suitable data. The effect of the location of the intervertebral joint on predicted muscle forces and joint loads has been demonstrated. Given the impact of IVJ location on these outcomes, it is highly likely that it could also affect the properties determined in the personalization of IVJ models. Despite this, it is not an aspect that has been considered, highlighting the need for further investigation to understand the implications of IVJ location on model properties. Additionally, when characterizing material properties for these models they are typically obtained from the

literature. Consequently, there is only a limited understanding regarding the inter-subject variability that may exist when personalising the material parameters.

Scoliotic models have proven to be valuable tools for investigating surgical procedures and instrumentation, yet there are still important considerations that have not been fully explored. One such consideration is the changes in the volume of the nerve canal and the associated risk of critical strains on the nerve during scoliotic surgeries. Future works should consider including these parameters in the outcomes of surgical simulations. Additionally, there is a need to investigate the postoperative risks associated with scoliotic surgeries, which modelling techniques can help to address. To achieve this, the combination of instrumented scoliotic spine models and simulations of daily activities during which instrumentation breakage occurs is recommended.

Underlying all computational models of the spine is the challenge of validation. This is primarily due to a lack of experimental data. In the case of scoliosis, this challenge is only exacerbated. To overcome this challenge, future studies should focus on designing experimental and computational studies in conjunction, which will work in tandem to inform each other. This would improve the possibilities for material characterization and allow for comprehensive validation of the models.

2.12. Conflict of interest

MV and GD were supported by the EU funded project Mobilise-D. The charity Reuse-With-Love is gratefully acknowledged for the financial support of this research. The authors declare that they do not have any financial or personal relationships with other people or organisations that could have inappropriately influenced this study.

Section 2 – Characterization of the intervertebral joint for multibody models of the spine

Experimental identification of a lumped-parameter model of the intervertebral disc

Samuele L. Gould[1,2], Giorgio Davico[1,2], Marco Palanca[1], Luca Cristofolini[1], Marco Viceconti[1, 2]

[1] Department of Industrial Engineering, Alma Mater Studiorum - University of Bologna (IT)

[2] Medical Technology Lab, IRCCS Istituto Ortopedico Rizzoli, Bologna (IT)

MANUSCRIPT IN PREPARATION

CORRESPONDING AUTHOR:

Prof. Luca Cristofolini

Biomechanics Lab

Department of Industrial Engineering (DIN)

Alma Mater Studiorum – University of Bologna

Via Terracini 24/28, 40131 Bologna (IT)

Email: luca.cristofolini@unibo.it

3.1. Introduction

Spinal pathologies, e.g. lower back and neck pain, are some of the most prevalent causes of disability and are predicted to become increasingly widespread [259,260]; in particular, lower back pain prevalence globally increased from approximately 386 million to 568 million cases (age-standardized prevalence of about 7/1000) between 1990 and 2019 [259]. Spinal disorders such as scoliosis reduce individuals' ability to work, and quality of life [259,260], and may require treatment. Selecting the optimal treatment can be complex because of the lack of clearly defined guidelines for optimal treatment [243] and the high cost of the treatments [261].

To better address these challenges and improve the treatment of spinal pathologies, computational models may be a useful tool to aid surgical planning and identify optimal treatments [106,243]. This can be achieved through predictive simulations that replicate possible surgical procedures by simulating the forces expected to be applied during surgery, and constraints to replicate the instrumentation. Therefore, multiple surgical procedures and instrumentation techniques can be simulated, and the best-performing ones selected. Multibody models (MBM) of the spine have also been applied to investigate vertebral fracture risk and kinematics via gait analysis in non-pathological and pathological populations [44,46,126]. Fracture risks can be investigated for different activities by simulating the kinematics of an activity and estimating the necessary muscle forces. This information can be used, in combination with subject-specific anthropometric data, to calculate joint loads which provide an estimate of the compressive load applied to the vertebrae. Additionally, they may be used to determine subject-specific parameters which are challenging to measure *in vivo* and are necessary for the previously mentioned applications [126]. A key component for accurate models of the spine is the representation of passive soft tissues between adjacent vertebrae such as intervertebral discs (IVDs) and ligaments [40], for which the biomechanical community has not yet established a standardized approach. Various approaches have been proposed and used. For instance, one may assign parameters from literature to the individual passive structures [48,115,226,262–264]. These models have been used to predict the ranges of motion, facet joint forces, and compressive forces on the IVD. These same variables have been used to perform limited validation of the models by comparing them to the ranges of motion reported in the literature, computationally predicted facet joint forces, and compressive forces on the IVD [226,262,264].

Another approach, often used in MBM, is to represent the individual passive structures between adjacent vertebrae, as a single lumped parameter model, commonly referred to as the intervertebral joint (IVJ) [104]. The IVJ has been defined in different ways, typically as kinematic constraints. It is either simplified to three rotational degrees of freedom (DoF) [40,123,127,250,265] or includes all rotational and translational DoFs [50,107,266] which are assigned linear [43,52,107] or nonlinear stiffness [40,265], or no stiffness at all [41,42,218]. Due to the implementation of the stiffness at the joints, to avoid moments in neutral positions, the stiffness elements must be set coincident and aligned with the reference system defining the IVJ [106]. The stiffnesses can be defined as coupled or uncoupled. Although neither one has been shown to result in improved kinematic prediction accuracy, the use of uncoupled stiffness parameters should not be used interchangeably with coupled stiffness parameters [107]. Linear and non-linear stiffnesses have resulted in varying degrees of similarity for the predicted joint reaction forces and muscle forces (ranging from 0.9% to 43.4% for joint forces) while omitting any stiffness resulted in lower force predictions (>70% in some cases) [72]. The similarity of the predictions depended on several factors: the initial position of the model, the muscle being considered, the method for specifying

the motion, and the degree of flexion at the instant being analysed. Assigning no stiffness or generic stiffnesses results in less accurate kinematic predictions (errors up to a couple of centimetres) than when using carefully tuned stiffnesses [126]. Therefore, the selection of appropriate stiffness values is important to achieve accurate predictions. Generic stiffness values have been calculated directly from literature values [40,50] or tuned so that the predicted range of spinal motion fell within the range observed across different *in vivo* or *ex vivo* studies [43,107]. These models can predict joint forces, muscle activation and load sharing within the ranges reported by the literature [40,43,69,114,123,224,226,263,264]. Wang et al. developed a model that allowed for subject variability to be accounted for by expressing a range of stiffnesses [69]. Given the sensitivity of MBM to the stiffness of the IVJ and its considerable variation between subjects [58], personalisation of the stiffness may enable more accurate prediction of spinal forces, muscle activity [114,165,267], and spinal kinematics. Ghezelbash et al. parametrised the passive stiffness based on body weight, body height, age and sex [165,177]. Based on optimisation for *in vivo* motion, subject-specific lumped parameters across the whole spine have been calculated as one of three adjustment parameters applied to the IVJ stiffnesses [127] and as values specific to each vertebral level [126]. Alternatively, *ex vivo* data from porcine experiments have been used to optimise the joint stiffness and damping parameters in the inferior-superior and anterior-posterior directions for the C6-C2 levels [52].

Predicted joint reaction forces and muscle forces were also sensitive to the type of kinematic input and the position assigned to the centre of rotation (CoR) [72]. Although studies have investigated the migration of the CoR during motion [268–270], most MBMs of the spine assume that the IVJs have a fixed centre of rotation [41,43,52,69,106,107,126,218]. Based on two possible fixed CoR, the sensitivity of the predicted joint reaction forces and muscle forces seemed to change with the position of the fixed CoR [72]. Similarly, other studies investigated the sensitivity of muscle forces and joint reaction forces to the position of the CoR by repeating inverse dynamic simulations for different fixed CoR locations [267,271]. Muscle forces increased the further the CoR was positioned from the default location [267,271]. The most extensive study (which investigated 47 different CoR locations) supported the previous findings that as the CoR location was positioned more anteriorly the joint reaction force was reduced [114,267]. However, it was also shown that these trends were highly dependent on the spine pose (upright or flexed) [114].

Previous methods have personalised the IVJ stiffness via the parametrisation of anthropometric details [165,177], however, such an approach may not accurately represent subject-specific parameters [272]. Another approach has been to optimise the stiffness based on kinematic predictions. One study focused on the cervical spine. Mechanical properties of the human spine are highly dependent on the spine level; thus, the mechanical properties of the cervical spine do not accurately represent the lumbar spine. Further, data from porcine spines were used. They are a limited representation of the human spine [273]. While geometrically similar, porcine and human vertebrae are characterised by IVDs of different heights (up to four times higher in humans [274]). In addition, the porcine spine generally has a larger range of motion (RoM) [275,276], lower stiffness [277] and less coupling than the human spine [278]. Whereas, studies which have optimised the IVJ stiffness for lumbar spines were based on *in vivo* motion and have been associated with errors in vertebral positions of up to 8.5mm and several degrees [126,127]. Furthermore, to the best of the Author's knowledge, the influence of the location of the CoR on both the predicted kinematics and the optimised IVJ stiffness has not yet been investigated. Thus, studies which investigate the optimisation of specimen-specific stiffnesses of the human lumbar

spine from highly accurate *ex vivo* kinematic data are lacking. Additionally, the current literature does not address the sensitivity of the optimised IVJ parameters to the CoR location.

The aim of this study was twofold: (1) to test the feasibility of optimising the linear stiffnesses for a specimen-specific lumped parameter model of the IVJ from a Digital Image Correlation (DIC) dataset and (2) to investigate the sensitivity of the model to the assigned location of the joint CoR and orientation of the joint (which determines the direction in which the IVJ stiffnesses are applied).

3.2. Materials and methods

The experimental study [279], which the current study sought to model, was approved by the Bioethics Committee of the University of Bologna (n. 17325, 8 February 2019). The human cadaver specimen for the experimental study was supplied by an ethically approved donation program (Anatomic Gifts Registry, USA). The current study simulated the flexion-extension experiment of an L1-L4 specimen from a 73-year-old female donor: total body mass 72.6 kg, diagnosed with lung cancer, and metastatic vertebrae [279]. The presence of metastatic vertebrae can drive spinal instability (presenting a risk of vertebral fracture), the loads applied in the experiment did not cause fracture. Therefore, the deformation of the vertebrae is orders of magnitude smaller than the deformation of the disc and thus should not affect the estimated stiffness. The effect of metastases on IVJ stiffness is unknown, however, the objectives of this study were not to establish stiffnesses that would be widely applicable or investigate the influence (if any) of metastases on IVJ stiffness. Rather it was to investigate the feasibility of determining IVJ stiffnesses from DIC data and to better understand the sensitivity of the model to the joint pose, to these ends, it is assumed the effect of metastases will be negligible.

The specimen was imaged using computed tomography (CT) (AquilonOne, Toshiba, Japan). The scan parameters were: slice thickness, 1mm; pixel spacing, 0.24-by-0.24 mm; voltage, 120 kVp; tube current, 200 mA.

Following the CT scan the specimen was cleaned of soft tissue, removing the anterior longitudinal After the CT scan, the specimen was cleaned of soft tissue, removing the anterior longitudinal ligaments and the periosteum, but leaving the posterior ligaments and facet joints intact. A random speckle pattern (white on black) was prepared on the external surface of the spine segments through an airbrush airgun [280] in order to measure the displacement via a DIC system [280]. The extreme vertebrae (L1 and L4) were embedded in acrylic bone cement inside two metal pots. A uniaxial testing machine (Instron 8800, load cell 10kN) was used. The most inferior vertebra was completely constrained in the testing machine during the test. For the experiment, the loading and motion direction of interest was flexion. A flexion loading was generated by applying a monotonic eccentric compressive load with a displacement-controlled actuator. The load was applied to the superior-most vertebrae through the top metal pot via a ball joint with an assigned anterior-posterior offset (equal to 10% of the anterior-poster dimension of the middle intervertebral disc). The individual loading cycle was repeated three times. The ball joint was mounted on low-friction bearings in the anterior-posterior direction to eliminate unintended anterior-posterior forces. The actuator displacement was tuned to reach a minimum target strain of ~3000 (2500 to 3500) microstrain on average on the vertebral body (corresponded to a maximum eccentric compressive force of 54N, resulting in a flexion moment of ~1Nm), in 1 second. The full field displacements across the anterior and lateral surfaces of the vertebrae were measured at 25Hz using a state-of-the-art four-camera digital image correlation (DIC) system (Aramis Adjustable 12M,

GOM, Braunschweig, Germany). Additionally, the DIC captured parts of the transverse processes, providing distinctive anatomical features which enabled the registration described later. Markers were placed on the top and bottom pots and were used to track the motion of the top pot. For additional details on the experimental procedure, the reader is referred to [279].

The rigid body motion (rotations and translations) of each vertebra was calculated from the DIC coordinate data using singular value decomposition about the adjacent inferior IVJ with a custom MatLab (MathWorks, 2021b) code. The markers on the top pot (Figure 3.1) were used to calculate the orientation of the pot and the position of the ball joint at each frame. The orientation of the top pot enabled the measured uniaxial force to be decomposed into axial and right-left force components, while the forces in the anterior-posterior direction were assumed to be null, because of the low-friction linear bearings.

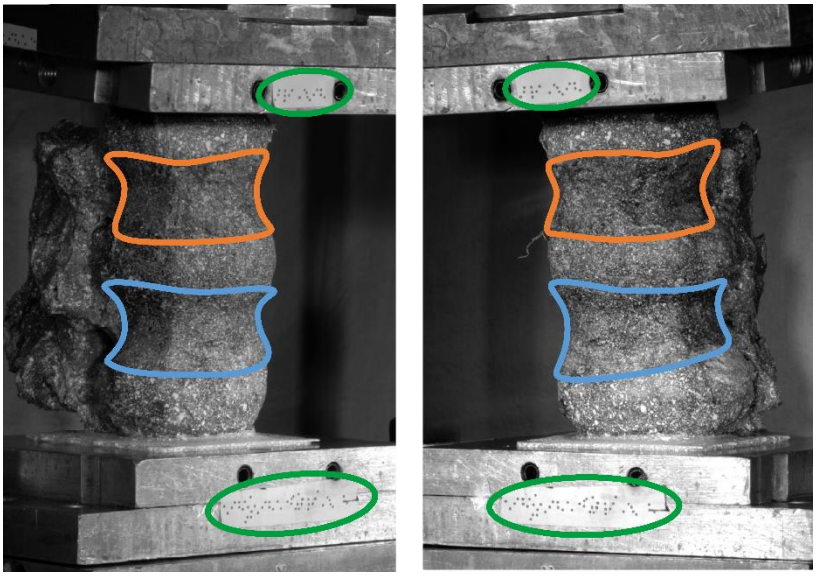

Figure 3.1: Experimental set-up showing the top pot, the bottom pot, the markers attached to each pot (circled green) and the body of the vertebrae (L2 outlined orange, L3 outlined blue).

Model preparation

To provide a roadmap for the reader of the workflow used to create the model a brief outline is given here. The individual steps are described in detail below. The CT scan and experimental *ex vivo* data (Figure 3.1) were used to create an MBM and simulate the flexion experiment [279]. To do so, the CT data were segmented, and a virtual palpation of anatomical landmarks was performed. Then a registration of the CT data to the experimental data was performed. The transformation matrix from the registration was used to move the segmentations and the virtually palpated landmarks into the experimental pose. The MBM model was then created and simulations with boundary conditions were defined from the experimental data.

The CT data were manually segmented in Mimics v24 (Materialise, Leuven, BE), twice. Once to reconstruct just the vertebrae, and a second time to further include the surrounding soft tissues. To segment the vertebrae a thresholding was applied, followed by the application of the region growing and automatic hole-filling tools. Finally, the segmented regions were manually edited to add and remove pixels as necessary.

The rigid body parameters (CoM, mass, and inertia) of the vertebrae (L2, L3) were calculated from the volume of the segmented vertebral geometries, assuming a bone density of 1.14 g/cm^3 [281].

The joint mass of the superior-most vertebra and top pot was estimated to be 1kg, while the CoM was calculated based on the markers on the top pot, assigning the offset applied in the experiment (50 mm).

By virtual palpation, a set of anatomical landmarks (the centre of the vertebral endplates and the bases of the pedicles) were identified on the 3D bony geometries that would be used to define the joint reference systems according to ISB guidelines [82]. To ensure that the MBM model (initially positioned in the CT pose) was in the experimental pose, a global registration was performed to get transformation matrices required to overlay the CT segmentations (of vertebrae with soft tissue) onto a surface created from DIC data acquired in the unloaded condition (Figure 3.2) [256]. The resulting transformation matrix for each vertebra was applied to the corresponding body and associated landmarks. Following the ISB guidelines, the experimental joint poses (position and orientation) were then calculated [82].

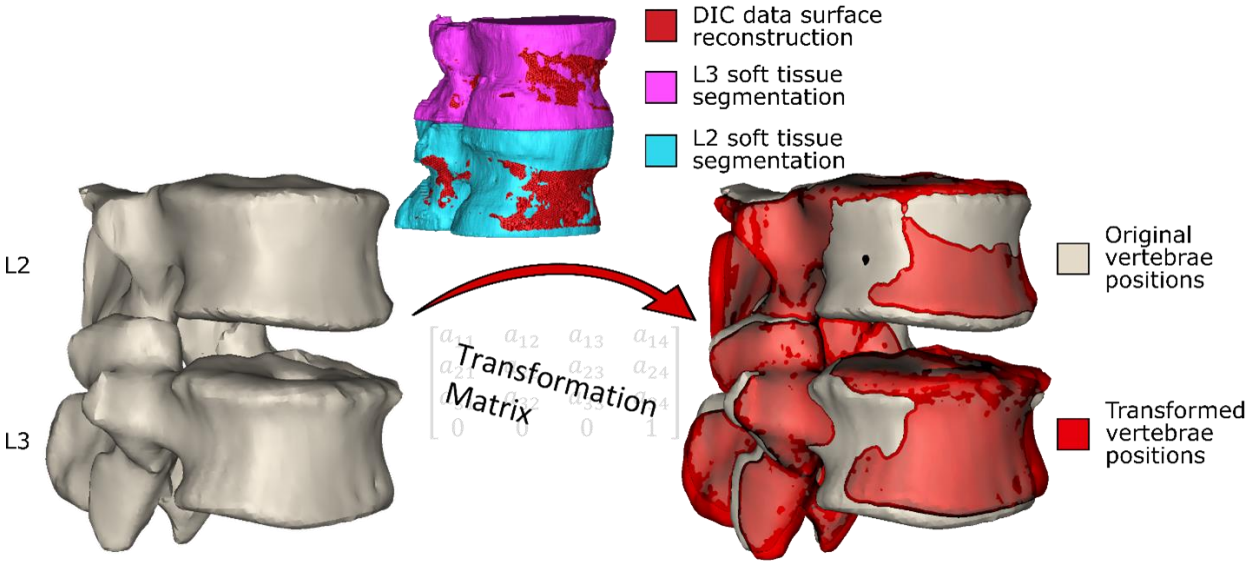

Figure 3.2: The vertebrae in the original positions. The segmentations of the vertebrae including the soft tissue are registered to the surface created from the DIC data, and the resulting transformation matrices (one for each vertebra) are obtained. The transformation matrices are applied to the segmented (without soft tissue) vertebrae in the original position (left) to move them into the experimental pose, shown in red (right, the vertebrae in the experimental pose overlayed on the original vertebrae pose).

Using NMSbuilder 2.1 [282], an OpenSim [89,90] model was created from the segmented geometries (Figure 3.3). Six DoF joints connecting the vertebrae were placed in the experimental joint poses previously calculated from the transformed landmarks. To represent the IVJ mechanics a spring-damper element (bushing force) per DoF was used, placed coincident and aligned with each other and the reference frames of the joints [106]. Initial stiffness values for the elements were estimated from the literature (Table 3.1). The translational stiffness in the inferior-superior direction was calculated from the data of Newell *et al.* [176] as the RoM of the study by Newell *et al.* was of the same order of magnitude as the RoM of the present study. Literature data reported larger RoMs in the anterior-posterior and right-left translational directions compared to the RoMs in the present study. Therefore, the anterior-posterior and right-left translational stiffnesses were calculated from the literature [283,284] and scaled down. To determine the scaling factor, the compressive stiffness calculated from the study by Newell *et al.*, which reported a RoM of the same order of magnitude as the present study, was compared to the compressive stiffness utilized in Senteler *et al*. [43]. This comparison was made because the compressive stiffness utilized by

Senteler *et al*. was calculated from literature which reported RoMs of the same of magnitude as the literature [283,284] used to calculate the anterior-posterior and right-left translational stiffnesses. This comparison found an order of magnitude difference in the compressive stiffness. Therefore, to determine the initial stiffness in the anterior-posterior and right-left translational directions a scaling factor of 0.1 was applied to the stiffnesses reported in the literature [283,284]. The stiffnesses in the rotational DoF were taken from the literature [43,285]. Damping coefficients of 1000 N/(m/s) [286] and 1.4 Nm/(rad/s) [287] were assigned to all translational DoFs and rotational DoFs, respectively.

Table 3.1: Initial stiffnesses used for the intervertebral joints. [43,176,283–285].

DoF	Stiffness	
	Translation, N/m	Rotation, Nm/rad
In/About X	24,600	64
In/About Y	110,000	268
In/About Z	13,500	37 [285]

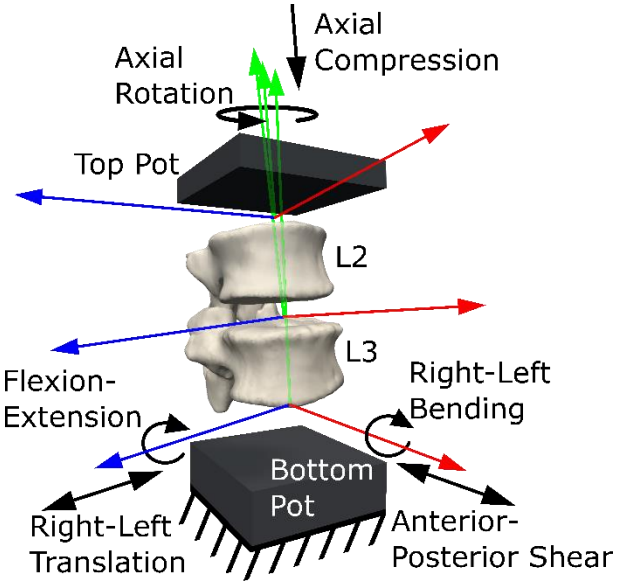

Figure 3.3: Multibody model of the experimental set-up, showing the joint locations and orientations, the constraint on the bottom pot and the degrees of freedom.

The lowermost vertebra (L4) was completely constrained. A quasi-static loading condition was assumed. To apply a quasi-static load, the maximum axial and right-left component loads were applied at the actuator position to the uppermost vertebra (L1). To ensure the model reached static equilibrium the loads were applied for 1.5 s.

Optimisation of the lumped-parameter model

The developed MBM model was used in OpenSim v4.3 to run a forward dynamic simulation (under the quasi-static loading conditions, ie. constant application of the maximum loads for 1.5 s) via the MatLab API and predict joint motion. The boundary conditions previously described were introduced to replicate the experimental setup. This enabled direct comparison between predicted and measured IVJ motion, which was necessary to guide the routine to optimise the IVJ parameters (Figure 3.4).

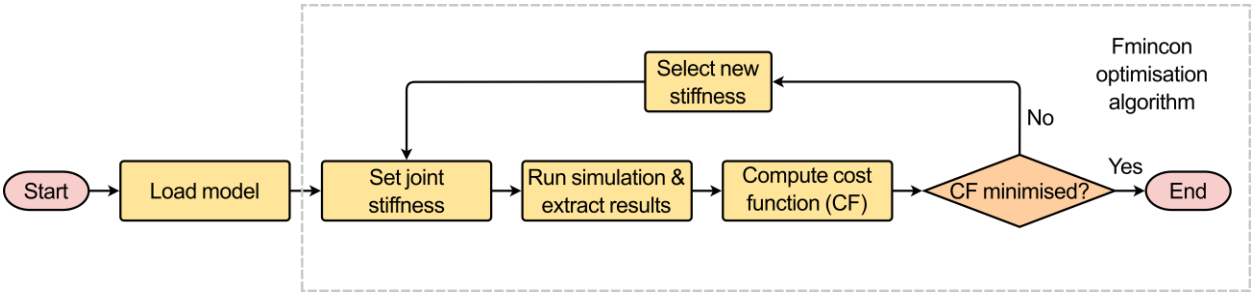

Figure 3.4: Optimisation routine

Using an interior-point optimisation algorithm ('fmincon') in MatLab the rotational stiffness in flexion-extension (FE), and the translational stiffnesses in the axial and the anterior-posterior directions were optimised to minimise the following cost function (Eqn. 3.1):

$$\boldsymbol{cf} = \sum_{\boldsymbol{i}=1}^{\boldsymbol{n}} \boldsymbol{w_i}(\boldsymbol{p_i} - \boldsymbol{m_i})^2$$

Eqn. 3.1

The cost function was the sum of the weighted squared absolute error between predicted (p_i) and measured (m_i) motion in anterior-posterior, axial, right-left translation, and flexion-extension.

The right-left translation was included as it improved the accuracy of the predicted motion in anterior-posterior and axial directions. The weights (w_i) were chosen heuristically (Table 3.2) based on two considerations: so that the error in each DoF was of the same order of magnitude, and to ensure that the cost function was sufficiently sensitive to the DoF of interest to optimise them.

Table 3.2: Weighting applied to the DoF included in the cost function

DoF	Anterior-posterior	Axial compression	Right-Left Translation	Flexion/ Extension
Weighting	10	100	1	1

Sensitivity studies

Initial bootstrapping investigations

To check if the optimised stiffnesses were independent of the initial stiffness values, a bootstrap investigation was performed, with a parameter space defined from values found in the literature (Table 3.3).

Table 3.3: The parameter space used for the initial bootstrapping stiffness investigation

Direction	Minimum stiffness (translations in N/m; rotations in Nm/rad)	Maximum stiffness (translations in N/m; rotations in Nm/rad)
Anterior-posterior translation	31,600 [288]	857,000[289]
Inferior-superior translation	108,000 [176]	3,330,000[290]
Right-left translation	53,000 [291]	584,000[284]
Right-left bending	9.0 [109,292]	249 [109,291]
Axial rotation	43 [293]	1,250 [109,292]
Flexion-extension	12 [109,292]	750 [109,294]

Additionally, an initial bootstrap investigation was performed to check if the simulations were independent of the damping parameters used. A range of values was sampled from a parameter space which contained the values reported in the literature (Table 3.4, Appendix E) [112,287,290].

Table 3.4: The parameter space used for the initial bootstrapping damping investigation.

Direction	Minimum damping	Maximum damping
Translation, N/(m/s)	0	2,000
Rotation, Nm/(rad/s)	0	5

Finally, the quasi-static (constant maximum load for 1.5 s) assumption was investigated. For all the damping and stiffness parameters used, simulations were run using dynamic boundary conditions. As previously described, the load measured by the uniaxial load cell was decomposed into component loads, this was performed at each time step (corresponding to the imaging frequency, every 0.04 s). To impose dynamic loading conditions, the component load was applied at the corresponding time step (ie. a ramp loading was applied). The force was applied at the actuator position.

In the analysis of the initial bootstrapping investigations, only the results from optimisations which were considered successful (defined as a change in stiffnesses by more than 1% of the initial stiffness values) were considered.

Sensitivity to joint pose

To test the sensitivity of the model to the joint pose (Figure 3.5), the virtual palpation of the set of anatomical landmarks used to define the joint was repeated 5 times and the average position of each marker was calculated. A standard deviation was assigned to each marker (maximum resultant 2.9 mm) from an in-house study on the inter-operator variability of the virtual palpation of the landmark set. Using MatLab, a Latin hypercube sampling technique was used to randomly generate 500 marker sets based on a normal probability distribution. From each marker set, a joint pose was determined separately for each IVJ and a corresponding model was created (a total of 500 unique models). Likewise, the rigid body motion was recalculated based on the updated joint

pose for each model. The optimisation simulations were run using the new models. The optimised stiffnesses and errors of the predicted motion were compared to the results of the other models. Results were controlled for optimisation failure, defined as the optimised stiffnesses being within 1% of the initial value as this would indicate the optimisation being trapped in a local minimum under the initial conditions. Results were also checked for outliers by identifying large predicted stiffnesses such that they are unlikely to be physiologically realistic (an order of magnitude greater than the initial stiffness). Following these criteria, the models which were successfully optimised were identified. This group of models will henceforth be referred to as the *reduced dataset*.

Two-factor analysis – joint pose and stiffness

From the *reduced dataset*, the 10 best-performing models were identified (based on kinematic error). To conduct a two-way factor analysis (Figure 3.5) to investigate the influence of the joint pose and stiffness, for each of the models in the *reduced dataset*, another ten versions were created. Each version used the joint pose from the corresponding model in the *reduced dataset* and the stiffnesses were changed to the stiffnesses of the ten best-performing models. For each model, the forward dynamic simulations with the boundary conditions previously described were re-run (Figure 3.3, Figure 3.4) but without the optimisation loop.

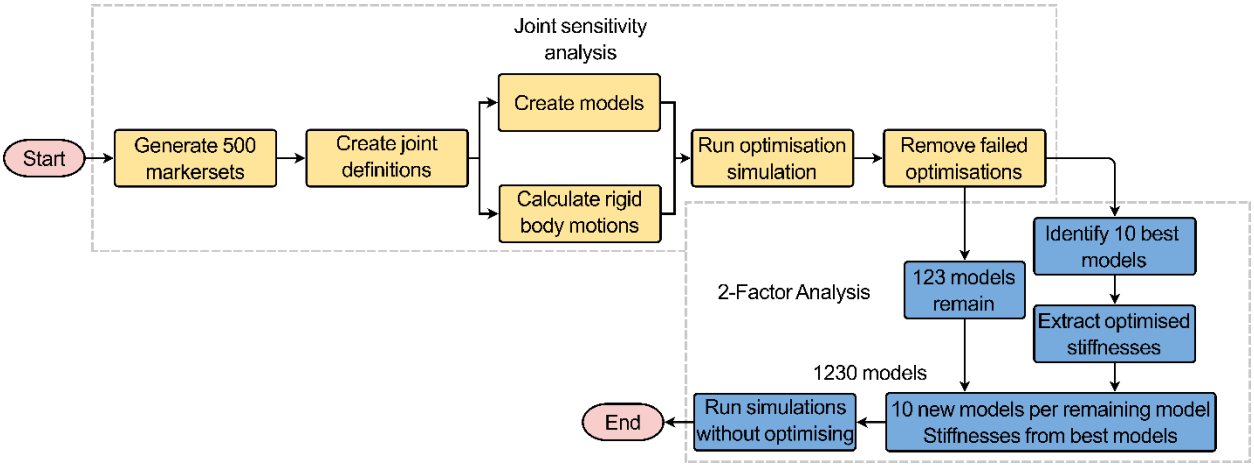

Figure 3.5: Workflow of the joint sensitivity analysis (yellow boxes) and the 2-factor analysis (blue boxes). The successful models and the stiffnesses from the 10 best-performing models are outputs from the joint sensitivity analysis that are used as inputs for the 2-factor analysis.

Metrics

The results of the sensitivity analysis were analysed in terms of the kinematic errors and predicted stiffnesses in the optimised DoF. The kinematic errors and predicted stiffnesses were analysed in terms of the variation of the joint pose defined by the rotational DoF and the Euclidean distances from the average CoR. Specifically, for each rotational DoF, the average of the joint orientation in that DoF across the three joints in the model was used. Likewise, the average Euclidean distance across the three joints was used. Only results from simulations of the *reduced dataset* were included in the analysis.

The initial bootstrapping investigations considered the sets of parameters (damping and the initial stiffnesses) under two loading conditions, quasi-static loading and dynamic loading. The impact of these parameters was analysed in terms of kinematic errors and predicted stiffnesses. For each parameter set under the two loading conditions: the magnitude of the median and range of the

prediction errors were compared, and the magnitude of the predicted stiffness ranges were compared.

Statistical analysis

The optimisation results were statistically analysed with a custom code in MatLab, using the statistics toolbox. Chi-squared goodness of fit test was used to test the null hypothesis of normal distribution for the joint poses, optimised stiffnesses, and kinematic prediction error of the *reduced dataset*. Where the chi-squared goodness of fit test was unsuitable the one-sample Kolmogorov-Smirnov test was used to test the null hypothesis of normality. The null hypothesis was rejected for $p<0.05$. When the null hypothesis of normality was rejected, Spearman's rank correlation was used to test for correlation between the stiffness in each optimised DoF and the prediction error in each optimised DoF. Likewise, Spearman's rank correlation was used to test for correlation between joint pose and the kinematic prediction error, and between joint pose and the optimised stiffness. Potential biases between the measured motion and predicted motion were investigated using Bland-Altman plots.

The results of the two-factor analysis were statistically analysed in R (v4.2.1) [295], using the *stats* and *rpart*, packages. Spearman's rank correlation tests were used to test for correlation between prediction error and joint pose for each stiffness in the *reduced dataset*, in cases of tied data Kendall tau rank correlation test was used. Likewise, using either Spearman's or Kendall correlation tests, correlations were tested for between prediction error and stiffness for each model in the *reduced dataset*. As this results in multiple correlations for the same dependent variable a Bonferroni correction was applied [296], and significance is reported only when the Bonferroni correction has been considered. The parameters describing the joint poses (defined by 18 parameters) and the stiffnesses (defined by three parameters of interest) were grouped as joint and stiffness blocks. Friedman rank sum tests with unreplicated blocked data were used to investigate if there were significant differences ($p<0.05$) in the prediction error with joint pose and stiffness. To analyse the influence of the joint pose and the stiffness on the prediction error a tree regression analysis was performed.

3.3. Results

Using this pipeline, a lumped parameter model of the IVJ was identified from an experimental dataset. The experimental motion in this joint configuration was 0.34 mm for L2 and 0.33 mm for L3 in the anterior-posterior direction; 0.14mm for L2 and 0.25 mm for L3 in axial compression; and 1.4° for L2 and 1.8° for L3 in flexion. The measurement uncertainty was 0.0013 mm in the anterior-posterior direction and 8.1×10^{-4} mm in axial compression. The initial model with the optimised stiffnesses resulted in errors in the predicted motion of 0.32 mm (maximum percentage error 93%) in the anterior-posterior direction, 0.05 mm (maximum percentage error 37%) in axial compression, and 0.26° (maximum percentage error 12%) in flexion-extension.

After removing failed optimisations, 124 (of 500) successful simulations remained. For one of the models, the optimised stiffness in flexion-extension was 470 Nm/rad, this was identified as an outlier and excluded from the analysis as this stiffness was an order of magnitude larger than all other optimised stiffnesses and the error in flexion for both vertebral levels was 97% for L2 and L3. The following analysis was performed on the results of the remaining 123 simulations, these form the *reduced dataset*.

3.3.1. Sensitivity to joint pose

The ten best-performing models, when using the optimised stiffness, had the largest median error in the anterior-posterior direction at L3, in the anterior-posterior direction the largest interquartile range (IQR) (Table 3.5). This is also reflected in the range of the optimised stiffnesses, with the IQR being 72% and the range being 112% of the median value. The median, IQR, and range have not been calculated as percentage errors of the experimental motion as the experimental motion is unique for each model due to the unique joint configurations. The median errors could be reduced by selecting a smaller sample of the optimal models; however, this would result in a smaller sample of stiffnesses for the two-factor analysis.

Table 3.5: The median, interquartile range (IQR), and range of the prediction errors and the optimised stiffnesses for the ten best-performing models.

DoF	Vertebra Level	Prediction errors			Optimised Stiffnesses		
		Median	IQR	Range	Median	IQR	Range
Anterior-Posterior	L2	0.075 mm	0.22 mm	0.31 mm	12,200 N/m	8,960 N/m	13,700 N/m
	L3	0.14 mm	0.18 mm	0.29 mm			
Axial Compression	L2	0.016 mm	0.026 mm	0.052 mm	454,000 N/m	72,000 N/m	397,000 N/m
	L3	0.11 mm	0.055 mm	0.13 mm			
Flexion-Extension	L2	0.15°	0.062°	0.20°	14.5 Nm/rad	2.16 Nm/rad	4.90 Nm/rad
	L3	0.095°	0.11°	0.20°			

The best-performing model had maximum errors of 0.033mm in anterior-posterior translation, 0.11mm in axial compression and 0.077° in flexion-extension (Table 3.6). These values could be used as an indication of a lumped parameter model of the IVJ at small RoMs, however, this data is from a single specimen. Furthermore, the purpose of this study is not to provide a final stiffness value that can be more widely applied but rather to test the feasibility of an approach and the sensitivity of optimisation approaches to the joint pose. The best-performing model is therefore a better indication of the accuracy that can be achieved using a lumped parameter model of the IVJ obtained through an optimisation approach.

Table 3.6: Experimental vs predicted motion from the simulation of the best-performing model using the optimised stiffness in those same DoFs, percentage error is calculated as the $\frac{Experimental - Predicted}{Experimental}$

DoF	Vertebra Level	Motion		Percentage Error	Optimised Stiffness
		Experimental	Predicted		
Anterior-Posterior	L2	0.39 mm	0.43 mm	10%	11,900 N/m
	L3	0.40 mm	0.42 mm	5.0%	
Axial Compression	L2	0.13 mm	0.15 mm	15%	437,000 N/m
	L3	0.24 mm	0.14 mm	41%	

Flexion-Extension	L2 L3	1.50° 1.92°	1.42° 1.91°	5.3% 0.52%	14.9 Nm/rad

Considering the error distribution across all of the joint poses, there was a wider distribution of errors in the anterior-posterior and flexion-extension directions than in axial compression for both vertebral levels (Figure 3.6). The median errors were largest in the anterior-posterior direction, followed by the flexion-extension direction, with the smallest median errors in axial compression (Figure 3.6). For the different joint poses, the median stiffness and the IQR (0.25-0.75) of optimised stiffnesses were 28,900 (10,100-46,000) N/m in the anterior-posterior direction, 365,000 (314,000-428,000) N/m in axial compression, and 13.4 (12.4-14.3) Nm/rad in flexion-extension (Figure 3.7). No statistically significant correlations between the average absolute errors and the joint pose were found (Appendix A). While a statistically significant linear correlation between the optimised stiffness and the joint pose was only found between the flexion-extension stiffness and the average joint centre in axial torsion ($p = 0.045$, $r = 0.18$) (Appendix B). A statistically significant correlation was seen between the stiffnesses and the kinematic error (Table 3.7, Appendix C). However, a statistically significant correlation was not seen between all stiffnesses and all kinematic errors. There was no statistically significant correlation between the compressive axial stiffness and the flexion error, nor between the flexion-extension stiffness and the anterior-posterior translation or the axial compression. For both L2 and L3, the error depended on the experimental motion in anterior-posterior translation and in flexion-extension, however, in axial compression the error and experimental motion were independent (Appendix D).

Table 3.7: r values of the statistically significant correlation between the different stiffnesses and the kinematic errors from the Spearman's rank correlation test.

		Stiffness in DoF		
		Anterior-Posterior	Axial compression	Flexion-extension
Kinematic Error Direction	Anterior-Posterior	0.33	-0.39	-
	Axial compression	-0.58	0.29	-
	Flexion-extension	-0.45	-	-0.42

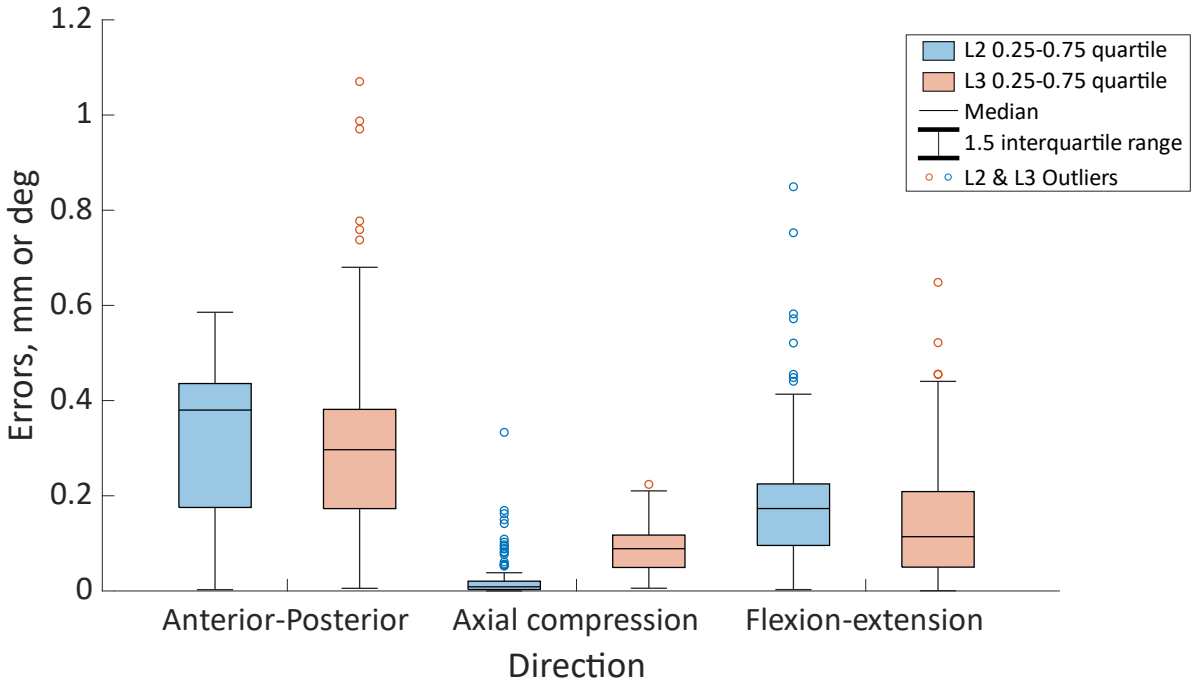

Figure 3.6: The ranges of the motion error in the anterior-posterior, axial compression and flexion directions for the different joint poses when using the optimised stiffness.

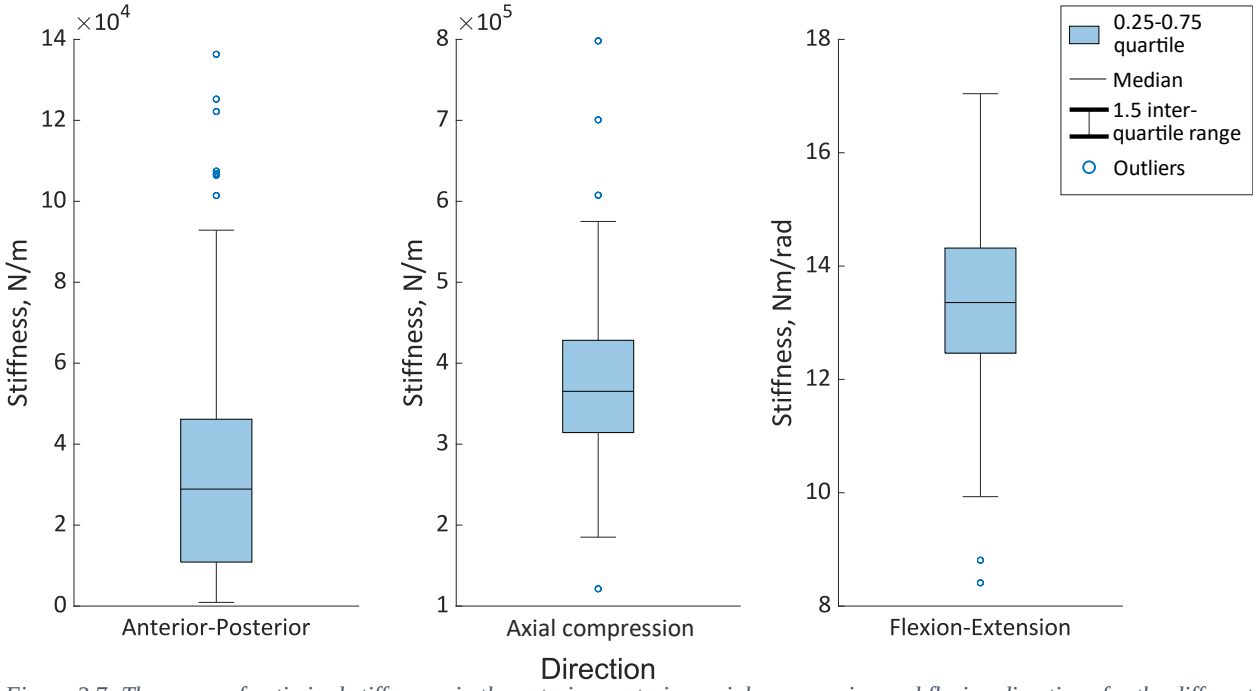

Figure 3.7: The range of optimised stiffnesses in the anterior-posterior, axial compression and flexion directions for the different joint poses.

3.3.2. Two-factor analysis – joint pose and stiffness

The predicted errors were nonparametrically distributed ($p<0.05$) therefore the Spearman's rank and Kendall tau rank correlations were used.

The Spearman's rank or Kendall tau rank correlations were used to test the correlation between the kinematic error in each direction (three directions) against each of the three orientations describing the joint pose. These tests were performed for each vertebra ten times (once for each stiffness group). The correlations between the kinematic error and the stiffness were tested in each direction against each of the three stiffnesses that were optimised. These correlations were performed for each vertebra 123 times (corresponding to each of the models). In sets of correlations with at least one test returning statistically significant correlation only the range of the correlation coefficients is reported, due to the number of correlations. Further comments on the correlations are also provided (Table 3.8).

Statistically significant correlations between the joint pose and the errors were found for most of the stiffnesses. However, the correlations were weak to moderate, and in the case of the flexion-extension orientation in opposite directions for L2 and L3. Relatively few of the models had a statistically significant correlation between stiffnesses and kinematic errors. However, when the correlations were significant, they were strong. Correlations indicated that as the anterior-posterior stiffness increased the errors in anterior-posterior translation and in flexion-extension decreased. Increased flexion-extension stiffness was associated with decreasing anterior-posterior transition errors but increasing flexion-extension errors.

Table 3.8: Statistical significance for the correlations performed between the kinematic error and the joint orientations and between the kinematic error and the stiffness. Statistical significance ($p<0.5$) is reported if at least one of the tests performed in each combination of error and joint or error and stiffness was significant after considering Bonferroni correction. The test (Spearman's or Kendall Tau) is indicated, and a comment is provided to describe what the correlation suggested.

Joint orientation	Vertebra level	Anterior-posterior translation error	Axial compression error	Flexion-extension error	Comment on correlation
Lateral bend	L2	NA, τ	NA, τ	NA, τ	
	L3	NA, τ	NA, τ	NA, τ	
Axial Rotation	L2	NA, τ	NA, τ	NA, τ	
	L3	NA, τ	NA, τ	$p<0.05$, $0.18<\tau<0.20$	Weak correlation.
Flexion-extension	L2	$p<0.05$, $0.19<\tau<0.22$	NA, τ	$p<0.05$, $-0.18<\tau<-0.12$	Correlations are in opposite directions for the anterior-posterior. Correlations are weak/moderate.
	L3	$p<0.05$, $-0.49<\tau<-0.47$	$p<0.05$, $0.47<\tau<0.48$	$p<0.05$, $-0.16<\tau<-0.12$	Correlations were present for only 2 stiffnesses flexion-extension for L2 and L3.
Stiffness					
	L2	$p<0.05$, $-0.95<\rho<0.99$	NA, ρ	NA, ρ	Strong negative correlations. Small numbers

Anterior posterior	L3	NA, ρ	NA, ρ	NA, ρ	of significant correlations, <38 out of 123.
Axial compression	L2	NA, ρ	NA, ρ	NA, ρ	
	L3	NA, ρ	NA, ρ	NA, ρ	
Flexion-extension	L2	p<0.05, -0.98<ρ <-0.67	NA, ρ	p<0.05, 0.67<ρ <1.00	Strong correlations, negative in anterior-posterior and positive in flexion-extension. <60 out of 123 significant correlations in all directions.
	L3	NA, ρ	NA, ρ	p<0.05, 0.85<ρ <1.00	
ρ – Spearman's Rank				τ – Kendall tau	

Although a statistically significant correlation was not found in all cases, the Friedman test showed statistically significant differences ($p<0.05$) in the prediction error against all stiffnesses and joint poses. This does not allow for correlations to be determined; however, the tree regression analysis found the prediction accuracy to be more heavily influenced by the joint pose than the stiffness for all directions (Table 3.9).

Table 3.9: The variable importance reported by the tree regression analysis in the three directions where most motion was observed for both L2 and L3. The larger the value of the variable importance the more influence it has on the predicted kinematics.

Direction	Vertebra level	Variable importance	
		Joint pose	Stiffness
Anterior-posterior	L2	63.8	5.93
	L3	197	53.1
Axial compression	L2	1.23	0.41
	L3	1.77	0.30
Flexion-extension	L2	53.3	23.8
	L3	57.0	56.8

3.3.3. Joint pose

The distribution of the landmark positions was normal by definition as they were created using a Latin Hypercube sampling technique, and a normal distribution was assumed. The standard deviation of the landmark was 2.9 mm, indicating the variability of the landmark position due to the operator. This resulted in a distribution of possible joint poses. The chi-squared goodness of fit test rejected the null hypothesis (normal distribution) for joint poses (ie $p>0.05$ was not true for all DoF at all levels) for the *reduced*. The chi-squared goodness of fit test accepted the null hypothesis (normal distribution) for the joint poses of the *complete dataset*.

The positions of the centre of rotations of the joints (Table 3.10)) are expressed relative to the centre of the upper surface of the bottom pot (Figure 3.3). The median and IQR of the position of the CoR across the *complete dataset* and the *reduced dataset* showed the median position to differ by less than 1 mm in all directions and the IQR was within 0.2mm in all directions (Table 3.10).

Table 3.10: The median and interquartile range (IQR) of the position of the centre of rotation relative to the centre of the upper surface of the bottom pot in each DoF for the complete and reduced set of models

Model set	Joint Level	Median Position, mm			IQR Positions, mm		
		Anterior-Posterior	Inferior-Superior	Right-Left	Anterior-Posterior	Inferior-Superior	Right-Left
Complete	L1-L2	2.40	95.82	11.48	0.88	0.92	0.97
	L2-L3	4.88	56.61	7.80	1.00	0.90	1.04
	L3-L4	3.93	20.61	4.16	1.01	0.93	0.92
Reduced	L1-L2	2.31	95.78	11.47	0.95	0.95	1.00
	L2-L3	4.87	56.52	8.03	0.85	0.81	1.23
	L3-L4	3.86	20.64	4.12	1.04	0.87	0.96

Examining the influence of using the *reduced dataset* instead of the *complete dataset*, the variation of the position of the models in terms of the joint poses at each changed the orientation by no more than 1° (median) and 1° (IQR) (Table 3.11). There are two exceptions to this in flexion-extension at the L1-L2 and L3-L4 levels in flexion-extension where the IQR of the *reduced dataset* is substantially smaller than for the *complete dataset*, with a reduction in the IQR of 5.6° for L1-L2 and 4.3° for L3-L4.

Table 3.11: The median and interquartile range of the joint orientation in each DoF for the complete and reduced set of models

Model set	Joint Level	Median Orientation, °			IQR Orientation, °		
		Right-Left bending	Axial rotation	Flexion-Extension	Right-Left bending	Axial rotation	Flexion-Extension
Complete	L1-L2	1.51	3.28	6.90	3.00	2.84	8.44
	L2-L3	5.13	6.10	2.63	2.90	2.96	3.60
	L3-L4	6.51	8.60	-7.04	3.00	2.98	7.24
Reduced	L1-L2	1.66	3.14	6.97	2.76	2.84	2.84
	L2-L3	5.44	5.99	2.27	3.47	2.73	2.73
	L3-L4	6.71	8.54	-6.21	3.54	2.95	2.95

3.3.4. Initial simulations

The bootstrapping investigations showed the results were not independent of the initial stiffness nor of the damping parameters (Appendix E). The median and range of the kinematic error of the predicted motion across all the damping parameters and all initial stiffnesses tested was overall lower under quasi-static loading conditions than it was under simulated dynamic loading conditions (Table 3.12, Table 3.13, Appendix E).

Of the ten damping parameter sets used, four resulted in successful optimizations of the stiffness. Under a quasi-static load, the range of the predicted kinematic errors in anterior-posterior translation was negligible compared to the median prediction error. While in flexion-extension the range was negligible compared to experimental motion. The median errors were smaller in axial compression compared to the other directions; however, the range was not negligible. The range

of the kinematic error is reflected in the range of predicted stiffnesses (12,000 N/m in anterior-posterior, 230,000 N/m in axial compression, and 0.5 Nm/rad in flexion-extension). Using dynamic loading conditions, the median and range of the kinematic errors were higher (Table 3.12).

Of the 100 initial stiffness parameter sets tested, 66 were successful. The trends of the median and range of the kinematic errors for the initial stiffnesses were similar to those of the damping parameters. However, the bootstrapping of the initial stiffnesses resulted in a larger range of predicted kinematic errors than the damping parameter (Table 3.13). This is also reflected in a higher range of the predicted stiffnesses (550,000 N/m in anterior-posterior, 390,000 N/m in axial compression, and 3528 Nm/rad in flexion-extension). Some of the predicted stiffnesses are unphysiological (an order of magnitude greater than the initial stiffness), if these results are removed the range reduces (233,000 N/m in anterior-posterior, 390,000 N/m in axial compression, and 4.4 Nm/rad in flexion-extension) however it is still larger than the range due to damping parameters.

Table 3.12: Results from the damping parameter bootstrapping test. The median (range) of the prediction errors and the maximum median error as a percentage of the experimental motion in each of the different directions under quasi-static (QS) and dynamic (Dyn) loading conditions.

Load	Anterior-Posterior			Axial compression			Flexion-extension		
	L2, mm	L3, mm	Max % err	L2, mm	L3, mm	Max % err	L2, °	L3, °	Max % err
QS	0.42 (0.01)	0.19 (0.07)	102	$5x10^{-4}$ (0.35)	0.1 (0.16)	35	0.14 (0.05)	0.25 (0.12)	13
Dyn	0.45 (0.06)	0.28 (0.1)	110	0.06 (0.14)	0.05 (0.06)	35	0.48 (1.2)	0.52 (1.5)	29

Table 3.13: Results from the initial stiffness parameter bootstrapping test. The median (range) of the prediction errors and the maximum median error as a percentage of the experimental motion in each of the different directions under quasi-static (QS) and dynamic (Dyn) loading conditions.

Load	Anterior-Posterior			Axial compression			Flexion-extension		
	L2, mm	L3, mm	Max % err	L2, mm	L3, mm	Max % err	L2, °	L3, °	Max % err
QS	0.42 (0.24)	0.31 (0.41)	102	$4x10^{-4}$ (0.36)	0.09 (0.26)	35	0.03 (1.5)	0.07 (1.9)	4
Dyn	0.41 (0.11)	0.31 (0.34)	102	$9x10^{-4}$ (0.36)	0.09 (0.27)	35	0.04 (1.5)	0.09 (1.9)	5

The least-square error of the registration was 0.38mm for L2 and 0.22mm for L3.

3.4. Discussion

This study aimed to test the feasibility of determining a lumped parameter model of the IVJ from a DIC dataset and to investigate the sensitivity of the model to the joint definition. The results showed that it is possible to determine a lumped parameter model of the IVJ from a DIC dataset.

However, the results showed that the lumped parameter model (ie. the stiffness found through the optimisation) and the kinematic error were highly sensitive to the definition of the joint pose.

To determine a lumped parameter model of a specimen and test specific IVJ stiffness from an experimental dataset, the following data is required: a specimen-specific geometry, the 3D experimental pose of the vertebrae, 3D loading position relative to the vertebra, and their motion. This study created the specimen-specific geometry from segmentations of CT data of the specimen subjected to experimental testing. The methodology would still work with other approaches provided they allow for the creation of the specimen-specific, for example, biplanar X-ray data would also be suitable [297]. In this study, DIC data of the specimen in the unloaded position was used to determine the 3D experimental pose. The methodology is not limited to only DIC data, biplanar X-rays would be an alternative method to determine the 3D experimental pose [298]. The position of the applied load was determined from the DIC data as the experimental study had placed markers on the top pot which, together with the most cranial vertebra, was a rigid body connected to the actuator via a ball-and-socket joint. Finally, with the available data, the stiffnesses were only optimised in three anterior-posterior shear, axial compression, and flexion-extension, specifically those which had the larger RoM for the loading conditions explored. This choice was due to the cost function being insensitive to the other DoF. Having more loading conditions, and larger motion in the other DoF could overcome this. Thus, to optimise all DoF multiple loading conditions may be required. Such considerations are relevant for experimental protocols if the data is to be used in specimen-specific and test-specific computational studies.

This study assumed that the stiffnesses were independent of joint level. Although it is suggested within the literature that the IVJ stiffness varies between joint levels [278,285]; the joints are within the lumbar spine across a short spine segment so a large variation is not expected. However, the experimental setup required the removal of the posterior ligaments between L3 and L4 (the vertebra fixed within the lower pot). These ligaments are known to contribute to the stiffness for flexion-extension and anterior-posterior translation [285,299] thus further exacerbating the effect of assuming level-independent stiffnesses. Despite this assumption, the motion was accurately predicted to within a median (and IQR) of 0.15 (18) mm in anterior-posterior translation, 0.12 (0.06) mm in axial compression and 0.15 (0.15) ° in flexion-extension for the ten best performing models (Table 3.5). These errors are of the same order of magnitude as previous studies [52,69]. Furthermore, the optimised stiffnesses of the ten best models were within range of the optimised stiffness of the best performing (which had prediction errors in all but one DoF below 10%). Therefore, this may be a suitable method for calibrating a subject-specific, test-specific IVJ stiffness simultaneously in multiple DoF.

The optimised stiffnesses in axial compression and flexion-extension were lower than most of the literature, but they did still fall within the range reported in the literature [176,292]. The anterior-posterior stiffness was lower than the values found in the literature but was still the same order of magnitude [288]. Low stiffness values were expected given the experimental motions occurred in the laxest zone of the entire range of motion (the range of motion of the experiment was less than 1mm in translation and less than 2° rotation, and the fact that the intervertebral joint is highly non-linear [273,284,299]).

The second aim of this study was to investigate if the model was robust concerning the uncertainties affecting the joint pose. To do this, a space of possible landmark positions was sampled and used to define different joint poses. Assuming a potential standard deviation of the landmark positions by up to 2.9mm, the joint poses showed little variation (IQR <1.25mm) in the

location of the CoR (Table 3.10). The variation in the joint orientation was larger (IQR< 3.6° in lateral bending and axial rotation, and up to 8.5° in flexion-extension). The largest variations were seen at the joint levels adjacent to the potted vertebra, this is explained by the fact that only the endplate of the potted vertebra adjacent to the joint could be virtually palpated. Therefore, the joint flexion-extension orientation was based on the flexion-extension orientation of only one vertebra, rather than two. The variation of the joint pose results in a wide range of optimised stiffnesses. Previous studies support this finding as they have similarly demonstrated the IVJ loads are sensitive to the joint pose [72,114,267], which implies optimised stiffnesses would be sensitive to the joint pose. Further, although the joint pose influences the optimised joint stiffness (statistically significant differences), there was no clear relationship between the joint poses and the optimised stiffness (correlation was not statistically significant). Thus, when determining subject-specific stiffnesses with optimisation approaches the precision of every anatomical landmark for defining the joints should be less than 2.9 mm.

The combination of different joint poses and optimised stiffness resulted in a range of kinematic errors (Figure 3.7). However, there were also multiple combinations of joint pose and optimised stiffnesses that accurately predicted the kinematics (Table 3.5). A similar study performed on the cervical spine has shown the predicted motion to be sensitive to the stiffness [52]. Therefore, to investigate the influence of the stiffness or the joint pose, a two-factor analysis was conducted. This showed both the joint stiffness and the joint pose had a significant effect on the predicted motion (Table 3.8), which is in agreement with the findings of Byrne *et al*., that there is an interaction between the joint pose and joint stiffness [72]. Further, the regression tree analysis showed the joint pose (which is determined by the anatomical landmarks) to influence the kinematic prediction more than the stiffness.

Therefore, given the sensitivity of both the optimised stiffness and the predicted kinematics to the joint pose, and the sensitivity of the predicted kinematics to the optimised stiffness, the question arises, how should the most suitable combination be selected? Further research could investigate how to determine the most suitable combination by investigating which particular joint pose and stiffness combinations accurately predict the motion in conditions where the stiffnesses and joints are expected to behave similarly.

Dynamic and quasi-static loading conditions were considered to simulate the loading conditions. Quasi-static loading was chosen as using dynamic loading conditions did not offer any improvement in the accuracy of the simulations but required more computational time. Additionally, in this case given the low loading rate (54 N over 1 s) the use of dynamic loading conditions introduced an error at the start of the simulation where the gravity forces were larger than the loading and thus induced unrealistic motion. Similar behaviour (referred to as a gravitational settling process) was observed in the study by Meszaros-Beller *et al.* [272]

The initial bootstrapping studies for both the stiffness and damping parameters indicated the presence of local minima. Thus, when applying optimisation studies to determine stiffness properties the damping parameters should also be considered.

There were several limitations to this study. Firstly, this study was performed on a single specimen. However, this study was exploring a method to determine a specimen and test-specific lumped parameter model of the IVJ, thus as a proof of concept, a single specimen was sufficient. Secondly, registration errors, result in position errors of the anatomical landmarks, which result in errors in the joint pose. However, they were of the same order of magnitude as previous studies which used

similar methods [256,300,301]. Additionally, these errors are an order of magnitude smaller than the potential error introduced due to operator variability. Thirdly, a fixed centre of rotation was assumed. Although it is well documented that the IVJ centre of rotation migrates, determining the path is experimentally challenging [114,302]. Using a fixed centre of rotation has become the most common approach in computational models of the spine. Such an assumption may lead to inaccurate muscle activity and joint reaction forces [114,267]. However, under small moments (1.5 Nm) the centre of rotation has been found to remain at the centre of the IVD [302]. Given the offset and magnitude of the applied force in the experiment, the specimen would have been subject to comparably small loads, thus assuming a fixed centre of rotation seemed reasonable. Another limitation was the modelling of the stiffnesses as linear. Given the small range of motion, this may be a reasonable assumption and one that is used widely used in the musculoskeletal modelling of the spine [43,50,52,106,107,265].

Future studies should look to reapply the method to a larger number of specimens. Other optimisation methods could be tested, such as neural networks [52]. Given the sensitivity to the joint pose, future work should establish a more robust method for determining the joint pose or defining a trajectory for the centre of rotation instead of using a fixed point.

In conclusion, it is feasible to identify a specimen and test-specific lumped-parameter model of the IVJ. To do so requires the 3D motion, 3D loading position, 3D experimental pose and specimen-specific geometry. To identify a lumped-parameter model that describes a specimen in all DoF multiple loading conditions are needed. Both the predicted motion and the optimised stiffnesses are sensitive to the joint pose and multiple configurations of joint pose and optimised stiffnesses can result in accurately predicted motion. Therefore, when optimising specimen-specific stiffnesses the potential influence of joint pose should be considered and the precision of anatomical landmarks should be less than 2.9 mm.

3.5. Appendix A

Plots of the errors against 4 parameters that define the joint pose (lateral bending, axial rotation, flexion-extension orientation, and the joint CoR position).

The model has three joints, L1L2, L2L3, and L3L4. In order to have a single parameter to describe the joint pose in each rotational DoF the average orientation across the three joints was taken each direction. To have a single parameter to describe the location of the CoR, the average CoR for each level was calculated as the average position of all the models. Then for each model, at each level, the Euclidean distance from the average CoR was calculated. The distance of the CoR from the average CoR was expressed as the average distance of the three levels.

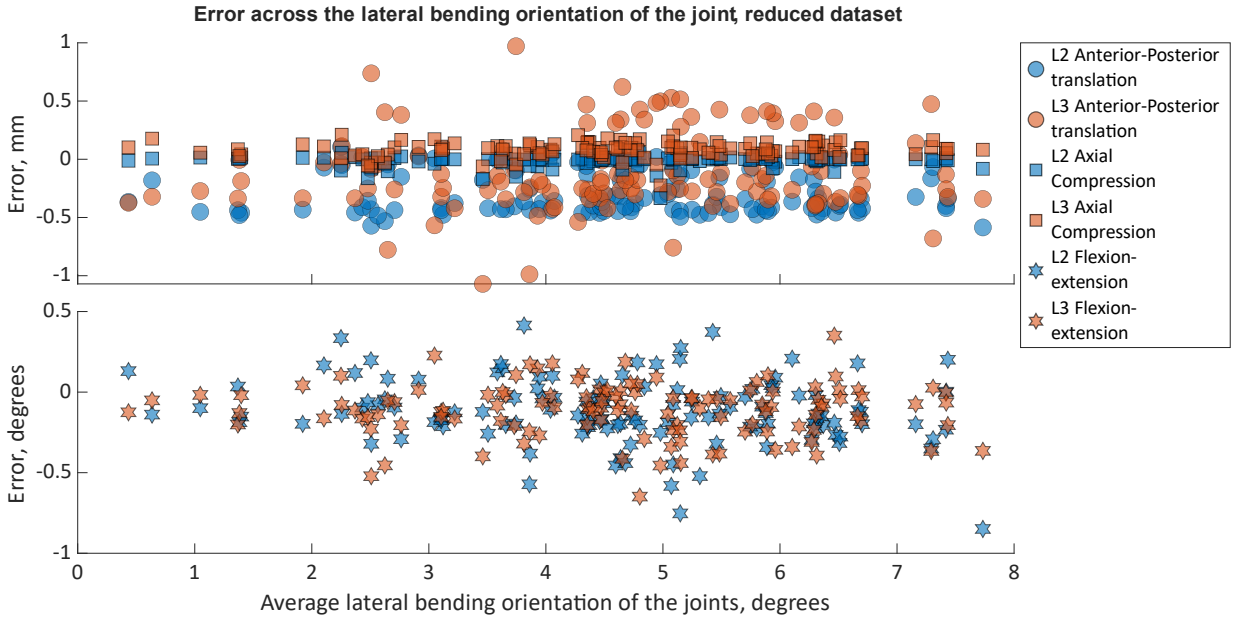

Figure 3.8: The predicted error in the three DoF of interest for L2 and L3 across the different joint orientations in lateral bending that were tested.

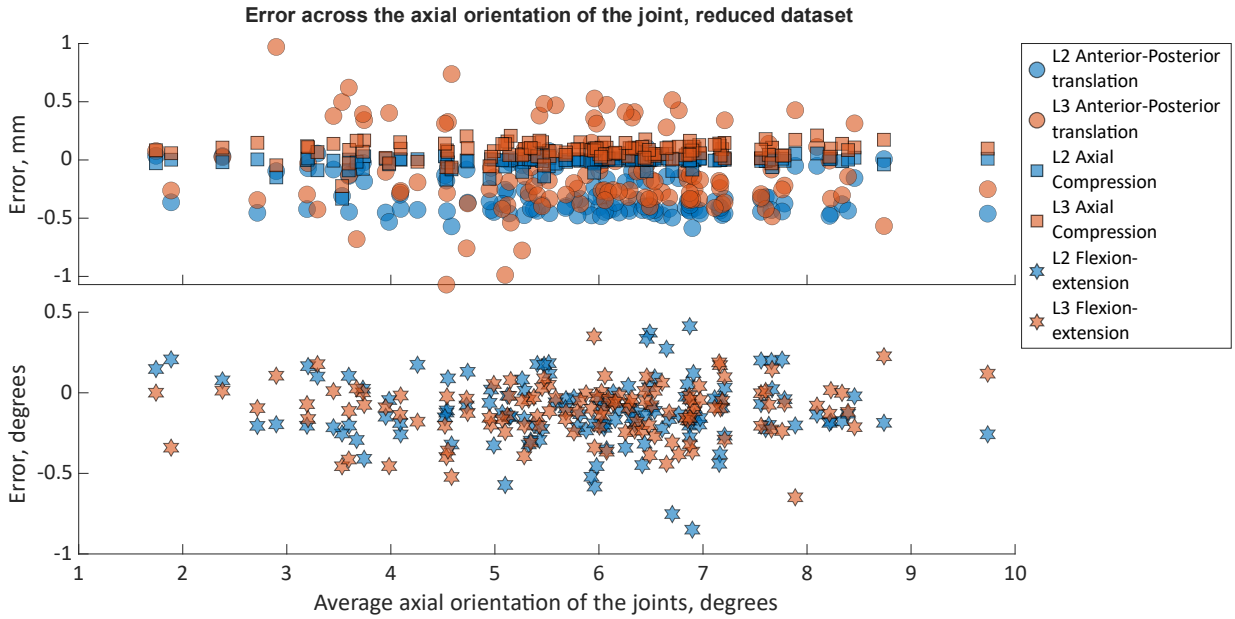

Figure 3.9: The predicted error in the three DoF of interest for L2 and L3 across the different joint orientations in the axial rotations that were tested.

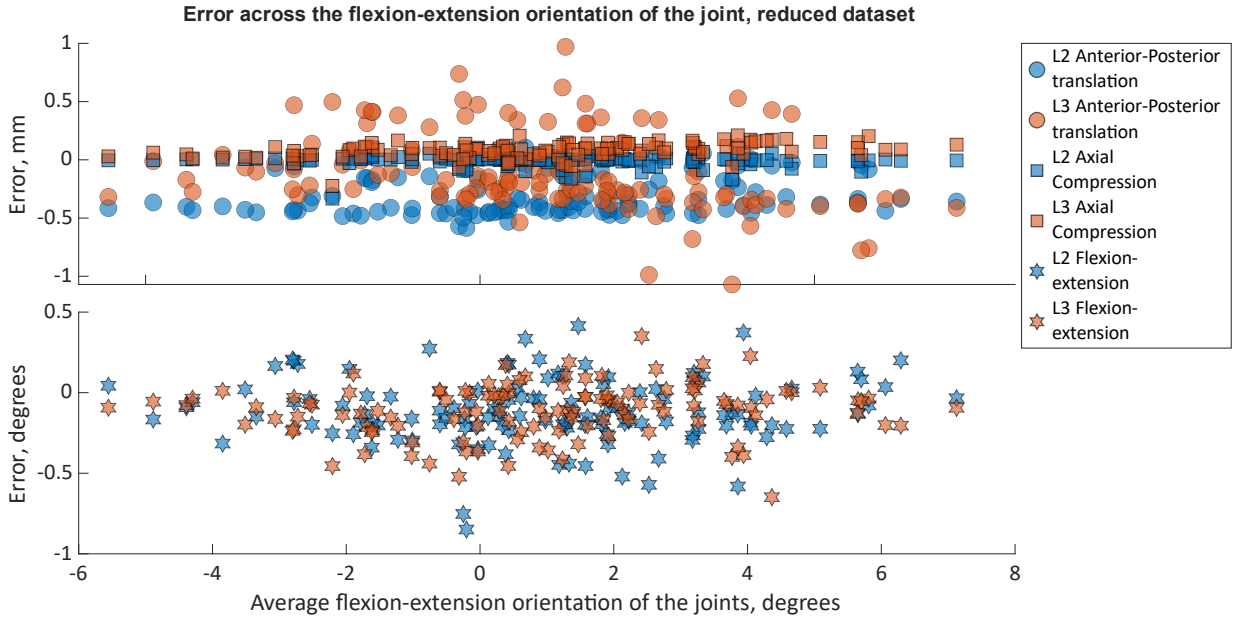

Figure 3.10: The predicted error in the three DoF of interest for L2 and L3 across the different joint orientations in flexion-extension that were tested.

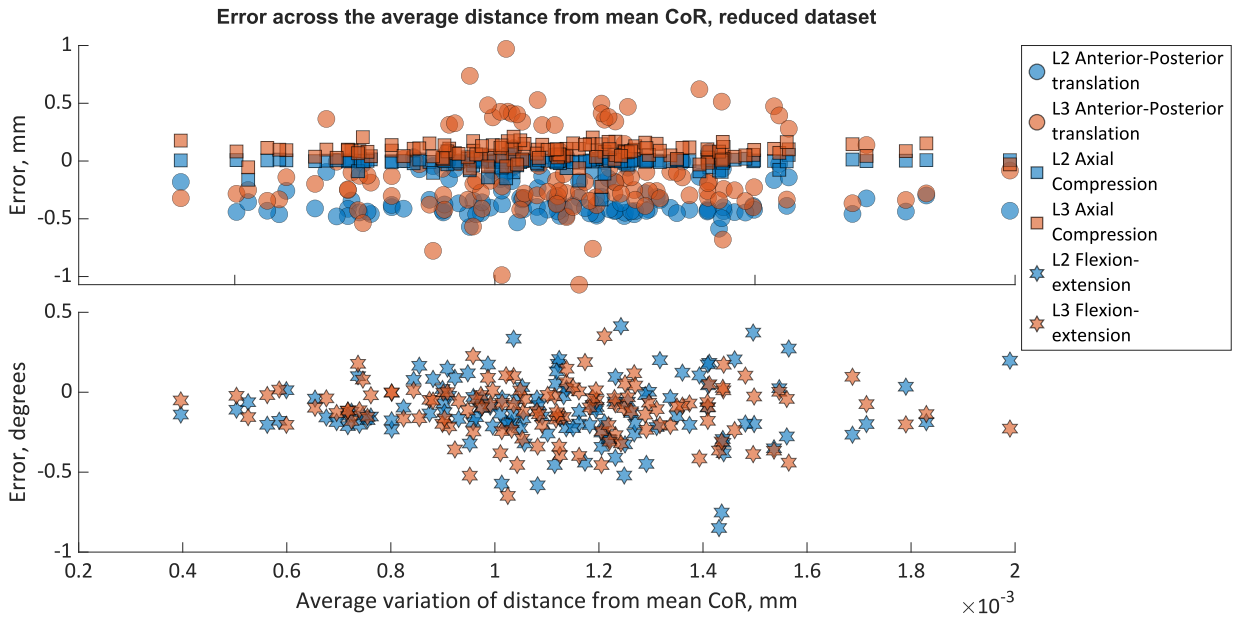

Figure 3.11: The predicted error in the three DoF of interest for L2 and L3 across the different distances of the joint CoR from the average CoR location

3.6. Appendix B

Plots of the optimised stiffness against the four parameters that can be used to define the joint pose. They are the joint orientation in right-left bending (Figure 3.12), the joint orientation in axial rotation (Figure 3.13), the joint orientation in flexion-extension (Figure 3.14), and the Euclidean distance of the joint CoR from the average joint CoR position (Figure 3.15). Each of these parameters is calculated as the average across the three joints.

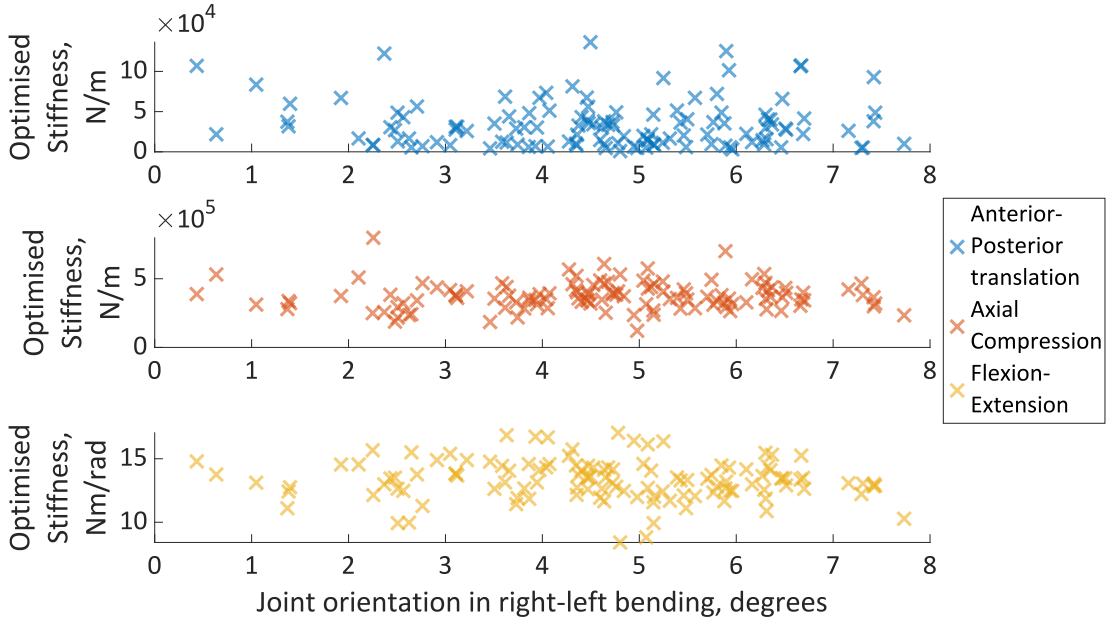

Figure 3.12: The optimised stiffness for the different lateral bending orientations of the joint poses.

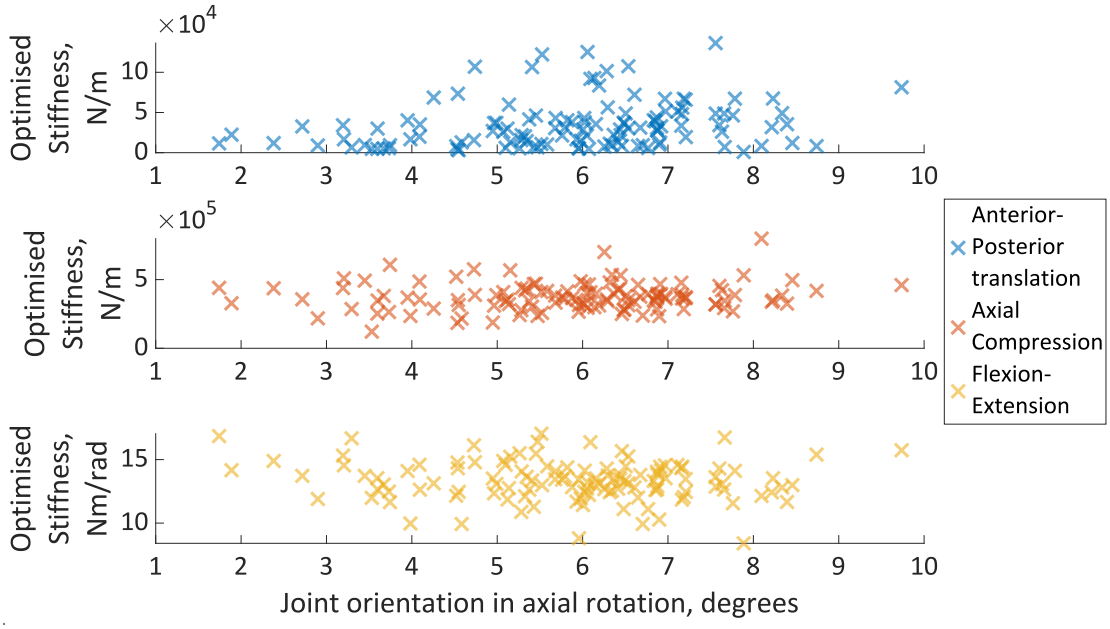

Figure 3.13: The optimised stiffness for the different axial rotation orientations of the joint poses.

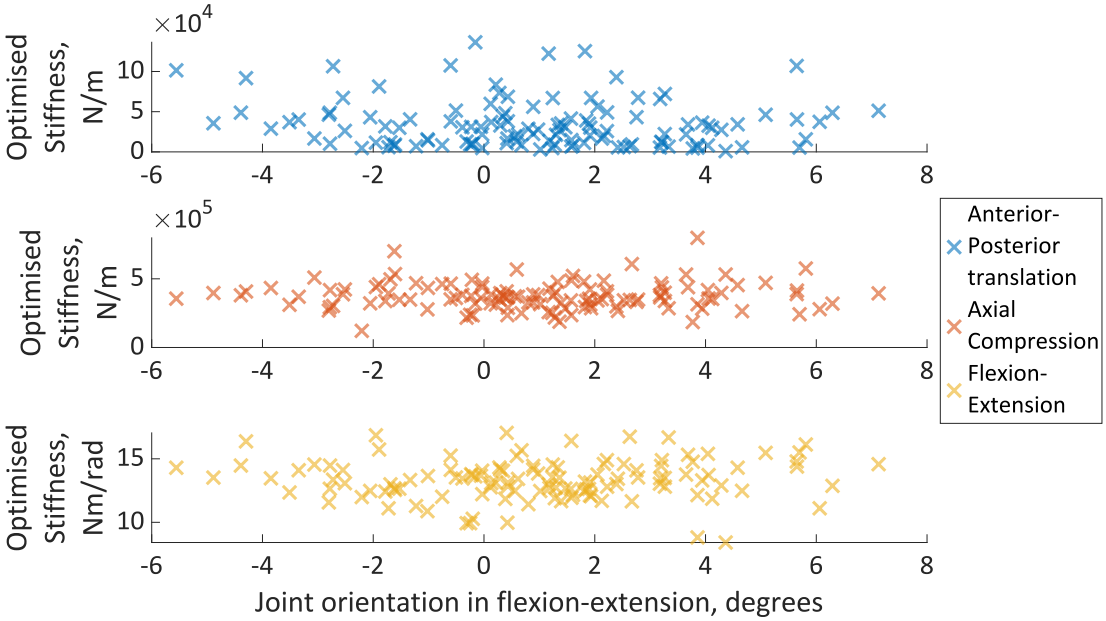

Figure 3.14: The optimised stiffness for the different flexion-extension orientations of the joint poses.

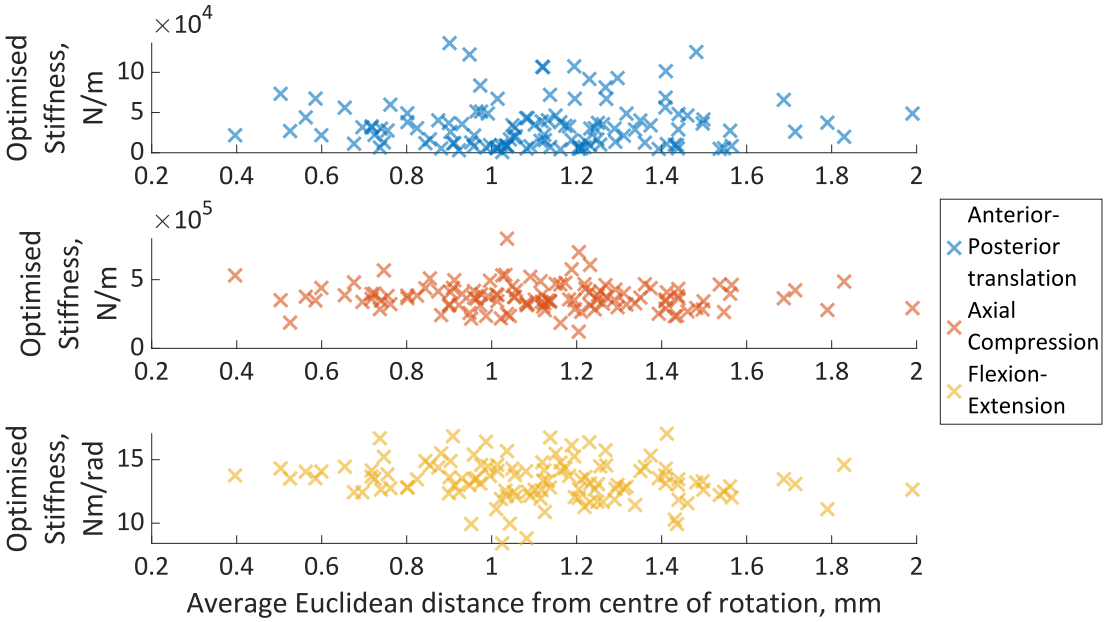

Figure 3.15: The optimised stiffness for the different distances from the average CoR of the joint poses.

3.7. Appendix C

Plots of the errors in each direction against the optimised stiffness in each direction. Errors are calculated as the average error of L2 and L3.

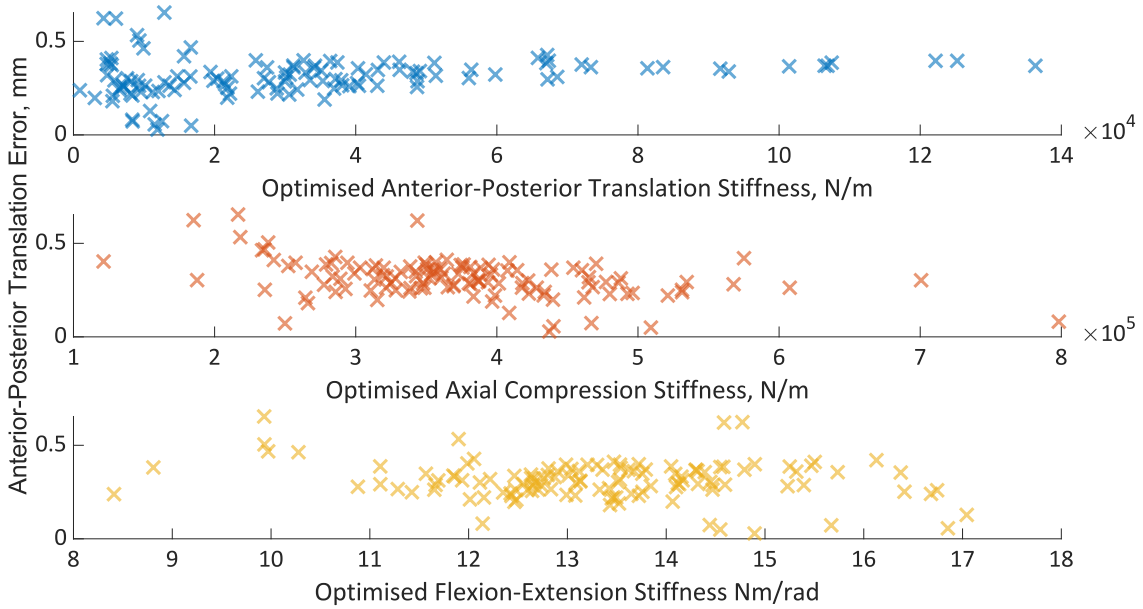

Figure 3.16: Average error in anterior-posterior translation compared to each of the optimised stiffnesses. No clear correlation between the error and the stiffnesses

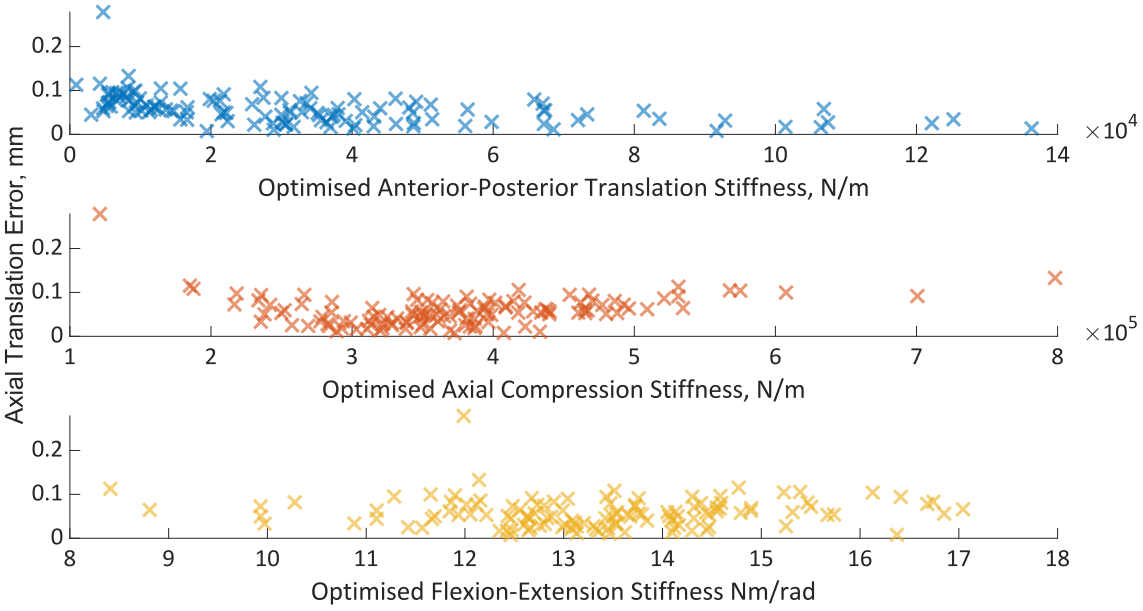

Figure 3.17: Average error in axial compression translation compared to each of the optimised stiffnesses. No clear correlation between the error and the stiffnesses

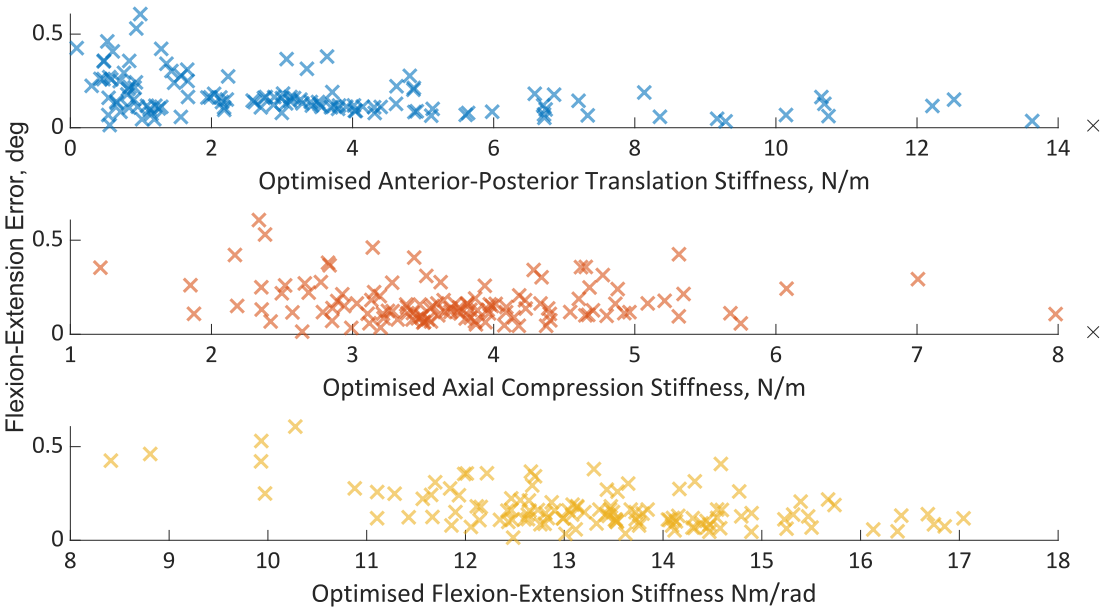

Figure 3.18: Average error in flexion-extension compared to each of the optimised stiffnesses. No clear correlation between the error and the stiffnesses

3.8. Appendix D

The positive linear relationship in the anterior-posterior and flexion-extension DoF for both vertebrae indicates a proportional bias (Figure 3.19, Figure 3.20). As the translation in the anterior-posterior direction increases the error decreases until an average translation of 0.4 mm for L2 and L3. As the rotation in flexion increase the error decreases until an average rotation of 1.5° for L2 and 1.9° for L3, after which the error starts to increase. The error in axial compression appeared to be independent of the experimental axial compression for both vertebrae.

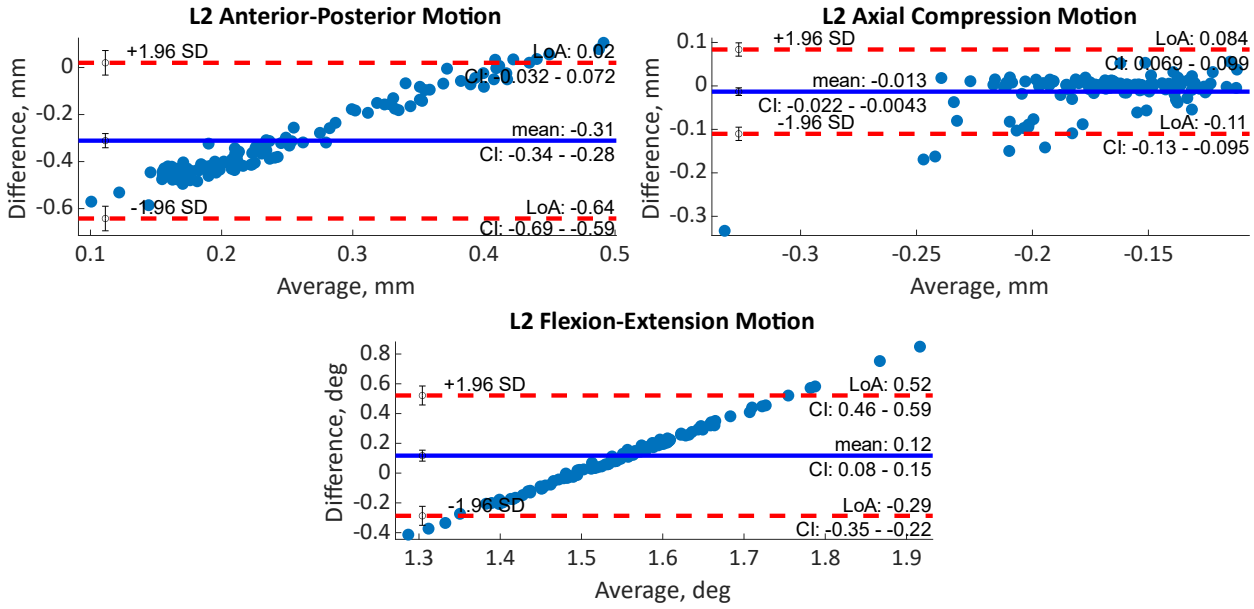

Figure 3.19: Bland-Altman plots showing the dependence of the prediction error (Difference) on the average value of the predicted motion and the experimental motion for L2 in each of the DoF for which the stiffness is optimised.

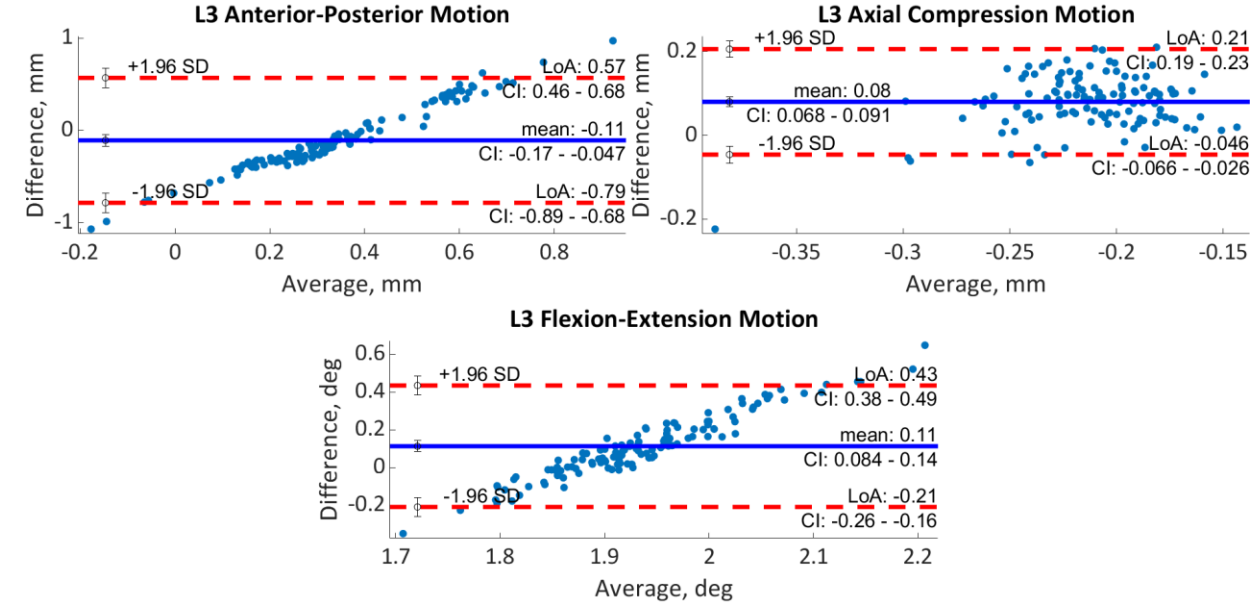

Figure 3.20: Bland-Altman plots showing the dependence of the prediction error (Difference) on the average value of the predicted motion and the experimental motion for L3 in each of the DoF for which the stiffness is optimised.

3.9. Appendix E

To test the optimisation for independence from the damping parameters ten damping parameters were tested (Table 3.14). The damping parameters were selected by dividing the range of damping parameters (0-2000N/(m/s) in translation and 0-5Nm/(rad/s) in rotation) reported in the literature into a ten evenly distributed parameters spaces and then selecting a value at random from within each parameter space.

Table 3.14: The initial translational and rotational damping parameters tested, values are rounded to two significant figures.

Model ID	1	2	3	4	5	6	7	8	9	10
Translational damping	19	220	560	780	920	1100	1300	1500	1700	1800
Rotational damping	0.34	0.94	1.2	1.9	2.3	2.6	3.4	3.7	4.2	4.9

For each parameter, the optimisation simulations were applied using quasi-static and dynamic loading conditions. The optimised stiffness and the average prediction error across the three joints were compared for the different damping parameters and loading conditions (Figure 3.21, Figure 3.22).

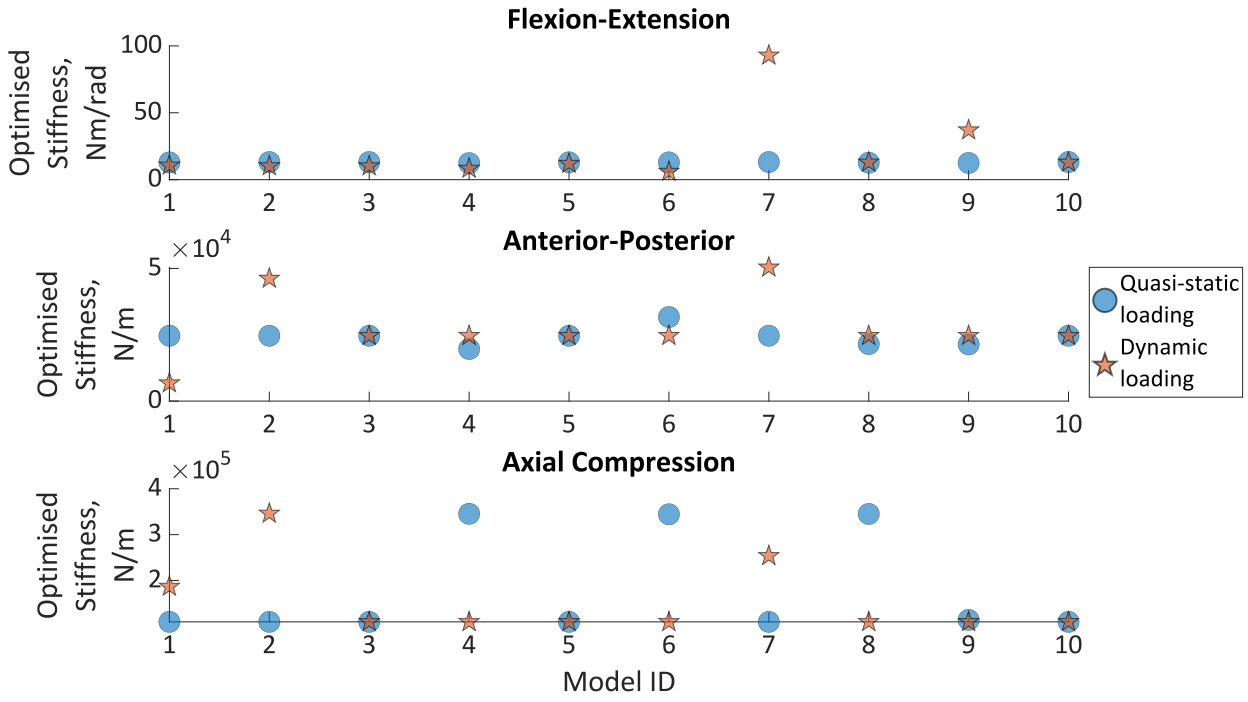

Figure 3.21: The optimised stiffness in flexion-extension, anterior-posterior translation, and axial compression for ten different initial damping parameters and under quasi-static and dynamic loading conditions.

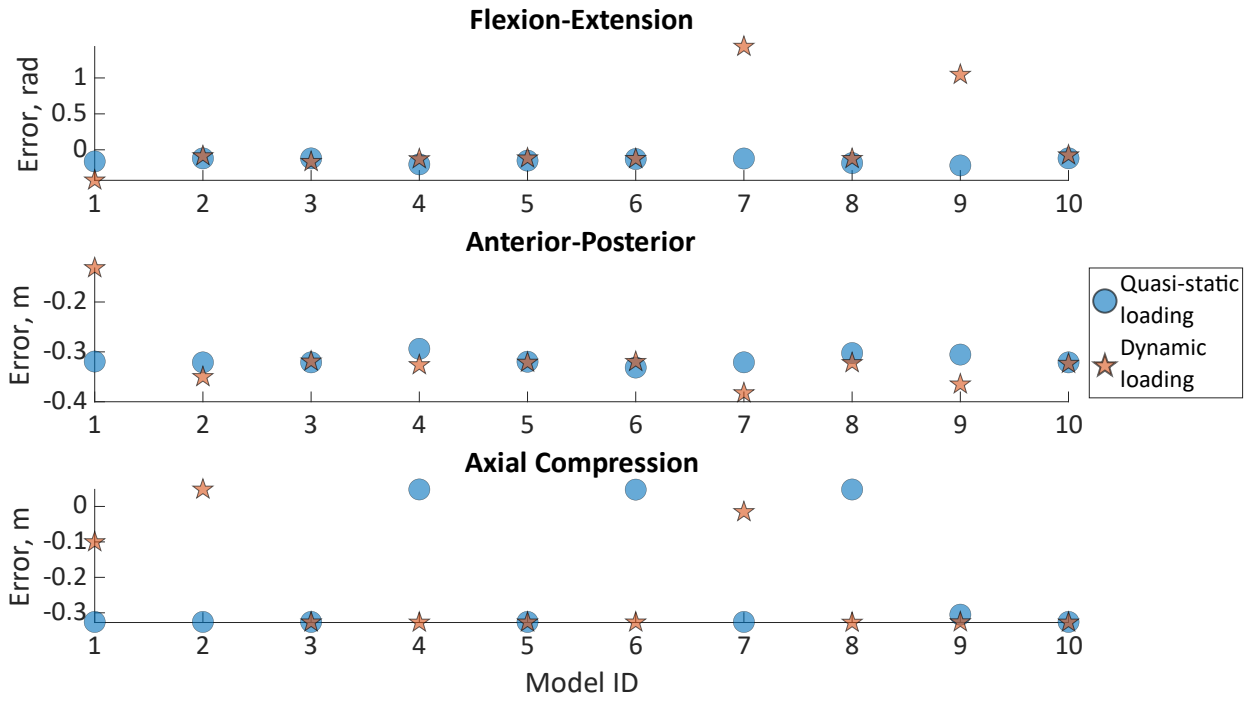

Figure 3.22: The average prediction error across the three joints in flexion-extension, anterior-posterior translation, and axial compression for ten different initial damping parameters and under quasi-static and dynamic loading conditions.

One hundred initial stiffnesses were tested to check for independence from the starting stiffnesses. The initial stiffnesses were selected by dividing the range of stiffnesses reported in the literature (Table 3.3) into one hundred equally distributed parameter spaces. From each parameter space, a stiffness value was selected at random. For each initial stiffness, the optimisation simulations were applied using quasi-static and dynamic loading conditions. The optimised stiffness and the average prediction error across the three joints were compared for the different damping parameters and loading conditions (Figure 3.23, Figure 3.24).

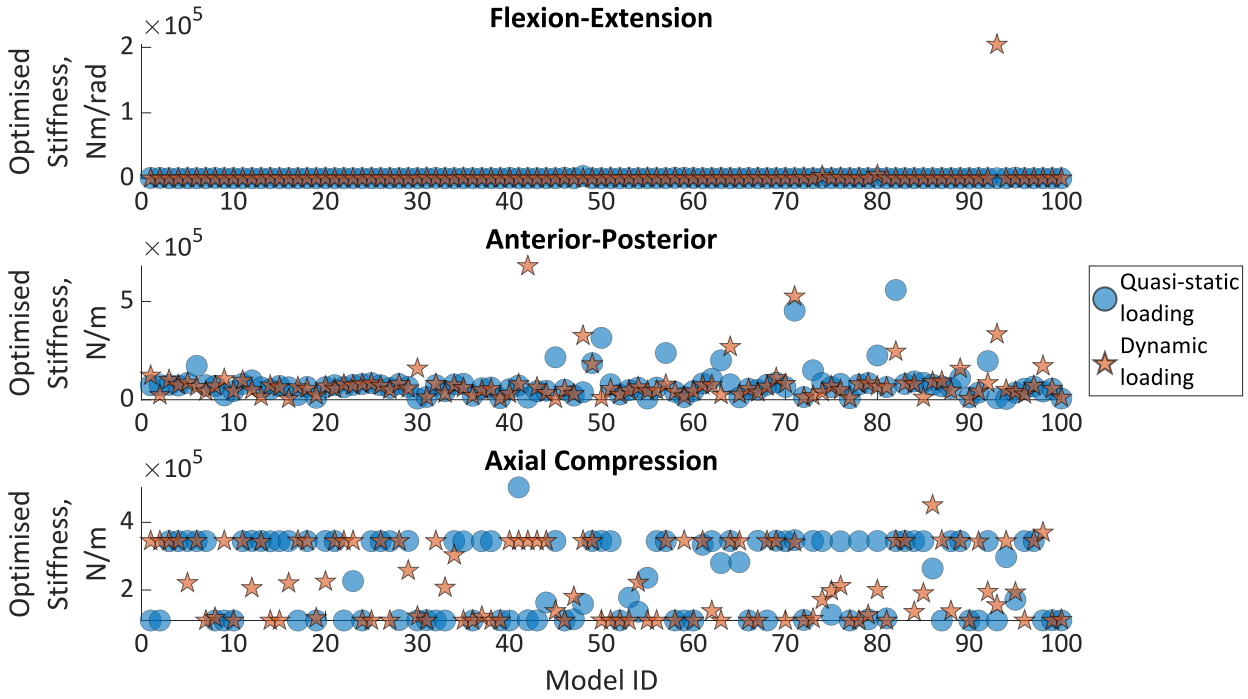

Figure 3.23: The optimised stiffness in flexion-extension, anterior-posterior translation, and axial compression for 100 different initial stiffness parameters, under quasi-static and dynamic loading conditions.

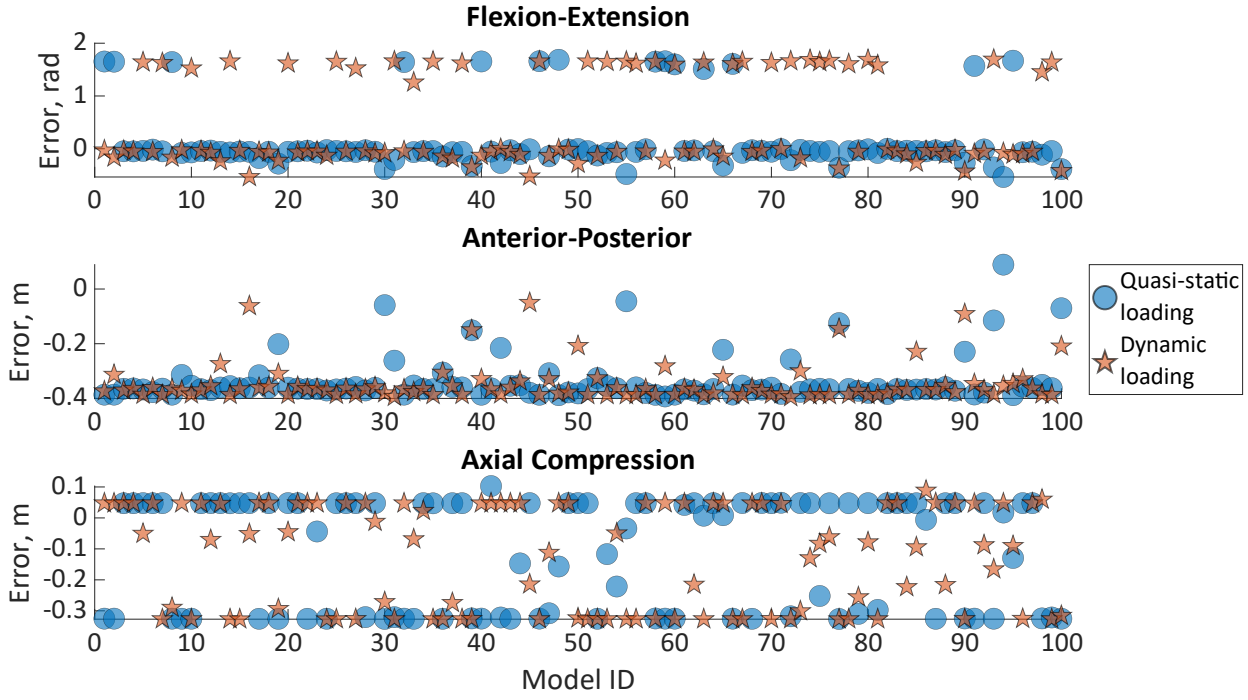

Figure 3.24: The average prediction error across the three joints in flexion-extension, anterior-posterior translation, and axial compression for 100 different initial stiffness parameters, under quasi-static and dynamic loading conditions.

Variability of intervertebral joint stiffness between spine levels and between specimens

Samuele L. Gould[1,2], Giorgio Davico[1,2], Christian Liebsch[3], Hans-Joachim Wilke[3] Luca Cristofolini[1,2], Marco Viceconti[1,2]

[1] Department of Industrial Engineering, Alma Mater Studiorum - University of Bologna (IT)

[2] Medical Technology Lab, IRCCS Istituto Ortopedico Rizzoli, Bologna (IT)

[3] Institute of Orthopaedic Research and Biomechanics, Ulm (DE)

MANUSCRIPT IN PREPARATION

CORRESPONDING AUTHOR:

Prof. Luca Cristofolini

Dept. of Industrial Engineering

Alma Mater Studiorum – University of Bologna

Via Umberto Terracini 24-28

40131 Bologna, Italy

Email: luca.cristofolini@unibo.it

4.1. Introduction

Spinal injuries and disorders carry a high societal and personal cost [303]. An individual may experience intense pain, reduced quality of life, and have their ability to work and participate in society limited [303]. Musculoskeletal multi-body models (MSK) of the human spine allow for the investigations, such as soft tissue characterisation, which would present ethical and practical challenges *in vivo* [126]. Additionally, MSK models allow investigating situations which could present a risk to human subjects (e.g., large loads on the cervical spine) [52]. The study by Silvestros *et al.* showed a proof-of-concept application to investigate injury mechanisms cervical spine using an MSK model [52]. Beaucage-Gauvreau *et al.* developed a model to allow for the non-invasive investigation of lower back loads during lifting activities [42]. Other studies have investigated ways of improving surgical treatments by simulating different instrumentation strategies for the same patient [35]. Further, MSK models allow for sensitivity analyses, such as the effect of intervertebral joint (IVJ) location and soft tissue properties on the compressive loads the vertebrae experience [43,72]. They, therefore, have the potential to reduce the risk of spinal injuries and improve spinal surgery outcomes [36,42,104], and so reducing the cost to individuals and society.

The passive soft tissues (the intervertebral joint, and ligaments) between adjacent vertebrae, commonly referred to as the IVJ, contribute to the functional behaviour of the spine and are crucial to maintaining spinal stability [304]. MSK models of the spine often simplify the IVJ to three rotational degrees of freedom (DoF) with a fixed centre of rotation [40,127], although more recent studies have included translational DoF [50,107,266]. Further, although each soft tissue has different mechanical properties when the mechanical properties are represented they are often simplified to a lumped parameter model and represented with a spring-damper in each DoF [51,104]. Given the importance of the IVJ in the behaviour of the spine and the simplifications made to represent it, accurate subject-specific characterisation is necessary to develop reliable models.

Although not always included, when the mechanical properties are modelled, the stiffness is often based on a limited number of values found within the literature [40,43,50,106,109,139,266,305]. Yet, it has been widely reported in the literature that IVJ properties vary strongly between spine levels, and present high inter-specimen variability in all DoF [112,127,176,284,288,289,291,293,306–309]. Furthermore, various studies have shown that predicted muscle forces, intervertebral disc loads, and range of motion are highly sensitive to their representation [72,226,266]. The role of the IVJ is additionally complicated by the interaction between joint pose and stiffness which influence the predicted joint loads and muscle forces [72]. Moreover, several studies have highlighted the importance of determining subject- or specimen-specific and condition-specific stiffnesses [51,69,165]. Optimised stiffnesses have been shown to improve the accuracy of predicted kinematics [126].

Optimisation of the IVJ stiffness has been done using hybrid models [139], with finite element models and then implemented into MSK models [72]. Another method to determine subject-specific properties has been to scale the stiffness based on anthropometric data [165]. The meta-analysis of studies of the rotational behaviour of human cadaveric spines segments by Zhang *et al*. has established a regression model of the moment-rotation behaviour of the IVJ [109] which could be used to assign stiffnesses to the IVJ in MSK models. However, few studies have directly optimised the stiffness within MSK models. Typically, to represent the mechanical properties of the IVJ in MSK models a spring-damper element, commonly referred to as a bushing force, is used

in the relevant degrees of freedom (DoF) [52,126,226]. Wang *et al*. developed a generalised stiffness model from literature data of the IVJ which was incorporated into an MSK model [69], using this model they went a step further, optimising a subject-specific stiffness based on *in vivo* motion [126]. To simulate spinal surgeries Petit *et al*. developed a method using functional bending tests to optimise patient-specific stiffnesses [127]. One study has used a genetic algorithm with the MSK simulations to optimise the IVJ stiffness of the model for *ex vivo* porcine specimens [52]. The IVJ level dependency of the stiffness has also been accounted for at the individual IVJ levels [52,126] and by dividing the L5 to T12 section into 3 regions, with an optimisation parameter for each region [127].

In the study by Wang *et al*., the subject-specific stiffnesses of the MSK model were optimised with *in vivo* marker position data. However, they suggest more accurate motion tracking would enable a stiffness optimisation without including optimisation of the joint kinematics [126]. Motion capture data from *ex vivo* experiments could enable this. Stiffnesses were optimised in flexion-extension and lateral bending under flexion-extension motion and lateral bending motion, however, axial stiffnesses were not reported, nor were the stiffnesses optimised in axial rotation. Previous studies have shown that IVJ stiffness is direction-dependent [288,289,291], therefore stiffnesses predicted under one loading condition cannot be assumed to be true of all loading conditions. Silvestros *et al*. optimised the stiffness and damping parameters of porcine cervical spines in axial compression and anterior-posterior shear using motion capture data [52]. However, given the large variation of IVJ stiffness by IVJ level, parameters of the cervical spine may not apply to the lumbar spine [8,69]. Additionally, porcine spines have different kinematics and typically lower stiffnesses than the human spine [275,277]. Finally, as predicted motions appear to be more sensitive to the stiffnesses in rotational DoF than translational DoF [107], further study of the optimised stiffnesses in rotational DoF could be beneficial. While these studies have shown optimisation of the subject or specimen-specific stiffnesses improves the accuracy of the spinal MSK models [52,126], the aims of the previous studies were not to investigate the inter-specimen variability or the variation between spine levels of optimised stiffnesses. A study focusing on the inter-specimen and spine level variability which optimises stiffnesses within MSK models is lacking and would evidence the need for specimen-specific optimisation which accounts for the difference between spine levels. Moreover, a study using highly accurate motion tracking in combination with MSK models to simultaneously optimise the stiffnesses of the lumbar spine in all rotational DoF for multiple loading conditions would strengthen and build upon the existing studies.

Therefore, the current study aimed to investigate the variability of optimised stiffnesses across different specimens and different spinal levels in all rotational DoF using accurate motion capture data collected *ex vivo* to allow for highly accurate tracking. This also included investigating these aspects under different loading.

4.2. Materials and methods

This study reanalysed the results from the study by Volkheimer *et al.* [310]. The specimens were acquired from the ScienceCare (USA) donation program. The experimental study [310] provided data for six sacrum-T12 human cadaver specimens (Table 4.1). In brief, the specimens were cleaned of soft tissue leaving the intervertebral disc, all ligaments and facet joints intact. The sacrum was completely constrained and pure cyclic torques were applied to T12 using a spine tester [311]. Three loading conditions were individually applied, flexion-extension, axial torsion,

and left-right bending with pure moments implemented directly with a gimbal and stepper motor [311]. The loading cycles were applied at 1.0°/s in flexion-extension and lateral bending and 0.5°/s with pure moments of 7.5Nm. The moment in the loaded DoF and resulting coupled moments in the non-loaded DoF were measured using a six-component load cell mounted above the specimens (FT 1500/40, Schunk GmbH, Lauffen/Neckar, Germany) (Figure 4.1a). Three reflective markers were attached to the anterior surface of each vertebra (Figure 4.1b) [310]. The vertebral motion was measured with a motion tracking system (Vicon MX13+, Vicon Motion Systems Ltd., Oxford, UK) including six infrared cameras, from this, the rotation in each DoF at each joint was calculated. These rotations were then provided as inputs for the current computational study. Additionally, CT data with a pixel size of 0.39x0.39mm and slice increment of 0.5mm (thickness 1mm) (obtained with a Brilliance 64, Philips CT device using a voltage of 120kVp and a tube current of 356mA) and an X-ray of the experimental setup was provided for each specimen. The experimental study was not originally intended to be used as the input for the current computational study, therefore the CT scans were not performed with the markers attached to the vertebrae.

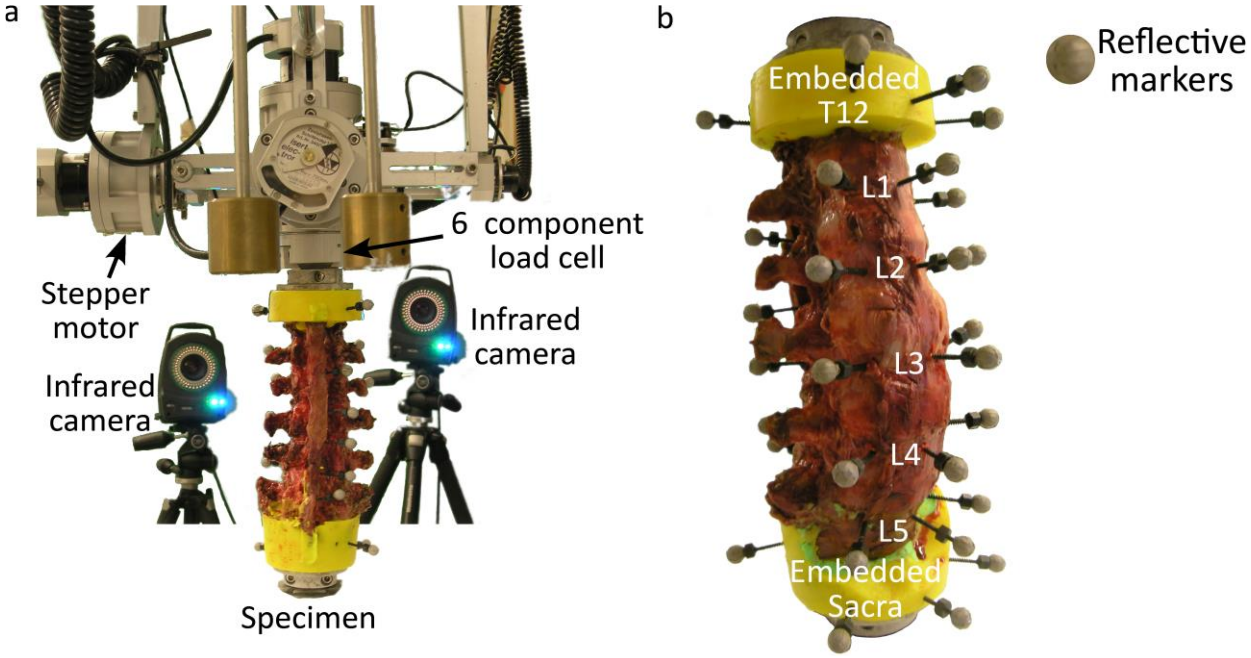

Figure 4.1: a. Experimental setup showing the specimen held in place by a lower fixture and the load cell above which attaches to the stepper motors, and two of the infrared cameras. b. An anterior view of a specimen with three reflective markers attached to the anterior surface of each vertebra.

Table 4.1: Specimen details

Specimen	Age	Sex	Height (m)	Mass (kg)	Cause of death
1	57	Female	1.57	59	metastatic lung cancer
2	54	Female	1.57	36	malignant colon cancer
3	56	Female	1.72	48	melanoma

4	59	Female	1.65	113	lung carcinoma/COPD
5	44	Female	1.63	49	Cardiac arrest
6	49	Male	1.72	59	Lung cancer

4.2.1. Workflow overview

The workflow for optimising the stiffnesses will be discussed in two stages, first pre-processing and model creation, and second optimisation (Figure 4.2). The pre-processing required two steps, first was an alignment of the CT data to the sagittal plane of the spine. This was followed by a registration procedure. Then the models and boundary conditions could be defined and passed to the optimisation process which optimised the stiffnesses.

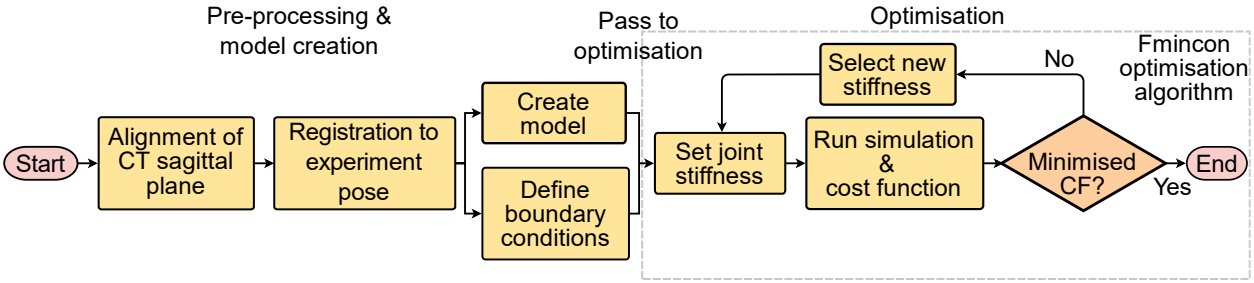

Figure 4.2: Workflow for optimising the stiffnesses starting from the experimental data.

4.2.2. Alignment of CT data to the sagittal plane of the spine

The specimens were imaged in different poses (both globally, and also possibly with different inter-vertebral angles) in the CT scanner and with the X-ray during the experiment. To ensure the model was in the same pose as the physical specimen, the CT data needed to be registered to the X-ray taken during the experiment. To do this the X-ray was assumed to be aligned with the sagittal plane of the spine. The sagittal plane of the CT data was not aligned with the sagittal plane of the spine (Figure 4.3a). To align the sagittal plane of the CT data with the sagittal plane of the spine a four-step process (see Appendix A for details) was followed:

1. In Mimics (Mimics Innovation Suite v24, Materialise, Leuven, Belgium) – virtual palpation of the CT data was performed to identify landmarks on the sagittal plane (Figure 4.3b).
2. A custom script in MatLab (MatLab R2021b, The Mathworks, Natick, MA, USA) – a plane was fitted to these landmarks to define the sagittal plane of the spine.
3. In Mimics – the sagittal plane of the spine is defined (Figure 4.3c).
4. In Mimics – CT data is resampled along the sagittal plane of the spine (Figure 4.3d).

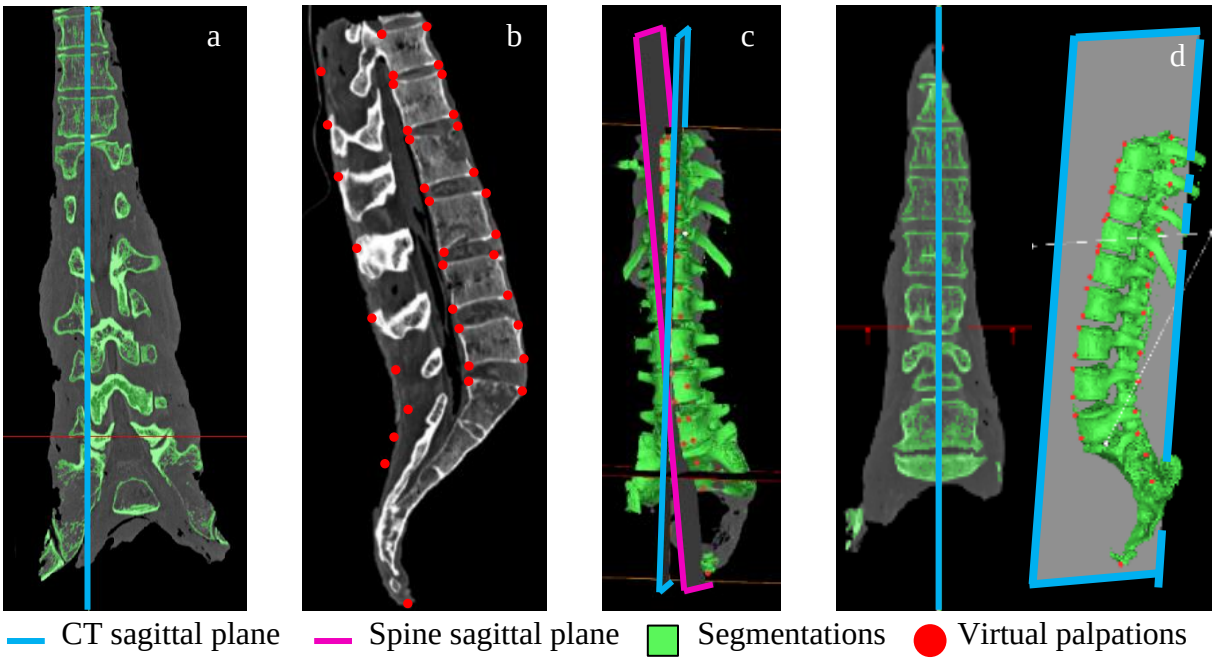

Figure 4.3: Realignment of the CT sagittal plane. a) original sagittal plane of the CT scan, b) virtual palpation of landmarks defining the spine sagittal plane, c) definition of the spine sagittal plane and the original CT sagittal plane in the CT scan, d) CT scan after realigning the CT sagittal plane to the spine sagittal plane.

4.2.3. Registration of CT data to X-ray

Following the alignment of the CT data, it was segmented, and two virtual palpations were performed. One set of virtual palpations identified the landmarks necessary to define the IVJ pose following the ISB recommendations [82] (Figure 4.4a). The second set enables the registration of the CT data to the X-ray (Figure 4.4b).

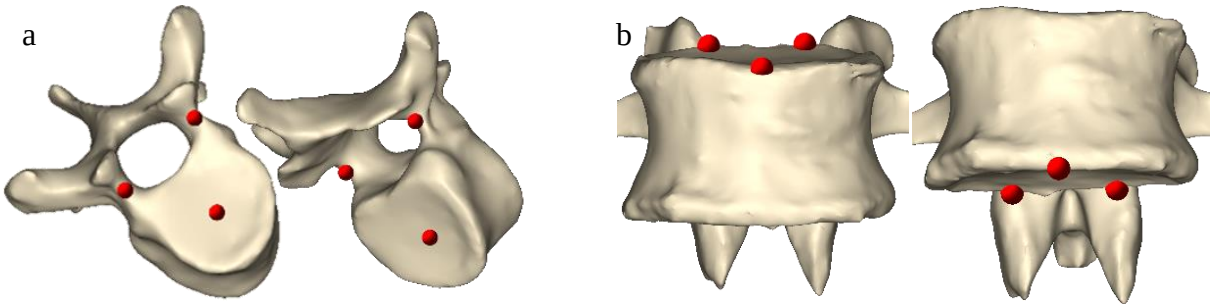

Figure 4.4: Virtually palpated landmarks on each vertebra. a) markers for defining the joint, placed on top and bottom of the pedicles and the centres of the vertebral endplates. b) markers placed for the registration of the CT scan to the X-ray, on the most anterior point of the endplate, and the two most superior points on the posterior of the endplate.

To register the CT data to the X-ray acquired during the experiment, the X-ray was virtually palpated with markers placed on the inferior-most and superior-most anterior-most and posterior-most points of the endplates. Where this was unclear multiple markers were placed and the average was taken.

The CT markers were projected onto the sagittal plane of the spine. The CT markers were moved into the same reference system as the X-ray markers. The X-ray markers were scaled using an estimation from the Euclidean distance of the markers on the endplates. The estimation was necessary as the X-ray was originally intended for grading the state of disc degeneration, therefore

information quantitative information regarding the field of view, the pixel size and detector element dimension was not available.

The rotational component of the transformation matrix to perform the registration on each vertebra was calculated using the average angle of the superior and inferior endplates. The translations needed for the registration were calculated based on the centre of the markers on each vertebra. A transformation matrix was defined for each vertebra, which was then applied to the segmentation of each vertebra and the associated joint markers (Appendix A). The joint markers were then used to define the joint pose following as best as possible the ISB recommendations [82]. The accuracy of the resulting models was qualitatively evaluated by inspection (comparing the curvature of the model to the curvature on the X-ray). A quantitative evaluation was not possible due to the data available from the X-ray data.

4.2.4. Model Creation and Simulation

An OpenSim model of each specimen was created using a custom MatLab script and the OpenSim API (code provided at OpenSim project Specimen specific spine models). In the models, the sacrum was fully constrained. A 6DoF joint was created for each IVJ in the pose previously defined (Figure 4.5). A bushing force (spring-damper element) was defined as coincident with the joint in each DoF, with generic stiffness values taken from the literature for the L3L4 IVJ level (Table 4.2)[43]. These stiffnesses were different in each DoF but uniform across the joint levels, these models will be referred to as $Models_{LitUniStiff}$. A uniform stiffness was applied in order to reduce the cardinality for the optimisation routine (reducing the computational expense) as optimising the stiffnesses at each level in all rotational DoF would require a cardinality of 18. This was considered necessary as a preliminary optimisation for a single model with a cardinality of 3 that lasted >8 hours. This represents an overall spine stiffness. Damping parameters of 1000 N/(m/s) were used for the translational dampers and 2.3 Nm/(rad/s) for the rotational dampers.

Table 4.2: Generic stiffnesses taken from literature and used in the models before the optimisation

Degree of freedom	Stiffness	
	Translation, N/m	Rotation, Nm/rad
Anterior-Posterior Shear/ Right-Left Bending	149,000	68.8
Inferior-Superior Translation/ Axial Rotation	1,890,000	291
Right-Left Translation/ Flexion-Extension	135,000	51.0

The approach of a uniform stiffness across the joints represents an overall spine stiffness. To also investigate the representation of the variation of stiffnesses across the joints, a set of models which incorporated level-dependent stiffnesses were also created (Table 4.3). These models are referred to as $Models_{LitLvlDepStiff}$ (Table 4.3). To introduce level-dependent stiffness a scaling factor was applied to the rotational stiffnesses. The scaling factor was calculated as the ratio of the stiffnesses based on the data used for fitting the regression models in the meta-analysis by Zhang *et al* [109].

Table 4.3: The initial stiffness in the rotational degrees of freedom for each spinal level after the scaling factor was applied.

Spinal level	Stiffness		
	Right-Left Bending, Nm/rad	Axial Rotation, Nm/rad	Flexion-Extension, Nm/rad
T12L1	36.4	136.8	16.3
L1L2	43.6	128.1	27.5
L2L3	19.9	291.1	36.7
L3L4	12.4	291.1	49.5
L4L5	13.8	291.1	50.0
L5S1	68.8	183.4	51.0

Quasi-static loading conditions were used to take into account the low loading rate of the experiment, and due to the computational expense of running a fully dynamic optimisation. Preliminary simulations using fully dynamic loading conditions found a single iteration could take over an hour, and an optimisation typically required over 200 iterations. The loading cycles were analysed to determine the loads to apply to the model. The first cycle was excluded as the initial recorded load in the first cycle was not always 0N. The other cycles were examined to identify the one with the smallest range of the coupled moments. The maximum torque in that cycle and the corresponding coupled moments were applied for the loading cycle duration to T12 to simulate flexion, left axial rotation, and left lateral bending (Figure 4.5).

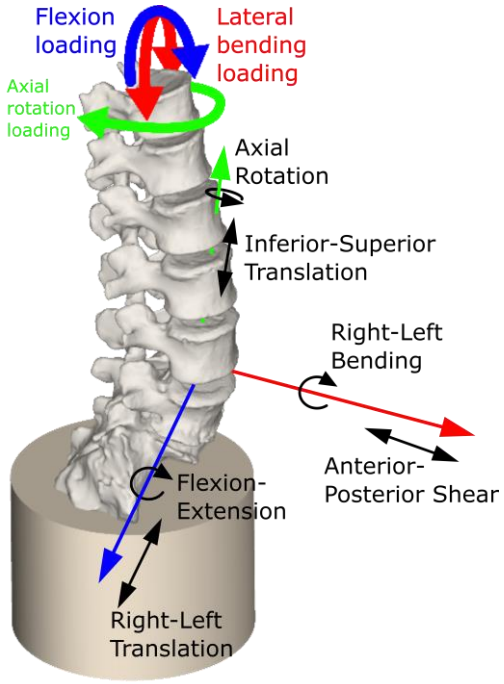

Figure 4.5: Model showing constrained sacrum, the loading conditions applied, and a single joint with the allowed degrees of freedom (others are not shown for clarity but have the same DoF)

The kinematics corresponding to the selected cycle were extracted from the joint kinematic data.

4.2.5. Optimisation

A custom MatLab script and the OpenSim API used these boundary conditions and the models with stiffnesses from literature ($Models_{LitUniStiff}$ and $Models_{LitLvlDepStiff}$) to run forward dynamic simulations within an interior-point optimisation algorithm (*fmincon*). In each loop, the optimisation algorithm optimised the stiffness parameters in all rotational DoF. For the optimisations using $Models_{LitUniStiff}$e uniform stiffness across the joints was maintained, the optimised models are referred to as $Models_{OptimUniStiff}$. For the optimisations using $Models_{LitLvlDepStiff}$ the ratio between the levels was maintained, the optimised models are referred to as $Models_{OptimLvlDepStiff}$. The optimiser sought to minimise the sum of the squared motion tracking error (Eqn. 4.1).

$$\boldsymbol{cf} = \sum_{\boldsymbol{i}=1}^{\boldsymbol{n}} (\boldsymbol{p_i} - \boldsymbol{m_i})^2$$

Eqn. 4.1

Where i was the DoF, and for the corresponding DoF, p_i was the predicted motion, m_i was the measured motion.

Optimisations were performed for each loading condition (lateral bending, axial rotation, and flexion). In all scenarios, all rotational DoF stiffnesses were optimised. The cost function was sensitive to the tracking error of different DoF depending on the loading direction. Therefore, for each loading condition, the cost function only included the predicted motion errors for the DoF to which it was sensitive (Table 4.4). This corresponded to the DoF in which the loading was applied, as in this DoF there was the largest motion. Then the other rotational DoF were included if the measured motion in these DoF was of the same order of magnitude as the largest motion.

Table 4.4: The degrees of freedom used within the cost function for the different loading conditions

Loading Direction	DoF included in the cost function
Left lateral bending	Flexion, lateral bending
Left axial rotation	Flexion, lateral bending, axial rotation
Flexion	Flexion, lateral bending

4.2.6. Validation and analysis of results

A cross-validation was performed for both sets of optimised models ($Models_{OptimUniStiff}$ and $Models_{OptimLvlDepStiff}$) in each loading condition (a total of six cross-validations). In all but one case, this was a five-fold cross-validation, the exception being in axial rotation for $Models_{OptimUniStiff}$ which was a three-fold cross-validation as for two of the models the optimisation was unable to complete. To perform each cross-validation the median stiffness of the subset of optimised models for the specific loading condition was found, with the subset formed from all but one of the models. The median stiffness was applied to the model excluded from the subset. The new model was used in the simulation of that loading condition but without the optimisation routine. This process was repeated for each of the models under that loading condition.

To assess the inter-specimen variability the median and range of the optimised stiffnesses for each specimen in $Models_{OptimUniStiff}$ and $Models_{OptimLvlDepStiff}$ were evaluated. The difference in the prediction accuracy of the specimens and the corresponding cross-validation models were evaluated using the normalised root mean square error (RMSE) of all joint levels in all DoF. To test if the prediction accuracy for any particular model was significantly different to the other models a Kruskal-Wallis was performed by sampling, from each specimen, the error of all the joints in the DoF in which the load was applied. The null hypothesis was rejected for $p<0.05$. This test was performed for $Models_{OptimUniStiff}$ and $Models_{OptimLvlDepStiff}$.

To investigate the importance of accounting for the variation of stiffness between spine levels Kruskal-Wallis were performed to evaluate any statistically significant differences in the errors between joint levels. The errors in the DoF in which the load was applied were used in the test (e.g., under a flexion load, errors in the flexion DoF were analysed) as it was in that direction that the largest motion occurred. The null hypothesis was rejected for $p<0.05$. These tests were performed for $Models_{OptimUniStiff}$ and $Models_{OptimLvlDepStiff}$. Additionally, the RMSE of the joint levels were compared.

To test for statistically significant improvements following the optimisation Wilcoxon signed-rank tests were performed on the kinematic errors for each individual model pre ($Models_{LitUniStiff}$) and post-optimisation ($Models_{OptimUniStiff}$) and then for post-optimisation ($Models_{OptimUniStiff}$) and the validation models. The null hypothesis was rejected for $p<0.05$. A Bonferroni correction was applied to account for the multiple tests [296]. This was repeated for $Models_{LitLvlDepStiff}$ and $Models_{OptimLvlDepStiff}$.

Finally, to analyse the effectiveness of using a ratio to introduce level dependency the RMSE of each specimen in the separate DoF and the overall RMSEs (ie. across all joints and all DoF) of each specimen for $Models_{OptimUniStiff}$ and $Models_{OptimLvlDepStiff}$ are reported and the magnitudes compared. Furthermore, Kruskal-Wallis tests were used to test for statistically significant differences between the errors of the two optimised model sets ($Models_{OptimUniStiff}$ and $Models_{OptimLvlDepStiff}$). The null hypothesis was rejected for $p<0.05$. The samples for the tests consisted of the RMSE in the separate DoF and for the overall RMSE of all models.

4.3. Results

4.3.1. Inter-specimen variability

Optimised stiffnesses

The optimised stiffness ($Models_{OptimUniStiff}$) showed a larger range of optimised stiffnesses in the loading direction than in the directions in which the loading was not applied (Table 4.5). Three loading conditions were considered, a lateral bending load, an axial rotation load, and a flexion load. Considering the optimised stiffness with respect to the initial stiffness: under a lateral bending load the optimised stiffness in lateral bending showed a minimum change of: 5Nm/rad and an average percentage change of 26%; under an axial rotation load the optimised stiffness in axial rotation changed by a minimum of 4Nm/rad with an average percentage change of 14%; and under a flexion load the optimised stiffness in flexion change by a minimum of 11Nm/rad with an average percentage change of 51%. The optimised stiffness in the DoF in which the load was not applied (e.g., the optimised stiffness in flexion when a lateral load was applied) deviated from the initial stiffness less than the optimised stiffness in the DoF which corresponded to the loading direction (e.g., stiffness in lateral bending when a lateral bending load was applied). The largest change from

the initial stiffness to the optimised stiffnesses in the DoF in which the load was not applied was under axial rotation loading (Table 4.8, Table 4.9, Table 4.10).

Although the optimisation algorithm was able to converge for Specimen 5 without any level dependency under lateral bending loads the optimised stiffnesses were the same as the initial stiffnesses. Under axial rotation loads without any level dependency, the optimisation algorithm was unable to converge for specimens 2 and 6.

Table 4.5: Median and range of the optimised stiffnesses without level dependency for each loading direction

Loading direction	Median optimised stiffnesses			Range of optimised stiffnesses		
	Lateral bending, Nm/rad	Axial rotation, Nm/rad	Flexion, Nm/rad	Lateral bending, Nm/rad	Axial rotation, Nm/rad	Flexion, Nm/rad
Lateral bending	82.6	290.8	50.8	43.9	23.5	18.4
Axial rotation	96.9	303.0	52.9	8.0	136.1	125.8
Flexion-extension	69.0	291.5	72.1	20.7	5.4	41.7

Likewise, when level dependency was introduced to the optimisation, large changes in the optimised stiffnesses compared to the initial stiffnesses in the same direction as that in which the loading was applied were seen (Figure 4.10, Figure 4.13, Figure 4.16). In the direction in which the load was not applied the optimised stiffness remained similar to the initial stiffness (Appendix B).

Prediction error

When using the optimised stiffness, the normalised RMSE were reduced for all specimens in all loading conditions, however uniform improvement was not seen (Figure 4.6). Significant differences in prediction accuracy between the specimens were not present for the literature stiffnesses or the optimised stiffnesses but were found for the cross-validation stiffnesses. Therefore, suggesting the cross-validation stiffnesses were suitable for some specimens but even within the small sample sizes a cross-validated stiffness is not always suitable (Figure 4.11, Figure 4.14, Figure 4.17). Considering improvements due to the optimisation the Wilcoxon tests found the optimised stiffnesses resulted in statistically significant differences in the prediction accuracy between the literature and optimised stiffnesses for lateral bending but not in the other loading directions.

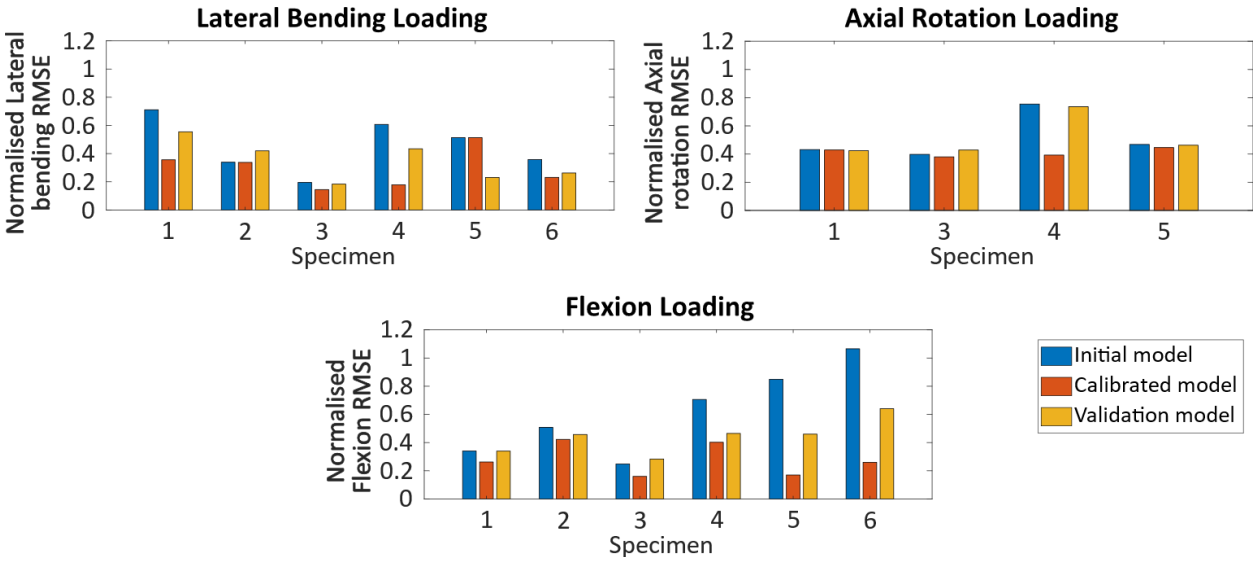

Figure 4.6: Normalised root mean square error (normalised against the experimental motion) for each load condition in the DoF corresponding to the loading direction across all spine levels for each specimen when using the model uniform stiffness across all joints for the literature, optimised, and cross-validation stiffnesses.

When considering all of the specimens, the median of the mean absolute error showed improvements of less than 1° in lateral bending and axial rotation. However, the errors were substantially reduced with the optimised stiffness in flexion (Table 4.6).

Table 4.6: Results from the uniform stiffness models - the medians and interquartile ranges of the mean absolute errors (MAE) of the specimens and the median MAEs as a percentage of the maximum mean absolute motions in each direction when under loading in the same direction.

	MAE in the loading direction, °					
Loading direction	Initial stiffness			Optimised stiffness		
	Median	IQR	% error	Median	IQR	% error
Lateral bending	1.1	0.5	75%	1.1	0.5	74%
Axial rotation	0.3	0.2	50%	0.3	0.2	50%
Flexion	3.2	1.6	44%	1.2	0.7	17%

A similar trend was seen with the introduction of level dependency. Considering the normalised RMSE in the same direction as the loading, optimised stiffnesses resulted in more accurately predicted motion for all specimens (Figure 4.7). However, the Wilcoxon test found statistical significance was not found consistently for any specimen in any direction. The optimisation of the stiffness improved the accuracy of the predicted motion for some specimens more than for others, although the Kruskal-Wallis test found this variation to be statistical significance in the case of axial loading for the cross-validation stiffnesses (Figure 4.12, Figure 4.15, Figure 4.18).

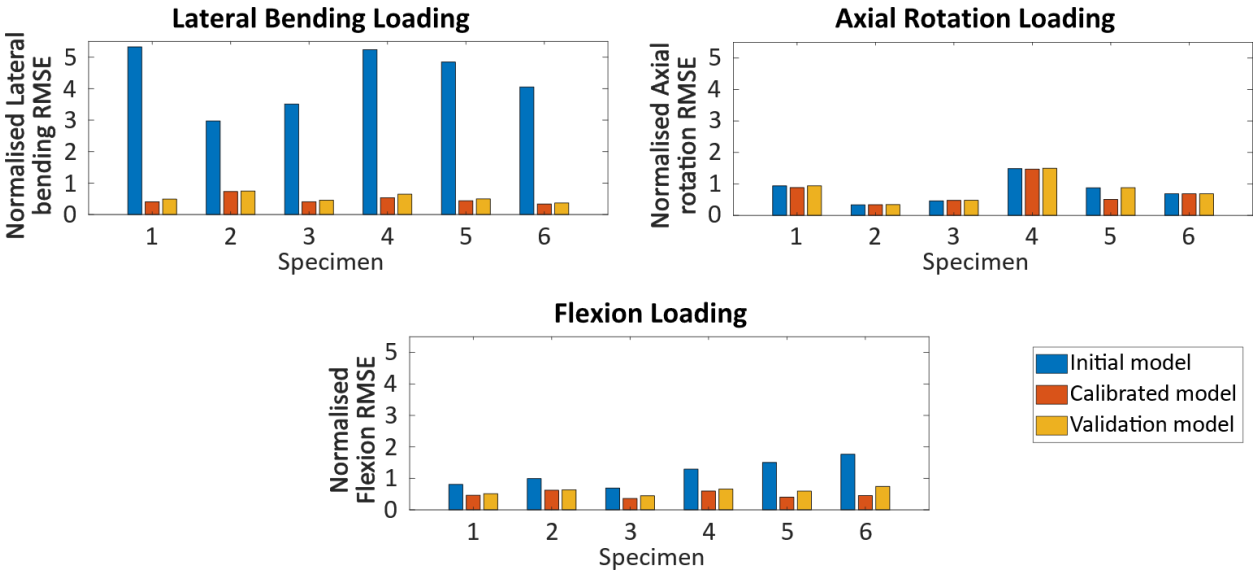

Figure 4.7: Normalised root mean square error (normalised against the experimental motion) for each load condition in the DoF corresponding to the loading direction across all spine levels for each specimen when using the model level-dependent stiffness for the literature, optimised, and cross-validation stiffnesses.

The optimisation of the stiffnesses with level dependency resulted in a greater improvement in the prediction accuracy than the optimised of the stiffness without level dependency (Table 4.6, Table 4.7). However, the prediction errors of the initial stiffness were much larger than those of the stiffnesses without level dependency. With optimised stiffnesses, the median of the mean absolute errors was larger with the introduction of level dependency than with uniform stiffnesses. Notably, the maximum errors tended to be much higher with level-dependent stiffness (Figure 4.12, Figure 4.15, Figure 4.18) than with uniform stiffnesses (Figure 4.11, Figure 4.14, Figure 4.17).

Table 4.7: Results from the level-dependent stiffness models - the medians and interquartile ranges of the mean absolute errors (MAE) of the specimens and the median MAEs as a percentage of the maximum mean absolute motions in each direction when under loading in the same direction.

Loading direction	MAE in the loading direction, °					
	Initial stiffness			Optimised stiffness		
	Median	IQR	% error	Median	IQR	% error
Lateral bending	1.5	1.1	100	1.2	0.6	76
Axial rotation	0.3	0.3	50	0.3	0.2	51
Flexion	5.3	1.6	75	2.4	0.9	33

4.3.2. Variation between spinal levels

Optimised stiffnesses

Under lateral bending loads and flexion loads, a generic stiffness tended to result in prediction errors overpredicting the motion for all levels. With the optimised stiffnesses some levels underpredicted the motion while others overpredicted it without any clear relationship to the spinal level (Figure 4.11, Figure 4.17). Under axial rotation loading (where the motion was smaller than in lateral bending and flexion), some specimens underpredicted the motion across most levels, and others overpredicted at most levels (Figure 4.14).

Prediction error

The prediction errors were considered in terms of the error in the DoF that corresponded to the loading direction (the changes were smaller between the initial stiffness and optimised stiffness in the DoF which were not the same as the loading direction, Appendix C). The predicted error for the models with an optimised stiffness without any level dependency resulted in a normalised RMSE (of the same joint across all specimens) of similar magnitudes for each level (Figure 4.8). Examining each specimen individually, the variation between spine levels in the prediction error for the optimised model without any level dependency showed some specimens had similar prediction errors across all spine levels, while for others the magnitude of the error varied between the spine levels (Figure 4.11, Figure 4.14, Figure 4.17). However, the Kruskal-Wallis tests did not find these differences to be statistically significant.

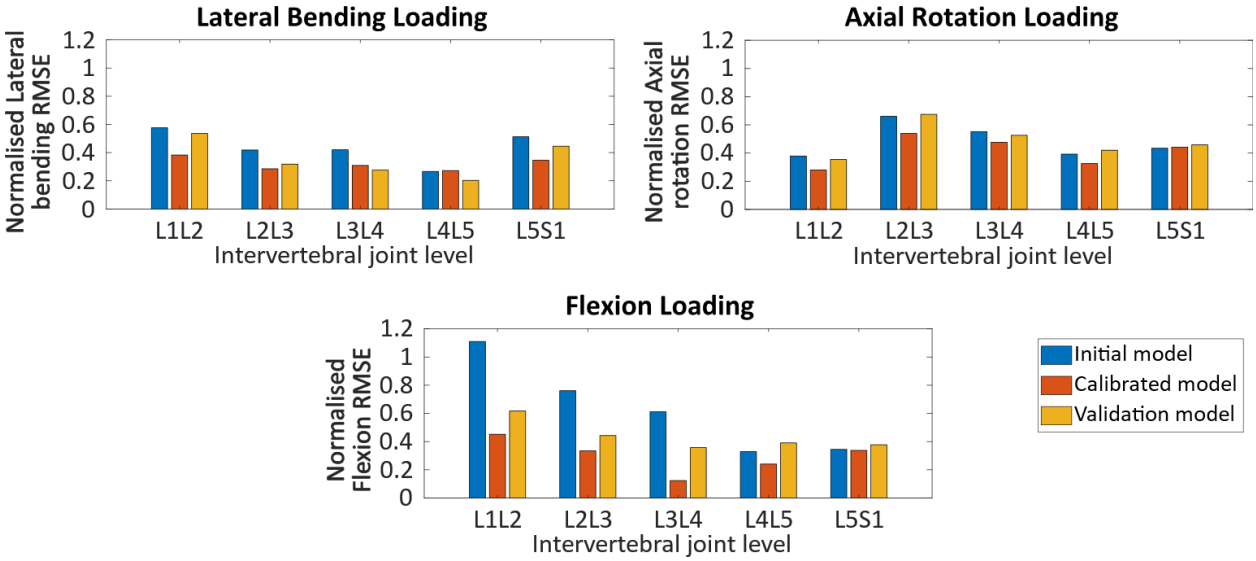

Figure 4.8: Normalised root mean square error (normalised against the experimental motion) for each load condition in the DoF corresponding to the loading direction across all specimens for each joint level when using the model without level dependency for the literature, optimised, and cross-validation stiffnesses.

For the models without the optimised stiffness, the introduction of level dependency via the use of a fixed scaling factor resulted in larger prediction errors at each joint level compared to the results from models without level dependency (Figure 4.8, Figure 4.9). Further, with the optimised stiffness the normalised RMSE was higher with level dependency than without. However, for certain specimens at certain joint levels, the prediction error was smaller compared to models without any level dependency, for example, L3L4 for specimen 6 in the flexion direction under a flexion load (Figure 4.12, Figure 4.15, Figure 4.18). The differences in the errors between levels were also found to be statistically significant.

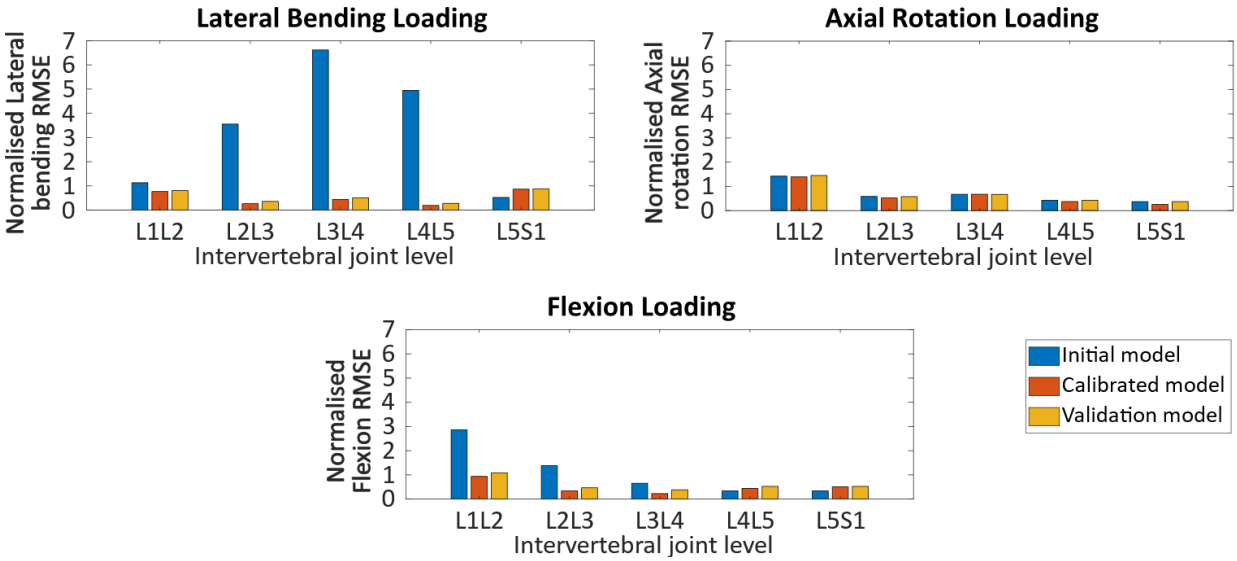

Figure 4.9: The normalised root mean square error (normalised against the mean absolute motion) for each load condition in the DoF corresponding to the loading direction across all specimens for each joint level when using the model with level dependency for the literature, optimised, and cross-validation stiffnesses.

For both the inter-specimen variation and the variation between spinal levels similar trends were observed in the DoF which did not correspond to the loading direction for the prediction errors (Appendix C). Generally, changes in the optimised stiffness and the prediction error were smaller in under axial rotation loading compared to lateral bending loading and flexion loading. Some specimens would be more accurate overall in a particular DoF under a certain loading condition, but they would not necessarily be more accurate in all DoF for that loading condition. The predicted motion was not consistently more accurate in any particular DoF or for any particular spinal level.

4.3.3. Results from lateral bending loads

Predicted stiffnesses

Table 4.8: The first row contains the initial stiffness values taken from the literature. Optimised stiffnesses without level dependency under a lateral bending load for each specimen in each DoF.

Specimen	Lateral bending, Nm/rad	Axial rotation, Nm/rad	Flexion, Nm/rad
Initial	68.8	291	51.0
1	107.0	291.0	49.5
2	63.0	270.0	68.0
3	77.8	293.8	50.7
4	105.5	289.7	50.1
5	68.8	291.1	51.0
6	87.5	291.5	65.1

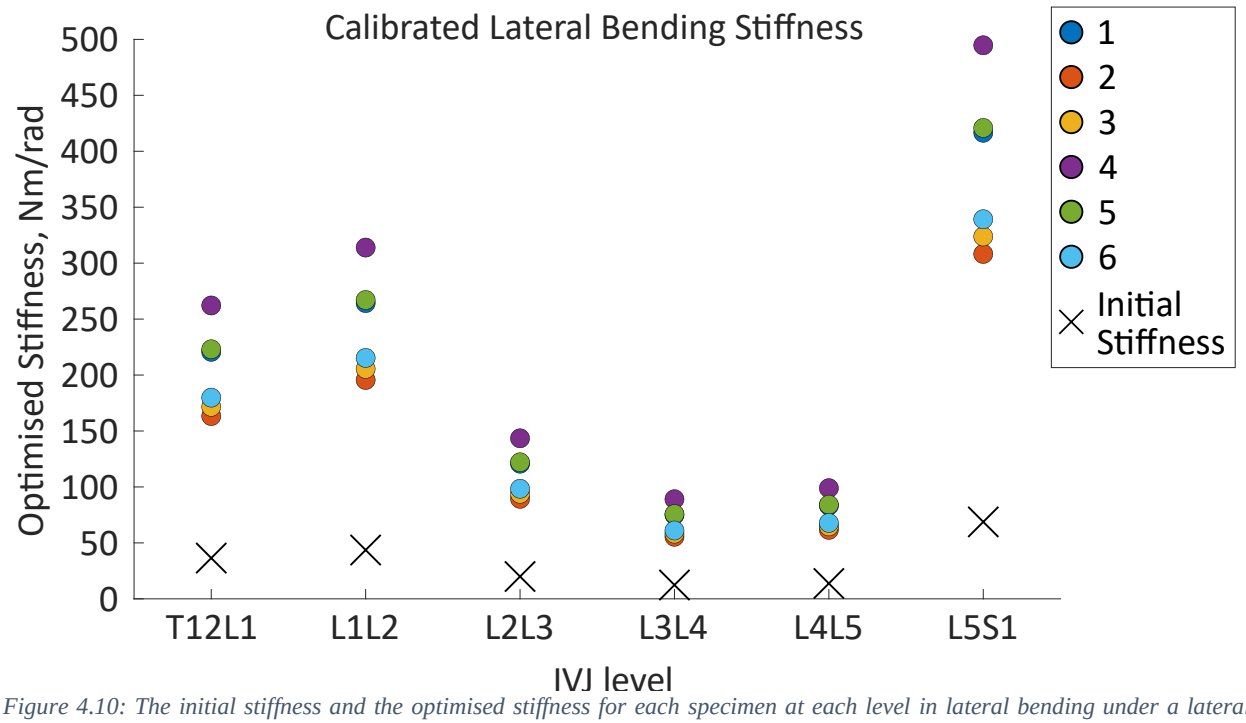

Figure 4.10: The initial stiffness and the optimised stiffness for each specimen at each level in lateral bending under a lateral loading.

Prediction errors

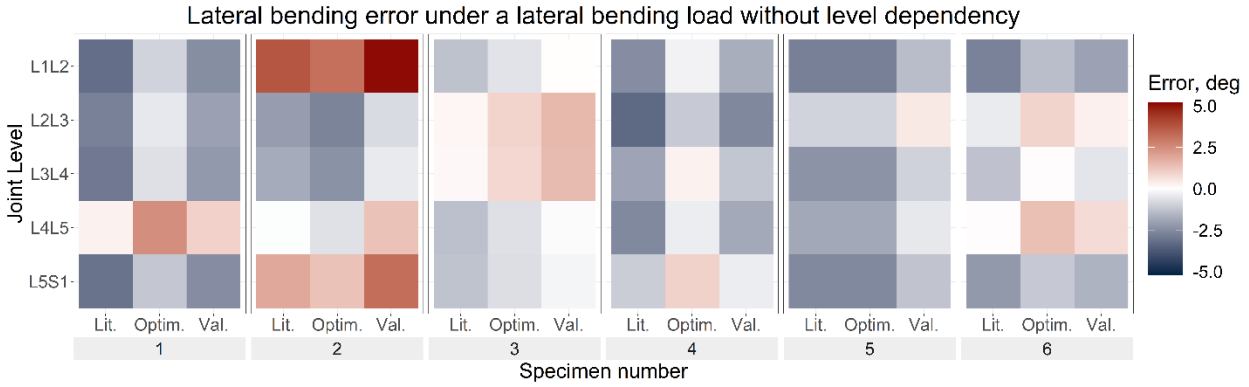

Figure 4.11: Error of the predicted motion in lateral bending under a lateral bending load with uniform stiffnesses for the literature (Lit.), optimised (Optim.) and cross-validation (Val.) stiffnesses. Blue indicates an overprediction of the motion (ie too much bending) while red indicates an underprediction of the motion.

With a uniform stiffness across all spine levels, the Kruskal-Wallis was used to test for significant differences in the prediction error between specimens, significant differences ($p<0.05$) were only found for the cross-validation stiffnesses. The Kruskal-Wallis tested for differences in the prediction error between joint levels. No significant differences ($p>0.05$) were found for the literature stiffnesses, the optimised stiffnesses or the cross-validation stiffnesses.

With a uniform stiffness across all spine levels, the Wilcoxon tests found significant differences ($p<0.05$) between the prediction errors of the models using literature stiffnesses and optimised stiffness for all specimens except specimen 5 (the specimen which remained unchanged following the optimisation). Comparing the predicted errors of the optimised stiffnesses with those of the

cross-valuation stiffnesses significant differences ($p<0.05$) were found for all specimens except specimen 3.

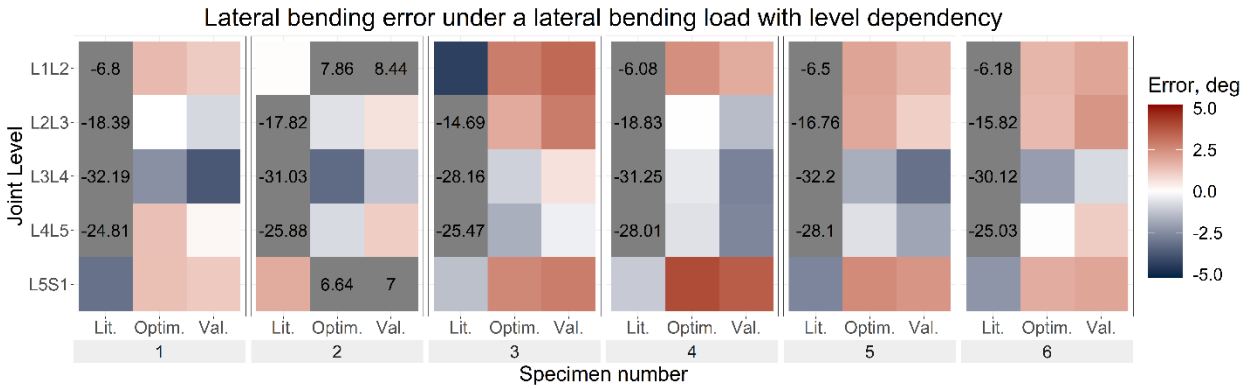

Figure 4.12: Error of the predicted motion in lateral bending under a lateral bending load with level-dependent stiffnesses for the literature (Lit.), optimised (Optim.) and cross-validation (Val.) stiffnesses. Blue indicates an overprediction of the motion (ie too much bending) while red indicates an underprediction of the motion.

With a level-dependent stiffness, the Kruskal-Wallis was used to test for significant differences in the prediction error between specimens, no significant differences ($p>0.05$) were found for any of the three groups of models (literature, optimised, and cross-validation stiffnesses). The Kruskal-Wallis tested for differences in the prediction error between joint levels. Significant differences ($p<0.05$) for the literature stiffnesses, the optimised stiffnesses and the cross-validation stiffnesses were found.

With level-dependent stiffnesses, the Wilcoxon tests found significant differences ($p<0.05$) between the prediction errors of the models using literature stiffnesses and optimised stiffness only for specimen 4. Comparing the predicted errors of the optimised stiffnesses with those of the cross-valuation stiffnesses significant differences ($p<0.05$) were found for all specimens except specimens 1 and 5.

4.3.4. Results from axial rotation loads

Predicted stiffness

Table 4.9: The first row contains the initial stiffness values taken from the literature. Optimised stiffnesses without level dependency under an axial rotation load for each specimen in each DoF, optimisation failed for specimens 2 and 6.

Specimen	Lateral bending, Nm/rad	Axial rotation, Nm/rad	Flexion, Nm/rad
Initial	68.8	291	51.0
1	93.3	295.1	58.5
2	-	-	-
3	99.0	282.7	47.2
4	101.3	418.7	143.8
5	94.9	310.9	18.0
6	-	-	-

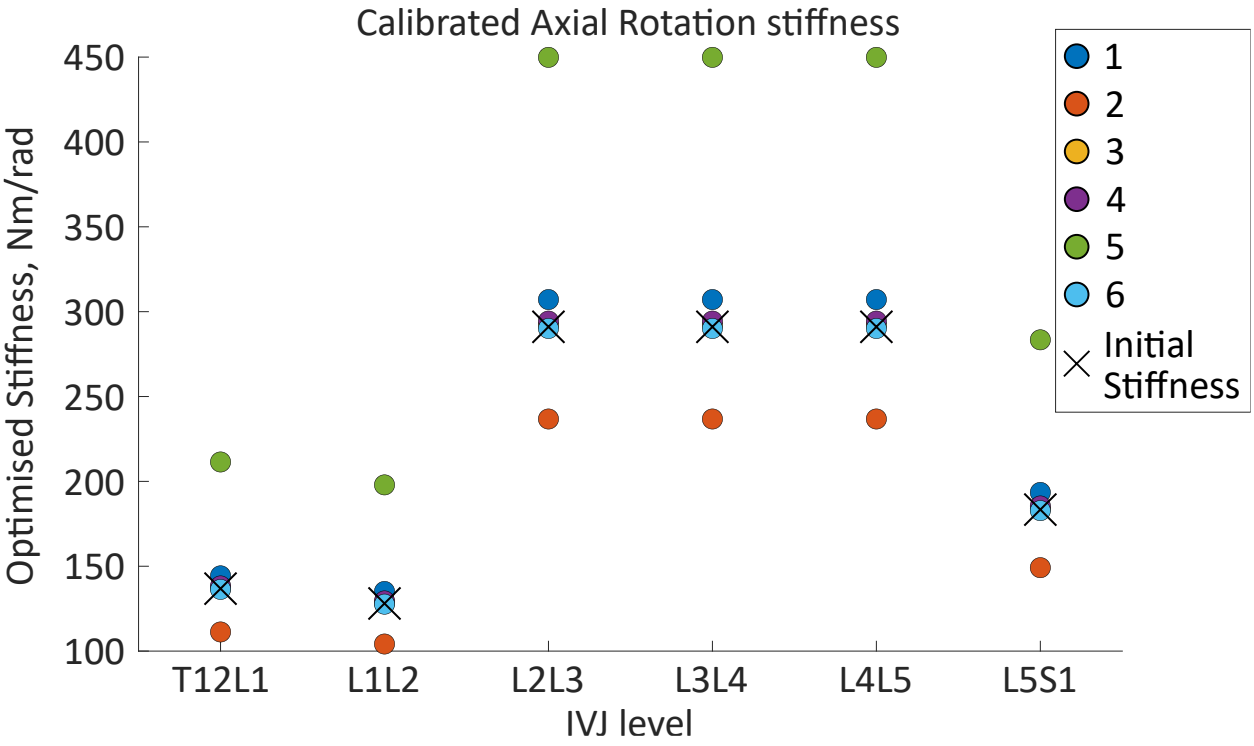

Figure 4.13: The initial stiffness and the optimised stiffness for each specimen at each level in axial rotation under axial rotation loading.

Prediction errors

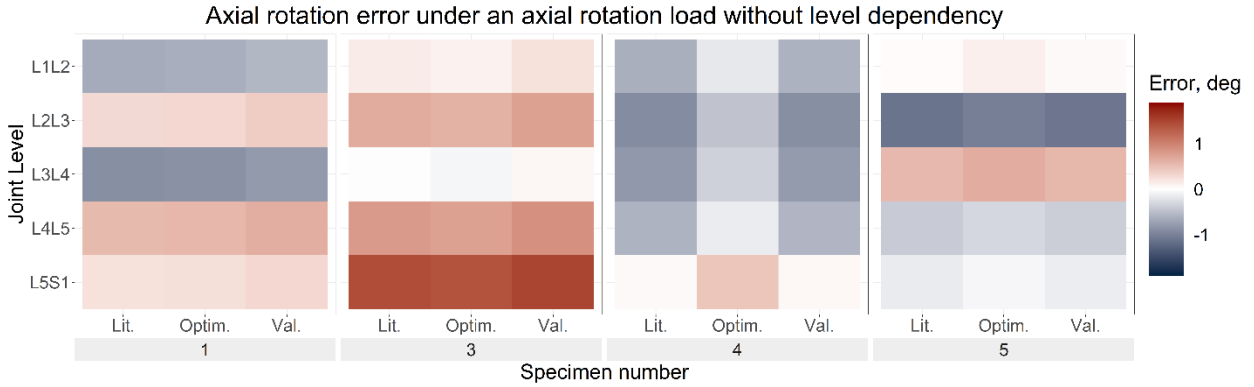

Figure 4.14: Error of the predicted motion in axial rotation under an axial rotation load with uniform stiffnesses for the literature (Lit.), optimised (Optim.) and cross-validation (Val.) stiffnesses. Blue indicates an overprediction of the motion (ie too much bending) while red indicates an underprediction of the motion.

With a uniform stiffness across all spine levels, the Kruskal-Wallis was used to test for significant differences in the prediction error between specimens, significant differences ($p<0.05$) were only found for the cross-validation stiffnesses. The Kruskal-Wallis tested for differences in the prediction error between joint levels. No significant differences ($p>0.05$) for the literature stiffnesses, the optimised stiffnesses or the cross-validation stiffnesses were found.

With a uniform stiffness across all spine levels, the Wilcoxon tests found no significant differences ($p>0.05$) between the prediction errors for any of the models using literature stiffnesses and optimised stiffness or between the optimised stiffness and cross-validation stiffness models.

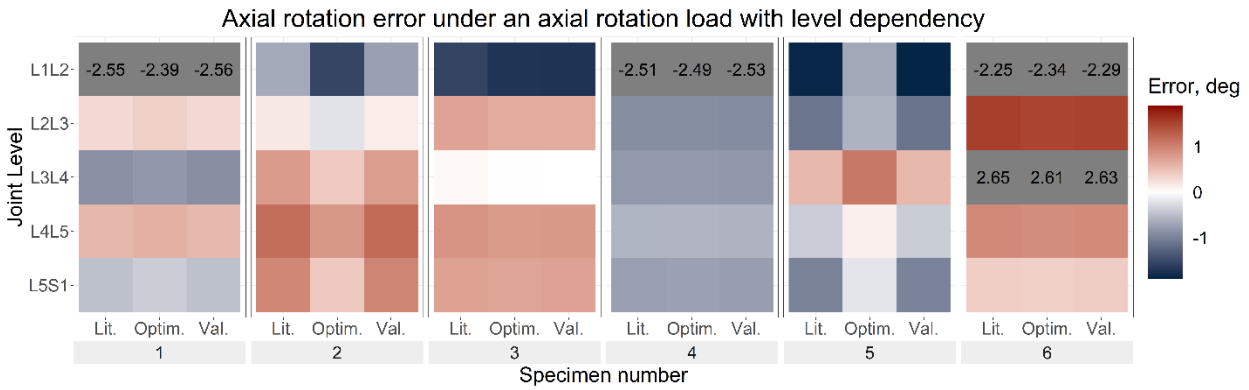

Figure 4.15: Error of the predicted motion in axial rotation under an axial rotation load with level-dependent stiffnesses for the literature (Lit.), optimised (Optim.) and cross-validation (Val.) stiffnesses. Blue indicates an overprediction of the motion (ie too much bending) while red indicates an underprediction of the motion.

With a level-dependent stiffness, the Kruskal-Wallis was used to test for significant differences in the prediction error between specimens, no significant differences ($p>0.05$) were found for any of the three groups of models (literature, optimised, and cross-validation stiffnesses). The Kruskal-Wallis tested for differences in the prediction error between joint levels. Significant differences ($p<0.05$) for the literature stiffnesses, the optimised stiffnesses and the cross-validation stiffnesses were found.

With level-dependent stiffnesses, the Wilcoxon tests found significant differences ($p<0.05$) in the prediction errors only for specimen 2 when comparing the literature and optimised stiffnesses and the optimised and cross-validation stiffnesses. No statistically significant differences were found for any of the other specimens.

4.3.5. Results from flexion loads

Predicted stiffnesses

Table 4.10: The first row contains the initial stiffness values taken from the literature. Optimised stiffnesses without level dependency under a flexion load for each specimen in each DoF.

Specimen	Lateral bending, Nm/rad	Axial rotation, Nm/rad	Flexion, Nm/rad
Initial	68.8	291	51.0
1	69.4	291.1	61.9
2	79.8	296.4	65.2
3	67.3	291.0	60.5
4	70.5	291.3	79.0
5	59.1	292.7	94.2
6	68.6	291.7	102.2

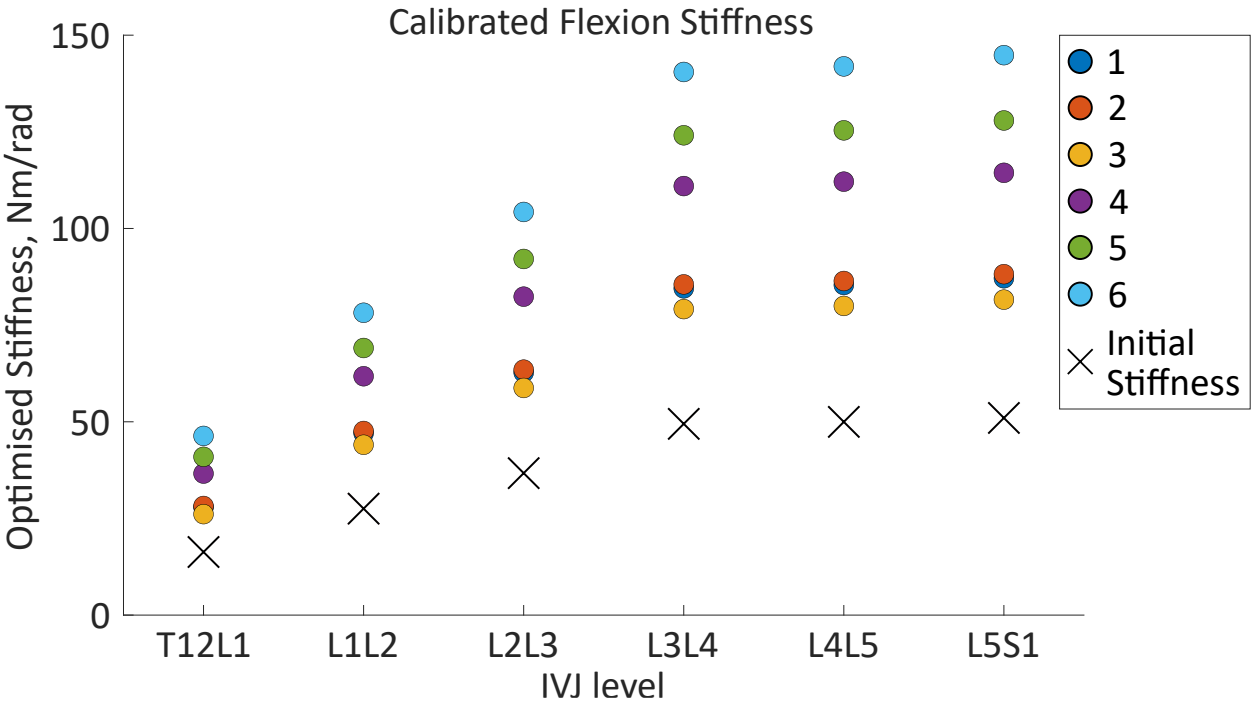

Figure 4.16: The initial stiffness and the optimised stiffness for each specimen at each level in flexion under flexion loading

Prediction errors

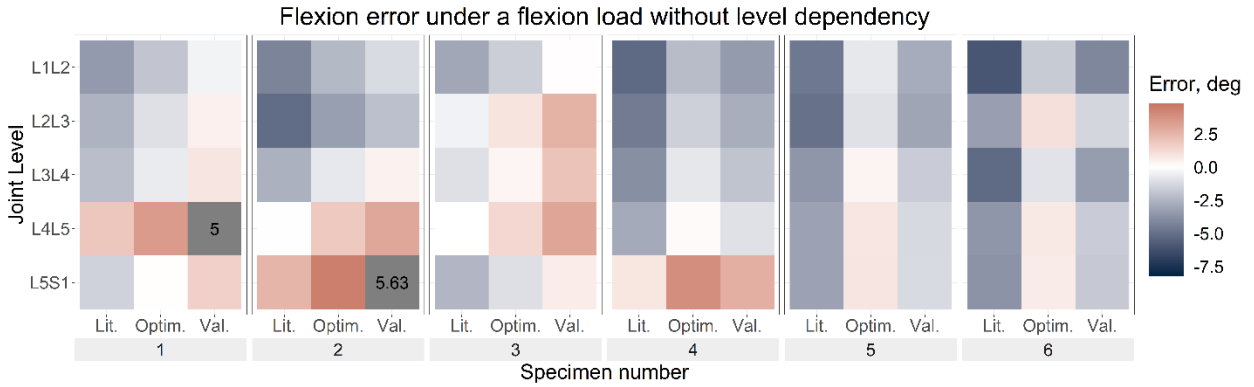

Figure 4.17: Error of the predicted motion in flexion under a flexion load with uniform stiffnesses for the literature (Lit.), optimised (Optim.) and cross-validation (Val.) stiffnesses. Blue indicates an overprediction of the motion (ie too much bending) while red indicates an underprediction of the motion.

With a uniform stiffness across all spine levels, the Kruskal-Wallis was used to test for significant differences in the prediction error between specimens, significant differences ($p<0.05$) were found for the literature and cross-validation stiffnesses but not the optimised stiffnesses. The Kruskal-Wallis tested for differences in the prediction error between joint levels. Significant differences ($p<0.05$) for the literature stiffnesses and the optimised stiffnesses were found but not for the cross-validation stiffnesses.

With a uniform stiffness across all spine levels, the Wilcoxon tests found significant differences ($p<0.05$) between the prediction errors only for specimen 2 when comparing the literature and optimised stiffness models. No other significant differences were found.

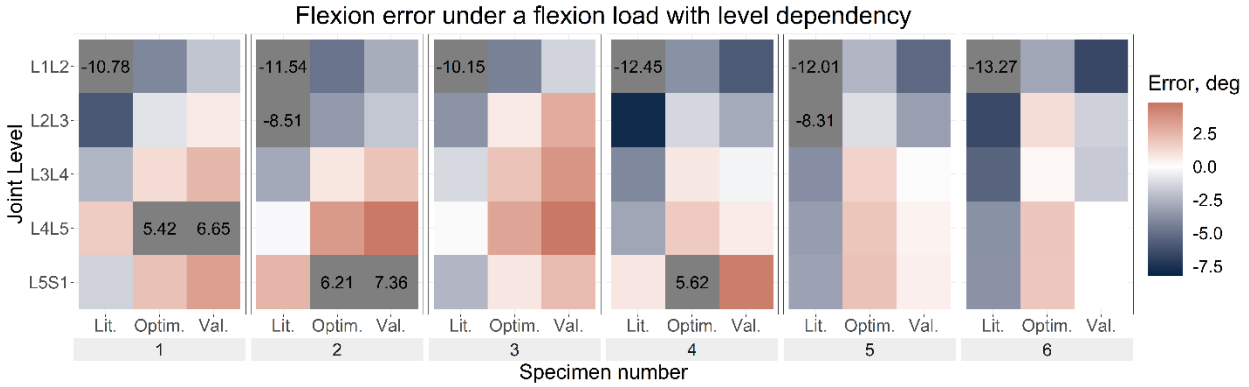

Figure 4.18: Error of the predicted motion in flexion under a flexion load with level-dependent stiffnesses for the literature (Lit.), optimised (Optim.) and cross-validation (Val.) stiffnesses. Blue indicates an overprediction of the motion (ie too much bending) while red indicates an underprediction of the motion.

With a level-dependent stiffness, the Kruskal-Wallis was used to test for significant differences in the prediction error between specimens, no significant differences ($p>0.05$) were found for any of the three groups of models (literature, optimised, and cross-validation stiffnesses). The Kruskal-Wallis tested for differences in the prediction error between joint levels. Significant differences ($p<0.05$) for the literature stiffnesses, the optimised stiffnesses and the cross-validation stiffnesses were found.

With level-dependent stiffnesses, the Wilcoxon tests found significant differences ($p<0.05$) between the prediction errors for specimen 5 when comparing the literature and optimised stiffness models. No other significant differences were found.

4.3.6. Comparison of uniform and level-dependent approaches

The introduction of level-dependent stiffnesses with a ratio resulted in a higher optimised stiffness across most levels compared to the optimised stiffness with a uniform stiffness across all levels (Table 4.11). The IQR was larger for $Models_{OptimUniStiff}$ than the IQR of $Models_{OptimLvlDepStiff}$ at the central levels (L2L, L3L4, and L4L5) in lateral bending, at all levels in axial rotation and at levels L1L2 and L2L3 in flexion (Table 4.11).

Table 4.11: A comparison of the median (and interquartile range) of the optimised stiffnesses in the same DoF as the loading direction. A single stiffness is reported for models with a uniform stiffness across the IVJs and for the level-dependent models the stiffnesses at each level are reported.

Loading & Stiffness direction	Median and IQR of optimized stiffnesses, Nm/rad					
	$Models_{OptimUniStiff}$	$Models_{OptimLvlDepStiff}$				
		L1L2	L2L3	L3L4	L4L5	L5S1
Lateral	83 (37)	240 (62)	110 (28)	68 (17)	76 (19)	378 (97)
Axial	303 (76)	129 (7)	293 (17)	293 (17)	293 (17)	185 (11)
Flexion	72 (32)	55 (22)	73 (29)	98 (40)	99 (40)	101 (41)

In all loading conditions for all specimens (except for specimen 5 under lateral bending) the RMSE error was larger for the optimised stiffness models which included level dependency ($Models_{OptimLvlDepStiff}$) than for the models with uniform stiffnesses across the IVJ ($Models_{OptimUniStiff}$) (Table 4.12, Table 4.13, Table 4.14).

Table 4.12: The root mean square errors under lateral bending loading for each specimen (errors across all joints and in all DoF) for the two different methods used to represent the joint stiffness.

Specimen	RMSE for $Models_{OptimUniStiff}$, deg	RMSE for $Models_{OptimLvlDepStiff}$, deg
1	1.50	1.59
2	1.97	3.32
3	1.29	1.80
4	1.35	1.85
5	1.61	1.48
6	1.36	1.61

Table 4.13: The root mean square errors under axial rotation loading for each specimen (errors across all joints and in all DoF) for the two different methods used to represent the joint stiffness.

Specimen	RMSE for $Models_{OptimUniStiff}$, deg	RMSE for $Models_{OptimLvlDepStiff}$, deg
1	1.24	1.41
3	0.77	1.03
4	0.33	0.84
5	0.87	1.04

Table 4.14: The root mean square errors under flexion loading for each specimen (errors across all joints and in all DoF) for the two different methods used to represent the joint stiffness.

Specimen	RMSE for $Models_{OptimUniStiff}$, deg	RMSE for $Models_{OptimLvlDepStiff}$, deg
1	1.34	2.04
2	2.03	2.70
3	1.01	1.64
4	1.47	2.04
5	0.59	1.19
6	0.84	1.51

As can be seen through a visual analysis of the RMSE across each specimen the Models$_{OptimUniStiff}$ predicted the kinematics less accurately than Models$_{OptimLvlDepStiff}$ (Figure 4.18, Figure 4.19, Figure 4.20). The RMSE is higher in the DoF in which the model was being loaded.

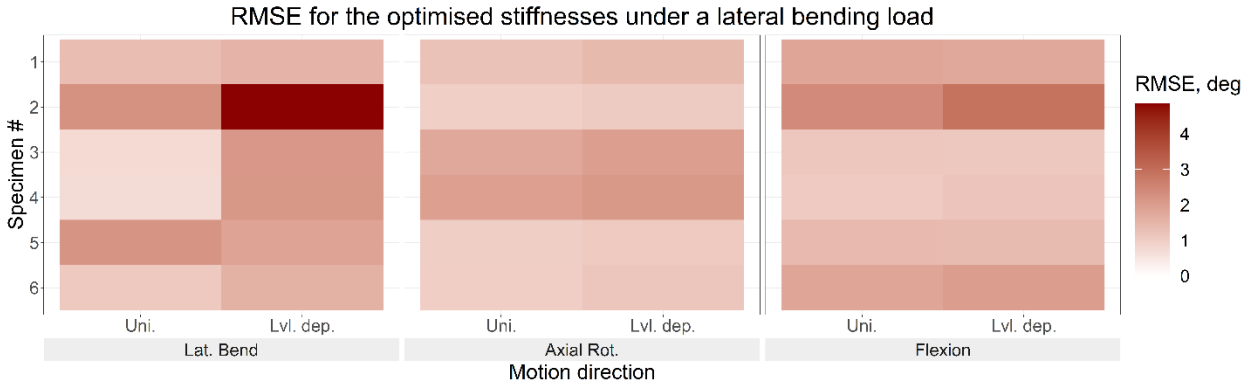

Figure 4.19: The root mean square error of each specimen using the optimised stiffness in each direction using the uniform and level-dependent stiffness under a lateral bending load.

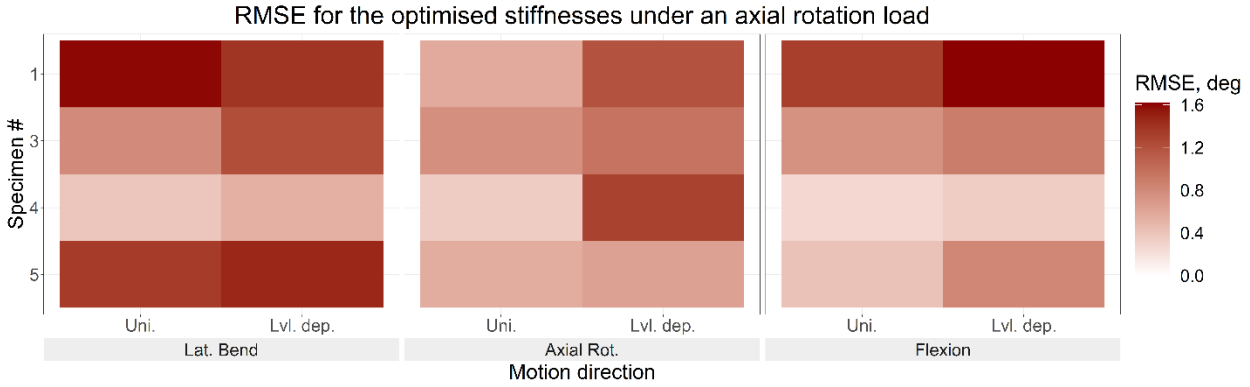

Figure 4.20: The root mean square error of each specimen using the optimised stiffness in each direction using the uniform and level-dependent stiffness under an axial rotation load.

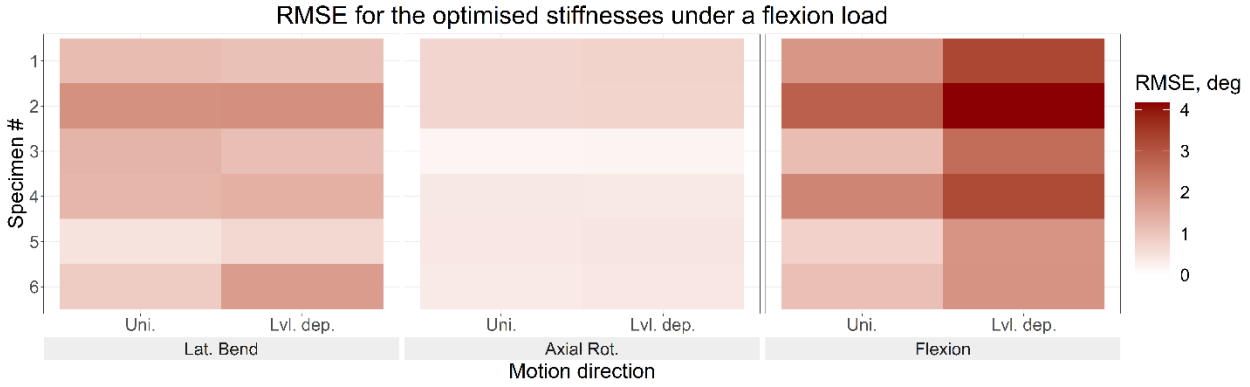

Figure 4.21: The root mean square error of each specimen using the optimised stiffness in each direction using the uniform and level-dependent stiffness under a flexion load.

Despite the errors for both methods being substantial, the differences in the predicted error were only statistically significant in axial rotation under axial rotation loading, in flexion under flexion loading, and overall under flexion loading (Table 4.15).

Table 4.15: Results from the Kruskal-Wallis test comparing the error in each direction and overall between the uniform and level-dependent models under each loading condition. For $p<0.05$ the H values and the critical H values (H_c) are also reported, for a result to be statistically significant $p<0.05$ and $H>H_c$.

Loading Direction	Motion Direction			
	Lateral	Axial	Flexion	Overall RMSE
Lateral	p>0.05	p>0.05	p>0.05	p>0.05
Axial	p>0.05	p = 0.04, H = 4.1, H_c = 6.0	p>0.05	p>0.05
Flexion	p>0.05	p>0.05	p = 0.04 H = 4.3, H_c = 6.0	p = 0.04, H = 4.3, H_c = 6.0

4.4. Discussion

This study aimed to investigate the inter-subject variation and the difference between spinal levels under different loading conditions. Six specimen-specific models were constructed, and for each specimen left lateral bending, left axial rotation, and flexion experiments were simulated. The IVJ stiffness was optimised with an optimisation algorithm which minimised the predicted motion error. The optimisation was performed for two conditions: without any level dependency, and with level dependency (implemented as a fixed ratio between the levels).

Within the general population, a large variation of intervertebral joint stiffness is expected between individuals. Optimising stiffnesses using the tracking error reflected this, as a wide range of optimised stiffnesses were calculated. These stiffnesses fell within the range of experimentally reported stiffnesses [288,307–309]. This implies this optimisation approach was effective at identifying specimen-specific stiffnesses and is able to capture the inter-specimen differences.

The inter-specimen variation of the stiffnesses was reflected in the uniform stiffness models and the level-dependent stiffness models as a wide range of stiffnesses were predicted for both (Table 4.5, Table 4.11, Figure 4.10, Figure 4.13, Figure 4.16). For the uniform stiffness models, the optimisation was averaging out the errors across the spine, thus the resulting stiffness represents an overall spinal stiffness for each specimen in each loading condition. Analysing the kinematic prediction errors, resulted in similar errors across all spine levels. Despite this simplification, substantial improvements were seen between the literature and optimised stiffnesses for each specimen (Figure 4.6), with the improvement even being statistically significant for some specimens (Figure 4.11, Figure 4.14, Figure 4.17). Similarly, when using level-dependent stiffnesses the optimiser was attempting to average out the errors across the levels; however, a fixed ratio defines the distribution of the stiffnesses across the joint levels. The level-dependent models with optimised stiffnesses predicted substantially smaller tracking errors (Figure 4.7). This supports the findings of the study by Wang *et al.* [126]; that specimen-specific stiffness plays an important role in the accuracy of predictive spinal simulations. Therefore, given the inter-specimen stiffness variation found and the resulting effect of the specimen-specific on the kinematic errors, whether level-dependent stiffnesses or uniform (overall spinal) stiffnesses are used the stiffnesses should be specimen or subject-specific in order to accurately predict the kinematics. Furthermore, the cross-validation models had higher kinematic errors than all the optimised models and also than some of the literature models. This further supports the need for specimen or subject-specific

properties. However, the kinematic accuracy varied between specimens following the identification of an optimised stiffness other factors may need to be considered, such as joint pose [72,114] and cost function sensitivity to obtain accurate optimisations and simulations.

Considering the influence of the loading conditions, the predicted stiffnesses varied greatly for the different loading conditions. The stiffnesses were optimised simultaneously in all three rotational DoF for each loading condition. This is necessary as the spine exhibits coupled behaviour [312]. The study by Meng *et al.* found that either coupled or uncoupled stiffnesses could represent the spinal properties however coupled and uncoupled stiffnesses should not be used interchangeably [107]. The modelling approach in the present study represented the spinal stiffness as uncoupled. Therefore, the variation in optimised stiffness due to different loading conditions indicates that when modelling the IVJ stiffness as uncoupled it should not only be specimen-specific but also specific to the loading conditions.

The uncoupled representation limited the accuracy of the models in the DoF in which the load was not applied. Although the stiffnesses were optimised in these DoF they did not change much relative to the literature values (Table 4.8, Table 4.9, Table 4.10). This could be due to the motion being smaller in the unloaded directions, thus reducing the sensitivity of the cost function to these directions. Consequently, the kinematic errors in the DoF in which the load was not applied were similar to the literature and optimised models. Therefore, future research could address this limitation by either introducing coupling terms or by identifying a cost function that results in a better representation of the spinal in the DoF in which the load is not applied.

The extent of the motion is largely dependent on the IVJ stiffness, which has been reported to vary between spine levels [8,289]. The initial stiffnesses were based on literature data for the L3L4 IVJ level, yet the errors at the L3L4 IVJ level were comparable to the errors at the other levels when looking at the generic stiffnesses ($Models_{LitUniStiff}$). This suggests that using a generic but level-dependent stiffness may not offer any improvement over a generic uniform stiffness in the prediction accuracy. The optimisation of the uniform stiffnesses across spinal levels ($Models_{OptimUniStiff}$) showed similar errors at all spinal levels for some specimens while for other specimens there were low errors at some levels and high errors at others, although statistically significant differences were not found. This suggests a variation in the difference of the stiffness between spinal levels by specimen, implying some specimens exhibit higher level dependency than others. The presence of higher errors at some levels indicates the need for optimisation to account for differences in stiffnesses between spine levels.

The need to account for differences between spine levels is highlighted by some of the optimised level-dependent models resulting in highly accurate predicted motion (errors <0.1°). However, for most cases at the individual IVJ levels, the predicted errors were higher for the level-dependent models than for the uniform stiffness models. Examining the average errors across all spinal levels showed all the level-dependent models performed more poorly than the uniform stiffness models. This held for both the literature stiffnesses and the optimised stiffnesses ($Models_{OptimUniStiff}$ vs $Models_{OptimLvlDepStiff,}$ Table 4.12, Table 4.13, Table 4.14). Therefore, the introduction of level dependency via a fixed scaling factor is not suitable. However, this could also be due to the specific scaling factors used. The scaling factors were calculated from data presented in the meta-analysis by Zhang *et al.* [109] (maximum rotations without a compressive preload), and the moments reported were higher than the moments used in the experiments the current study simulated. Therefore, if a ratio is used to describe the variation of the stiffness between levels, it needs to be calibrated for the loading conditions.

The present study was limited by using a generic ratio to introduce a level dependency, this was done to reduce computational expense. The optimisation had a cardinality of three, had subject-specific level dependency been introduced the cardinality would have increased to 18 (three DoF per IVJ level), which would likely have resulted in much longer simulation times. Additionally, the simulations were not dynamic and did not attempt to account for the non-linearity of the disc stiffness. Given the low loading rate and the high computational expense of running fully dynamic simulations with non-linear stiffnesses, this seems to be a justifiable simplification. However, an avenue for future research would be to identify more efficient optimisation techniques, for example investigating the use of static optimisation. This study did not seek to optimise the stiffnesses in the translational DoF as the dataset contained the rotation of the vertebrae but not the translations. However, doing so would allow for a more complete characterization of the IVJ. Finally, the data used was not collected with the intention of simulating the experiments, therefore the X-rays were taken for qualitative purposes. Therefore, as the registration was based on the X-ray image, the accuracy could only be assessed qualitatively, potentially resulting in joint pose errors.

In conclusion, this study has shown that optimisation of the intervertebral joint stiffness can characterise the expected inter-specimen variability and result in more accurate motion prediction. Using a generic ratio to account for the difference of stiffnesses between spine levels results in inaccurate predicted motion, therefore specimen or subject-specific level dependency should be used to achieve more accurate predictions. Finally, the optimised stiffnesses vary widely depending on the loading direction, therefore an optimised stiffness should not only be considered specimen-specific but also load-specific.

4.5. Appendix A

The registration of the CT scan to the X-ray can be considered in two distinct steps. First, the pre-processing of the CT data, followed by the registration of the CT data to the experimental position.

Pre-processing of CT data
Outputs:

1. A virtual palpation marker set for defining the sagittal plane of the CT scan.
2. A virtual palpation marker set for defining intervertebral joints.
3. A virtual palpation marker set for defining the endplate angles.
4. Segmented specimen

Steps:

1. Perform a virtual palpation of the marker set to define the sagittal plane of the CT scan. On the CT scan, virtually palpate the posterior-most part of the spinous process, and the anterior-most part of the superior and inferior endplates of each vertebra and the most inferior part of the sacrum and the process of S1, S2, S3, and apex of the coccyx (Figure 4.22).

Figure 4.22: Virtual palpation of the marker set to define the sagittal plane of the CT scan.

2. Fit a plane to these points based on the least squares normal distance and calculate the necessary rotations to align the plane with the vertical.
3. Apply these rotations to the CT scan (this can be done in Mimics for example with the Reslice tool)
4. Segment the vertebrae and sacrum in the CT scan (Figure 4.23).
5. Perform virtual palpation for the joint markers and the endplate angles (Figure 4.23).

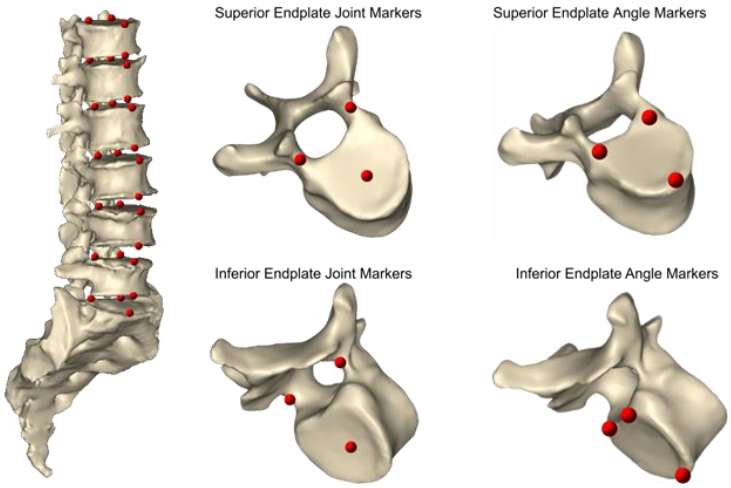

Figure 4.23: Left – Segmented specimen with markers for calculating the endplate angle. Centre – Exploded view of markers for defining the joint pose. Right – Exploded view of markers for defining the endplate angle.

CT data registration to the X-ray

1. Perform a virtual palpation on the X-ray and calculate the endplate angles (Figure 4.24).

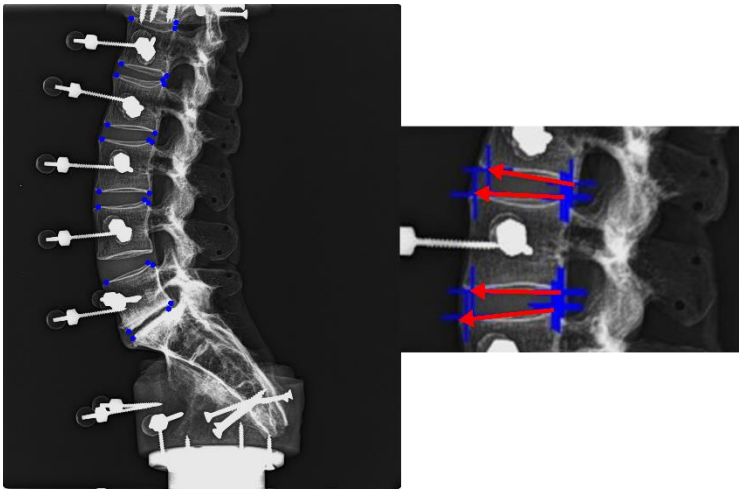

Figure 4.24: Left - Virtual palpation of the endplate on the X-ray and calculation of the endplate angles. Right – determining the endplate angles.

2. Move the CT scan and X-ray into a common reference system based on the sacral slope. Find the rotation to align the sacral slope of the CT to the X-ray and apply to all the markers in the CT scan (Figure 4.25).

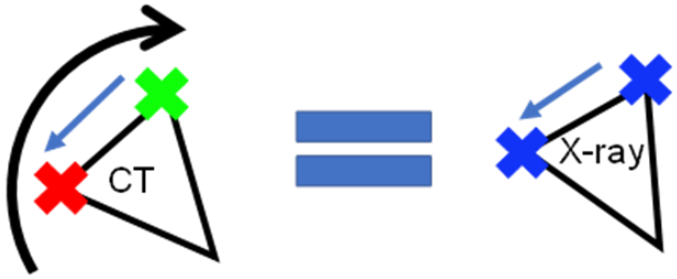

Figure 4.25: Representation of finding the rotations to align the sacrum in the CT scan with the sacrum in the X-ray.

3. Scale the X-ray to the CT scan based on the average Euclidean distances of each vertebra's body height and width.
4. Calculate the endplate angles on the CT scan and the rotation matrix to rotate the CT endplate angles to the X-ray endplate angles.
5. Using endplates angle markers calculate the centre of the vertebrae and the translations to move the CT vertebrae centres onto the X-ray vertebrae centres.
6. Form the transformation matrix for each vertebra from the translations and rotations and apply to the virtual palpation markers on the CT scan and the segmented geometries.

4.6. Appendix B

Plots of the optimised stiffnesses for the level-dependent models in the unloaded directions for each of the different loading conditions.

4.6.1. Lateral loading

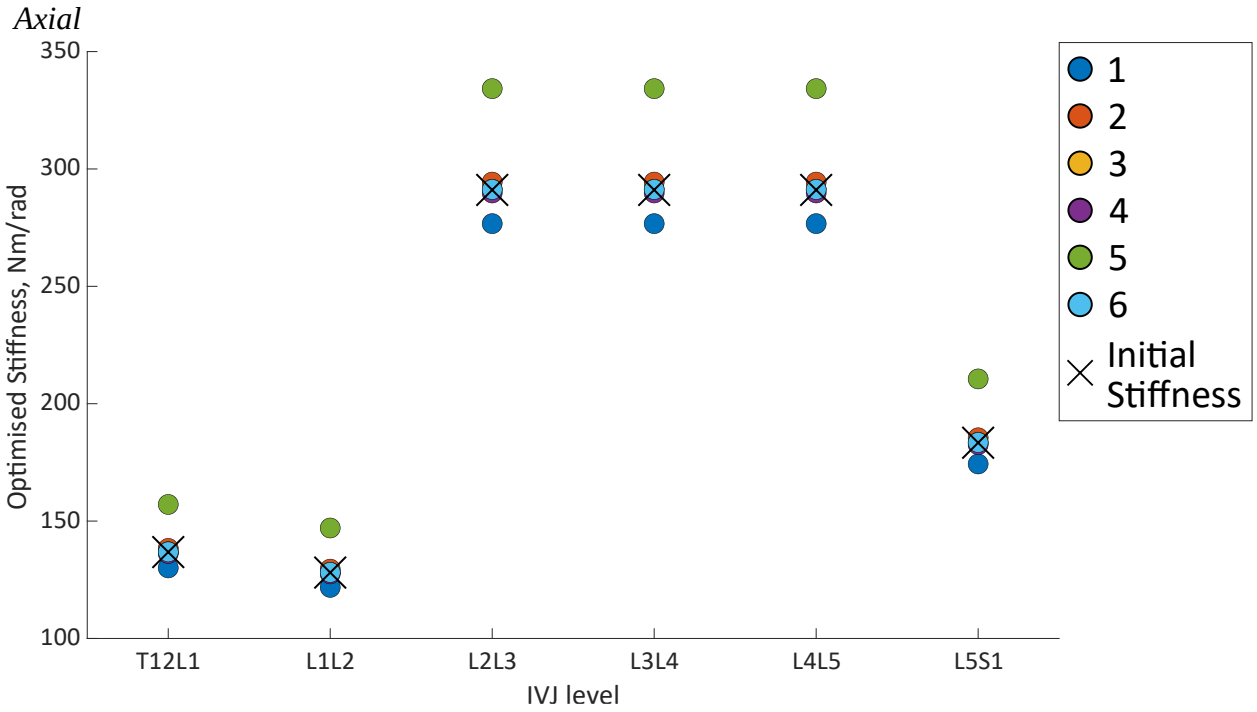

Figure 4.26: Optimised stiffness in axial rotation for the level-dependent models under a lateral bending load.

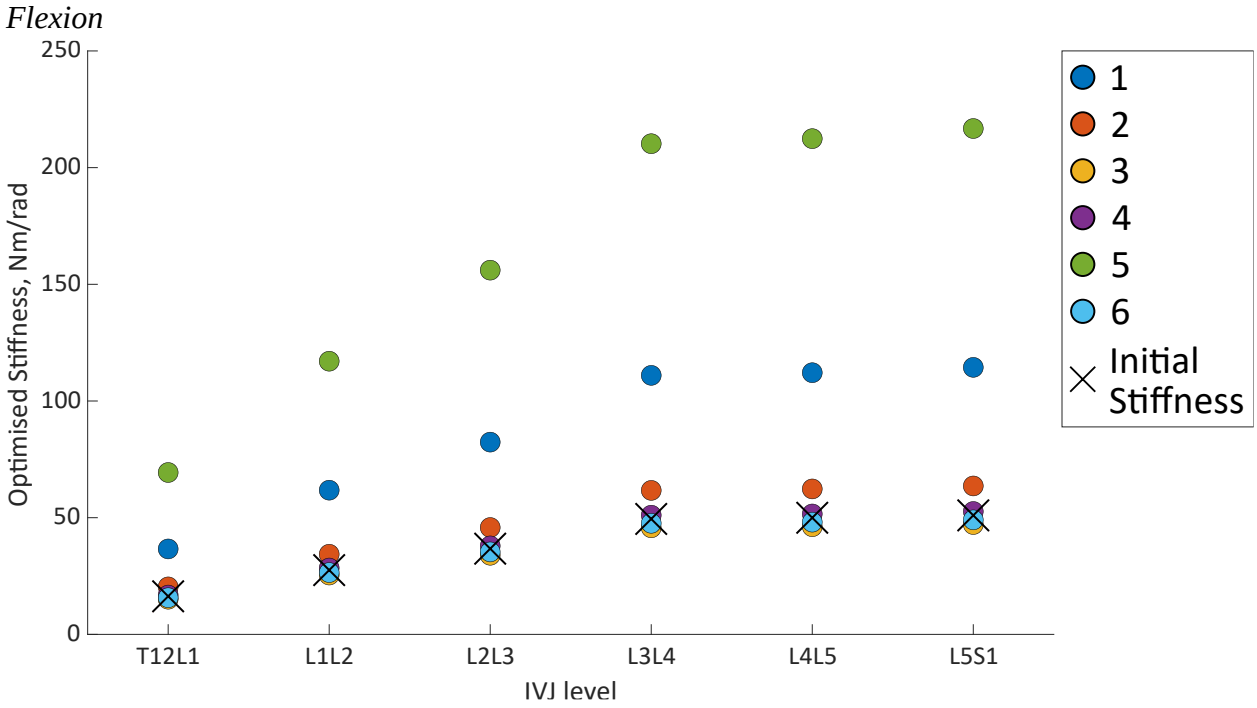

Figure 4.27: Optimised stiffness in flexion-extension for the level-dependent models under a lateral bending load.

4.6.2. Axial Loading

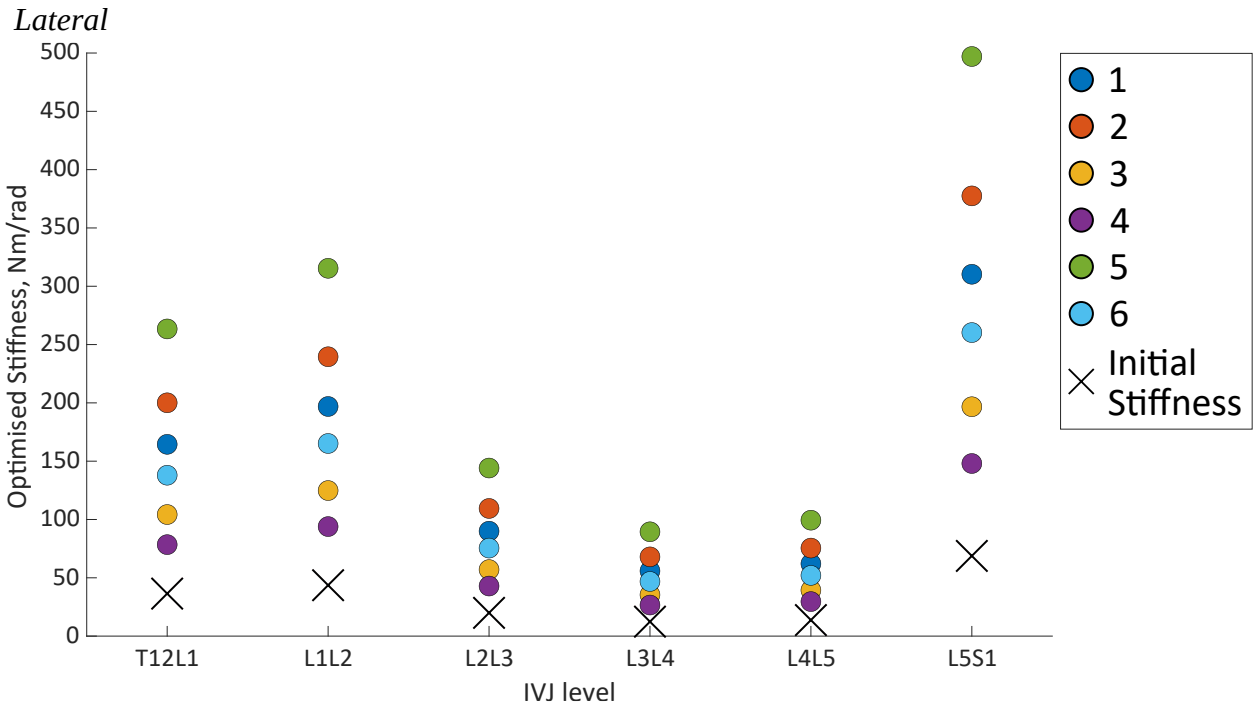

Figure 4.28: Optimised stiffness in lateral bending for the level-dependent models under an axial rotation load.

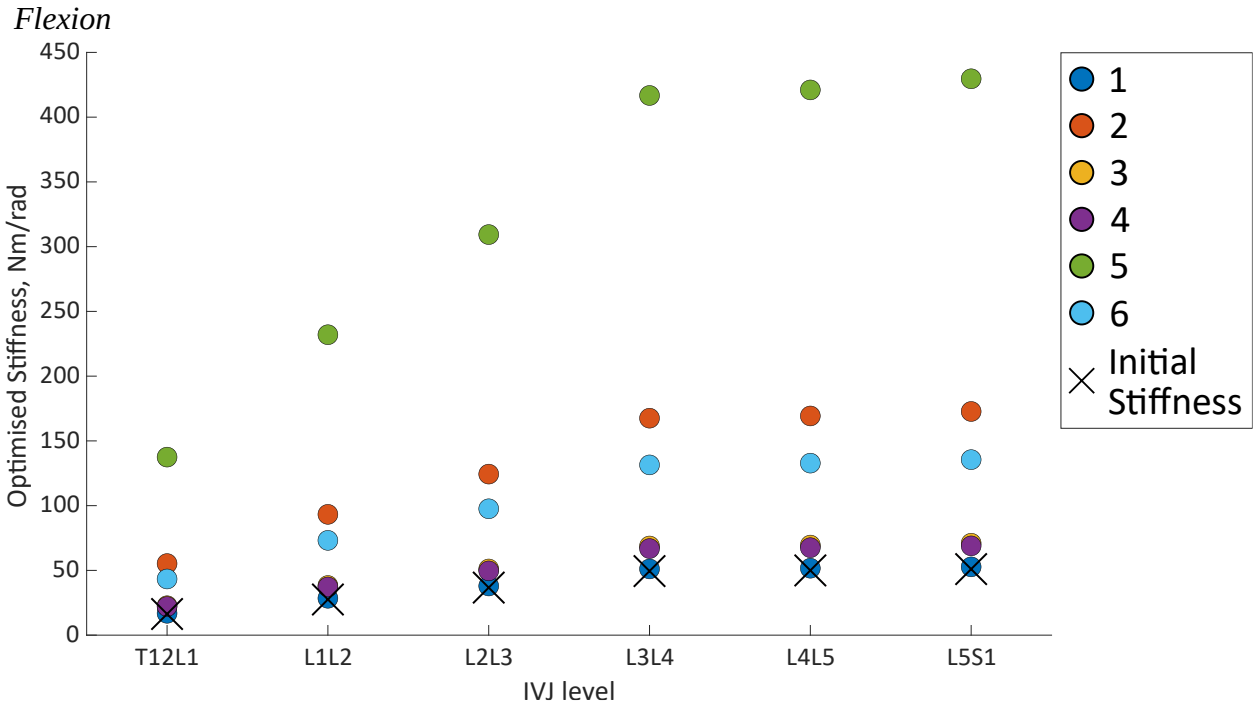

Figure 4.29: Optimised stiffness in flexion-extension for the level-dependent models under an axial rotation load.

4.6.3. Flexion loading

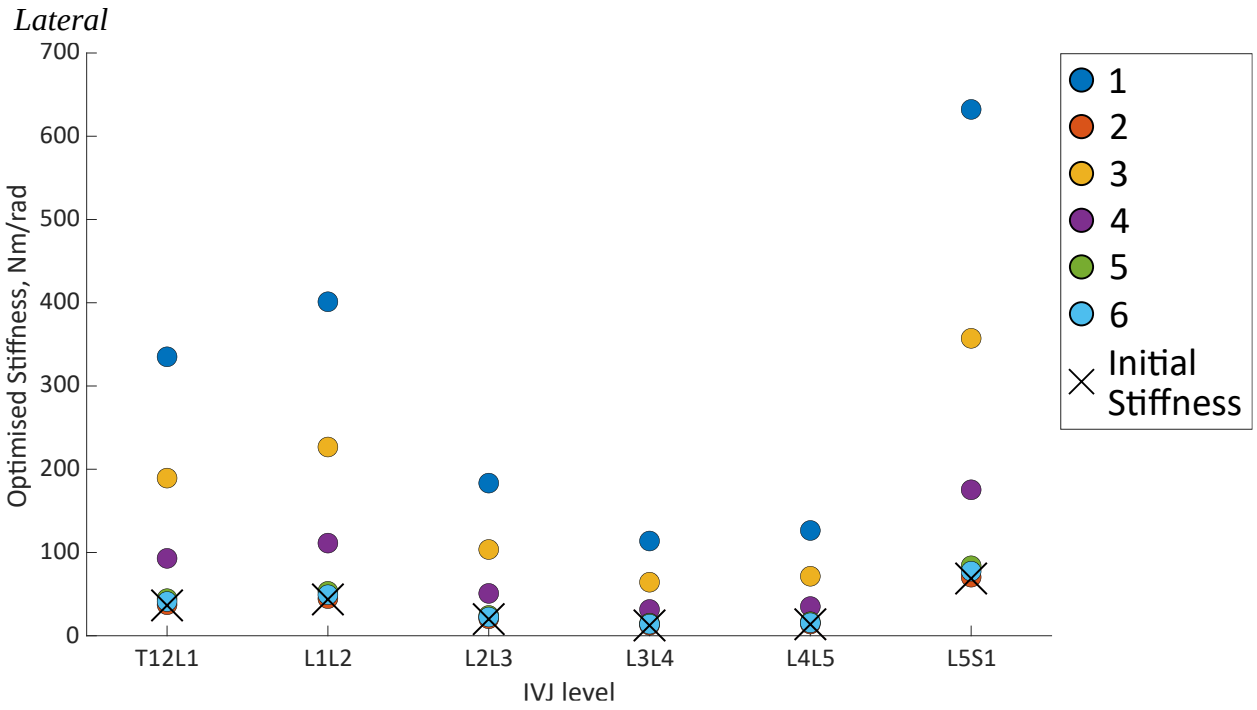

Figure 4.30: Optimised stiffness in lateral bending for the level-dependent models under a flexion load.

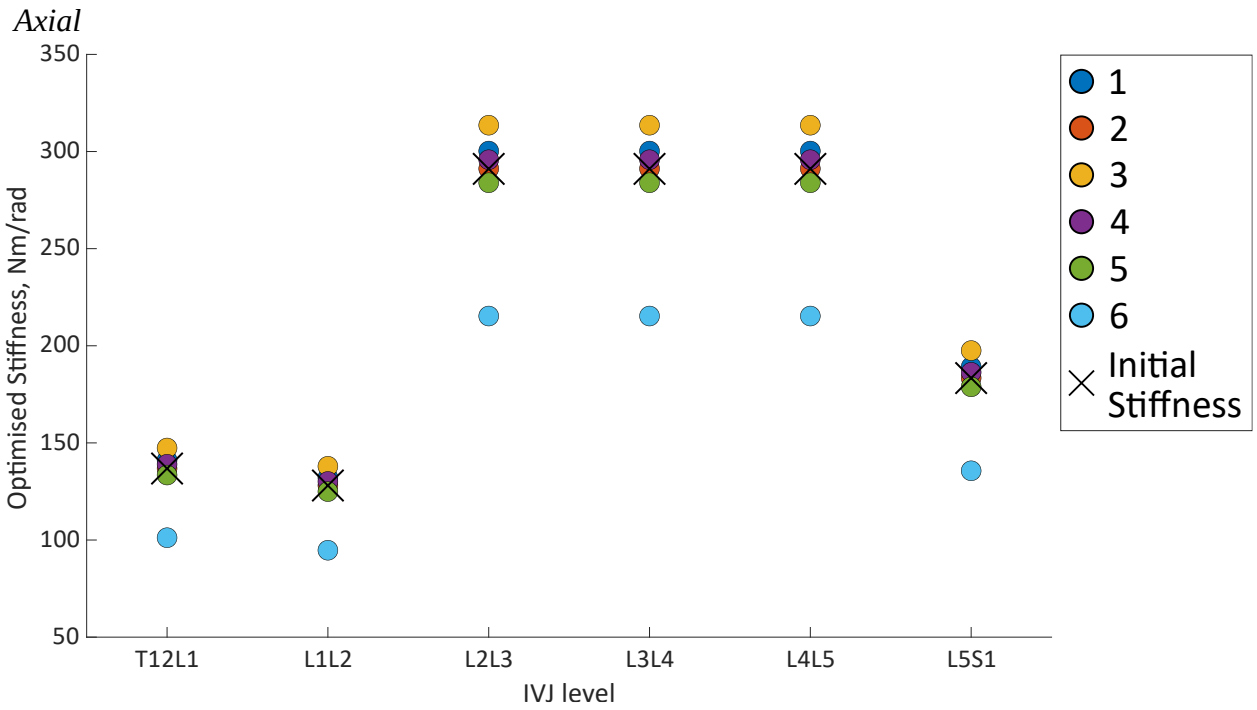

Figure 4.31: Optimised stiffness in axial rotation for the level-dependent models under a flexion load.

4.7. Appendix C

Plots of the prediction errors in the DoFs which do not correspond to the loading direction. Each plot shows the error at each level for the literature stiffness model, the optimised stiffness model, and the cross-validation stiffness model.

4.7.1. Lateral bending load

Uniform stiffnesses

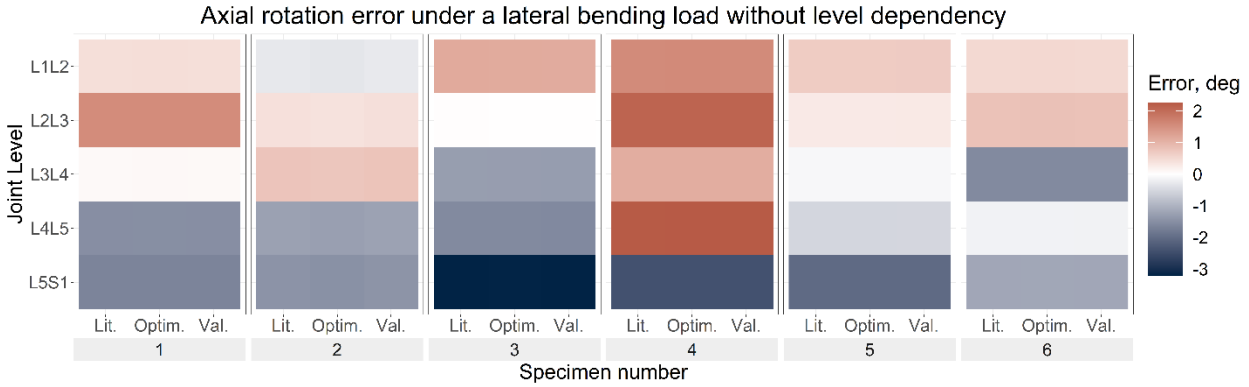

Figure 4.32: Error of the predicted motion in axial rotation under a lateral bending load with uniform stiffnesses for the literature (Lit.), optimised (Optim.) and cross-validation (Val.) stiffnesses. Blue indicates an overprediction of the motion (ie too much bending) while red indicates an underprediction of the motion.

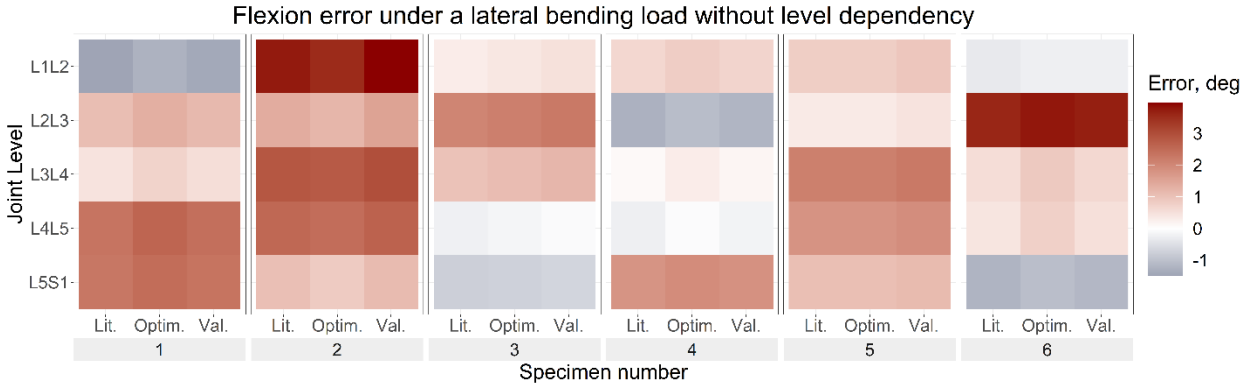

Figure 4.33: Error of the predicted motion in flexion-extension under a lateral bending load with uniform stiffnesses for the literature (Lit.), optimised (Optim.) and cross-validation (Val.) stiffnesses. Blue indicates an overprediction of the motion (ie too much bending) while red indicates an underprediction of the motion.

Level-dependent stiffnesses

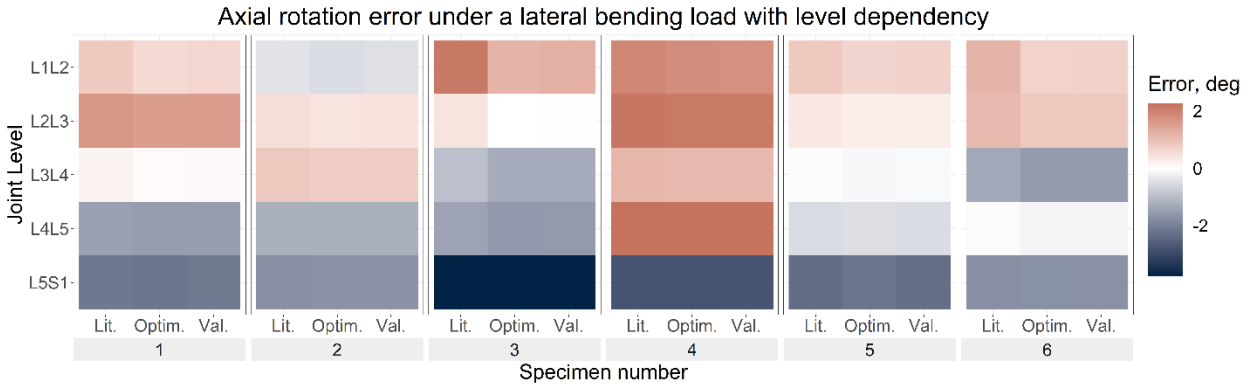

Figure 4.34: Error of the predicted motion in axial rotation under a lateral bending load with level-dependent stiffnesses for the literature (Lit.), optimised (Optim.) and cross-validation (Val.) stiffnesses. Blue indicates an overprediction of the motion (ie too much bending) while red indicates an under-prediction of the motion.

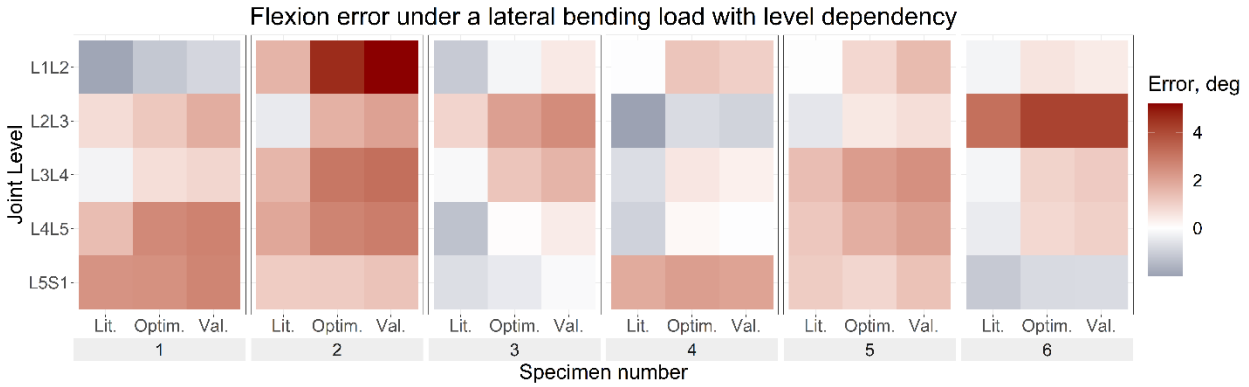

Figure 4.35: Error of the predicted motion in flexion-extension under a lateral bending load with level-dependent stiffnesses for the literature (Lit.), optimised (Optim.) and cross-validation (Val.) stiffnesses. Blue indicates an overprediction of the motion (ie too much bending) while red indicates an underprediction of the motion.

4.7.2. Axial rotation loading

Uniform stiffnesses

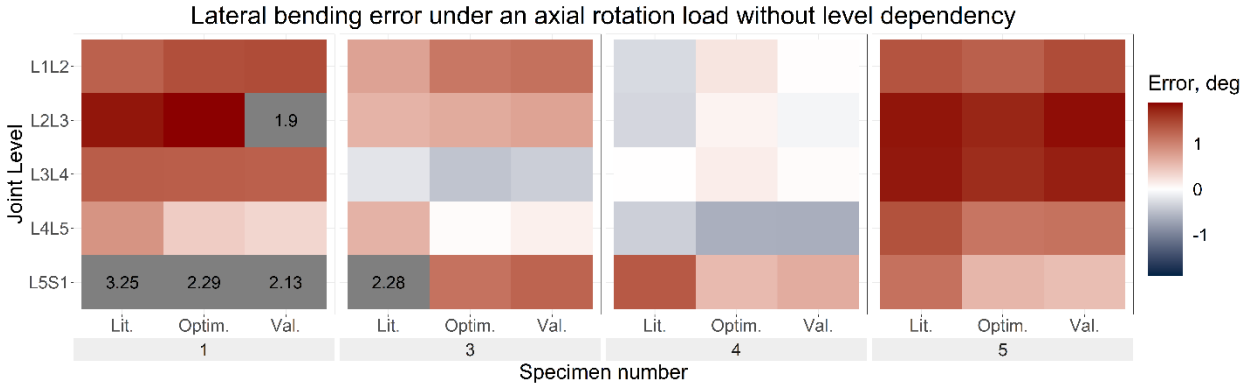

Figure 4.36: Error of the predicted motion in lateral bending under an axial rotation load with uniform stiffnesses for the literature (Lit.), optimised (Optim.) and cross-validation (Val.) stiffnesses. Blue indicates an over-prediction of the motion (ie too much bending) while red indicates an under-prediction of the motion.

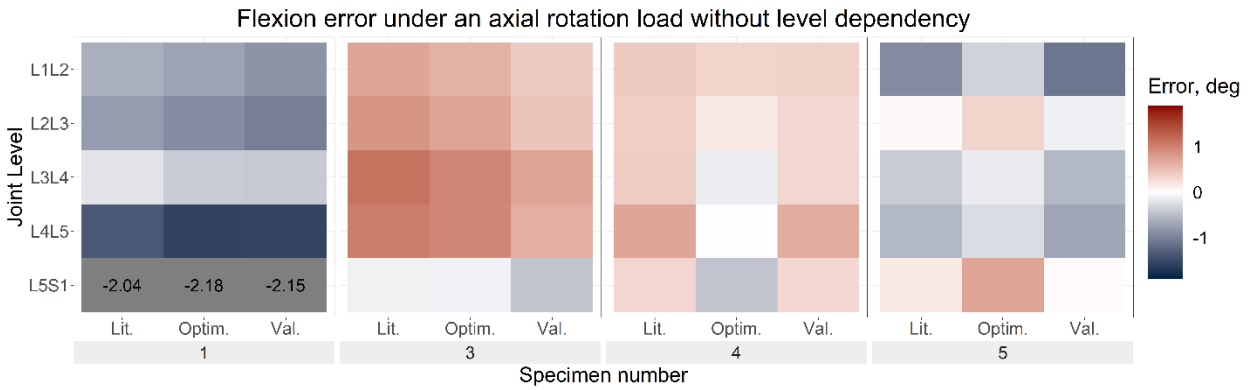

Figure 4.37: Error of the predicted motion in flexion-extension under an axial rotation load with uniform stiffnesses for the literature (Lit.), optimised (Optim.) and cross-validation (Val.) stiffnesses. Blue indicates an overprediction of the motion (ie too much bending) while red indicates an underprediction of the motion.

Level-dependent stiffnesses

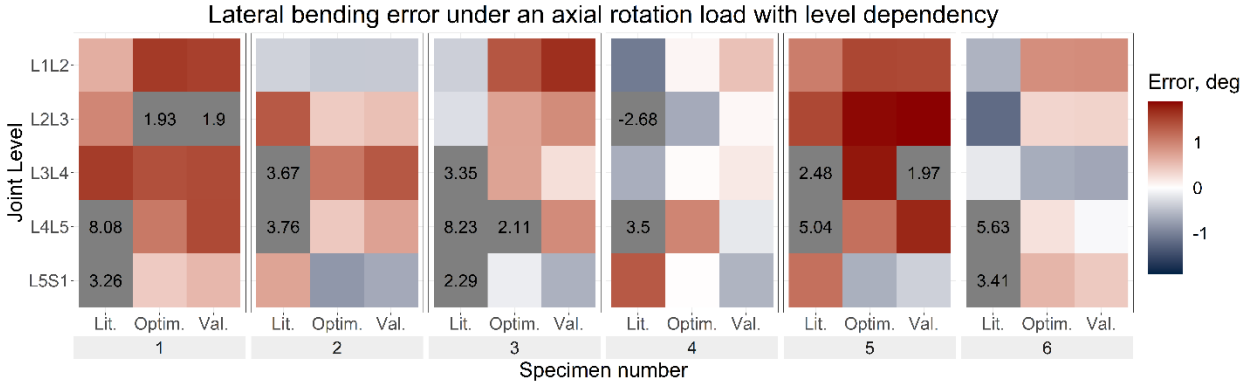

Figure 4.38: Error of the predicted motion in lateral bending under an axial rotation load with level-dependent stiffnesses for the literature (Lit.), optimised (Optim.) and cross-validation (Val.) stiffnesses. Blue indicates an overprediction of the motion (ie too much bending) while red indicates an underprediction of the motion.

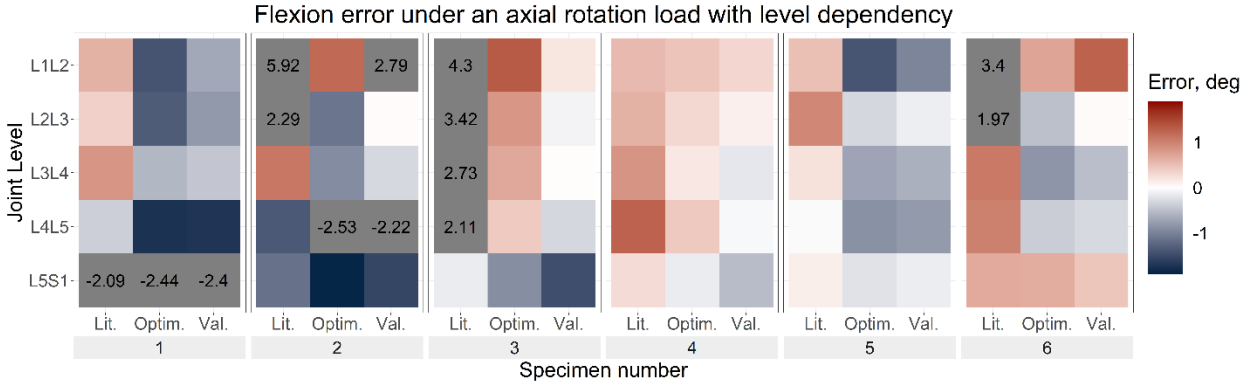

Figure 4.39: Error of the predicted motion in flexion-extension under an axial rotation load with level-dependent stiffnesses for the literature (Lit.), optimised (Optim.) and cross-validation (Val.) stiffnesses. Blue indicates an overprediction of the motion (ie too much bending) while red indicates an underprediction of the motion.

4.7.3. Flexion loading

Uniform stiffnesses

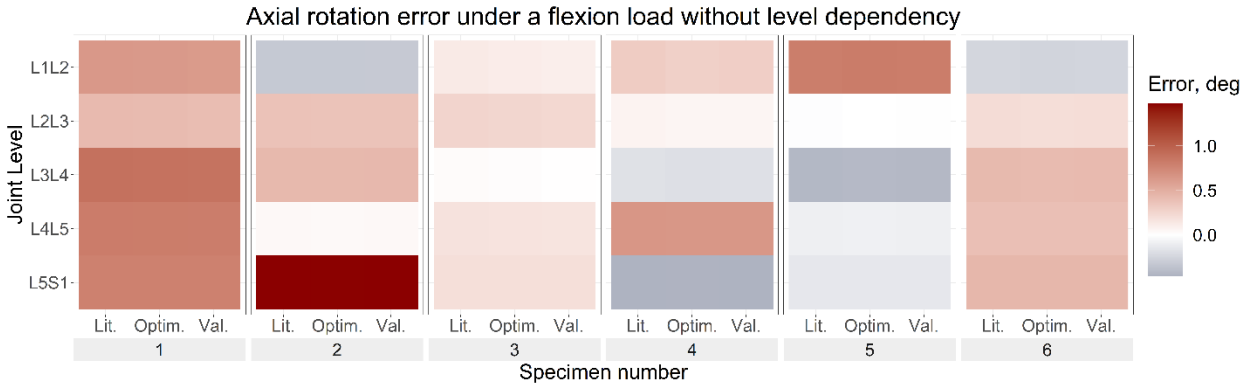

Figure 4.40: Error of the predicted motion in axial rotation under a flexion load with uniform stiffnesses for the literature (Lit.), optimised (Optim.) and cross-validation (Val.) stiffnesses. Blue indicates an overprediction of the motion (ie too much bending) while red indicates an underprediction of the motion.

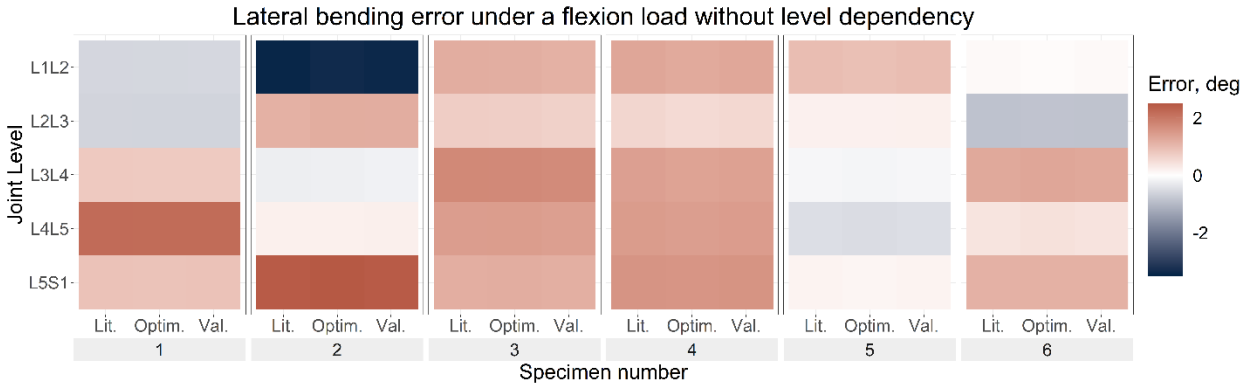

Figure 4.41: Error of the predicted motion in lateral bending under a flexion load with uniform stiffnesses for the literature (Lit.), optimised (Optim.) and cross-validation (Val.) stiffnesses. Blue indicates an overprediction of the motion (ie too much bending) while red indicates an underprediction of the motion.

Level-dependent stiffnesses

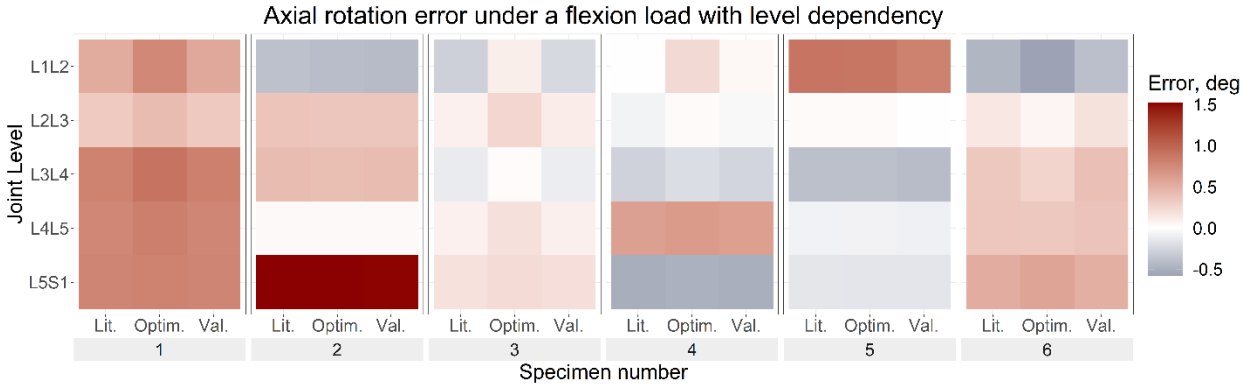

Figure 4.42: Error of the predicted motion in axial rotation under a flexion load with level-dependent stiffnesses for the literature (Lit.), optimised (Optim.) and cross-validation (Val.) stiffnesses. Blue indicates an overprediction of the motion (ie too much bending) while red indicates an underprediction of the motion.

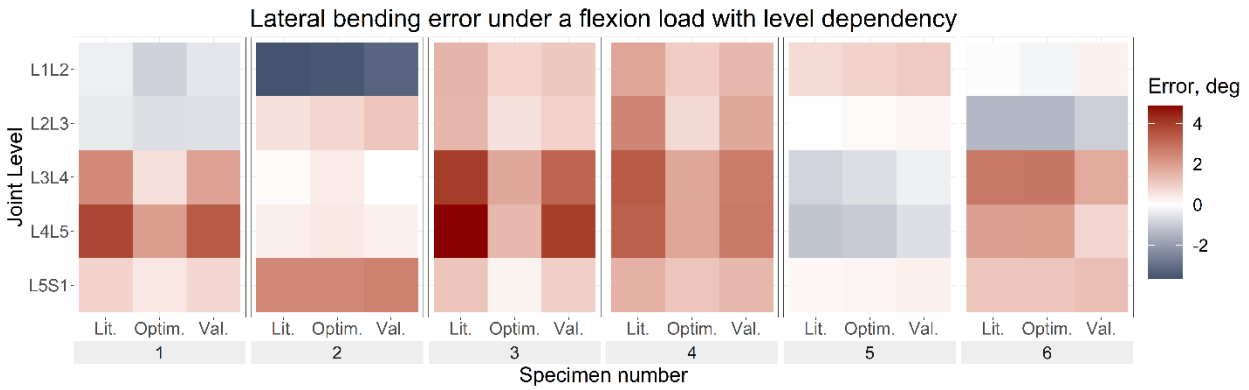

Figure 4.43: Error of the predicted motion in lateral bending under a flexion load with level-dependent stiffnesses for the literature (Lit.), optimised (Optim.) and cross-validation (Val.) stiffnesses. Blue indicates an overprediction of the motion (ie too much bending) while red indicates an underprediction of the motion.

Section 3 – Scoliotic spine modelling

Generation of severely scoliotic subject-specific musculoskeletal models

5.1. Introduction

Severe scoliosis may require surgical treatment to restore pulmonary and cardiac function, improve quality of life, and reduce back pain and the risk of future disability [16,26]. These surgeries are complex, and aside from sagittal spine alignment being the most important priority, the aims of the surgery may vary greatly between surgeons, which also results in a large variation of instrumentation strategies [18]. The treatment strategy is not necessarily selected based on predicted post-operation function [313]. Reported scoliotic surgery complication rates vary widely, from 0% to 89% depending on the type of scoliosis, time post-operation, and the definition of complication [26]. Reports include a follow-up rate of 9.9% for major complications and 6% requiring reoperation within ten years of the original operation [314], although other studies have found reoperation rates as high as 46.7% within two years [315]. The risk factors involved with reoperation include time post-operation, age of operation, and surgical treatment technique [315–318]. Computational models may help guide surgeons to objectively select the optimal procedure for complex spine correction surgeries by simulating virtual instrumentation strategies and predicting treatment outcomes [313,319], which would potentially improve surgical outcomes and reduce complication rates. However, this requires suitable computational models.

Musculoskeletal multibody modelling techniques have been used to simulate the scoliotic spine [122,123] and scoliotic surgical corrections [34,35], for example identifying optimal instrumentation techniques and complication risks [122,243]. This has been done with both commercial software such as AnyBody [122] as well as with open-source software, such as OpenSim [123]. Opensource software allows for models to be shared and reused, making them more accessible [89,116]. Some generic open-source models of the healthy spine already exist [41,120]. However, for such models to be clinically useful they require personalisation [116,313].

The study by Bruno *et al.* created a generic body model with a fully articulated spine, representative of a 25-year-old male [41], from which a female model has been developed [44]. Each intervertebral joint (IVJ) from the sacrum to T1 included three rotational degrees of freedom (DoF): lateral bending, axial rotation, and flexion-extension. Additionally, the ribs (with costovertebral joints) and sternum, and the major trunk muscle groups were included [41]. Using a non-linear scaling technique, these models were further developed to create models of adolescents from 6 to 18 years old [120]. Segmental lengths, mass distribution, spinal alignment, as well as muscle properties were adjusted [120]. One recent study has developed an automated pipeline using deep learning to create a musculoskeletal model of the lumbar spine [305]. Other studies have looked to develop scoliotic models. Using medical imaging data of mildly scoliotic subjects, a pipeline was developed to create subject-specific scoliotic spine models in AnyBody [121]; it has also been applied in the case of severe scoliosis [122]. This pipeline has been adapted for use with OpenSim models to create mildly scoliotic models [123]. Overbergh *et al*. developed a pipeline to create subject-specific scoliotic models starting from markers to define the kinematic constraints between vertebrae, then incorporating subject-specific vertebral geometries by segmenting computed tomography (CT) data which allowed registration of the vertebrae to biplanar X-rays to define the scoliotic curvature [118]. Other studies have created subject-specific MSK models of scoliosis, including bone deformity directly from bi-planar X-rays [34]. Scoliotic models including the musculature have been used to investigate muscle activation and shear loading and compressive forces conditions within the IVJ [122,123]. Other models have simulated surgical corrections but not included musculature [35].

While pipelines to create scoliotic models exist, they have often relied on manual segmentation of CT data, or geometric reconstruction and data from biplanar images [35,118,121](EOS Imaging Systems, Paris, France [320]). Manual segmentation is a time-consuming process [305], and although automatic segmentation methods for the creation of MSK spine models have been applied to healthy spines, as the review by Galbusera *et al.* notes, work is ongoing to achieve high-quality segmentations [321]. Alternatively, semi-automatic methods for creating scoliotic spines models recreate the subject-specific curvature using virtual palpation to identify anatomical landmarks [121], or marker clusters placed on the subject [118]. However, to the best of the author's knowledge, a pipeline to create subject-specific scoliotic spine models from CT data, which is compatible with OpenSim is not available.

Studies of the lower limb have investigated the sensitivity of models to inter and intra-operator variability of virtually palpated landmarks [322,323]. Studies focusing on the spine have investigated the sensitivity of spine curvature and scaling of personalised healthy spine models to between-session variability of reflective marker placement [324]. However such studies need to be extended to include pathological cases [118]. Furthermore, this does not account for the intra- and inter-rater variability of virtually palpated anatomical landmarks. This is a necessary step for pathological models to be considered reliable and representative of an individual [323,325] and is especially relevant if the models are to be used in clinical applications [116]. Furthermore, the variability of the virtual palpation of anatomical landmarks in scoliotic cases could be expected to increase compared to a non-pathological spine given the deformity of scoliotic vertebrae.

The sensitivity of creating personalised scoliotic models to intra- and inter-rater variability may not have been considered due to the use of EOS imaging systems. This system simplifies the reconstruction of vertebrae and the virtual palpation process as it results in a bi-planar radiograph compared to the many slices generated by a CT scan. However, EOS imaging systems are less widely available than CT imaging systems.

In addition to the curvature of the scoliotic spine, the definition of soft tissues such as the intervertebral disc, ligaments and muscles should be considered when creating MSK models of the spine. The inclusion of these tissues is necessary for estimating the necessary corrective forces, and forces and moments that the instrumentation may experience post-operation. Both the rotational and translational stiffnesses of the IVJ play an important role in the kinematics of the spine [126], Schmid *et al*. incorporated non-linear stiffnesses in the rotational DoF, but not in translation [123], Bassani *et al.* included stiffnesses in translational DoF however the version of the software used in the study did not allow for stiffnesses to be defined in the rotational DoF [121]. Stiffnesses of the IVJ may play an important role in the effectiveness of a surgical correction for scoliosis [125], meaning their inclusion in models for the prediction of surgical outcomes is important. Other studies which have included stiffnesses in all DoF have not included the musculature [34,35]. Considering the muscles, muscle parameters are assumed to be the same for scoliotic cases as for non-pathological cases [122]. The muscle paths are straight based on attachment and insertion points [41,121]. However, in cases of severe scoliosis where sagittal misalignment may affect the muscle paths, a straight path may be inaccurate. The use of wrapping surfaces and via points may result in a more accurate muscle path [326], however, such techniques have not yet been incorporated into scoliotic spine models.

Therefore, this study aimed to: (i) develop an opensource package for the generation of subject-specific scoliotic MSK models in OpenSim, from CT data, accounting for muscle paths and IVJ stiffnesses; (ii) to assess the robustness of the method to intra and inter-operator variability.

5.2. Materials and methods

Development of a base model

The OpenSim MatLab API 4.1 [89,90] with a custom script was used to create the base model, which was developed from the generic full-body female model with a fully articulated spine [41]. First, some simplifications were made, and certain bones, muscles, and actuators as well as the existing marker set were removed. This left the vertebrae (T1 to L5), the sacrum, and the pelvis. Muscles between the remaining bodies were kept. After this, parts of the model were enhanced. The existing IVJ allowed the three rotational DoF, these were modified to also allow the three translational DoF (a total 6 DoF at each IVJ). At each IVJ a lumped parameter spring-damper element (referred to in OpenSim as a bushing element) was added, this element is often used to represent the mechanical properties of the IVJ in MSK spine models [327]. It has a linear spring-damper element defined in each DoF (Table 5.1), and stiffness and damping parameters were assigned based on the literature values [43]. This simplification was made as the properties in scoliotic may be highly subject-dependent meaning the use of any particular values adds little value. Rather the properties likely would require personalisation, therefore, incorporated within the pipeline is a function that allows the properties to be easily changed.

Table 5.1: Stiffness and damping parameters used to define the IVJ.

Degree of freedom	Stiffness		Damping	
	Translation, N/m	Rotation, Nm/rad	Translation, N/(m/s)	Rotation, Nm/(rad/s)
Anterior-Posterior Shear/ Right-Left Bending	149,000	68.8	1000	2.3
Inferior-Superior Translation/ Axial Rotation	1,890,000	291	1000	2.3
Right-Left Translation/ Flexion-Extension	135,000	51.0	1000	2.3

The sacrum on the original model lacked sufficient detail to allow a virtual palpation of anatomical landmarks. Therefore, CT data of 18 sacra including the coccyx from the Cancer Image Archive (https://www.cancerimagingarchive.net/) [328–332], were manually segmented in Mimics Innovation Suite v24 (Materialise, Leuven, BE) and exported as .stl files. These files were cleaned and aligned and converted to a .wrl file in MeshLab [333]. A statistical shape model was created with the GIAS2 Shape Modelling software [334]. This allowed for the palpation of the necessary anatomical landmarks and maintained a generic representation of the sacrum.

The script to create the base model replaced the original geometry of the sacrum with the mean geometry of the statistical shape model.

To create a scoliotic model from the base model a marker set was required. The markers set was created by a virtual palpation of the vertebral geometries in NMS builder [282] and then added programmatically.

The muscle paths in the base model were direct paths between attachment points. Therefore, when the scoliotic curvature was created some of the muscle paths pass through the vertebrae. To stop the muscles from taking these unrealistic paths, wrapping spheres were introduced to ensure the

muscles could not pass through the vertebrae. Wrapping spheres were manually added to each vertebral body. The radius and position of each wrapping sphere were determined by fitting a sphere to the anterior surface of the .stl files of the vertebral bodies (Figure 5.1), repurposing the code by Modenese *et al.* which was developed for a similar purpose on the lower limbs [335]. This fits a sphere by minimising the least squares distance between the nodes selected on the .stl. This approximately corresponds to the centre of the vertebral body.

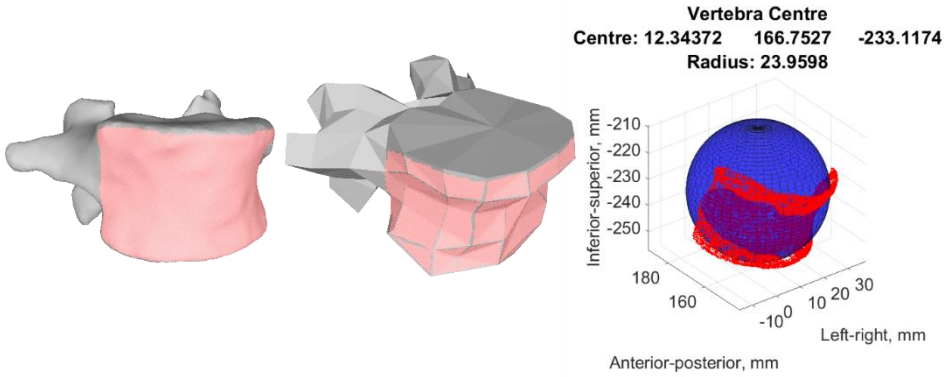

Figure 5.1: The segmented (left) and generic (centre) .stls of L5 and the selected nodes on the anterior surface (red). The sphere (blue) fitted to those nodes using a least squares distance algorithm (right).

Processing of the CT data

The CT data were manually segmented in Mimics (Figure 5.2), segmentation of a single vertebrae required approximately an hour. The centres of the vertebral bodies were estimated using the same methodology for finding the position of the wrapping spheres (Figure 5.1).

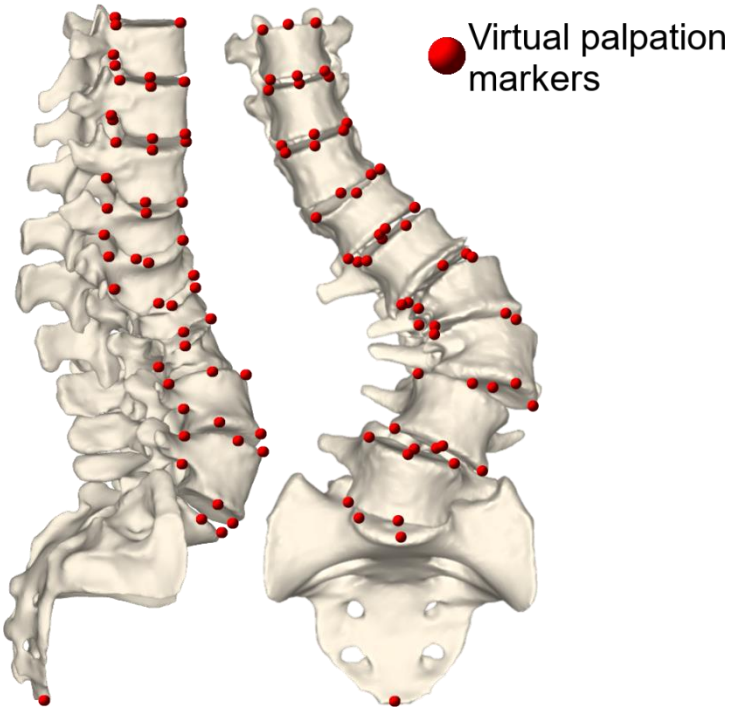

Figure 5.2: Sagittal (left) and frontal (right) view of the geometries from the segmentation of the CT data, the sacrum and vertebrae L5 to T9 were segmented. The 3D positions of the virtual palpation markers performed on the CT scan that are visible in these views are also shown by the red spheres.

A protocol established was established that defined two groups of virtual landmarks, one group to define the joint poses and the other to enable scaling (Figure 5.3). Locations for the markers used to define the joint poses were selected based on the ISB recommendations [82], and locations of the markers for scaling were chosen based on locations used in previous studies [118,336]. Additionally, a naming convention was applied so that it was compatible with the code used to create the scoliotic model and the markers on the model. Virtual palpations were performed on the CT data of a scoliotic patient (56-year-old, female, adult scoliosis, lumbar scoliosis, Cobb angle 75° (Table 5.2) measured with Surgimap [337,338]).

Table 5.2: Radiographic evaluation of the standing X-ray of the scoliotic case used in the study. Third curve parameters are not reported as the Cobb angle for the third curve was <10°. Lumbar lordosis in the supine position is also reported as a substantial difference was seen in this parameter between supine and standing. All parameters were measured with Surgimap.

Radiographic Evaluation	
Pelvic tilt, °	18.2
Pelvic incidence, °	45.9
Sacral slope, °	27.7
Lumbar lordosis - standing, °	-4.3
Lumbar lordosis - supine, °	-34.0
Thoracic kyphosis, °	11.0
Pelvic incidence-lumbar lordosis mismatch, °	44.6
Main curve Cobb angle, °	-75
Main curve type	Lumbar
Main curve apex	L2-L3
Main curve extent	T12 superior – L4 inferior
Secondary curve Cobb angle, °	51.9
Secondary curve type	Main thoracic
Secondary curve apex	T9-T10
Secondary curve extent	T3 superior – T12 inferior
Coronal alignment, mm	-42
Sagittal vertical axis, mm	104

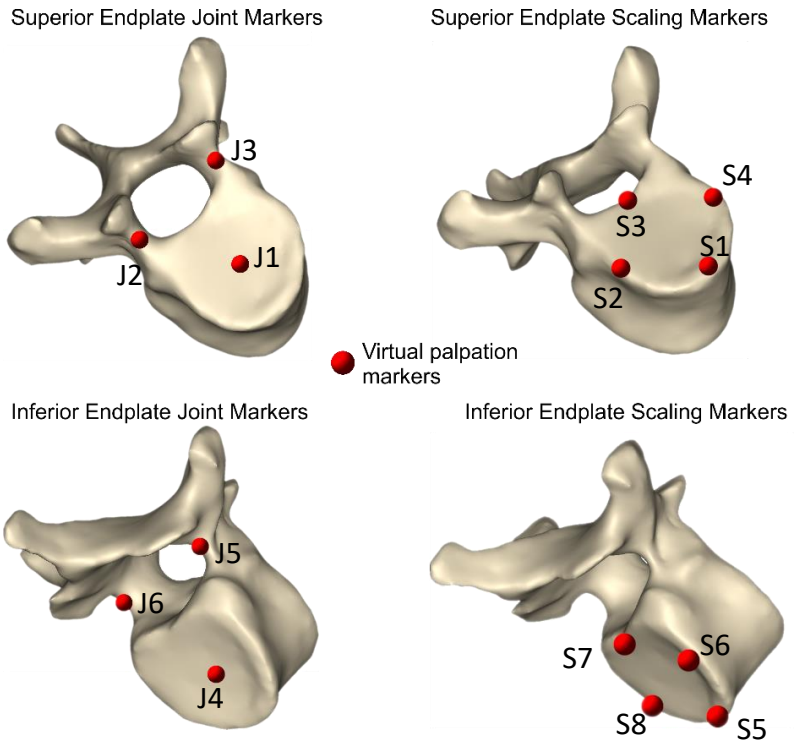

Figure 5.3: Locations of the virtual palpation landmarks for defining the joints and the scaling of the vertebrae. To define the joints, landmarks are virtually palpated on the top and the base of the pedicle arches and the centre of the superior and inferior endplates. To define the scaling factor landmarks are virtually palpated on the anterior and posterior-most points and the most lateral points of the superior and inferior endplates.

The palpations were performed 10 times by two operators and 3 times by 3 operators (total 29 measurements).

Creation of the scoliotic model

Another custom script with OpenSim MatLab API 4.1 [89,90] to create the scoliotic model from the base model and the virtual palpations. The code first ensures the virtual palpations and the model share the same reference system. An affine scaling was applied to the vertebral bodies. The sacral slope of the model was aligned with the virtual palpation. The joint poses of each IVJ were redefined following the ISB recommendation [82]. Finally, the vertebrae were realigned based on the vertebral body alignment which was calculated from the scaling markers.

An initial evaluation of the method was performed by visual inspection, controlling for anatomically plausible vertebrae position, vertebrae orientations, and muscle paths.

Evaluation of intra and inter-operator variability

Following the established protocol, the palpation was repeated 10 times by two operators and 3 times by 3 operators (total 29 measurements).

All statistical analysis was performed in R [295] using the *stats*, *PMCMRplus*, and *irr* packages. Markers were grouped first by function (scaling or joint definition). The virtual palpation markers were checked for normality using the Shapiro-Wilk test. Inter- and intra-operator variability was tested with intraclass correlation coefficient (ICC) using a two-way random effects model for

absolute agreement for single measurement (ICC 2,1) [339,340]. The inter-operator ICC was calculated on the third repetition performed by each operator. The intra-operator variability was assessed for the two operators that performed the virtual palpations ten times. The ICC of the markers was assessed by X, Y, and Z coordinate as well as their global position (defined as the Euclidean distance to the X, Y, and Z coordinate). Where X corresponds to the anterior-posterior position, Y the inferior-superior position, and Z the left-right position.

For non-parametric data, unbalanced Friedman tests were performed for each marker location (e.g., all markers on the centres of the superior vertebral endplates) to control for significant differences ($p<0.05$) in each coordinate. To test for statistically significant inter-operator variation the markers were grouped by operator with each repetition tested separately. To test for statistically significant intra-operator variation the markers were grouped by repetition, with the test performed separately for the two operators that performed the palpations ten times. In both cases, the markers were blocked by vertebra level (this accounts for the differences in the position of markers due to being placed on different vertebrae). As unbalanced Friedman tests were used, in cases of significance post hoc one-to-many two-sided Nemenyi tests were applied to search for trends (such as a specific operator or repetition with significant differences) with a significance level of $p<0.05$ and a critical z value of 2.728 for the inter-operator variability and 3.164 for the intra-operator variability [341].

Additionally, to evaluate the magnitude of the variation of the marker positions in X, Y, Z and the Euclidean distance the IQR for each marker was calculated for the overall variability (all operators and all repeat palpations). To summarize the overall variability of the markers the median and IQR of the IQR were then calculated for the X, Y, Z position and the Euclidean distance.

Assessment of model accuracy

Models were created for each virtual palpation and the variability of the curvature, and the centre of the vertebral bodies was assessed.

The accuracy of the model was assessed based on the distance between the centre of the vertebral bodies in the model and a segmentation of the patient CT data. The centre of the vertebral bodies was calculated as the centre of a sphere fitted to the anterior surface of the vertebral bodies using an adapted version of the code developed by Modenese *et al.* [335].

A custom code in MatLab was used to assess the model's accuracy. The accuracy of the vertebral positions was evaluated with the RMSE between the model vertebral centres and the CT vertebral centres. The vertebral centres of the model were estimated as the centre of the sphere fitted to the vertebrae that formed the wrapping surface. To have the centres in a common reference frame, all centres were defined relative to the centre of L5. The RMSE of the vertebral centres was analysed with regard to the inter- and intra-operator and overall variability. The intra-operator variability was considered by analysing the median and IQR of the RMSE for the models from the two operators that performed the palpations 10 times. The inter-operator variability was considered by analysis of the median and IQR of the RMSE for the models created from the third palpation performed by each operator. The overall variability was considered by analysing the median and IQR of the RMSE of all the models.

Further, the curvature was assessed by fitting 4^{th}-order polynomials to the centres of the vertebral bodies, and the match between the model and the patient was assessed based on the RMSE and R^2 values. The order of the polynomial was selected based on a visual inspection of the fitting. To avoid biasing the assessment of the curvature when comparing spine models the same order of

polynomial was used for all models. A 4th-order polynomial was chosen as it represented the lowest-order polynomial that could be fitted without displaying a visibly poor fit. The RMSE of the curve and the R^2 values were also analysed in terms of the inter- and intra-operator and overall variability.

The Cobb angle (CA) of the main curve, lumbar lordosis (LL), apex of the main curve, and apex of the secondary curve were calculated for all the models. The LL was calculated using the sacral slope and the orientation of the body reference frame (which aligned with the vertebral endplates) of L1. The CA was calculated from the orientations of the body reference frames of L4 and T12. Normal distributions for the CA and LL were tested with chi-squared goodness of fit. The mean, standard deviation, and maximum and minimum values for the models were compared to the measurements from the radiographic evaluation (Table 5.2). The main curve apex was identified by determining the vertebra with the highest displacement relative to the apex of the sacrum (a common reference system for all models). The main curve apex of the model was then compared to the main curve apex identified in the radiographic evaluation (Table 5.2).

The CT scan only extended from the sacrum to T9, additionally, the acetabulum and iliac crest were not completely visible. Due to this, the model was not evaluated based on secondary curve characteristics, pelvic parameters or sagittal and coronal alignment.

5.3. Results

Creation of a scoliotic spine model

The code successfully created a personalised scoliotic musculoskeletal model from the base spine model, and a virtually palpated landmark set (Figure 5.4). The vertebrae are scaled, the curvature of the spine is adjusted, and the muscles wrap around the vertebral bodies. The visual evaluation of the model reconstruction implied the reconstruction method was effective for the majority of the models.

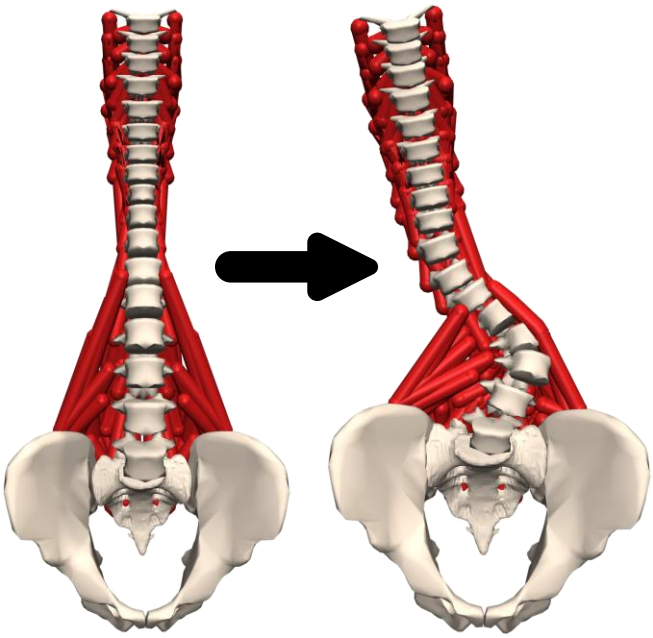

Figure 5.4: The base spine model and the resulting scoliotic model after applying the workflow, the muscles can be seen to be wrapping around the vertebral bodies.

Intra- and inter-operator variability

Interclass correlation coefficient (two-way random effects, single, with agreement model) showed excellent intra- and inter-operator repeatability (>0.9) for all cases (intra and inter-operator in X, Y, Z, and Euclidean distance for both the scaling markers and the joint markers).

Shapiro-Wilk test established the positions of the virtually palpated landmarks were nonparametrically distributed. The Friedman tests showed no statistically significant differences in the scaling marker positions due to inter- or intra-operator variability. The Friedman tests showed statistically significant differences for some of the joint marker positions due to inter- and intra-operator variability (Table 5.3). However, none of the markers consistently (i.e. across all groups) exhibited a statistically significant difference in position due to inter- or intra-operator variability.

Table 5.3: Results from the unbalanced Friedman tests in each coordinate. Markers for which there were statistically significant differences ($p<0.05$) are reported. Joint markers were labelled 1-6 (Figure 5.3). In the case of intra-operator variability – operator 2 in the anterior-posterior coordinates significant differences were not found for any of the markers.

Group	Coordinates		
	X	Y	Z
Inter-operator variability – repetition 1	J4, J5	J1, J2, J3	J1, J4, J5, J6
Inter-operator variability – repetition 2	J2, J4, J5	J1, J2, J3, J4, J6	J3, J4, J5, J6
Inter-operator variability – repetition 3	J1, J2, J5	J4	J1, J4
Intra-operator variability – operator 1	J2, J3, J4	J1	J3
Intra-operator variability – operator 2	J1	J1, J2, J3, J4, J5, J6	-

Post hoc Nemenyi test indicated significant differences for some of the markers (Table 5.4) in some of the coordinates, however, no trends were apparent. For joint markers 5 and 6 there were no significant differences.

Table 5.4: Significant results from the Nemenyi tests, the operator or repetition for which there was significance, the z, and the p-value are reported. For the inter-operator variability, 4 comparisons were made, for the intra-operator 10 comparisons were made. Comparisons for the inter-operator variability were made with operator 1 and for the intra-operator variability comparisons were made to the first repeat. There were no significant results for joint markers 5 and 6.

Group	Coordinate	Joint marker #			
		1	2	3	4
Inter-operator variability – repetition 1	X	2nd z=-2.8, p=0.02	-	-	-
	Y	-	4th z=2.8, p=0.02	4th z=3.3, p=0.004	-
	Z	-	-	-	-
	X	-	-	-	-
	Y	3rd z=2.8, p=0.02	-	-	-

Inter-operator variability – repetition 2	Z	-	-	-	-
Inter-operator variability – repetition 3	X	-	2nd z=3.4, p=0.002	-	-
	Y	-	-	5th z=3.0, p=0.01	-
	Z	-	-	2nd z=2.8, p=0.02	-
Intra-operator variability – operator 1	X	-	3rd z=-2.9, p=0.03	6th z=3.4, p=0.005	8th z=-2.7, p=0.04
	Y	-	-	-	-
	Z	-	-	-	-
Intra-operator variability – operator 2	X	5th z=-2.8, p=0.04 9th z=-3.5, p=0.004	-	-	-
	Y	2nd z=-3.7, p=0.002 6th z=-3.9, p<0.001 8th z=-4.9, p<0.001 9th z=-2.9, p=0.03	-	-	10th z=3.2, p=0.01
	Z	-	-	-	-

The overall variability of the markers was calculated as the median and IQR of the IQR measurements of all the markers as the X, Y, Z, and Euclidean positions (Table 5.5). Outliers are present within the IQR up to a maximum of 10.3 mm (Figure 5.5). The general variability did not exceed 2mm.

Table 5.5: General variability of the marker X, Y, Z, and Euclidean positions described by the median and interquartile range of the interquartile ranges for all the markers.

Position	Median, mm	IQR, mm
X	1.1	0.9
Y	1.6	1.5
Z	0.7	0.5
Euclidean	1.3	1.3

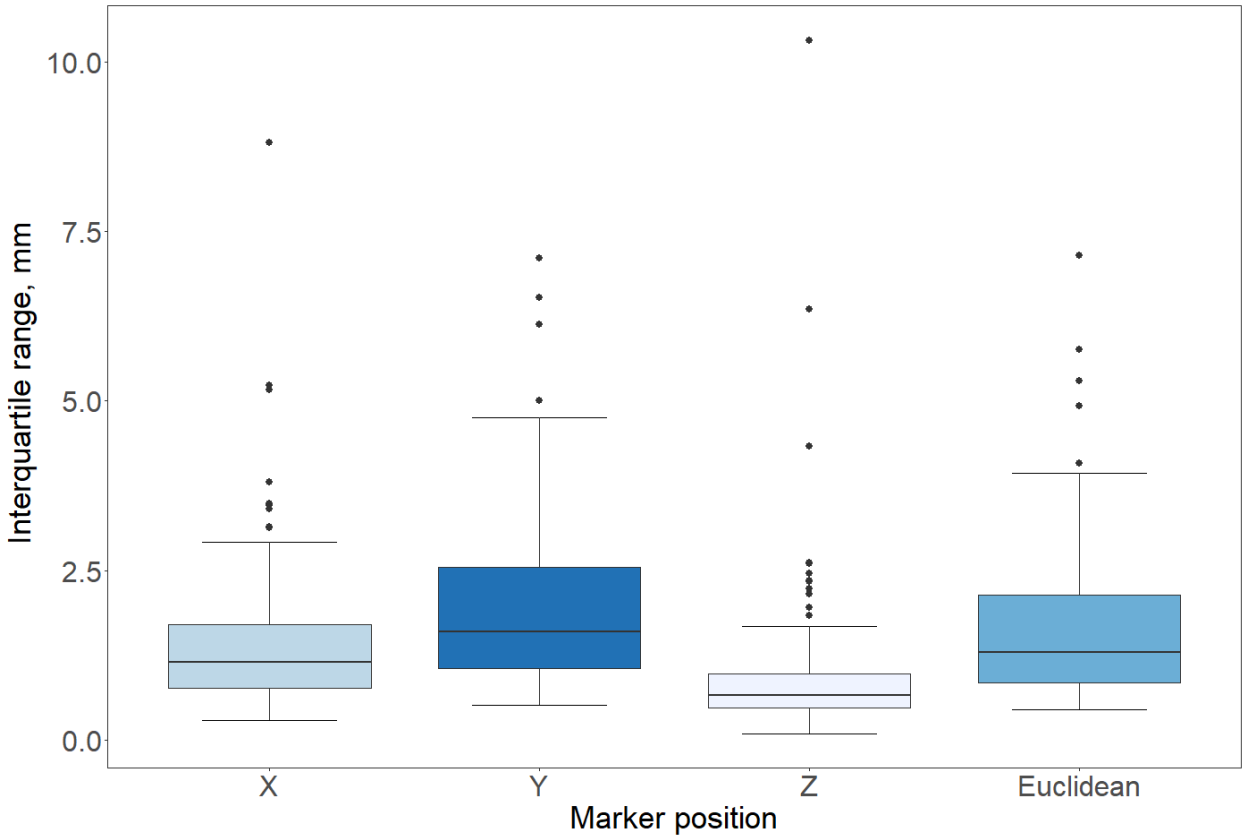

Figure 5.5: Variation of the interquartile range showing the median, interquartile range, and outliers of the markers in X, Y, Z and Euclidean positions.

Model accuracy

The centres of the vertebral bodies were successfully found for both the segmentation of the CT data and the model (Figure 5.6) and 4th-order polynomials were fitted in both the sagittal and frontal planes (Figure 5.7). A visual inspection of the positions of the vertebral centres shows the positions were consistent between models although there is an offset from the CT vertebral centres at many of the vertebral levels (Figure 5.6). This is consistent with the RMSE errors of the vertebral centres that are substantially larger than the IQRs.

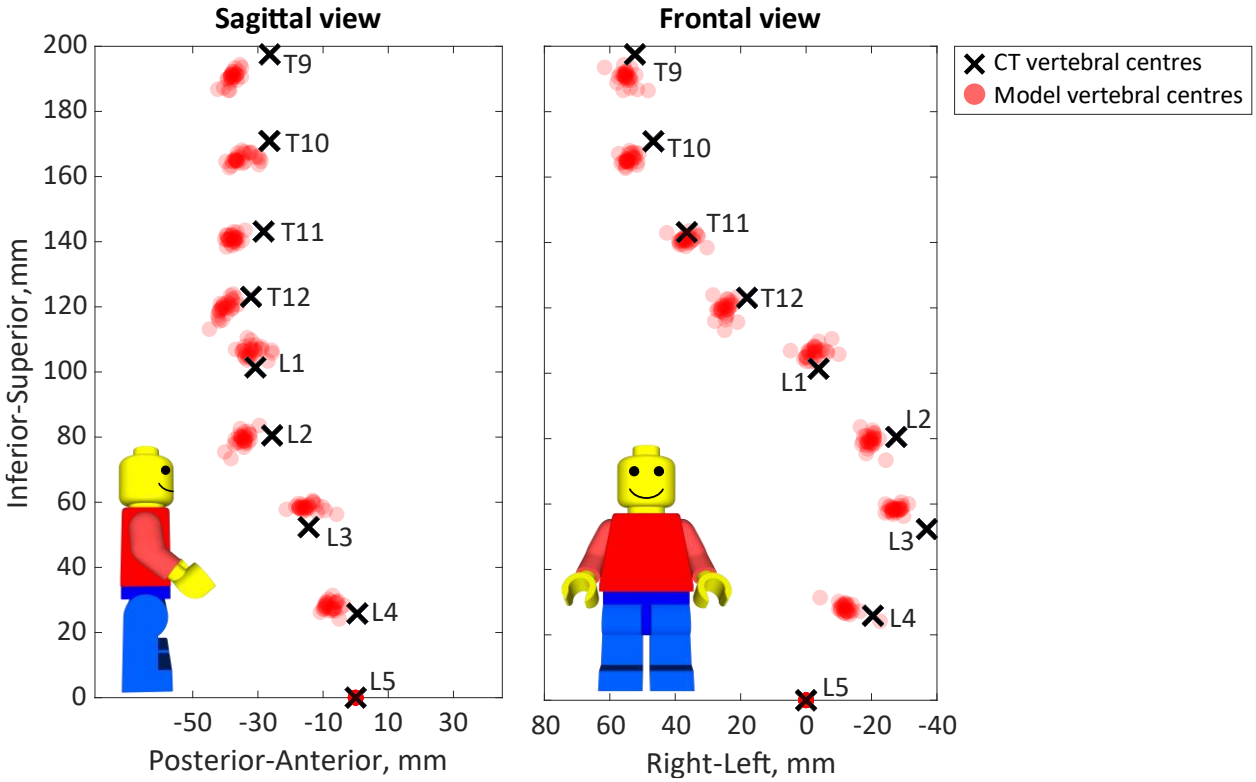

Figure 5.6: The centres of the vertebrae from the models and the CT segmentations in the sagittal and frontal views.

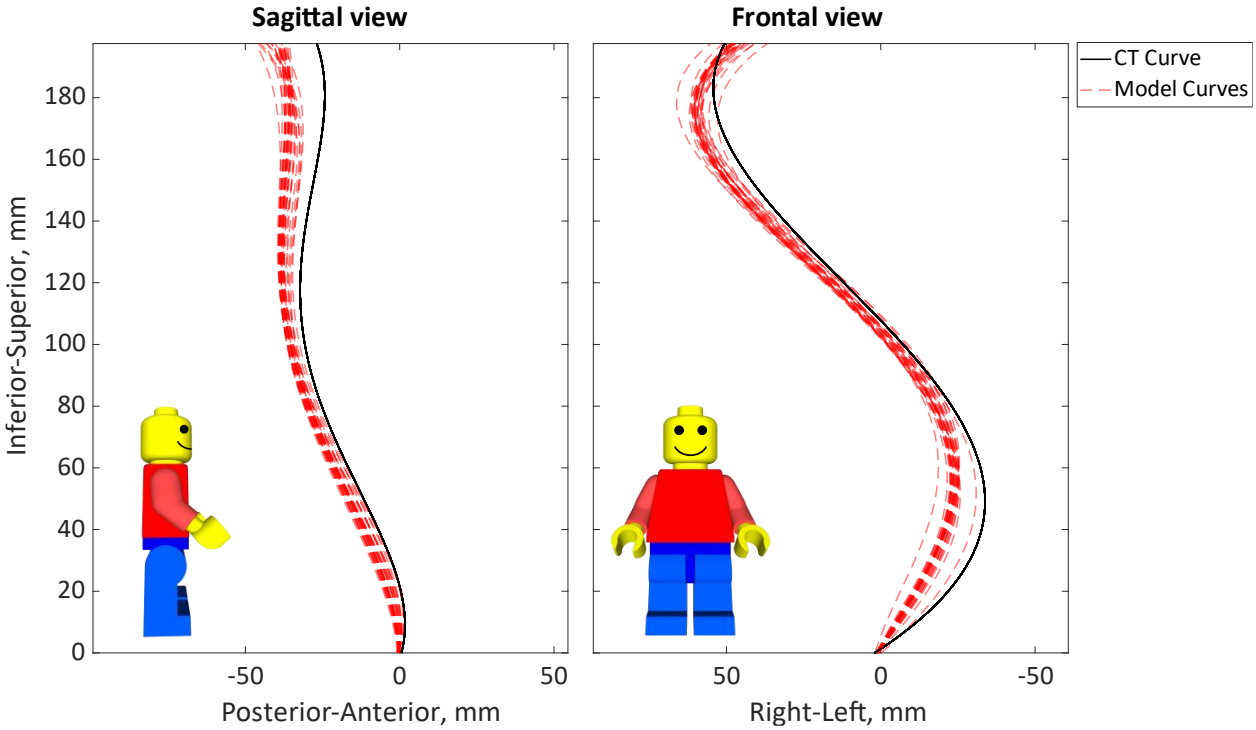

Figure 5.7: The vertebral centres identified from the CT data and the 4th order polynomial line fitted to them, and the 4th order polynomial line fitted to the vertebral centres of the model

All error measurements were similar for intra-, inter-, or overall variability (Table 5.6), suggesting neither inter- nor intra-operator variability directly affected the error of the reconstruction, rather it may be due to errors in the positioning of specific markers. The RMSE for the curves in the sagittal and frontal planes are similar, indicating the mean error in one plane is not greater than in the other. However, the R^2 value is notably better in the frontal plane than the sagittal plane, suggesting the majority of the error may occur in the sagittal plane (Table 5.6).

Table 5.6: The variability of the reconstruction accuracy due to the intra-, inter-, and overall operator variability. The median and interquartile range of the 3D root mean square error of all the vertebral centres, the RMSE of the fitted curves in the sagittal and frontal planes, and the R^2 of the fitted curves in the sagittal and frontal planes.

Variability factor	Median (and IQR) vertebral centre 3D RMSE, mm	Median (and IQR) curve RMSE, mm Sagittal	Median (and IQR) curve RMSE, mm Frontal	Median (and IQR) curve R^2 Sagittal	Median (and IQR) curve R^2 Frontal
Intra operator 1	9.5 (1.3)	6.7 (0.7)	6.3 (1.0)	0.66 (0.1)	0.96 (0.0)
Intra operator 2	9.5 (0.9)	7.3 (1.0)	7.4 (1.1)	0.60 (0.1)	0.95 (0.0)
Inter	10.2 (2.3)	5.9 (2.5)	6.6 (0.5)	0.73 (0.2)	0.96 (0.0)
Overall	9.5 (1.4)	7.0 (1.1)	7.1 (1.0)	0.63 (0.1)	0.95 (0.0)

The maximum error occurred at the T9 for the majority of the models, with the largest errors occurring in the sagittal plane (Table 5.7). The errors are substantially larger than those reported in the study by Overbergh *et al.* [118]. The largest errors were not associated with the spinal deformity (the apex of the main curve was at L2L3 (Table 5.2) yet the largest errors occur in the thoracic levels).

Table 5.7: The median and interquartile range of the absolute error across all the models at each vertebral level in the anterior-posterior, inferior-superior, and right-left directions. The median, interquartile range, and RMSE of the errors in each direction across all levels are also reported. The final three rows reports the mean, standard deviation, and RMSE of the absolute errors of the reconstruction performed in the study by Overbergh et al. [118].

	Median absolute error (IQR), mm		
Vertebral level	AP	IS	RL
T9	11.41 (1.77)	6.82 (1.58)	2.92 (1.67)
T10	9.59 (4.23)	5.85 (1.78)	7.61 (2.05)
T11	9.45 (1.92)	2.25 (1.44)	1.36 (1.67)
T12	8.07 (3.55)	3.31 (2.16)	6.52 (2.01)
L1	2.01 (2.09)	5.07 (1.99)	2.45 (2.51)
L2	8.62 (1.56)	1.41 (1.60)	7.81 (2.15)
L3	2.08 (1.79)	6.13 (0.89)	9.65 (2.42)
L4	8.20 (2.82)	2.06 (1.95)	8.49 (1.77)
Median	8.20	3.31	6.52

	IQR	7.42	4.02	5.81
	RMSE	7.65	4.30	6.17
Overbergh et al.	Mean	0.83	0.71	1.59
	SD	0.67	0.59	0.83
	RMSE	1.05	0.91	1.78

The Cobb angles and lumbar lordosis were normally distributed. The mean Cobb angle was in close agreement with the radiographic evaluation whereas there were substantial errors (>20°) at the maximum and minimum angles. The mean lumbar lordosis agreed well with the radiographic evaluation of the supine radiographs but poorly for the standing radiographs. The maximum lumbar lordosis was within the range of the supine radiograph while the error of the minimum lumbar lordosis was more substantial. The standard deviation for both Cobb angle and lumbar lordosis was found to be within or in close proximity to the uncertainty of radiographic measurements. The apex of the curve was found at L2 for all models.

Table 5.8: The mean (standard deviation), minimum and maximum Cobb angle (CA) and the lumbar lordosis (LL)

	Model			Radiograph Evaluation
	Mean (SD)	Min	Max	
CA, °	-77 (10)	-59	-103	-75
LL, °	-34 (4)	-19	-40	-34 †, -4 *

† Supine * Standing

5.4. Discussion

This study aimed to create a codified workflow to create a severely scoliotic patient-specific musculoskeletal model from a generic spine model and a set of virtually palpated landmarks on CT data. A generic model was developed from an existing spine model [44], this involved the addition of a new set of landmarks to allow each vertebra to be individually, anisotropically scaled; 6 DoF joint at each vertebral level with a linear spring-damper element to represent the mechanical properties of the IVJ; and wrapping spheres at each vertebral body to ensure the muscle paths do not pass through the vertebral bodies when the scoliotic curvature is introduced. The virtual palpation requires 14 markers per vertebra, 8 to scale the vertebrae and 6 to determine the joint pose. The codified workflow aligned the sacral slope of the model with the CT scan, scaled the vertebrae and then redefined the position and orientation of the IVJs to create the scoliotic curvature.

The intraclass correlation coefficient showed the virtual landmark palpation positions could be selected with excellent reliability between operators and between repeats for the same operator. Furthermore, for the scaling markers, there were no significant differences in the positioning, and although there were significant differences for some of the joint markers the differences were not associated with any specific marker. This suggests that the virtual palpation of the anatomical landmarks can be consistently performed to within 2 mm even in the case of severe scoliosis, although it is necessary to control for outliers.

The variability of the identification of anatomical landmarks through virtual palpation translated into variability in the models. This was assessed based on the fitted curves (RMSE and R^2) and the RMSE between the centre of the vertebrae. The IQR of the RMSE and R^2 of the curvature were low, suggesting the intra- and inter-operator variation had a negligible effect (relative to the total error) on the curvature of the model. The IQR of the RMSE of the vertebral centres was higher for the inter-operator variation than the intra-operator variation, however, it remained negligible compared to the median of the RMSE. This suggests the virtual palpations were robust against operator variability.

There was a strong agreement in the shape of the curvature of the models and the curvature estimated from the CT scan in the frontal plane, whereas the agreement was weaker in the sagittal plane. The mismatch of the curvature in the frontal plane was due to an overextension of the models. The flexion-extension of the joints is defined by the joint markers on the centre of the endplates. This suggests a better definition or method is required for identifying the centre of the vertebral endplates. It should also be considered, the definition of the joint orientation is based on that of a non-pathological spine, meaning this definition may not be suitable in the case of severe scoliosis.

Despite the weaker agreement in curve shape in the sagittal plane, the RMSE of the sagittal and frontal curves were similar. However, analysis of the RMSE of the vertebral centres in the anterior-posterior, inferior-superior, and left-right directions indicated higher errors in the anterior-posterior direction, which corresponds to errors in the sagittal plane. The errors in the anterior-posterior direction also increased in the cranial direction, which can be explained by the over-extension of the models.

The RMSE of the vertebral centres were larger than those reported in a similar study [118]. The use of generic vertebra geometries rather than subject-specific geometries may be a contributing factor. The geometries can differ substantially, especially at levels where severe deformation is present such as at L2 and L3 in the case of the subject used in the current study. This would reduce the correspondence of the positioning of the virtual palpitations between the model and the CT scan. This would alter the scaling and joint definition both of which would affect the position of the vertebral centres. Other studies which have used similar methods to construct scoliotic models with generic vertebral geometries have not reported the accuracy of the position of the centre of each vertebra [121,122]. Therefore, it is challenging to assess the influence of a generic compared to subject-specific geometry on the accuracy of the vertebral position. Nonetheless, the errors are large, as they go up to 12mm, therefore future work should focus on reducing this error.

The Cobb angle of the model agreed well with the radiographic evaluation and the standard deviation was within the same order of magnitude as the uncertainty associated with radiographic evaluations, which is commonly stated to be 5° [257,342]. The apex of the curve for the model was found at L2 for all models, this agrees well with the radiographic evaluation which reported the apex of the curve to be at L2L3. The model lumbar lordosis matched the lumbar lordosis in the supine position, however, there was a large error compared to the standing position. Differences in the lumbar lordosis are expected when comparing the standing and supine positions [343]. The CT was acquired in the supine position, explaining the concordance between the model and the lumbar lordosis in the supine position. The standard deviation of the lumbar lordosis was even lower than that of the Cobb angle. This suggests the model was able to accurately capture these two parameters. The sacral slope was not evaluated as the alignment of the model sacral slope to

the sacral slope of the CT scan was enforced as this was used to define a common reference system for the model and the CT scan.

Only one subject was used in this study, and future studies should increase the number of participants. However, the subject used represents a severe case of adult scoliosis, possibly one of the more complex types of scoliosis to model as degeneration and compensatory mechanisms may be present. Therefore, the adaptation of the methodology to represent less severe or complex cases should be possible in future work. Given compensatory mechanisms may be present, evaluation of other spinopelvic parameters (such as pelvic incidence, thoracic kyphosis, and pelvic incidence lumbar lordosis mismatch) and global alignments are important. Unfortunately, the CT scan only extended to T9, and the field of view did not capture the entire pelvis. Likewise, an X-ray with the femoral heads and extending to the cervical spine was not available. Therefore, a more comprehensive comparison of spinopelvic parameters to the radiographic evaluation was not possible. Future studies should include an evaluation of these parameters as well as CT or MRI scans to enable an assessment of the muscle paths. The model incorporated generic stiffnesses, accurate representation of the scoliotic spine would require subject-specific stiffnesses and it is expected reuse of this model will incorporate that aspect. To this end, the package provided to create the subject-specific models includes an easy-to-use function which allows the user to assign the desired stiffnesses.

In conclusion, the codified workflow (OpenSim project: Personalised scoliotic spine models) generates subject-specific models which accurately capture the Cobb angle and lumbar lordosis. This is the first scoliotic model that includes muscle paths that wrap around the vertebrae. The models appear to be robust to inter-and intra-operator variability. However, further work is needed to improve the definition of the intervertebral joint poses which will likely reduce errors in the vertebral positions.

Section 4 – Closing remarks

Conclusions and future work

6.1. General reflections

The term *in silico* medicine, also known as computational medicine, refers to the development and use of models and simulations that contribute to interpreting, diagnosing, predicting, preventing, planning, and performing treatments, or managing diseases. Multibody modelling is a promising avenue for conducting *in silico* research on the treatment of severe scoliosis. This modelling technique enables the simulation of large systems, such as the spine; therefore it facilitates the investigation of surgical correction of scoliosis and the biomechanical behaviour of the spine, such as muscle activity. Like other *in silico* modelling methodologies, it allows subject-specific predictions of quantities, which are crucial to informing medical decisions or diagnoses, which are otherwise difficult or impossible to measure. Subject-specific predictions require subject-specific models. While the curvature of multibody non-pathological spine models has been personalised, considerably less attention has been given to the personalisation of severely scoliotic multibody models. This is a labour and time-intensive process, with few frameworks for doing so and limited focus on the robustness of existing frameworks. Furthermore, the personalisation of the material parameters has received considerably less attention in comparison to the geometrical personalisation.

In this context, the focus of this PhD project was to apply multibody modelling techniques to investigate the characterisation of the intervertebral joint as a lumped parameter model. The main objective was to contribute to the development of methodologies for determining personalised intervertebral joint models, including the sensitivity of the models to joint pose, and the variability of such models within and between specimens. The next objective of the thesis was to establish a framework for generating patient-specific scoliotic spine models that would allow for the easy incorporation of subject-specific joint parameters into the model.

The project started with a literature review of the current state-of-the-art of finite element and musculoskeletal models of healthy and scoliotic spines, with a focus on spine models used to simulate corrective surgeries. Overall, computational models have often been used to investigate surgical corrections. However, the validation of spine models was limited by data availability, especially in clinical applications. Moreover, the personalisation of models is broadly recognised as an important factor, especially if the model is being used in a clinical context. The anatomies (especially the bony anatomies) have been personalised extensively. However, the personalisation of the biomechanical properties of soft tissues had received considerably less attention. A limited number of studies had looked at the personalisation of the muscles and individual intervertebral soft tissues. Several approaches have been used to model intervertebral joints (the joint that represents the collection of ligaments and the intervertebral disc connecting two adjacent vertebrae), but few studies have personalised the properties of the joints, particularly in multibody modelling.

The first investigative study of this PhD project sought to research the characterisation of personalised intervertebral joint properties. Previous studies have used optimisation-based techniques but had not investigated the sensitivity of the optimisation to the definition of the joint. Furthermore, they have focused on the cervical spine, or used *in vivo* data, limiting the applicability to the lumbar spine and accuracy of the predicted kinematics. Therefore, this study tested the feasibility of a method for calibrating specimen-specific stiffness properties of a lumped parameter model of the intervertebral joint from an *ex vivo* experimental dataset. To do so, a specimen-specific model was created from CT data, and the model was placed in the experimental pose by performing a registration between the model and the digital image correlation data. The characterisation of specimen-specific material properties may be sensitive to the joint pose definition. The joint pose is defined from virtual palpations of anatomical landmarks. Therefore, to investigate this sensitivity, a Latin hypercube technique was employed to sample virtual palpations and define multiple joint poses. The method optimised the stiffnesses of a spine segment of four vertebrae (from L1 to L4) in anterior-posterior and axial compression translation and flexion-extension rotation. The sensitivity analysis demonstrated that a small number of combinations of optimised joint stiffnesses and joint poses could predict with high accuracy the kinematics (within 0.35mm and 0.25°). However, there was a large range of calibrated stiffnesses, indicating the optimisation methods and the resulting calibrated stiffnesses are highly sensitive to the joint pose definition. Both the stiffness and the joint pose contribute to the accuracy of the predicted kinematics; therefore, a two-factor analysis was performed to investigate the contribution of each. This found the joint pose definition was more important than the stiffness. This study indicated that the virtual palpation of the anatomical landmarks used to define the joint pose needs to be performed to a precision greater than 2.9 mm. However, this study was conducted on a single specimen over a small range of motion, which limits the findings' generalisability to longer segments and larger ranges of motion. Additionally, the stiffnesses were simplified to linear models. Nonetheless, the study highlights the importance of considering the joint pose when determining subject-specific lumped parameter models.

The second study sought to address some of these limitations, specifically, it sought to increase the sample size, the segment length, and the range of motion. The Institute of Orthopaedic Research and Biomechanics group at the University of Ulm generously shared an experimental dataset of the motion of six human cadaver specimens consisting of seven vertebrae (from T12 to S1) The specimens were loaded with pure moments (lateral bending, axial rotation, and flexion-extension torques). With multiple loading directions, it was also possible to address the influence of loading direction on stiffness optimisation. The previously established method was adapted to calibrate the stiffness properties for each of the six specimens under different loading conditions. Specifically, this dataset tracked the motion using a motion capture system. From this data, it was not possible to determine the experimental pose, rather an X-ray that had been taken for qualitative purposes had to be used. The stiffnesses were calibrated under two conditions, uniform stiffnesses across all levels (but independent in direction) and level-dependent stiffnesses. The level dependency was implemented with a fixed ratio that described the stiffness distribution. Results highlighted a high inter-specimen stiffness variability of the estimated joint stiffnesses in the same direction as that in which the loading was applied (e.g. the flexion-extension stiffness estimated from the flexion-extension experiment). The specimen-specific stiffnesses also differed substantially by loading condition. Thus, suggesting optimised stiffnesses should be not only considered specimen-specific but also load-specific. The calibration was less successful for the stiffnesses estimated for directions other than the one of the applied load (e.g. the flexion-extension

stiffness estimated from the lateral bending experiment). This implied a need for more sophisticated cost functions that better optimise the stiffnesses in the off-load directions or the inclusion of a coupled model. In addition, these longer spine segments allowed an investigation into the difference in stiffness between spinal levels. When simplifying the model with a uniform stiffness across all levels similar errors were seen at each level. The introduction of level-dependent stiffnesses allowed for the motion to be predicted much more accurately at some levels. Although the overall error for the level-dependent models may have been higher than for the uniform models, this is a reflection of the method used to implement the level dependency. The results therefore suggest that level-dependent stiffnesses are necessary to further improve prediction accuracy. However, the level dependency should not be implemented through a fixed ratio. A more suitable approach could be to allow complete independence between the spine levels. One of the limitations of this study was that the data had not originally been collected with the intention of being used in this study. Therefore, the X-ray used to determine the joint pose had only been taken for qualitative purposes. This limited the accuracy of the model reconstruction. Another major limitation of the study was the implementation of level dependency. A fixed ratio was not optimal; however, the computational expense was already high for the optimisation with a cardinality of three. To have the optimisation calibrate the stiffness at each level independently would have required increasing the cardinality to eighteen, and an associated increase in computational costs. Finally, the stiffness was modelled as linear. This is suitable if only a single point of the load curve is of interest but not if the entire curve is to be characterised. Despite these limitations, this study clearly shows the need for specimen- and load-specific stiffnesses for accurate kinematic predictions. Furthermore, it established that generic ratios are not a suitable method for describing the stiffness distribution across spine levels.

The stiffnesses identified in the previous studies were based on data from non-pathological spines. Therefore, they cannot be assumed to be appropriate representations of the stiffnesses of a scoliotic spine. However, the previous studies did contribute to the knowledge and understanding of the intervertebral joint and to building more realistic spine models, concepts which can be reapplied. However, before applying this knowledge, a scoliotic spine model was needed.

The final study of this thesis focused on developing a framework to create musculoskeletal models of the scoliotic spine from CT data. To do so, an existing healthy spine model was adapted to include six degrees of freedom as well as lumped parameters at each joint. In addition, wrapping surfaces were added to each vertebra to better guide the muscle paths and avoid in-bone penetration. To create the subject-specific scoliotic curvature a virtual palpation protocol was established to identify anatomical landmarks that allowed for the joint pose definition and the scaling of the vertebrae. The inter- and intra-operator variability of the method was investigated by an analysis of the variability of the position of repeated virtual palpations of anatomical landmarks. Then the sensitivity of the resulting model to this variability was evaluated. The analysis of the inter- and intra- operator variability of the virtual palpations found significant variation in the position of some landmarks used to define the joint, however further analysis found no trend or commonality in the variations. The overall variability of the virtually palpated landmark positions was 2 mm however outliers showed variation up to 12 mm. The models appeared to be robust to the inter- and intra- operator variability. However, the models tended to overextend while the shape of the curvature in the frontal plane matched well with the actual curvature of the patient. Consequently, larger errors in the vertebral centre position were observed in the anterior-posterior direction compared to the other directions. This error increased in the cranial direction. Despite this, the evaluation of the Cobb angle and the lumbar lordosis of the

models agreed well with the measurements from the radiographic evaluation. The field of view of the CT scan extended to T9 and did not capture the femoral heads. This limited the evaluation that was possible against other common radiographic measurements such as pelvic incidence and coronal imbalances. Additionally, the accuracy of the muscle paths was not evaluated against clinical data. The errors present in the positioning of the vertebral centres may be partly due to the use of generic vertebral geometries, however, future studies should seek to reduce these errors through refinement of the joint definition. Furthermore, the models incorporated generic stiffnesses rather than the ones determined in the previous studies. This was because the stiffnesses determined in the previous studies came from non-scoliotic spines. They are therefore unlikely to be representative of the stiffness in scoliotic spines, much less a patient-specific scoliotic stiffness. Instead, the package which was released includes an easy-to-implement function that will allow future researchers to easily change the stiffness to one that they deem more suitable. This study created an open-access package on the OpenSim SimTK forum (Personalised scoliotic spine models) which allows for the generation of subject-specific scoliotic models. The variability of the virtual palpation is 2mm, to which the models appear to be robust. Future works should look to include evaluation against more radiographic measurements and incorporate subject-specific stiffnesses.

6.2. Directions for future studies

Computational modelling of the spine is a promising avenue for future research. Some areas of study that could be especially interesting in the context of this thesis are:

- Calibration of non-linear specimen-specific lumped parameter models. Work has already begun in this area [52,126], but further investigation into inter-specimen variability, the effect of loading conditions, and different spine segments, to list a few, would enhance our understanding.
- Calibration of the subject-specific lumped parameters for scoliotic subjects. This would likely require a new methodology to be established to collect *in vivo* data (e.g., fluoroscopy data) suitable for the calibration techniques discussed in this thesis. Alternatively, *ex vivo* experiments would require the development of methods to model a scoliotic spine, as scoliotic specimens are hard to obtain. This would provide valuable information regarding the joint properties of scoliotic subjects which are crucial if musculoskeletal models are to be used as a tool to aid surgical planning.
- Similarly, there is a lack of data regarding other soft tissues, such as muscles, in scoliotic subjects. Research into these properties would be another important step towards creating models that are representative of scoliotic subjects.

6.3. Conclusions

To conclude, this work has tested the feasibility a methodology for calibrating specimen-specific lumped parameter models of the intervertebral joint from experimental data. The importance of specimen-specific parameters for accurate kinematic predictions was highlighted. Furthermore, as the use of optimisation techniques to determine specimen and subject-specific parameters becomes more widespread, researchers should be aware of the influence of the joint pose. In addition, a framework to generate scoliotic spine models has been developed and released in open access on the OpenSim forum. To further develop scoliotic spine models, future studies could start with the framework developed and incorporate more sophisticated models of the joints that better represent

scoliotic patients. In addition, simulations of corrective surgeries and postoperative complications could also be investigated and predicted, for instance, by simulating daily activities and estimating the resulting loads on instrumentation.

References

1. Galbusera F. Chapter 1 - The Spine: Its Evolution, Function, and Shape. In: Galbusera F, Wilke H-J, eds. *Biomechanics of the Spine*. Academic Press; 2018:3–9.

2. White AA, Panjabi MM. *Clinical biomechanics of the spine*. 2nd ed. Philadelphia: Lippincott; 1990.

3. Ruspi ML, Chehrassan M, Faldini C, Cristofolini L. In Vitro Experimental Studies and Numerical Modeling to Investigate the Biomechanical Effects of Surgical Interventions on the Spine. *Critical Reviews in Biomedical Engineering* 2019; **47**(4):295–322. doi:10.1615/CritRevBiomedEng.2019029498.

4. Oxland TR. Fundamental biomechanics of the spine—What we have learned in the past 25 years and future directions. *Journal of Biomechanics* 2016; **49**(6):817–832. doi:10.1016/j.jbiomech.2015.10.035.

5. Pollintine P, Przybyla AS, Dolan P, Adams MA. Neural arch load-bearing in old and degenerated spines. *Journal of Biomechanics* 2004; **37**(2):197–204. doi:10.1016/S0021-9290(03)00308-7.

6. Stokes IAF. Mechanical function of facet joints in the lumbar spine. *Clinical Biomechanics* 1988; **3**(2):101–105. doi:10.1016/0268-0033(88)90052-6.

7. Newell N, Little J, Christou A, Adams M, Adam C, Masouros S. Biomechanics of the human intervertebral disc: A review of testing techniques and results. *Journal of the Mechanical Behavior of Biomedical Materials* 2017; **69**:420–434. doi:10.1016/j.jmbbm.2017.01.037.

8. Pintar FA, Yoganandan N, Myers T, Elhagediab A, Sances A. Biomechanical properties of human lumbar spine ligaments. *Journal of Biomechanics* 1992; **25**(11):1351–1356. doi:10.1016/0021-9290(92)90290-H.

9. Stokes IAF, Bigalow LC, Moreland MS. Three-dimensional spinal curvature in idiopathic scoliosis. *Journal of Orthopaedic Research* 1987; **5**(1):102–113. doi:10.1002/jor.1100050113.

10. Negrini S, Donzelli S, Aulisa AG, et al. 2016 SOSORT guidelines: orthopaedic and rehabilitation treatment of idiopathic scoliosis during growth. *Scoliosis and Spinal Disorders* 2018; **13**(1):3. doi:10.1186/s13013-017-0145-8.

11. Weinstein SL, Dolan LA, Cheng JC, Danielsson A, Morcuende JA. Adolescent idiopathic scoliosis. *The Lancet* 2008; **371**(9623):1527–1537. doi:10.1016/S0140-6736(08)60658-3.

12. Stokes IAF, Aronson DD, Ronchetti PJ, Labelle H, Dansereau J. Reexamination of the Cobb and Ferguson Angles: Bigger Is Not Always Better. *Clinical Spine Surgery* 1993; **6**(4):333–338.

13. Malfair D, Flemming AK, Dvorak MF, et al. Radiographic Evaluation of Scoliosis: *Review*. *American Journal of Roentgenology* 2010; **194**(3_supplement):S8–S22. doi:10.2214/AJR.07.7145.

14. Dobbs MB, Weinstein SL. INFANTILE AND JUVENILE SCOLIOSIS. *Orthopedic Clinics of North America* 1999; **30**(3):331–341. doi:10.1016/S0030-5898(05)70090-0.

15. White AA, Panjabi MM. The Clinical Biomechanics of Scoliosis: *Clinical Orthopaedics and Related Research* 1976; (118):100–112. doi:10.1097/00003086-197607000-00018.

16. Negrini S, Grivas TB, Kotwicki T, et al. Why do we treat adolescent idiopathic scoliosis? What we want to obtain and to avoid for our patients. SOSORT 2005 Consensus paper. *Scoliosis* 2006; **1**(1):4. doi:10.1186/1748-7161-1-4.

17. Lenke LG, Betz RR, Harms J, et al. Adolescent Idiopathic Scoliosis : A New Classification to Determine Extent of Spinal Arthrodesis. *JBJS* 2001; **83**(8):1169.

18. Majdouline Y, Aubin C-E, Robitaille M, Sarwark JF, Labelle H. Scoliosis Correction Objectives in Adolescent Idiopathic Scoliosis. *Journal of Pediatric Orthopaedics* 2007; **27**(7):775–781. doi:10.1097/BPO.0b013e31815588d8.

19. Le Navéaux F, Larson AN, Labelle H, Aubin C-E. Significant variability in surgeons' preferred correction maneuvers and instrumentation strategies when planning adolescent idiopathic scoliosis surgery. *Scoliosis and Spinal Disorders* 2018; **13**:21. doi:10.1186/s13013-018-0169-8.

20. Schlösser TP, Abelin-Genevois K, Homans J, et al. Comparison of different strategies on three-dimensional correction of AIS: which plane will suffer? *European Spine Journal* 2021; **30**(3):645–652. doi:10.1007/s00586-020-06659-2.

21. Kim G-U, Yang JH, Chang D-G, et al. Effect of Direct Vertebral Rotation in Single Thoracic Adolescent Idiopathic Scoliosis: Better 3-Dimensional Deformity Correction. *World Neurosurgery* 2019; **129**:e401–e408. doi:10.1016/j.wneu.2019.05.164.

22. Cheung ZB, Selverian S, Cho BH, Ball CJ, Kang-Wook Cho S. Idiopathic Scoliosis in Children and Adolescents: Emerging Techniques in Surgical Treatment. *World Neurosurgery* 2019; **130**:e737–e742. doi:10.1016/j.wneu.2019.06.207.

23. Chang SY, Kim JH, Mok S, Chang B-S, Lee C-K, Kim H. The Use of High-Density Pedicle Screw Construct with Direct Vertebral Derotation of the Lowest Instrumented Vertebra in Selective Thoracic Fusion for Adolescent Idiopathic Scoliosis: Comparison of Two Surgical Strategies. *Asian Spine Journal* 2023. doi:10.31616/asj.2022.0111.

24. Chang MS, Lenke LG. Vertebral Derotation in Adolescent Idiopathic Scoliosis. *Operative Techniques in Orthopaedics* 2009; **19**(1):19–23. doi:10.1053/j.oto.2009.04.001.

25. Chen L, Sun Z, He J, et al. Effectiveness and safety of surgical interventions for treating adolescent idiopathic scoliosis: a Bayesian meta-analysis. *BMC Musculoskeletal Disorders* 2020; **21**(1):427. doi:10.1186/s12891-020-03233-1.

26. Weiss H-R, Goodall D. Rate of complications in scoliosis surgery – a systematic review of the Pub Med literature. *Scoliosis* 2008; **3**(1):9. doi:10.1186/1748-7161-3-9.

27. Kwan KYH, Koh HY, Blanke KM, Cheung KMC. Complications following surgery for adolescent idiopathic scoliosis over a 13-year period. *The Bone & Joint Journal* 2020; **102-B**(4):519–523. doi:10.1302/0301-620X.102B4.BJJ-2019-1371.R1.

28. Glassman SD, Carreon LY, Shaffrey CI, et al. Cost-effectiveness of adult lumbar scoliosis surgery: an as-treated analysis from the adult symptomatic scoliosis surgery trial with 5-year follow-up. *Spine Deformity* 2020; **8**(6):1333–1339. doi:10.1007/s43390-020-00154-w.

29. Roach JW, Mehlman CT, Sanders JO. "Does the Outcome of Adolescent Idiopathic Scoliosis Surgery Justify the Rising Cost of the Procedures?" *Journal of Pediatric Orthopaedics* 2011; **31**:S77. doi:10.1097/BPO.0b013e3181f73bfd.

30. Majdouline Y, Aubin C-E, Wang X, Sangole A, Labelle H. Preoperative assessment and evaluation of instrumentation strategies for the treatment of adolescent idiopathic scoliosis: computer simulation and optimization. *Scoliosis* 2012; **7**(1):21. doi:10.1186/1748-7161-7-21.

31. Aubin C-E, Labelle H, Ciolofan OC. Variability of spinal instrumentation configurations in adolescent idiopathic scoliosis. *European Spine Journal* 2007; **16**(1):57–64. doi:10.1007/s00586-006-0063-6.

32. Robitaille M, Aubin CE, Labelle H. Intra and interobserver variability of preoperative planning for surgical instrumentation in adolescent idiopathic scoliosis. *European Spine Journal* 2007; **16**(10):1604–1614. doi:10.1007/s00586-007-0431-x.

33. Holzbaur KRS, Murray WM, Delp SL. A Model of the Upper Extremity for Simulating Musculoskeletal Surgery and Analyzing Neuromuscular Control. *Annals of Biomedical Engineering* 2005; **33**(6):829–840. doi:10.1007/s10439-005-3320-7.

34. Aubin CE, Labelle H, Chevrefils C, Desroches G, Clin J, Eng ABM. Preoperative Planning Simulator for Spinal Deformity Surgeries. *Spine* 2008; **33**(20):2143–2152. doi:10.1097/BRS.0b013e31817bd89f.

35. La Barbera L, Larson AN, Aubin C-E. How do spine instrumentation parameters influence the 3D correction of thoracic adolescent idiopathic scoliosis? A patient-specific biomechanical study. *Clinical Biomechanics* 2021; **84**:105346. doi:10.1016/j.clinbiomech.2021.105346.

36. Dall'Ara E, Schmidt H, El-Rich M, O'Connell GD, Galbusera F. Editorial: Computational modeling for the assessment of the biomechanical properties of the healthy, diseased and treated spine. *Frontiers in Bioengineering and Biotechnology* 2022;

10.https://www.frontiersin.org/articles/10.3389/fbioe.2022.1016311AccessedOctober 27, 2022.

37. Mengoni M. Biomechanical modelling of the facet joints: a review of methods and validation processes in finite element analysis. *Biomechanics and Modeling in Mechanobiology* 2020; **20**(2):389–401. doi:10.1007/s10237-020-01403-7.

38. Niemeyer F, Wilke H-J, Schmidt H. Geometry strongly influences the response of numerical models of the lumbar spine—A probabilistic finite element analysis. *Journal of Biomechanics* 2012; **45**(8):1414–1423. doi:10.1016/j.jbiomech.2012.02.021.

39. Little JP, Adam CJ. Geometric sensitivity of patient-specific finite element models of the spine to variability in user-selected anatomical landmarks. *Computer Methods in Biomechanics and Biomedical Engineering* 2015; **18**(6):676–688. doi:10.1080/10255842.2013.843673.

40. Han K-S, Zander T, Taylor WR, Rohlmann A. An enhanced and validated generic thoraco-lumbar spine model for prediction of muscle forces. *Medical Engineering & Physics* 2012; **34**(6):709–716. doi:10.1016/j.medengphy.2011.09.014.

41. Bruno AG, Bouxsein ML, Anderson DE. Development and Validation of a Musculoskeletal Model of the Fully Articulated Thoracolumbar Spine and Rib Cage. *Journal of Biomechanical Engineering* 2015; **137**(8):081003. doi:10.1115/1.4030408.

42. Beaucage-Gauvreau E, Robertson WSP, Brandon SCE, et al. Validation of an OpenSim full-body model with detailed lumbar spine for estimating lower lumbar spine loads during symmetric and asymmetric lifting tasks. *Computer Methods in Biomechanics and Biomedical Engineering* 2019; **22**(5):451–464. doi:10.1080/10255842.2018.1564819.

43. Senteler M, Weisse B, Rothenfluh DA, Snedeker JG. Intervertebral reaction force prediction using an enhanced assembly of OpenSim models. *Computer Methods in Biomechanics and Biomedical Engineering* 2016; **19**(5):538–548. doi:10.1080/10255842.2015.1043906.

44. Bruno AG, Burkhart K, Allaire B, Anderson DE, Bouxsein ML. Spinal Loading Patterns From Biomechanical Modeling Explain the High Incidence of Vertebral Fractures in the Thoracolumbar Region: BIOMECHANICAL MODELING OF SPINAL LOADING PATTERNS. *Journal of Bone and Mineral Research* 2017; **32**(6):1282–1290. doi:10.1002/jbmr.3113.

45. Malakoutian M, Sanchez CA, Brown SHM, Street J, Fels S, Oxland TR. Biomechanical Properties of Paraspinal Muscles Influence Spinal Loading—A Musculoskeletal Simulation Study. *Frontiers in Bioengineering and Biotechnology* 2022; **10**.https://www.frontiersin.org/articles/10.3389/fbioe.2022.852201AccessedJanuary 20, 2023.

46. Alemi MM, Burkhart KA, Lynch AC, et al. The Influence of Kinematic Constraints on Model Performance During Inverse Kinematics Analysis of the Thoracolumbar Spine. *Frontiers in Bioengineering and Biotechnology* 2021;

9.https://www.frontiersin.org/articles/10.3389/fbioe.2021.688041AccessedOctober 27, 2022.

47. Ignasiak D, Valenzuela W, Reyes M, Ferguson SJ. The effect of muscle ageing and sarcopenia on spinal segmental loads. *European Spine Journal: Official Publication of the European Spine Society, the European Spinal Deformity Society, and the European Section of the Cervical Spine Research Society* 2018; **27**(10):2650–2659. doi:10.1007/s00586-018-5729-3.

48. Müller A, Rockenfeller R, Damm N, et al. Load Distribution in the Lumbar Spine During Modeled Compression Depends on Lordosis. *Frontiers in Bioengineering and Biotechnology* 2021; **9**:661258. doi:10.3389/fbioe.2021.661258.

49. Bassani T, Stucovitz E, Qian Z, Briguglio M, Galbusera F. Validation of the AnyBody full body musculoskeletal model in computing lumbar spine loads at L4L5 level. *Journal of Biomechanics* 2017; **58**:89–96. doi:10.1016/j.jbiomech.2017.04.025.

50. Ignasiak D, Dendorfer S, Ferguson SJ. Thoracolumbar spine model with articulated ribcage for the prediction of dynamic spinal loading. *Journal of Biomechanics* 2016; **49**(6):959–966. doi:10.1016/j.jbiomech.2015.10.010.

51. Alizadeh M, Knapik GG, Mageswaran P, Mendel E, Bourekas E, Marras WS. Biomechanical musculoskeletal models of the cervical spine: A systematic literature review. *Clinical Biomechanics* 2020; **71**:115–124. doi:10.1016/j.clinbiomech.2019.10.027.

52. Silvestros P, Preatoni E, Gill HS, et al. Musculoskeletal modelling of the human cervical spine for the investigation of injury mechanisms during axial impacts. *PLoS ONE* 2019; **14**(5). doi:10.1371/journal.pone.0216663.

53. Vasavada AN, Li S, Delp SL. Influence of Muscle Morphometry and Moment Arms on the Moment-Generating Capacity of Human Neck Muscles. *Spine* 1998; **23**(4):412.

54. Dreischarf M, Zander T, Shirazi-Adl A, et al. Comparison of eight published static finite element models of the intact lumbar spine: Predictive power of models improves when combined together. *Journal of Biomechanics* 2014; **47**(8):1757–1766. doi:10.1016/j.jbiomech.2014.04.002.

55. Schmidt H, Galbusera F, Antonius Rohlmann, Rohlmann A, Zander T, Wilke H-J. Effect of multilevel lumbar disc arthroplasty on spine kinematics and facet joint loads in flexion and extension: a finite element analysis. *European Spine Journal* 2012; **21**(5):663–674. doi:10.1007/s00586-010-1382-1.

56. Haddas R, Xu M, Lieberman I, Yang J. Finite Element Based-Analysis for Pre and Post Lumbar Fusion of Adult Degenerative Scoliosis Patients. *Spine Deformity* 2019; **7**(4):543–552. doi:10.1016/j.jspd.2018.11.008.

57. Naserkhaki S, Arjmand N, Shirazi-Adl A, Farahmand F, El-Rich M. Effects of eight different ligament property datasets on biomechanics of a lumbar L4-L5 finite element model. *Journal of Biomechanics* 2018; **70**:33–42. doi:10.1016/j.jbiomech.2017.05.003.

58. Affolter C, Kedzierska J, Vielma T, Weisse B, Aiyangar A. Estimating lumbar passive stiffness behaviour from subject-specific finite element models and in vivo 6DOF kinematics. *Journal of Biomechanics* 2020; **102**:109681. doi:10.1016/j.jbiomech.2020.109681.

59. Wang L, Zhang B, Chen S, Lu X, Li Z-Y, Guo Q. A Validated Finite Element Analysis of Facet Joint Stress in Degenerative Lumbar Scoliosis. *World Neurosurgery* 2016; **95**:126–133. doi:10.1016/j.wneu.2016.07.106.

60. Naserkhaki S, Jaremko JL, Adeeb S, El-Rich M. On the load-sharing along the ligamentous lumbosacral spine in flexed and extended postures: Finite element study. *Journal of Biomechanics* 2016; **49**(6):974–982. doi:10.1016/j.jbiomech.2015.09.050.

61. Dehghan-Hamani I, Arjmand N, Shirazi-Adl A. Subject-specific loads on the lumbar spine in detailed finite element models scaled geometrically and kinematic-driven by radiography images. *International Journal for Numerical Methods in Biomedical Engineering* 2019; **35**(4):e3182. doi:10.1002/cnm.3182.

62. Xu M, Yang J, Lieberman IH, Haddas R. Stress distribution in vertebral bone and pedicle screw and screw-bone load transfers among various fixation methods for lumbar spine surgical alignment: A finite element study. *Medical Engineering & Physics* 2019; **63**:26–32. doi:10.1016/j.medengphy.2018.10.003.

63. Schmidt H, Bashkuev M, Dreischarf M, et al. Computational biomechanics of a lumbar motion segment in pure and combined shear loads. *Journal of Biomechanics* 2013; **46**(14):2513–2521. doi:10.1016/j.jbiomech.2013.06.038.

64. Dreischarf M, Rohlmann A, Zhu R, Schmidt H, Zander T. Is it possible to estimate the compressive force in the lumbar spine from intradiscal pressure measurements? A finite element evaluation. *Medical Engineering & Physics* 2013; **35**(9):1385–1390. doi:10.1016/j.medengphy.2013.03.007.

65. Xu M, Yang J, Lieberman IH, Haddas R. Lumbar spine finite element model for healthy subjects: development and validation. *Computer Methods in Biomechanics and Biomedical Engineering* 2017; **20**(1):1–15. doi:10.1080/10255842.2016.1193596.

66. Zanjani-Pour S, Winlove CP, Smith CW, Meakin JR. Image driven subject-specific finite element models of spinal biomechanics. *Journal of Biomechanics* 2016; **49**(6):919–925. doi:10.1016/j.jbiomech.2016.02.025.

67. El Bojairami I, El-Monajjed K, Driscoll M. Development and validation of a timely and representative finite element human spine model for biomechanical simulations. *Scientific Reports* 2020; **10**(1):21519. doi:10.1038/s41598-020-77469-1.

68. Rohlmann A, Bauer L, Zander T, Bergmann G, Wilke H-J. Determination of trunk muscle forces for flexion and extension by using a validated finite element model of the lumbar spine and measured in vivo data. *Journal of Biomechanics* 2006; **39**(6):981–989. doi:10.1016/j.jbiomech.2005.02.019.

69. Wang W, Wang D, De Groote F, Scheys L, Jonkers I. Implementation of physiological functional spinal units in a rigid-body model of the thoracolumbar spine. *Journal of Biomechanics* 2020; **98**:109437. doi:10.1016/j.jbiomech.2019.109437.

70. Little JP, Adam C. Patient-specific computational biomechanics for simulating adolescent scoliosis surgery: Predicted vs clinical correction for a preliminary series of six patients. *International Journal for Numerical Methods in Biomedical Engineering* 2011; **27**(3):347–356. doi:10.1002/cnm.1422.

71. Little JP, Adam C. Development of a Computer Simulation Tool for Application in Adolescent Spinal Deformity Surgery. In: Bello F, Cotin S, eds. *Biomedical Simulation*, vol 5958. Berlin, Heidelberg: Springer Berlin Heidelberg; 2010:90–97.

72. Byrne RM, Aiyangar AK, Zhang X. Sensitivity of musculoskeletal model-based lumbar spinal loading estimates to type of kinematic input and passive stiffness properties. *Journal of Biomechanics* 2020; **102**:109659. doi:10.1016/j.jbiomech.2020.109659.

73. Demir E, Eltes P, Castro AP, Lacroix D, Toktaş İ. Finite element modelling of hybrid stabilization systems for the human lumbar spine. *Proceedings of the Institution of Mechanical Engineers, Part H: Journal of Engineering in Medicine* 2020; **234**(12):1409–1420. doi:10.1177/0954411920946636.

74. Musapoor A, Nikkhoo M, Haghpanahi M. A finite element study on intra-operative corrective forces and evaluation of screw density in scoliosis surgeries. *Proceedings of the Institution of Mechanical Engineers. Part H, Journal of Engineering in Medicine* 2018; **232**(12):1245–1254. doi:10.1177/0954411918810707.

75. Bojairami IE, Driscoll M. Coordination Between Trunk Muscles, Thoracolumbar Fascia, and Intra-Abdominal Pressure Toward Static Spine Stability. *Spine* 2021. doi:10.1097/brs.0000000000004223.

76. Fan W, Guo L-X. Influence of different frequencies of axial cyclic loading on time-domain vibration response of the lumbar spine: A finite element study. *Computers in Biology and Medicine* 2017; **86**:75–81. doi:10.1016/j.compbiomed.2017.05.004.

77. Castro APG. Computational Challenges in Tissue Engineering for the Spine. *Bioengineering* 2021; **8**(2):25. doi:10.3390/bioengineering8020025.

78. Eskandari AH, Arjmand N, Shirazi-Adl A, Farahmand F. Hypersensitivity of trunk biomechanical model predictions to errors in image-based kinematics when using fully displacement-control techniques. *Journal of Biomechanics* 2019; **84**:161–171. doi:10.1016/j.jbiomech.2018.12.043.

79. Viceconti M, Olsen S, Nolte L-P, Burton K. Extracting clinically relevant data from finite element simulations. *Clinical Biomechanics* 2005; **20**(5):451–454. doi:10.1016/j.clinbiomech.2005.01.010.

80. Grassi L, Schileo E, Taddei F, et al. Accuracy of finite element predictions in sideways load configurations for the proximal human femur. *Journal of Biomechanics* 2012; **45**(2):394–399. doi:10.1016/j.jbiomech.2011.10.019.

81. Seth A, Sherman M, Eastman P, Delp S. Minimal formulation of joint motion for biomechanisms. *Nonlinear Dynamics* 2010; **62**(1–2):291–303. doi:10.1007/s11071-010-9717-3.

82. Wu G, Siegler S, Allard P, et al. ISB recommendation on definitions of joint coordinate system of various joints for the reporting of human joint motion—part I: ankle, hip, and spine. *Journal of Biomechanics* 2002; **35**(4):543–548. doi:10.1016/S0021-9290(01)00222-6.

83. Huxley H, Hanson J. Changes in the Cross-Striations of Muscle during Contraction and Stretch and their Structural Interpretation. *Nature* 1954; **173**(4412):973–976. doi:10.1038/173973a0.

84. Röhrle O, Sprenger M, Schmitt S. A two-muscle, continuum-mechanical forward simulation of the upper limb. *Biomechanics and Modeling in Mechanobiology* 2017; **16**(3):743–762. doi:10.1007/s10237-016-0850-x.

85. Frey Law LA, Shields RK. Predicting human chronically paralyzed muscle force: a comparison of three mathematical models. *Journal of Applied Physiology* 2006; **100**(3):1027–1036. doi:10.1152/japplphysiol.00935.2005.

86. Caillet AH, Phillips ATM, Carty C, Farina D, Modenese L. Hill-type computational models of muscle-tendon actuators: a systematic review. 2022:2022.10.14.512218.

87. Xu X, Deng H, Zhang Y, Chen J. Continuous Grasping Force Estimation With Surface EMG Based on Huxley-Type Musculoskeletal Model. *IEEE Transactions on Neural Systems and Rehabilitation Engineering* 2023; **31**:346–355. doi:10.1109/TNSRE.2022.3214866.

88. Schmitt S, Günther M, Häufle DFB. The dynamics of the skeletal muscle: A systems biophysics perspective on muscle modeling with the focus on Hill-type muscle models. *GAMM-Mitteilungen* 2019; **42**(3):e201900013. doi:10.1002/gamm.201900013.

89. Seth A, Hicks JL, Uchida TK, et al. OpenSim: Simulating musculoskeletal dynamics and neuromuscular control to study human and animal movement. Schneidman D, ed. *PLOS Computational Biology* 2018; **14**(7):e1006223. doi:10.1371/journal.pcbi.1006223.

90. Delp SL, Anderson FC, Arnold AS, et al. OpenSim: Open-Source Software to Create and Analyze Dynamic Simulations of Movement. *IEEE Transactions on Biomedical Engineering* 2007; **54**(11):1940–1950. doi:10.1109/TBME.2007.901024.

91. Rasmussen J, Vondrak V, Damsgaard M, De Zee M, Christensen ST, Dostal Z. The anybody project–computer analysis of the human body. *Biomechanics of Man* 2002; **270**:274.

92. Millard M, Uchida T, Seth A, Delp SL. Flexing Computational Muscle: Modeling and Simulation of Musculotendon Dynamics. *Journal of Biomechanical Engineering* 2013; **135**(2). doi:10.1115/1.4023390.

93. Hicks JL, Uchida TK, Seth A, Rajagopal A, Delp SL. Is My Model Good Enough? Best Practices for Verification and Validation of Musculoskeletal Models and Simulations of Movement. *Journal of Biomechanical Engineering* 2015; **137**(020905). doi:10.1115/1.4029304.

94. De Groote F, Falisse A. Perspective on musculoskeletal modelling and predictive simulations of human movement to assess the neuromechanics of gait. *Proceedings of the Royal Society B: Biological Sciences* 2021; **288**(1946):20202432. doi:10.1098/rspb.2020.2432.

95. Aeles J, Lichtwark G, Peeters D, Delecluse C, Jonkers I, Vanwanseele B. Effect of a prehop on the muscle-tendon interaction during vertical jumps. *Journal of Applied Physiology* 2018; **124**(5):1203–1211. doi:10.1152/japplphysiol.00462.2017.

96. Mörl F, Siebert T, Schmitt S, Blickhan R, Günther M. Electro-mechanical delay in hill-type muscle models. *Journal of Mechanics in Medicine and Biology* 2012; **12**(05):1250085. doi:10.1142/S0219519412500856.

97. Stollenmaier K, Ilg W, Haeufle DFB. Predicting Perturbed Human Arm Movements in a Neuro-Musculoskeletal Model to Investigate the Muscular Force Response. *Frontiers in Bioengineering and Biotechnology* 2020; **8**.https://www.frontiersin.org/articles/10.3389/fbioe.2020.00308AccessedMarch 28, 2023.

98. Miller RH, Umberger BR, Caldwell GE. Limitations to maximum sprinting speed imposed by muscle mechanical properties. *Journal of Biomechanics* 2012; **45**(6):1092–1097. doi:10.1016/j.jbiomech.2011.04.040.

99. Silvestros P, Pizzolato C, Lloyd DG, Preatoni E, Gill HS, Cazzola D. Electromyography-Assisted Neuromusculoskeletal Models Can Estimate Physiological Muscle Activations and Joint Moments Across the Neck Before Impacts. *Journal of Biomechanical Engineering* 2021; **144**(3). doi:10.1115/1.4052555.

100. Guo J, Wang J, Chen J, Ren G, Tian Q, Guo C. Multibody dynamics modeling of human mandibular musculoskeletal system and its applications in surgical planning. *Multibody System Dynamics* 2023. doi:10.1007/s11044-023-09876-x.

101. Kapelner T, Sartori M, Negro F, Farina D. Neuro-Musculoskeletal Mapping for Man-Machine Interfacing. *Scientific Reports* 2020; **10**(1):5834. doi:10.1038/s41598-020-62773-7.

102. Serrancolí G, Kinney AL, Fregly BJ. Influence of musculoskeletal model parameter values on prediction of accurate knee contact forces during walking. *Medical Engineering & Physics* 2020; **85**:35–47. doi:10.1016/j.medengphy.2020.09.004.

103. Uhlrich SD, Jackson RW, Seth A, Kolesar JA, Delp SL. Muscle coordination retraining inspired by musculoskeletal simulations reduces knee contact force. *Scientific Reports* 2022; **12**(1):9842. doi:10.1038/s41598-022-13386-9.

104. Gould SL, Cristofolini L, Davico G, Viceconti M. Computational modelling of the scoliotic spine: A literature review. *International Journal for Numerical Methods in Biomedical Engineering* **n/a**(n/a):e3503. doi:10.1002/cnm.3503.

105. Rupp TK, Ehlers W, Karajan N, Günther M, Schmitt S. A forward dynamics simulation of human lumbar spine flexion predicting the load sharing of intervertebral discs, ligaments, and muscles. *Biomechanics and Modeling in Mechanobiology* 2015; **14**(5):1081–1105. doi:10.1007/s10237-015-0656-2.

106. Christophy M, Curtin M, Faruk Senan NA, Lotz JC, O'Reilly OM. On the modeling of the intervertebral joint in multibody models for the spine. *Multibody System Dynamics* 2013; **30**(4):413–432. doi:10.1007/s11044-012-9331-x.

107. Meng X, Bruno AG, Cheng B, Wang W, Bouxsein ML, Anderson DE. Incorporating Six Degree-of-Freedom Intervertebral Joint Stiffness in a Lumbar Spine Musculoskeletal Model—Method and Performance in Flexed Postures. *Journal of Biomechanical Engineering* 2015; **137**(10):101008. doi:10.1115/1.4031417.

108. Gardner-Morse MG, Stokes IAF. Structural behavior of human lumbar spinal motion segments. *Journal of Biomechanics* 2004; **37**(2):205–212. doi:10.1016/j.jbiomech.2003.10.003.

109. Zhang C, Mannen EM, Sis HL, et al. Moment-rotation behavior of intervertebral joints in flexion-extension, lateral bending, and axial rotation at all levels of the human spine: A structured review and meta-regression analysis. *Journal of Biomechanics* 2020; **100**:109579. doi:10.1016/j.jbiomech.2019.109579.

110. Kamal Z, Rouhi G, Arjmand N, Adeeb S. A stability-based model of a growing spine with adolescent idiopathic scoliosis: A combination of musculoskeletal and finite element approaches. *Medical Engineering & Physics* 2019; **64**:46–55. doi:10.1016/j.medengphy.2018.12.015.

111. Jalalian A, Tay FEH, Arastehfar S, Gibson I, Liu G. Finding line of action of the force exerted on erect spine based on lateral bending test in personalization of scoliotic spine models. *Medical & Biological Engineering & Computing* 2017; **55**(4):673–684. doi:10.1007/s11517-016-1550-5.

112. Izambert O, Mitton D, Thourot M, Lavaste F. Dynamic stiffness and damping of human intervertebral disc using axial oscillatory displacement under a free mass system. *European Spine Journal* 2003; **12**(6):562–566. doi:10.1007/s00586-003-0569-0.

113. Alkalay RN, Vader D, Hackney D. The degenerative state of the intervertebral disk independently predicts the failure of human lumbar spine to high rate loading: An experimental study. *Clinical Biomechanics* 2015; **30**(2):211–218. doi:10.1016/j.clinbiomech.2014.09.016.

114. Senteler M, Aiyangar A, Weisse B, Farshad M, Snedeker JG. Sensitivity of intervertebral joint forces to center of rotation location and trends along its migration path. *Journal of Biomechanics* 2018; **70**:140–148. doi:10.1016/j.jbiomech.2017.10.027.

115. Damm N, Rockenfeller R, Gruber K. Lumbar spinal ligament characteristics extracted from stepwise reduction experiments allow for preciser modeling than literature data. *Biomechanics and Modeling in Mechanobiology* 2020; **19**(3):893–910. doi:10.1007/s10237-019-01259-6.

116. Fregly BJ. A Conceptual Blueprint for Making Neuromusculoskeletal Models Clinically Useful. *Applied Sciences* 2021; **11**(5):2037. doi:10.3390/app11052037.

117. Bruno AG, Mokhtarzadeh H, Allaire BT, et al. Incorporation of CT-based measurements of trunk anatomy into subject-specific musculoskeletal models of the spine influences vertebral loading predictions: SUBJECT-SPECIFIC THORACOLUMBAR SPINE MODELS. *Journal of Orthopaedic Research* 2017; **35**(10):2164–2173. doi:10.1002/jor.23524.

118. Overbergh T, Severijns P, Beaucage-Gauvreau E, Jonkers I, Moke L, Scheys L. Development and validation of a modeling workflow for the generation of image-based, subject-specific thoracolumbar models of spinal deformity. *Journal of Biomechanics* 2020:109946. doi:10.1016/j.jbiomech.2020.109946.

119. Fasser M-R, Moritz Jokeit, Mirjam Kalthoff, et al. Subject-Specific Alignment and Mass Distribution in Musculoskeletal Models of the Lumbar Spine. *Frontiers in Bioengineering and Biotechnology* 2021; **9**:721042. doi:10.3389/fbioe.2021.721042.

120. Schmid S, Burkhart KA, Allaire BT, Grindle D, Anderson DE. Musculoskeletal full-body models including a detailed thoracolumbar spine for children and adolescents aged 6–18 years. *3rd International Workshop on Spine Loading and Deformation* 2020; **102**:109305. doi:10.1016/j.jbiomech.2019.07.049.

121. Bassani T, Ottardi C, Costa F, Brayda-Bruno M, Wilke H-J, Galbusera F. Semiautomated 3D Spine Reconstruction from Biplanar Radiographic Images: Prediction of Intervertebral Loading in Scoliotic Subjects. *Frontiers in Bioengineering and Biotechnology* 2017; **5**. doi:10.3389/fbioe.2017.00001.

122. Barba N, Ignasiak D, Villa TMT, Galbusera F, Bassani T. Assessment of trunk muscle activation and intervertebral load in adolescent idiopathic scoliosis by musculoskeletal modelling approach. *Journal of Biomechanics* 2021; **114**:110154. doi:10.1016/j.jbiomech.2020.110154.

123. Schmid S, Burkhart KA, Allaire BT, et al. Spinal Compressive Forces in Adolescent Idiopathic Scoliosis With and Without Carrying Loads: A Musculoskeletal Modeling Study. *Frontiers in Bioengineering and Biotechnology* 2020; **8**. doi:10.3389/fbioe.2020.00159.

124. Bassani T, Cina A, Ignasiak D, Barba N, Galbusera F. Accounting for Biomechanical Measures from Musculoskeletal Simulation of Upright Posture Does Not Enhance the Prediction of Curve Progression in Adolescent Idiopathic Scoliosis. *Frontiers in Bioengineering and Biotechnology* 2021; **9**:703144. doi:10.3389/fbioe.2021.703144.

125. Little JP, Adam CJ. The Effect of Soft Tissue Properties on Spinal Flexibility in Scoliosis: Biomechanical Simulation of Fulcrum Bending. *Spine* 2009; **34**(2):E76–E82. doi:10.1097/BRS.0b013e31818ad584.

126. Wang W, Wang D, Falisse A, et al. A Dynamic Optimization Approach for Solving Spine Kinematics While Calibrating Subject-Specific Mechanical Properties. *Annals of Biomedical Engineering* 2021. doi:10.1007/s10439-021-02774-3.

127. Petit Y, Aubin CÉ, Labelle H. Patient-specific mechanical properties of a flexible multi-body model of the scoliotic spine. *Medical and Biological Engineering and Computing* 2004; **42**(1):55–60. doi:10.1007/BF02351011.

128. Ignasiak D, Behm P, Mannion AF, et al. Association between sagittal alignment and loads at the adjacent segment in the fused spine: a combined clinical and musculoskeletal modeling study of 205 patients with adult spinal deformity. *European Spine Journal* 2023; **32**(2):571–583. doi:10.1007/s00586-022-07477-4.

129. Delikaris A, Wang X, Boyer L, Larson AN, Ledonio CGT, Aubin C-E. Implant Density at the Apex Is More Important Than Overall Implant Density for 3D Correction in Thoracic Adolescent Idiopathic Scoliosis Using Rod Derotation and En Bloc Vertebral Derotation Technique. *SPINE* 2018; **43**(11):E639–E647. doi:10.1097/BRS.0000000000002465.

130. Shen J, Parent S, Wu J, et al. Towards a new 3D classification for adolescent idiopathic scoliosis. *Spine Deformity* 2020; **8**(3):387–396. doi:10.1007/s43390-020-00051-2.

131. Weinstein SL. The Natural History of Adolescent Idiopathic Scoliosis. *Journal of Pediatric Orthopaedics* 2019; **39**:S44–S46. doi:10.1097/BPO.0000000000001350.

132. Yang S, Andras LM, Redding GJ, Skaggs DL. Early-Onset Scoliosis: A Review of History, Current Treatment, and Future Directions. *Pediatrics* 2016; **137**(1):e20150709. doi:10.1542/peds.2015-0709.

133. Maruyama T, Takeshita K. Surgical treatment of scoliosis: a review of techniques currently applied. *Scoliosis* 2008; **3**(1):6. doi:10.1186/1748-7161-3-6.

134. Al-Mohrej OA, Aldakhil SS, Al-Rabiah MA, Al-Rabiah AM. Surgical treatment of adolescent idiopathic scoliosis: Complications. *Annals of Medicine and Surgery* 2020; **52**:19–23. doi:10.1016/j.amsu.2020.02.004.

135. Majdouline Y, Aubin C-E, Sangole A, Labelle H. Computer simulation for the optimization of instrumentation strategies in adolescent idiopathic scoliosis. *Medical & Biological Engineering & Computing* 2009; **47**(11):1143. doi:10.1007/s11517-009-0509-1.

136. Fradet L, Wang X, Lenke LG, Aubin C-E. Biomechanical analysis of proximal junctional failure following adult spinal instrumentation using a comprehensive hybrid modeling approach. *Clinical Biomechanics (Bristol, Avon)* 2016; **39**:122–128. doi:10.1016/j.clinbiomech.2016.10.008.

137. Rajaee MA, Arjmand N, Shirazi-Adl A. A novel coupled musculoskeletal finite element model of the spine – Critical evaluation of trunk models in some tasks. *Journal of Biomechanics* 2021; **119**:110331. doi:10.1016/j.jbiomech.2021.110331.

138. Knapik GG, Mendel E, Marras WS. Use of a personalized hybrid biomechanical model to assess change in lumbar spine function with a TDR compared to an intact spine. *European Spine Journal* 2012; **21**(5):641–652. doi:10.1007/s00586-011-1743-4.

139. Remus R, Lipphaus A, Neumann M, Bender B. Calibration and validation of a novel hybrid model of the lumbosacral spine in ArtiSynth–The passive structures. *PLOS ONE* 2021; **16**(4):e0250456. doi:10.1371/journal.pone.0250456.

140. Khoddam-Khorasani P, Arjmand N, Shirazi-Adl A. Trunk Hybrid Passive–Active Musculoskeletal Modeling to Determine the Detailed T12–S1 Response Under In Vivo Loads. *Annals of Biomedical Engineering* 2018; **46**(11):1830–1843. doi:10.1007/s10439-018-2078-7.

141. Dreischarf M, Shirazi-Adl A, Arjmand N, Rohlmann A, Schmidt H. Estimation of loads on human lumbar spine: A review of in vivo and computational model studies. *Journal of Biomechanics* 2016; **49**(6):833–845. doi:10.1016/j.jbiomech.2015.12.038.

142. Wang W, Baran GR, Betz RR, Samdani AF, Pahys JM, Cahill PJ. The Use of Finite Element Models to Assist Understanding and Treatment For Scoliosis: A Review Paper. *Spine Deformity* 2014; **2**(1):10–27. doi:10.1016/j.jspd.2013.09.007.

143. Jalalian A, Gibson I, Tay EH. Computational Biomechanical Modeling of Scoliotic Spine: Challenges and Opportunities. *Spine Deformity* 2013; **1**(6):401–411. doi:10.1016/j.jspd.2013.07.009.

144. Fan N, Zang L, Hai Y, Du P, Yuan S. [Progression on finite element modeling method in scoliosis]. *Zhongguo Gu Shang = China Journal of Orthopaedics and Traumatology* 2018; **31**(4):391–394. doi:10.3969/j.issn.1003-0034.2018.04.018.

145. Byvaltsev VA, Kalinin AA, Belykh EG, Stepanov IA. [Simulation technologies in spinal surgery]. *Vestnik Rossiiskoi Akademii Meditsinskikh Nauk* 2016; **71**(4):297–303. doi:10.15690/vramn681.

146. Galbusera F, Wilke H-J, Brayda-Bruno M, Costa F, Fornari M. Influence of sagittal balance on spinal lumbar loads: A numerical approach. *Clinical Biomechanics* 2013; **28**(4):370–377. doi:10.1016/j.clinbiomech.2013.02.006.

147. Jackson RP, McManus AC. Radiographic Analysis of Sagittal Plane Alignment and Balance in Standing Volunteers and Patients with Low Back Pain Matched for Age, Sex, and Size: A Prospective Controlled Clinical Study. *Spine* 1994; **19**(14):1611–1618.

148. Duval-Beaupère G, Schmidt C, Cosson P. A barycentremetric study of the sagittal shape of spine and pelvis: The conditions required for an economic standing position. *Annals of Biomedical Engineering* 1992; **20**(4):451–462. doi:10.1007/BF02368136.

149. Mills MJ, Sarigul-Klijn N. Validation of an In Vivo Medical Image-Based Young Human Lumbar Spine Finite Element Model. *Journal of Biomechanical Engineering* 2019; **141**(3):031003. doi:10.1115/1.4042183.

150. Naserkhaki S, Jaremko JL, El-Rich M. Effects of inter-individual lumbar spine geometry variation on load-sharing: Geometrically personalized Finite Element study. *Journal of Biomechanics* 2016; **49**(13):2909–2917. doi:10.1016/j.jbiomech.2016.06.032.

151. Galbusera F, Brayda-Bruno M, Costa F, Wilke H-J. Numerical evaluation of the correlation between the normal variation in the sagittal alignment of the lumbar spine and the spinal loads. *Journal of Orthopaedic Research* 2014; **32**(4):537–544. doi:10.1002/jor.22569.

152. Cappetti N, Naddeo A, Naddeo F, Solitro GF. Finite elements/Taguchi method based procedure for the identification of the geometrical parameters significantly affecting the biomechanical behavior of a lumbar disc. *Computer Methods in Biomechanics and Biomedical Engineering* 2016; **19**(12):1278–1285. doi:10.1080/10255842.2015.1128529.

153. Jebaseelan DD, Jebaraj C, Yoganandan N, Rajasekaran S, Kanna RM. Sensitivity studies of pediatric material properties on juvenile lumbar spine responses using finite element analysis. *Medical & Biological Engineering & Computing* 2012; **50**(5):515–522. doi:10.1007/s11517-012-0896-6.

154. Schmidt H, Heuer F, Simon U, et al. Application of a new calibration method for a three-dimensional finite element model of a human lumbar annulus fibrosus. *Clinical Biomechanics* 2006; **21**(4):337–344. doi:10.1016/j.clinbiomech.2005.12.001.

155. Fan R-X, Liu J, Li Y-L, Liu J, Gao J-Z. Finite Element Investigation of the Effects of the Low-Frequency Vibration Generated by Vehicle Driving on the Human Lumbar Mechanical Properties. *BioMed Research International* 2018; **2018**:7962414. doi:10.1155/2018/7962414.

156. Zanjani-Pour S, Meakin JR, Breen A, Breen A. Estimation of in vivo inter-vertebral loading during motion using fluoroscopic and magnetic resonance image informed finite element models. *Journal of Biomechanics* 2018; **70**:134–139. doi:10.1016/j.jbiomech.2017.09.025.

157. Leivseth G, Brinckmann P, Frobin W, Johnsson R, Strömqvist B. Assessment of Sagittal Plane Segmental Motion in the Lumbar Spine: A Comparison Between Distortion-Compensated and Stereophotogrammetric Roentgen Analysis. *Spine* 1998; **23**(23):2648–2655.

158. Arjmand N, Shirazi-Adl A. Model and in vivo studies on human trunk load partitioning and stability in isometric forward flexions. *Journal of Biomechanics* 2006; **39**(3):510–521. doi:10.1016/j.jbiomech.2004.11.030.

159. Breen AC, Muggleton JM, Mellor FE. An objective spinal motion imaging assessment (OSMIA): reliability, accuracy and exposure data. *BMC Musculoskeletal Disorders* 2006; **7**:1. doi:10.1186/1471-2474-7-1.

160. Narain AS, Hijji FY, Yom KH, Kudaravalli KT, Haws BE, Singh K. Radiation exposure and reduction in the operating room: Perspectives and future directions in spine surgery. *World Journal of Orthopedics* 2017; **8**(7):524–530. doi:10.5312/wjo.v8.i7.524.

161. Keller MC, Hurschler C, Schwarze M. Experimental evaluation of precision and accuracy of RSA in the lumbar spine. *European Spine Journal* 2020. doi:10.1007/s00586-020-06672-5.

162. Frobin W, Brinckmann P, Leivseth G, Biggemann M, Reikerås O. Precision measurement of segmental motion from flexion—extension radiographs of the lumbar spine. *Clinical Biomechanics* 1996; **11**(8):457–465. doi:10.1016/S0268-0033(96)00039-3.

163. Mahallati S, Rouhani H, Preuss R, Masani K, Popovic MR. Multisegment Kinematics of the Spinal Column: Soft Tissue Artifacts Assessment. *Journal of Biomechanical Engineering* 2016; **138**(7):071003. doi:10.1115/1.4033545.

164. Shojaei I, Arjmand N, Meakin JR, Bazrgari B. A model-based approach for estimation of changes in lumbar segmental kinematics associated with alterations in trunk muscle forces. *Journal of Biomechanics* 2018; **70**:82–87. doi:10.1016/j.jbiomech.2017.09.024.

165. Ghezelbash F, Shirazi-Adl A, Arjmand N, El-Ouaaid Z, Plamondon A. Subject-specific biomechanics of trunk: musculoskeletal scaling, internal loads and intradiscal pressure estimation. *Biomechanics and Modeling in Mechanobiology* 2016; **15**(6):1699–1712. doi:10.1007/s10237-016-0792-3.

166. Patwardhan AG, Havey RM, Carandang G, et al. Effect of compressive follower preload on the flexion–extension response of the human lumbar spine. *Journal of Orthopaedic Research* 2003; **21**(3):540–546. doi:10.1016/S0736-0266(02)00202-4.

167. Zhang H, Zhu W. The path to deliver the most realistic follower load for a lumbar spine in standing posture: A finite element study. *Journal of Biomechanical Engineering* 2019. doi:10.1115/1.4042438.

168. Dreischarf M, Zander T, Bergmann G, Rohlmann A. A non-optimized follower load path may cause considerable intervertebral rotations. *Journal of Biomechanics* 2010; **43**(13):2625–2628. doi:10.1016/j.jbiomech.2010.05.033.

169. Foresto T, Song I, Kim BS, Lim T-H. Stabilization of the lumbar spine by spinal muscle forces producing compressive follower loads: 3-dimensional computational study. *Journal of Orthopaedic Research: Official Publication of the Orthopaedic Research Society* 2018; **36**(11):3004–3012. doi:10.1002/jor.24059.

170. Dreischarf M, Rohlmann A, Bergmann G, Zander T. Optimised in vitro applicable loads for the simulation of lateral bending in the lumbar spine. *Medical Engineering & Physics* 2012; **34**(6):777–780. doi:10.1016/j.medengphy.2012.04.002.

171. Azari F, Arjmand N, Shirazi-Adl A, Rahimi-Moghaddam T. A combined passive and active musculoskeletal model study to estimate L4-L5 load sharing. *Journal of Biomechanics* 2018; **70**:157–165. doi:10.1016/j.jbiomech.2017.04.026.

172. Liu T, Khalaf K, Adeeb S, El-Rich M. Effects of lumbo-pelvic rhythm on trunk muscle forces and disc loads during forward flexion: A combined musculoskeletal and finite element simulation study. *Journal of Biomechanics* 2019; **82**:116–123. doi:10.1016/j.jbiomech.2018.10.009.

173. Liu T, Khalaf K, Adeeb S, El-Rich M. Numerical Investigation of Intra-abdominal Pressure Effects on Spinal Loads and Load-Sharing in Forward Flexion. *Frontiers in Bioengineering and Biotechnology* 2019; **7**. doi:10.3389/fbioe.2019.00428.

174. Zander T, Rohlmann A, Calisse J, Bergmann G. Estimation of muscle forces in the lumbar spine during upper-body inclination. *Clinical Biomechanics* 2001; **16**:S73–S80. doi:10.1016/S0268-0033(00)00108-X.

175. Xie F, Zhou H, Zhao W, Huang L. A comparative study on the mechanical behavior of intervertebral disc using hyperelastic finite element model. *Technology and Health Care: Official Journal of the European Society for Engineering and Medicine* 2017; **25**(S1):177–187. doi:10.3233/THC-171320.

176. Newell N, Carpanen D, Grigoriadis G, Little JP, Masouros SD. Material properties of human lumbar intervertebral discs across strain rates. *The Spine Journal* 2019; **19**(12):2013–2024. doi:10.1016/j.spinee.2019.07.012.

177. Ghezelbash F, Shirazi-Adl A, Arjmand N, El-Ouaaid Z, Plamondon A, Meakin JR. Effects of sex, age, body height and body weight on spinal loads: Sensitivity analyses in a subject-specific trunk musculoskeletal model. *Journal of Biomechanics* 2016; **49**(14):3492–3501. doi:10.1016/j.jbiomech.2016.09.026.

178. Ghezelbash F, Shirazi-Adl A, El Ouaaid Z, Plamondon A, Arjmand N. Subject-specific regression equations to estimate lower spinal loads during symmetric and asymmetric static lifting. *Journal of Biomechanics* 2020; **102**:109550. doi:10.1016/j.jbiomech.2019.109550.

179. Ghezelbash F, Schmidt H, Shirazi-Adl A, El-Rich M. Internal load-sharing in the human passive lumbar spine: Review of in vitro and finite element model studies. *Journal of Biomechanics* 2020; **102**:109441. doi:10.1016/j.jbiomech.2019.109441.

180. Nishida N, Ohgi J, Jiang F, et al. Finite Element Method Analysis of Compression Fractures on Whole-Spine Models Including the Rib Cage. *Computational and Mathematical Methods in Medicine* 2019; **2019**:8348631. doi:10.1155/2019/8348631.

181. Little JP, Izatt MT, Labrom RD, Askin GN, Adam CJ. An FE investigation simulating intra-operative corrective forces applied to correct scoliosis deformity. *Scoliosis* 2013; **8**(1). doi:10.1186/1748-7161-8-9.

182. Hadagali P, Peters JR, Balasubramanian S. Morphing the feature-based multi-blocks of normative/healthy vertebral geometries to scoliosis vertebral geometries: development of personalized finite element models. *Computer Methods in Biomechanics and Biomedical Engineering* 2018; **21**(4):297–324. doi:10.1080/10255842.2018.1448391.

183. Delorme S, Petit Y, Guise JA de, Labelle H, Aubin C-, Dansereau J. Assessment of the 3-D reconstruction and high-resolution geometrical modeling of the human skeletal trunk from 2-D radiographic images. *IEEE Transactions on Biomedical Engineering* 2003; **50**(8):989–998. doi:10.1109/TBME.2003.814525.

184. Trochu F. A contouring program based on dual kriging interpolation. *Engineering with Computers* 1993; **9**(3):160–177. doi:10.1007/BF01206346.

185. Jobidon-Lavergne H, Kadoury S, Knez D, Aubin C-É. Biomechanically driven intraoperative spine registration during navigated anterior vertebral body tethering. *Physics in Medicine and Biology* 2019; **64**(11):115008. doi:10.1088/1361-6560/ab1bfa.

186. Duke K, Aubin C-E, Dansereau J, Labelle H. Biomechanical simulations of scoliotic spine correction due to prone position and anaesthesia prior to surgical instrumentation. *Clinical Biomechanics* 2005; **20**(9):923–931. doi:10.1016/j.clinbiomech.2005.05.006.

187. Driscoll CR, Aubin C-É, Canet F, Labelle H, Dansereau J. Impact of Prone Surgical Positioning on the Scoliotic Spine. *Journal of Spinal Disorders & Techniques* 2012; **25**(3):173–181. doi:10.1097/BSD.0b013e318211ffa6.

188. Jia S, Li Y, Xie J, Tian T, Zhang S, Han L. Differential response to vibration of three forms of scoliosis during axial cyclic loading: a finite element study. *BMC musculoskeletal disorders* 2019; **20**(1):370. doi:10.1186/s12891-019-2728-4.

189. Song X-X, Jin L-Y, Li X-F, et al. Effects of Low Bone Mineral Status on Biomechanical Characteristics in Idiopathic Scoliotic Spinal Deformity. *World Neurosurgery* 2018; **110**:e321–e329. doi:10.1016/j.wneu.2017.10.177.

190. Pasha S, Aubin C-E, Parent S, Labelle H, Mac-Thiong J-M. Biomechanical loading of the sacrum in adolescent idiopathic scoliosis. *Clinical Biomechanics* 2014; **29**(3):296–303. doi:10.1016/j.clinbiomech.2013.12.004.

191. Jia S, Lin L, Yang H, Fan J, Zhang S, Han L. The influence of the rib cage on the static and dynamic stability responses of the scoliotic spine. *Scientific Reports* 2020; **10**(1). doi:10.1038/s41598-020-73881-9.

192. Cheuk KY, Zhu TY, Yu FWP, et al. Abnormal Bone Mechanical and Structural Properties in Adolescent Idiopathic Scoliosis: A Study with Finite Element Analysis and Structural Model Index. *Calcified Tissue International* 2015; **97**(4):343–352. doi:10.1007/s00223-015-0025-2.

193. Li X-F, Li H, Liu Z-D, Dai L-Y. Low bone mineral status in adolescent idiopathic scoliosis. *European Spine Journal* 2008; **17**(11):1431–1440. doi:10.1007/s00586-008-0757-z.

194. Berger S, Marcello O, Schuman S, et al. Patient-specific spinal stiffness in AIS: a preoperative and noninvasive method. *European Spine Journal* 2015; **24**(2):249–255. doi:10.1007/s00586-014-3623-1.

195. Zheng J, Yang Y, Lou S, Zhang D, Liao S. Construction and validation of a three-dimensional finite element model of degenerative scoliosis. *Journal of Orthopaedic Surgery and Research* 2015; **10**:189. doi:10.1186/s13018-015-0334-1.

196. Fairhurst H, Little P, Adam C. The measurement of applied forces during anterior single rod surgical correction of adolescent idiopathic scoliosis. In: *Spine Society of Australia Annual Scientific Meeting*; 2011:1–1.

197. Xu M, Yang J, Lieberman I, Haddas R. Finite element method-based study for effect of adult degenerative scoliosis on the spinal vibration characteristics. *Computers in Biology and Medicine* 2017; **84**:53–58. doi:10.1016/j.compbiomed.2017.03.018.

198. Li X-F, Liu Z-D, Dai L-Y, Zhong G-B, Zang W-P. Dynamic response of the idiopathic scoliotic spine to axial cyclic loads. *Spine* 2011; **36**(7):521–528. doi:10.1097/BRS.0b013e3181d55fb0.

199. Xu M, Yang J, Lieberman I, Haddas R. The Effect of Surgical Alignment in Adult Scoliotic Spines on Axial Cyclic Vibration: A Finite Element Study. *Journal of Computing and Information Science in Engineering* 2019; **19**(2). doi:10.1115/1.4042326.

200. Ye J-D, Lu G-P, Feng J-J, Zhong W-H. Effect on Chest Deformation of Simultaneous Correction of Pectus Excavatum with Scoliosis. *Journal of Healthcare Engineering* 2017; **2017**:8318694. doi:10.1155/2017/8318694.

201. Pasha S, Aubin C-E, Labelle H, Parent S, Mac-Thiong J-M. The biomechanical effects of spinal fusion on the sacral loading in adolescent idiopathic scoliosis. *Clinical Biomechanics (Bristol, Avon)* 2015; **30**(9):981–987. doi:10.1016/j.clinbiomech.2015.06.019.

202. Lafage V, Dubousset J, Lavaste F, Skalli W. 3D finite element simulation of Cotrel–Dubousset correction. *Computer Aided Surgery* 2004; **9**(1–2):17–25. doi:10.3109/10929080400006390.

203. Le Navéaux F, Larson AN, Labelle H, Wang X, Aubin C-É. How does implant distribution affect 3D correction and bone-screw forces in thoracic adolescent idiopathic scoliosis spinal instrumentation? *Clinical Biomechanics (Bristol, Avon)* 2016; **39**:25–31. doi:10.1016/j.clinbiomech.2016.09.002.

204. Little JP, Adam C. Towards determining soft tissue properties for modelling spine surgery: current progress and challenges. *Medical & Biological Engineering & Computing* 2012; **50**(2):199–209. doi:10.1007/s11517-011-0848-6.

205. Cobetto N, Parent S, Aubin C-E. 3D correction over 2years with anterior vertebral body growth modulation: A finite element analysis of screw positioning, cable tensioning and postoperative functional activities. *Clinical Biomechanics (Bristol, Avon)* 2018; **51**:26–33. doi:10.1016/j.clinbiomech.2017.11.007.

206. Agarwal A, Zakeri A, Agarwal AK, Jayaswal A, Goel VK. Distraction magnitude and frequency affects the outcome in juvenile idiopathic patients with growth rods: finite element study using a representative scoliotic spine model. *The Spine Journal* 2015; **15**(8):1848–1855. doi:10.1016/j.spinee.2015.04.003.

207. Agarwal A, Jayaswal A, Goel VK, Agarwal AK. Patient-specific Distraction Regimen to Avoid Growth-rod Failure. *Spine* 2018; **43**(4):E221–E226. doi:10.1097/BRS.0000000000002286.

208. Aubin C-É, Clin J, Rawlinson J. Biomechanical simulations of costo-vertebral and anterior vertebral body tethers for the fusionless treatment of pediatric scoliosis. *Journal of Orthopaedic Research* 2018; **36**(1):254–264. doi:10.1002/jor.23648.

209. Cahill PJ, Wang W, Asghar J, et al. The Use of a Transition Rod May Prevent Proximal Junctional Kyphosis in the Thoracic Spine After Scoliosis Surgery: A Finite Element Analysis. *Spine* 2012; **37**(12):E687–E695. doi:10.1097/BRS.0b013e318246d4f2.

210. Chen K, Zhao J, Zhao Y, Yang C, Li M. A finite element analysis of different pedicle screw placement strategies for treatment of Lenke 1 adolescent idiopathic scoliosis: which is better? *Computer Methods in Biomechanics and Biomedical Engineering* 2020. doi:10.1080/10255842.2020.1826456.

211. Clin J, Le Navéaux F, Driscoll M, et al. Biomechanical Comparison of the Load-Sharing Capacity of High and Low Implant Density Constructs With Three Types of Pedicle Screws for the Instrumentation of Adolescent Idiopathic Scoliosis. *Spine Deformity* 2019; **7**(1):2–10. doi:10.1016/j.jspd.2018.06.007.

212. Driscoll M, Mac-Thiong J-M, Labelle H, Parent S. Development of a Detailed Volumetric Finite Element Model of the Spine to Simulate Surgical Correction of Spinal Deformities. *BioMed Research International* 2013; **2013**:1–6. doi:10.1155/2013/931741.

213. Galbusera F, Bassani T, La Barbera L, et al. Planning the Surgical Correction of Spinal Deformities: Toward the Identification of the Biomechanical Principles by Means of Numerical Simulation. *Frontiers in Bioengineering and Biotechnology* 2015; **3**:178. doi:10.3389/fbioe.2015.00178.

214. Rohlmann A, Richter M, Zander T, Klöckner C, Bergmann G. Effect of different surgical strategies on screw forces after correction of scoliosis with a VDS implant. *European Spine Journal* 2006; **15**(4):457–464. doi:10.1007/s00586-005-0923-5.

215. Rohlmann A, Zander T, Burra NK, Bergmann G. Flexible non-fusion scoliosis correction systems reduce intervertebral rotation less than rigid implants and allow growth of the spine: a finite element analysis of different features of orthobiom^{TM}. *European Spine Journal* 2008; **17**(2):217–223. doi:10.1007/s00586-007-0480-1.

216. Zhang H, Hu X, Wang Y, et al. Use of finite element analysis of a Lenke type 5 adolescent idiopathic scoliosis case to assess possible surgical outcomes. *Computer Aided Surgery* 2013; **18**(3–4):84–92. doi:10.3109/10929088.2012.763185.

217. Zhou Y, Xin D, Lei Z, Zuo Y, Zhao Y. Comparative Three-Dimensional Finite Element Analysis of 4 Kinds of Pedicle Screw Schemes for Treatment of Adult Degenerative Scoliosis. *Medical Science Monitor: International Medical Journal of Experimental and Clinical Research* 2020; **26**:e922050. doi:10.12659/MSM.922050.

218. de Zee M, Hansen L, Wong C, Rasmussen J, Simonsen EB. A generic detailed rigid-body lumbar spine model. *Journal of Biomechanics* 2007; **40**(6):1219–1227. doi:10.1016/j.jbiomech.2006.05.030.

219. Arjmand N, Gagnon D, Plamondon A, Shirazi-Adl A, Larivière C. Comparison of trunk muscle forces and spinal loads estimated by two biomechanical models. *Clinical Biomechanics* 2009; **24**(7):533–541. doi:10.1016/j.clinbiomech.2009.05.008.

220. Zander T, Dreischarf M, Schmidt H, Bergmann G, Rohlmann A. Spinal loads as influenced by external loads: A combined in vivo and in silico investigation. *Journal of Biomechanics* 2015; **48**(4):578–584. doi:10.1016/j.jbiomech.2015.01.011.

221. Gagnon D, Arjmand N, Plamondon A, Shirazi-Adl A, Larivière C. An improved multi-joint EMG-assisted optimization approach to estimate joint and muscle forces in a musculoskeletal model of the lumbar spine. *Journal of Biomechanics* 2011; **44**(8):1521–1529. doi:10.1016/j.jbiomech.2011.03.002.

222. Jamshidnejad S, Arjmand N. Variations in trunk muscle activities and spinal loads following posterior lumbar surgery: A combined in vivo and modeling investigation. *Clinical Biomechanics* 2015; **30**(10):1036–1042. doi:10.1016/j.clinbiomech.2015.09.010.

223. Ignasiak D, Ferguson SJ, Arjmand N. A rigid thorax assumption affects model loading predictions at the upper but not lower lumbar levels. *Journal of Biomechanics* 2016; **49**(13):3074–3078. doi:10.1016/j.jbiomech.2016.07.006.

224. Abouhossein A, Weisse B, Ferguson SJ. Quantifying the centre of rotation pattern in a multi-body model of the lumbar spine. *Computer Methods in Biomechanics and Biomedical Engineering* 2013; **16**(12):1362–1373. doi:10.1080/10255842.2012.671306.

225. Abedrabbo Ode G. Quantification of intervertebral efforts using a multibody dynamics approach : application to scoliosis. 2017.

226. Wang K, Wang L, Deng Z, Jiang C, Niu W, Zhang M. Influence of passive elements on prediction of intradiscal pressure and muscle activation in lumbar musculoskeletal models.

Computer Methods and Programs in Biomedicine 2019; **177**:39–46. doi:10.1016/j.cmpb.2019.05.018.

227. Sartori M, Farina D, Lloyd DG. Hybrid neuromusculoskeletal modeling to best track joint moments using a balance between muscle excitations derived from electromyograms and optimization. *Journal of Biomechanics* 2014; **47**(15):3613–3621. doi:10.1016/j.jbiomech.2014.10.009.

228. Mohammadi Y, Arjmand N, Shirazi-Adl A. Comparison of trunk muscle forces, spinal loads and stability estimated by one stability- and three EMG-assisted optimization approaches. *Medical Engineering & Physics* 2015; **37**(8):792–800. doi:10.1016/j.medengphy.2015.05.018.

229. Thelen DG, Anderson FC. Using computed muscle control to generate forward dynamic simulations of human walking from experimental data. *Journal of Biomechanics* 2006; **39**(6):1107–1115. doi:10.1016/j.jbiomech.2005.02.010.

230. Ghofrani M, Olyaei G, Talebian S, Bagheri H, Kazemi P. Reliability of SEMG measurements for trunk muscles during lifting variable loads in healthy subjects. *Journal of Bodywork and Movement Therapies* 2017; **21**(3):711–718. doi:10.1016/j.jbmt.2016.12.003.

231. Ghezelbash F, Shirazi-Adl A, Gagnon D, et al. Submaximal electromyography-driven musculoskeletal modeling of the human trunk during static tasks: Equilibrium and stability analyses. *Journal of Electromyography and Kinesiology* 2022; **65**:102664. doi:10.1016/j.jelekin.2022.102664.

232. Banks JJ, Brian R. Umberger, Graham E. Caldwell. EMG OPTIMIZATION IN OPENSIM: A MODEL FOR ESTIMATING LOWER BACK KINETICS IN GAIT. *Medical Engineering & Physics* 2022:103790–103790. doi:10.1016/j.medengphy.2022.103790.

233. Pizzolato C, Lloyd DG, Sartori M, et al. CEINMS: A toolbox to investigate the influence of different neural control solutions on the prediction of muscle excitation and joint moments during dynamic motor tasks. *Journal of Biomechanics* 2015; **48**(14):3929–3936. doi:10.1016/j.jbiomech.2015.09.021.

234. A. Moya-Esteban, H. van der Kooij, M. Sartori. Robust estimation of lumbar joint forces in symmetric and asymmetric lifting tasks via large-scale electromyography-driven musculoskeletal models. *Journal of Biomechanics* 2022; **144**:111307–111307. doi:10.1016/j.jbiomech.2022.111307.

235. Desroches G, Aubin C-E, Sucato DJ, Rivard C-H. Simulation of an anterior spine instrumentation in adolescent idiopathic scoliosis using a flexible multi-body model. *Medical & Biological Engineering & Computing* 2007; **45**(8):759–768. doi:10.1007/s11517-007-0214-x.

236. Jalalian A, Tay FEH, Arastehfar S, Liu G. A new method to approximate load-displacement relationships of spinal motion segments for patient-specific multi-body models of scoliotic

spine. *Medical & Biological Engineering & Computing* 2017; **55**(6):1039–1050. doi:10.1007/s11517-016-1576-8.

237. Jalalian A, Tay FEH, Arastehfar S, Liu G. A patient-specific multibody kinematic model for representation of the scoliotic spine movement in frontal plane of the human body. *Multibody System Dynamics* 2017; **39**(3):197–220. doi:10.1007/s11044-016-9556-1.

238. Aubin C-É, Petit Y, Stokes IAF, Poulin F, Gardner-Morse M, Labelle H. Biomechanical Modeling of Posterior Instrumentation of the Scoliotic Spine. *Computer Methods in Biomechanics and Biomedical Engineering* 2003; **6**(1):27–32. doi:10.1080/1025584031000072237.

239. Aubin C-E, Cammarata M, Wang X, Mac-Thiong J-M. Instrumentation Strategies to Reduce the Risks of Proximal Junctional Kyphosis in Adult Scoliosis: A Detailed Biomechanical Analysis. *Spine Deformity* 2015; **3**(3):211–218. doi:10.1016/j.jspd.2014.09.054.

240. Cammarata M, Aubin C-É, Wang X, Mac-Thiong J-M. Biomechanical Risk Factors for Proximal Junctional Kyphosis: A Detailed Numerical Analysis of Surgical Instrumentation Variables. *Spine* 2014; **39**(8):E500–E507. doi:10.1097/BRS.0000000000000222.

241. Fradet L, Wang X, Crandall D, Aubin C-E. Biomechanical Analysis of Acute Proximal Junctional Failure After Surgical Instrumentation of Adult Spinal Deformity: The Impact of Proximal Implant Type, Osteotomy Procedures, and Lumbar Lordosis Restoration. *Spine Deformity* 2018; **6**(5):483–491. doi:10.1016/j.jspd.2018.02.007.

242. Jalalian A, Tay FEH, Liu G. Data Mining in Medicine: Relationship of Scoliotic Spine Curvature to the Movement Sequence of Lateral Bending Positions. In: Perner P, ed. *Advances in Data Mining. Applications and Theoretical Aspects*, vol 9728. Cham: Springer International Publishing; 2016:29–40.

243. La Barbera L, Larson AN, Rawlinson J, Aubin C-E. In silico patient-specific optimization of correction strategies for thoracic adolescent idiopathic scoliosis. *Clinical Biomechanics* 2021; **81**:105200. doi:10.1016/j.clinbiomech.2020.105200.

244. Martino J, Aubin C-E, Labelle H, Wang X, Parent S. Biomechanical Analysis of Vertebral Derotation Techniques for the Surgical Correction of Thoracic Scoliosis: A Numerical Study Through Case Simulations and a Sensitivity Analysis. *Spine* 2013; **38**(2):E73–E83. doi:10.1097/BRS.0b013e31827a641e.

245. Robitaille M, Aubin C-É, Labelle H. Effects of alternative instrumentation strategies in adolescent idiopathic scoliosis: A biomechanical analysis. *Journal of Orthopaedic Research* 2009; **27**(1):104–113. doi:10.1002/jor.20654.

246. Wang X, Aubin C-E, Robitaille I, Labelle H. Biomechanical comparison of alternative densities of pedicle screws for the treatment of adolescent idiopathic scoliosis. *European Spine Journal* 2012; **21**(6):1082–1090. doi:10.1007/s00586-011-2089-7.

247. Wang X, Boyer L, Le Naveaux F, Schwend RM, Aubin C-E. How does differential rod contouring contribute to 3-dimensional correction and affect the bone-screw forces in adolescent idiopathic scoliosis instrumentation? *Clinical Biomechanics* 2016; **39**:115–121. doi:10.1016/j.clinbiomech.2016.10.002.

248. Wang X, Aubin C-E, Coleman J, Rawlinson J. Correction Capability in the 3 Anatomic Planes of Different Pedicle Screw Designs in Scoliosis Instrumentation. *Clinical Spine Surgery* 2017; **30**(4):E323–E330. doi:10.1097/BSD.0000000000000082.

249. Wang X, Larson AN, Crandall DG, et al. Biomechanical effect of pedicle screw distribution in AIS instrumentation using a segmental translation technique: computer modeling and simulation. *Scoliosis and Spinal Disorders* 2017; **12**(1):13. doi:10.1186/s13013-017-0120-4.

250. Wang X, Yeung K, Cheung JPY, et al. A novel scoliosis instrumentation using special superelastic nickel–titanium shape memory rods: a biomechanical analysis using a calibrated computer model and data from a clinical trial. *Spine Deformity* 2020; **8**(3):369–379. doi:10.1007/s43390-020-00075-8.

251. Babuska I. Verification and validation in computational engineering and science: basic concepts. *Computer Methods in Applied Mechanics and Engineering* 2004; **193**:4057–4066. doi:10.1016/j.cma.2004.03.002.

252. Henninger HB, Reese SP, Anderson AE, Weiss JA. Validation of Computational Models in Biomechanics. *Proceedings of the Institution of Mechanical Engineers. Part H, Journal of engineering in medicine* 2010; **224**(7):801–812.

253. Viceconti M, Juárez MA, Curreli C, Pennisi M, Russo G, Pappalardo F. Credibility of In Silico Trial Technologies—A Theoretical Framing. *IEEE Journal of Biomedical and Health Informatics* 2020; **24**(1):4–13. doi:10.1109/JBHI.2019.2949888.

254. Cristofolini L, Taddei F, Baleani M, Baruffaldi F, Stea S, Viceconti M. Multiscale investigation of the functional properties of the human femur. *Philosophical Transactions of the Royal Society A: Mathematical, Physical and Engineering Sciences* 2008; **366**(1879):3319–3341. doi:10.1098/rsta.2008.0077.

255. Dall'Ara E, Schmidt R, Pahr D, et al. A nonlinear finite element model validation study based on a novel experimental technique for inducing anterior wedge-shape fractures in human vertebral bodies in vitro. *Journal of Biomechanics* 2010; **43**(12):2374–2380. doi:10.1016/j.jbiomech.2010.04.023.

256. Garavelli C, Curreli C, Palanca M, Aldieri A, Cristofolini L, Viceconti M. Experimental validation of a subject-specific finite element model of lumbar spine segment using digital image correlation. *PLOS ONE* 2022; **17**(9):e0272529. doi:10.1371/journal.pone.0272529.

257. Vrtovec T, Pernuš F, Likar B. A review of methods for quantitative evaluation of spinal curvature. *European Spine Journal* 2009; **18**(5):593–607. doi:10.1007/s00586-009-0913-0.

258. Costi JJ, Ledet EH, O'Connell GD. Spine biomechanical testing methodologies: The controversy of consensus vs scientific evidence. *JOR Spine* 2021; **4**(1). doi:10.1002/jsp2.1138.

259. Chen S, Chen M, Wu X, et al. Global, regional and national burden of low back pain 1990–2019: A systematic analysis of the Global Burden of Disease study 2019. *Journal of Orthopaedic Translation* 2022; **32**:49–58. doi:10.1016/j.jot.2021.07.005.

260. Raciborski F, Gasik R, Kłak A. Disorders of the spine. A major health and social problem. *Reumatologia* 2016; **54**(4):196–200. doi:10.5114/reum.2016.62474.

261. Waheed MA-A, Hasan S, Tan LA, et al. Cervical spine pathology and treatment: a global overview. *Journal of Spine Surgery* 2020; **6**(1):340–350. doi:10.21037/jss.2020.01.12.

262. de Bruijn E, van der Helm FCT, Happee R. Analysis of isometric cervical strength with a nonlinear musculoskeletal model with 48 degrees of freedom. *Multibody System Dynamics* 2016; **36**(4):339–362. doi:10.1007/s11044-015-9461-z.

263. Abouhossein A, Weisse B, Ferguson SJ. A multibody modelling approach to determine load sharing between passive elements of the lumbar spine. *Computer Methods in Biomechanics and Biomedical Engineering* 2011; **14**(6):527–537. doi:10.1080/10255842.2010.485568.

264. Khurelbaatar T, Kim K, Hyuk Kim Y. A Cervico-Thoraco-Lumbar Multibody Dynamic Model for the Estimation of Joint Loads and Muscle Forces. *Journal of Biomechanical Engineering* 2015; **137**(11):111001. doi:10.1115/1.4031351.

265. Ghezelbash F, Eskandari AH, Shirazi-Adl A, Arjmand N, El-Ouaaid Z, Plamondon A. Effects of motion segment simulation and joint positioning on spinal loads in trunk musculoskeletal models. *Journal of Biomechanics* 2018; **70**:149–156. doi:10.1016/j.jbiomech.2017.07.014.

266. Arshad R, Zander T, Bashkuev M, Schmidt H. Influence of spinal disc translational stiffness on the lumbar spinal loads, ligament forces and trunk muscle forces during upper body inclination. *Medical Engineering & Physics* 2017; **46**:54–62. doi:10.1016/j.medengphy.2017.05.006.

267. Zander T, Dreischarf M, Schmidt H. Sensitivity analysis of the position of the intervertebral centres of reaction in upright standing – a musculoskeletal model investigation of the lumbar spine. *Medical Engineering & Physics* 2016; **38**(3):297–301. doi:10.1016/j.medengphy.2015.12.003.

268. Pearcy MJ, Bogduk N. Instantaneous Axes of Rotation of the Lumbar Intervertebral Joints. *Spine* 1988; **13**(9):1033.

269. Aiyangar A, Zheng L, Anderst W, Zhang X. Apportionment of lumbar L2-S1 rotation across individual motion segments during a dynamic lifting task. *Journal of Biomechanics* 2015; **48**(13):3709–3715. doi:10.1016/j.jbiomech.2015.08.022.

270. Aiyangar A, Zheng L, Anderst W, Zhang X. Instantaneous centers of rotation for lumbar segmental extension in vivo. *Journal of Biomechanics* 2017; **52**:113–121. doi:10.1016/j.jbiomech.2016.12.021.

271. Han K-S, Kim K, Park WM, Lim DS, Kim YH. Effect of centers of rotation on spinal loads and muscle forces in total disk replacement of lumbar spine. *Proceedings of the Institution of Mechanical Engineers, Part H: Journal of Engineering in Medicine* 2013; **227**(5):543–550. doi:10.1177/0954411912474742.

272. Meszaros-Beller L, Hammer M, Riede JM, Pivonka P, Little JP, Schmitt S. Effects of geometric individualisation of a human spine model on load sharing: neuro-musculoskeletal simulation reveals significant differences in ligament and muscle contribution. *Biomechanics and Modeling in Mechanobiology* 2023. doi:10.1007/s10237-022-01673-3.

273. Wilke H-J, Geppert J, Kienle A. Biomechanical in vitro evaluation of the complete porcine spine in comparison with data of the human spine. *European Spine Journal* 2011; **20**(11):1859–1868. doi:10.1007/s00586-011-1822-6.

274. Busscher I, Ploegmakers JJW, Verkerke GJ, Veldhuizen AG. Comparative anatomical dimensions of the complete human and porcine spine. *European Spine Journal* 2010; **19**(7):1104–1114. doi:10.1007/s00586-010-1326-9.

275. Busscher I, van der Veen AJ, van Dieën JH, Kingma I, Verkerke GJ, Veldhuizen AG. In Vitro Biomechanical Characteristics of the Spine: A Comparison Between Human and Porcine Spinal Segments. *Spine* 2010; **35**(2):E35. doi:10.1097/BRS.0b013e3181b21885.

276. Brandolini N, Cristofolini L, Viceconti M. EXPERIMENTAL METHODS FOR THE BIOMECHANICAL INVESTIGATION OF THE HUMAN SPINE: A REVIEW. *Journal of Mechanics in Medicine and Biology* 2014; **14**(01):1430002. doi:10.1142/S0219519414300026.

277. Dickey JP, Dumas GA, Bednar DA. Comparison of porcine and human lumbar spine flexion mechanics*. *Veterinary and Comparative Orthopaedics and Traumatology* 2003; **16**(1):44–49. doi:10.1055/s-0038-1632753.

278. Kingma I, Busscher I, van der Veen AJ, et al. Coupled motions in human and porcine thoracic and lumbar spines. *Journal of Biomechanics* 2018; **70**:51–58. doi:10.1016/j.jbiomech.2017.11.034.

279. Palanca M, Barbanti-Bròdano G, Marras D, et al. Type, size, and position of metastatic lesions explain the deformation of the vertebrae under complex loading conditions. *Bone* 2021; **151**:116028. doi:10.1016/j.bone.2021.116028.

280. Lionello G, Cristofolini L. A practical approach to optimizing the preparation of speckle patterns for digital-image correlation. *Measurement Science and Technology* 2014; **25**(10):107001. doi:10.1088/0957-0233/25/10/107001.

281. Gaddipati R, Jensen GL, Swanson G, Hammonds K, Morrow A. The Effect of High-Dose Radiation Therapy on Healthy Vertebral Bone Density. *Cureus* 2022; **14**(2). doi:10.7759/cureus.22565.

282. Valente G, Crimi G, Vanella N, Schileo E, Taddei F. nmsBuilder: Freeware to create subject-specific musculoskeletal models for OpenSim. *Computer Methods and Programs in Biomedicine* 2017; **152**:85–92. doi:10.1016/j.cmpb.2017.09.012.

283. Lu WW, Luk KDK, Holmes AD, Cheung KMC, Leong JCY. Pure Shear Properties of Lumbar Spinal Joints and the Effect of Tissue Sectioning on Load Sharing. *Spine* 2005; **30**(8):E204. doi:10.1097/01.brs.0000158871.14960.30.

284. Hendrik Schmidt, Kim Häußler, Hans-Joachim Wilke, Uwe Wolfram. Structural behavior of human lumbar intervertebral disc under direct shear. *Journal of Applied Biomaterials & Functional Materials* 2015. doi:10.5301/jabfm.5000176.

285. Heuer F, Schmidt H, Klezl Z, Claes L, Wilke H-J. Stepwise reduction of functional spinal structures increase range of motion and change lordosis angle. *Journal of Biomechanics* 2007; **40**(2):271–280. doi:10.1016/j.jbiomech.2006.01.007.

286. Jager MMD. Mathematical head-neck models for acceleration impacts. 1996.

287. Crisco JJ, Fujita L, Spenciner DB. The dynamic flexion/extension properties of the lumbar spine in vitro using a novel pendulum system. *Journal of Biomechanics* 2007; **40**(12):2767–2773. doi:10.1016/j.jbiomech.2006.12.013.

288. McGlashen KM, Miller JA, Schultz AB, Andersson GB. Load displacement behavior of the human lumbo-sacral joint. *Journal of Orthopaedic Research: Official Publication of the Orthopaedic Research Society* 1987; **5**(4):488–496. doi:10.1002/jor.1100050404.

289. Renner SM, Natarajan RN, Patwardhan AG, et al. Novel model to analyze the effect of a large compressive follower pre-load on range of motions in a lumbar spine. *Journal of Biomechanics* 2007; **40**(6):1326–1332. doi:10.1016/j.jbiomech.2006.05.019.

290. MARKOLF KL. Engineering Characteristics of the Human Intervertebral Joint. 1970.

291. Miller JA, Schultz AB, Warwick DN, Spencer DL. Mechanical properties of lumbar spine motion segments under large loads. *Journal of Biomechanics* 1986; **19**(1):79–84. doi:10.1016/0021-9290(86)90111-9.

292. Manohar M. Panjabi, Manohar M. Panjabi, Thomas R. Oxland, I Yamamoto, Joseph J. Crisco. Mechanical behavior of the human lumbar and lumbosacral spine as shown by three-dimensional load-displacement curves. *Journal of Bone and Joint Surgery, American Volume* 1994. doi:10.2106/00004623-199403000-00012.

293. Doulgeris JJ, Gonzalez-Blohm SA, Aghayev K, et al. Axial rotation mechanics in a cadaveric lumbar spine model: a biomechanical analysis. *The Spine Journal: Official Journal of the North American Spine Society* 2014; **14**(7):1272–1279. doi:10.1016/j.spinee.2013.11.037.

294. Adams MA, Hutton WC, Stott JR. The resistance to flexion of the lumbar intervertebral joint. *Spine* 1980; **5**(3):245–253. doi:10.1097/00007632-198005000-00007.

295. Team RC. R: A language and environment for statistical computing. R Foundation for Statistical Computing, Vienna, Austria. *http://www.R-project.org/* 2016.https://cir.nii.ac.jp/crid/1574231874043578752Accessed.

296. Bland JM, Altman DG. Multiple significance tests: the Bonferroni method. *BMJ* 1995; **310**(6973):170. doi:10.1136/bmj.310.6973.170.

297. Dumas R, Blanchard B, Carlier R, et al. A semi-automated method using interpolation and optimisation for the 3D reconstruction of the spine from bi-planar radiography: a precision and accuracy study. *Medical & Biological Engineering & Computing* 2008; **46**(1):85–92. doi:10.1007/s11517-007-0253-3.

298. Hajnal B, Eltes PE, Bereczki F, et al. New method to apply the lumbar lordosis of standing radiographs to supine CT-based virtual 3D lumbar spine models. *Scientific Reports* 2022; **12**(1):20382. doi:10.1038/s41598-022-24570-2.

299. Frank Heuer, Hendrik Schmidt, Lutz Claes, Hans-Joachim Wilke. Stepwise reduction of functional spinal structures increase vertebral translation and intradiscal pressure. *Journal of Biomechanics* 2007. doi:10.1016/j.jbiomech.2006.03.016.

300. Popescu F, Viceconti M, Grazi E, Cappello A. A new method to compare planned and achieved position of an orthopaedic implant. *Computer Methods and Programs in Biomedicine* 2003; **71**(2):117–127. doi:10.1016/S0169-2607(02)00091-3.

301. Väänänen SP, Amin Yavari S, Weinans H, Zadpoor AA, Jurvelin JS, Isaksson H. Repeatability of digital image correlation for measurement of surface strains in composite long bones. *Journal of Biomechanics* 2013; **46**(11):1928–1932. doi:10.1016/j.jbiomech.2013.05.021.

302. Schmidt H, Heuer F, Claes L, Wilke H-J. The relation between the instantaneous center of rotation and facet joint forces – A finite element analysis. *Clinical Biomechanics* 2008; **23**(3):270–278. doi:10.1016/j.clinbiomech.2007.10.001.

303. Dutmer AL, Schiphorst Preuper HR, Soer R, et al. Personal and Societal Impact of Low Back Pain: The Groningen Spine Cohort. *Spine* 2019; **44**(24):E1443. doi:10.1097/BRS.0000000000003174.

304. Widmer J, Cornaz F, Scheibler G, Spirig JM, Snedeker JG, Farshad M. Biomechanical contribution of spinal structures to stability of the lumbar spine—novel biomechanical insights. *The Spine Journal* 2020; **20**(10):1705–1716. doi:10.1016/j.spinee.2020.05.541.

305. Lerchl T, El Husseini M, Bayat A, et al. Validation of a Patient-Specific Musculoskeletal Model for Lumbar Load Estimation Generated by an Automated Pipeline From Whole Body CT. ; 2022; **10**.https://www.frontiersin.org/articles/10.3389/fbioe.2022.862804AccessedJuly 13, 2022.

306. Manohar M. Panjabi, Manohar M. Panjabi, Richard A. Brand, Augustus A. White. Mechanical properties of the human thoracic spine as shown by three-dimensional load-displacement curves. *Journal of Bone and Joint Surgery, American Volume* 1976. doi:10.2106/00004623-197658050-00011.

307. Andersson GB, Schultz AB. Effects of fluid injection on mechanical properties of intervertebral discs. *Journal of Biomechanics* 1979; **12**(6):453–458. doi:10.1016/0021-9290(79)90030-7.

308. Palanca M, Ruspi ML, Cristofolini L, et al. The strain distribution in the lumbar anterior longitudinal ligament is affected by the loading condition and bony features: An in vitro full-field analysis. *PLOS ONE* 2020; **15**(1):e0227210. doi:10.1371/journal.pone.0227210.

309. Garges KJ, Nourbakhsh A, Morris R, Yang J, Mody M, Patterson R. A comparison of the torsional stiffness of the lumbar spine in flexion and extension. *Journal of Manipulative and Physiological Therapeutics* 2008; **31**(8):563–569. doi:10.1016/j.jmpt.2008.09.002.

310. Volkheimer D, Galbusera F, Liebsch C, et al. Is intervertebral disc degeneration related to segmental instability? An evaluation with two different grading systems based on clinical imaging. *Acta Radiologica* 2018; **59**(3):327–335. doi:10.1177/0284185117715284.

311. Wilke H-J, Claes L, Schmitt H, Wolf S. A universal spine tester for in vitro experiments with muscle force simulation. *European Spine Journal* 1994; **3**(2):91–97. doi:10.1007/BF02221446.

312. Wu M, Wang S, Driscoll SJ, Cha TD, Wood KB, Li G. Dynamic motion characteristics of the lower lumbar spine: implication to lumbar pathology and surgical treatment. *European Spine Journal* 2014; **23**(11):2350–2358. doi:10.1007/s00586-014-3316-9.

313. Fregly BJ, Boninger ML, Reinkensmeyer DJ. Personalized neuromusculoskeletal modeling to improve treatment of mobility impairments: a perspective from European research sites. *Journal of NeuroEngineering and Rehabilitation* 2012; **9**(1):18. doi:10.1186/1743-0003-9-18.

314. Hariharan AR, Shah SA, Petfield J, et al. Complications following surgical treatment of adolescent idiopathic scoliosis: a 10-year prospective follow-up study. *Spine Deformity* 2022. doi:10.1007/s43390-022-00508-6.

315. Kwan KYH, Alanay A, Yazici M, et al. Unplanned Reoperations in Magnetically Controlled Growing Rod Surgery for Early Onset Scoliosis With a Minimum of Two-Year Follow-Up. *Spine* 2017; **42**(24):E1410. doi:10.1097/BRS.0000000000002297.

316. Drazin D, Al-Khouja L, Lagman C, et al. Scoliosis surgery in the elderly: Complications, readmissions, reoperations and mortality. *Journal of Clinical Neuroscience* 2016; **34**:158–161. doi:10.1016/j.jocn.2016.06.005.

317. Riouallon G, Bouyer B, Wolff S. Risk of revision surgery for adult idiopathic scoliosis: a survival analysis of 517 cases over 25 years. *European Spine Journal* 2016; **25**(8):2527–2534. doi:10.1007/s00586-016-4505-5.

318. Brodke DS, Annis P, Lawrence BD, Woodbury AM, Daubs MD. Reoperation and Revision Rates of 3 Surgical Treatment Methods for Lumbar Stenosis Associated With Degenerative Scoliosis and Spondylolisthesis. *Spine* 2013; **38**(26):2287. doi:10.1097/BRS.0000000000000068.

319. Galbusera F, Cina A, Panico M, Bassani T. The importance of curve severity, type and instrumentation strategy in the surgical correction of adolescent idiopathic scoliosis: an in silico clinical trial on 64 cases. 2020. doi:10.31224/osf.io/4snpv.

320. Luo TD, Stans AA, Schueler BA, Larson AN. Cumulative Radiation Exposure With EOS Imaging Compared With Standard Spine Radiographs. *Spine Deformity* 2015; **3**(2):144–150. doi:10.1016/j.jspd.2014.09.049.

321. Galbusera F, Casaroli G, Bassani T. Artificial intelligence and machine learning in spine research. *JOR SPINE* 2019; **2**(1):e1044. doi:10.1002/jsp2.1044.

322. Martelli S, Valente G, Viceconti M, Taddei F. Sensitivity of a subject-specific musculoskeletal model to the uncertainties on the joint axes location. *Computer Methods in Biomechanics and Biomedical Engineering* 2015; **18**(14):1555–1563. doi:10.1080/10255842.2014.930134.

323. Hannah I, Montefiori E, Modenese L, Prinold J, Viceconti M, Mazzà C. Sensitivity of a juvenile subject-specific musculoskeletal model of the ankle joint to the variability of operator-dependent input. *Proceedings of the Institution of Mechanical Engineers, Part H: Journal of Engineering in Medicine* 2017; **231**(5):415–422. doi:10.1177/0954411917701167.

324. Burkhart K, Grindle D, Bouxsein ML, Anderson DE. Between-session reliability of subject-specific musculoskeletal models of the spine derived from optoelectronic motion capture data. *Journal of Biomechanics* 2020; **112**:110044. doi:10.1016/j.jbiomech.2020.110044.

325. Carbone V, van der Krogt MM, Koopman HFJM, Verdonschot N. Sensitivity of subject-specific models to errors in musculo-skeletal geometry. *Journal of Biomechanics* 2012; **45**(14):2476–2480. doi:10.1016/j.jbiomech.2012.06.026.

326. Vasavada AN, Lasher RA, Meyer TE, Lin DC. Defining and evaluating wrapping surfaces for MRI-derived spinal muscle paths. *Journal of Biomechanics* 2008; **41**(7):1450–1457. doi:10.1016/j.jbiomech.2008.02.027.

327. Christophy M, Faruk Senan NA, Lotz JC, O'Reilly OM. A Musculoskeletal model for the lumbar spine. *Biomechanics and Modeling in Mechanobiology* 2012; **11**(1):19–34. doi:10.1007/s10237-011-0290-6.

328. Yorke AA, McDonald GC, Solis D, Guerrero T. Pelvic Reference Data [Dataset]. 2019.

329. Yorke A, Sala I, Solis D, Guerrero T. A Statistically Characterized Reference Data Set for Image Registration of Pelvis Using Combinatorial Affine Registration Optimization. In: *MEDICAL PHYSICS*, vol 46. WILEY 111 RIVER ST, HOBOKEN 07030-5774, NJ USA; 2019:E340–E340.

330. Clark K, Vendt B, Smith K, et al. The Cancer Imaging Archive (TCIA): Maintaining and Operating a Public Information Repository. *Journal of Digital Imaging* 2013; **26**(6):1045–1057. doi:10.1007/s10278-013-9622-7.

331. Runze Han, Ali Uneri, T. De Silva, et al. Atlas-based automatic planning and 3D-2D fluoroscopic guidance in pelvic trauma surgery. *Physics in Medicine and Biology* 2019. doi:10.1088/1361-6560/ab1456.

332. Roth H, Le L, Ari S, et al. A new 2.5 D representation for lymph node detection in CT. *The Cancer Imaging Archive* 2018.

333. Cignoni P, Callieri M, Corsini M, Dellepiane M, Ganovelli F, Ranzuglia G. MeshLab: an Open-Source Mesh Processing Tool.

334. Ju Zhang, J Hislop-Jambrich, Thor F. Besier. Predictive statistical models of baseline variations in 3-D femoral cortex morphology. *Medical Engineering & Physics* 2016. doi:10.1016/j.medengphy.2016.02.003.

335. Modenese L, Montefiori E, Wang A, Wesarg S, Viceconti M, Mazzà C. Investigation of the dependence of joint contact forces on musculotendon parameters using a codified workflow for image-based modelling. *Journal of Biomechanics* 2018; **73**:108–118. doi:10.1016/j.jbiomech.2018.03.039.

336. Forsberg D, Lundström C, Andersson M, Knutsson H. Model-based registration for assessment of spinal deformities in idiopathic scoliosis. *Physics in Medicine and Biology* 2013; **59**(2):311–326. doi:10.1088/0031-9155/59/2/311.

337. Akbar M, Terran J, Ames CP, Lafage V, Schwab F. Use of Surgimap Spine in Sagittal Plane Analysis, Osteotomy Planning, and Correction Calculation. *Neurosurgery Clinics of North America* 2013; **24**(2):163–172. doi:10.1016/j.nec.2012.12.007.

338. Lafage R, Ferrero E, Henry JK, et al. Validation of a new computer-assisted tool to measure spino-pelvic parameters. *The Spine Journal* 2015; **15**(12):2493–2502. doi:10.1016/j.spinee.2015.08.067.

339. Koo TK, Li MY. A Guideline of Selecting and Reporting Intraclass Correlation Coefficients for Reliability Research. *Journal of Chiropractic Medicine* 2016; **15**(2):155–163. doi:10.1016/j.jcm.2016.02.012.

340. Shrout PE, Fleiss JL. Intraclass correlations: uses in assessing rater reliability. *Psychological Bulletin* 1979; **86**(2):420–428. doi:10.1037//0033-2909.86.2.420.

341. Demšar J. Statistical comparisons of classifiers over multiple data sets. *The Journal of Machine learning research* 2006; **7**:1–30.

342. Shea KG, Stevens PM, Nelson M, Smith JT, Masters KS, Yandow S. A Comparison of Manual Versus Computer-Assisted Radiographic Measurement: Intraobserver Measurement Variability for Cobb Angles. *Spine* 1998; **23**(5):551.

343. Salem W, Coomans Y, Brismée J-M, Klein P, Sobczak S, Dugailly P-M. Sagittal Thoracic and Lumbar Spine Profiles in Upright Standing and Lying Prone Positions Among Healthy Subjects: Influence of Various Biometric Features. *Spine* 2015; **40**(15):E900. doi:10.1097/BRS.0000000000000918.

Acknowledgements

There are four names on the front of this thesis. This a poor reflection of the number of people who should also be credited, as without them it would have never come into existence.

When I think about how this began, I struggle to imagine going down this road without the inspiration of Dr. Cecile Perrault, Dr. Xinshan Li, and Prof. Claudia Mazza. Their support for me during my undergrad gave me enthusiasm and inspiration to attempt this.

Luca thank you for providing me with the opportunity to do this work. You encouraged me and I always felt free to ask for your help when I needed it. Marco (Vice), this thesis would have been just as impossible without your guidance and insight which gave me the direction I needed.

To Marco (P), Daniele, and the group Institute of Orthopaedic Research and Biomechanics at Ulm, you provided the data I needed for the majority of my research, thank you! Not only that but you always had time to explain and help me understand the data.

I was very fortunate to belong to not one but two labs. To each and every one of you at both Rizz and Lazz, you own a slice of this pie. Between coffees, group activities (mostly food and drink related) and a friendly atmosphere I will be able to look back on these three years with a degree of fondness.

Giorgio and Francesca, I am incredibly grateful, without you both I would have quit. You also helped me learn to use OpenSim and listened to my confused ramblings as I tried to figure out what I was meant to do and how to do it.

Chloe, because of you I did actually get to do some experiments! Thank you for the opportunity. Jennifer, Eduardo, Valentina, Sara, Domi, and Julia, you made the final year a lot less stressful than it might have otherwise been and at times even fun. Always around for friendly, supportive, funny, and sometimes absurd chats. Domi, the squash games were the catharsis I needed following many long days.

My friends from Sheffield, in particular Eloise thanks for the support and the laughs.

Family, I am blessed to have a family like you all. Thank you for being so understanding and supportive over the last three years, the combination of a global pandemic and a PhD thesis has meant I have not been able to see you as much as I would have wanted (and I would like to believe less than you would have wanted as well). You never once made me feel guilty for this, encouraging me to keep pushing and were a continual source of support that I could rely on and knew was and always will be there.

Sylvia, thank you. Being relatively close geographically we thought that in these years we would see each a bit more often than we did unfortunately the pandemic got in the way of that. Despite this you were patient and by my side throughout, celebrating when it was going well and commiserating when it wasn't. You provided more moral support than you realise.

There are many other people and communities (MatLab, Stack Exchange) who in some way or another who contributed to this PhD who probably do not even know that it exists. However, this PhD would have been a lot more difficult if it were not for you, so thank you.